Probing Our Universe with Sunyaev - Zel'dovich Effect

A Thesis

Submitted for the Degree of

Doctor of Philosophy

in the Faculty of Science

By

SUBHABRATA MAJUMDAR

DEPARTMENT OF PHYSICS
INDIAN INSTITUTE OF SCIENCE
BANGALORE - 560 012, INDIA

JUNE 2001

Declaration

I hereby declare that the work reported in this thesis titled "Probing our Universe with Sunyaev-Zel'dovich effect" is entirely original and has been carried out by me independently in the Department of Physics, Indian Institute of Science, and Indian Institute of Astrophysics, under the Joint Astronomy Programme, under the supervision of Dr. Pijushpani Bhattacharjee, Indian Institute of Astrophysics, Bangalore 560 034. I further declare that this work has not formed the basis for the award of any degree, diploma, fellowship, associateship or similar title of any University or Institution.

Subhabrata Majumdar
19 June, 2001

(Subhabrata Majumdar)

Department of Physics
Indian Institute of Science
Bangalore 560 012, India.

ABSTRACT

In this thesis, we look at both thermal Sunyaev-Zel'dovich (SZ) distortion as well kinematic Sunyaev-Zel'dovich distortion of the Cosmic Microwave Background due to several possible astrophysical sources, namely, clusters of galaxies, galactic winds at high redshifts and radio galaxies.

We find that presence of cooling flows can lead to over-estimation of the value of Hubble constant by $\sim 10\,\%$ using SZ and X-ray observations of clusters of galaxies. Based on comparison of rms temperature anisotropy, obtained from simulated maps of SZ distortions of the CMB due to galaxy clusters, with Australia Telescope Compact Array limits on arc-minute scale anisotropies, we have constrained cosmological models. We have further used the power spectrum of SZ effect from galaxy clusters as an additional cosmological probe and also as a probe of cluster specific properties, like the cluster gas mass fraction.

We have calculated the SZ distortion (the mean y-distortion and the angular power spectrum) by galactic winds originating at high redshifts and found the kinetic SZ effect to be more important than the thermal SZ effect. The total power spectrum of SZ distortion from galactic winds is found to dominate over that from clusters of galaxies at 217 GHz; the frequency at which the thermal SZ effect is zero. A possible detection of the power spectrum of SZ distortion due to winds has been proposed as a tool to yield information on bias at high redshifts.

Finally, we have looked at the SZ effect by radio galaxies and found the resultant $y \sim 6 \times 10^{-7}$ from distortion by the non-thermal plasma inside the cocoons. We also estimated the thermal SZ distortion from the gas heated by the work done by the cocoons to be $\sim 5 \times 10^{-8}$. For cocoons inside clusters, we have found the mean y distortion to be of order $\sim 5 \times 10^{-6}$.

Acknowledgements

In the August of 1996, I joined I.I.Sc., full of enthusiasm. Getting a 'Ph.D.' appeared to be just a matter of time. Everything felt perfect. The sense of utopia was extremely short lived and soon I went through phases of boredom, fatigue and despair which, I guess, everyone goes through. This dichotomy between hope and hopelessness has continued till now. More often than not, the feeling 'so_much_more_to_go' has made me pensive. Now, almost there, it feels as if the last few years went by too fast. Now, I wish to linger on for some more time in I.I.Sc, the place I have grown used to, the institute I feel proud to belong to and call my own.

I would not have been in a position to write this thesis and many dreams would have been unfulfilled had it not been for two people : Pijush-da and Biman (or plain 'dada' as I call him). As different as two people can be, I always felt them to be so much similar to one another in their inherent 'goodness' to everyone around them. Their enthusiasm were infectious, their reply to all my querries encouraging and their patience limitless. They were always there not only to answer even the silliest of questions but also to listen to all the crazy research ideas that I frequently came up with, most of which did not work. Infact, I cannot remember a single incident when they have not been supportive, both academically as well as emotionally. I was lucky to have, not one, but two people who believed in my capabilities. Especially, I am grateful to Pijush-da for believing in me (at a time when no one seemed to believe) and then giving me total academic freedom. Never did he complain about my willfulness. Rarely can one get someone like him as a supervisor and I realise how lucky I am. I am also greatly indebted to dada who, despite all the trouble he had to endure due to the proximity of his house to I.I.Sc, has always been helpful and supportive in every matter that I can think of. With all due respect, dada has been more of a friend to me than an 'esteemed faculty' in R.R.I. Away from Bangalore, I'll miss accompanying him to the corner shop for the daily dose of caffeine. The best part of any day in RRI was the time spent talking with dada on every conceivable topics. Finally, let me mention that this thesis would not have been in this shape but for the many advises from dada and the meticulous corrections by Pijush-da, who went through each and every word. He also stripped my writing of all irrelevant

'literary' expressions that did not directly pertain to the central topic of the thesis.

I would like to take this opportunity to thank Arnab RaiChoudhuri and Chanda Jog for being supportive during my initial and final years and also for taking the main responsibilities which has helped to keep 'JAP' alive through all these years; without JAP, I would not have been able to get the advantage of not one or two, but three premier institutes in this country. Apart from my interest in astrophysics, this was perhaps the main reason to leave SINP and come to Bangalore.

I did not spend much time in IIA, but I wish I could. I do wish I that I had spent more time working with Pijush-da since I fully enjoyed the time we spent in his office. This is perhaps a good time to thank Profs. Cowsik and Hasan for financially supporting me with IIA funds which made it possible for me to go abroad. The commute to IIA from IISc was tiring and took a long time, but little time I spend in IIA, I enjoyed. The main reason for this were the friendship I found in the my fellow students: Ravinder, Pavan, Suresh, Geetanjali, Mahesh, Bhargavi, Mangala, Ram, Srikanth, Sridharan and Preeti. Rajaguru, Manoj and Sonjoy were of great help with ideas when I needed them, especially in dealing with bureaucracy. I can never thank Dharam enough. He has always been the helpful 'senior'. Without him, I would have been an alien to IIA and its students.

JAP gave me the opportunity to get to know many more people that I would have had otherwise. Among RRI'ans, it is a pleasure to thank Dipankar, Anantha, Dwaraka, Rajaram, Sunita, Shukre, Madhavan, Sam, ŷ and Raghu. Apart from the academic environment that they help create, I am grateful to them for treating me the same way as they would treat any other student in RRI. I was also lucky to have had all students in RRI as friends, especially Amitesh, Ashish, Giri, Jaya, Mousumi, Sushan, Kheya, Pani, Reks, Niruj, Pandey, Sushil, Shrirang, Vatsa, Viswa and Dinesh. Special thanks goes to the juniors: Suparna, Uday, Bidisha, Sudipto, Ujjal, Navinder, Raj, Sanat, Rema, Roopa, Pratiti, Dhara, Utpal for making RRI a more lively place. And Chits for always being every student's friend . RRI gave me the privilege to be treated at par. I became an 'un-officially official' part of RRI and enjoyed every facilities as did the other students. The RRI library was fabulous : it makes one fall in love with books. In the computer section I would like to thank Jacob and Ravi for taking good care of the facilities. I only hope that they would do something to help the future students from freezing in the chill of the a/c and typing with numb fingers :)

My initial period in RRI was moulded by two people: Ravi and Dipanjan. Ravi Subrahmanyan, was my first collaborator; he was also the first person to initiate me into the fascinating field of CMB, and in some way he was also my first 'de-facto' supervisor! A man of least words, he would prefer his work to speak for himself. He gave me complete freedom to go about with the work we started. He was one of the best astronomers I have met till now. Infact, someone I know referred to him as a '10 σ' peak among many others. It is almost impossible to put my gratitude for Dipanjan in a few lines. He helped me during difficult times, helped in academically and helped me overcome my hang-ups about computers. He also wasted hours

of his precious time trying to teach me efficient programming skills.

Outside work, I spent many evenings at Pijush-da's or Biman's house; after all, who doesn't like good food and 'homely' atmosphere. Whenever I was in one of these houses, I felt the essence of Kolkata, my native place, in the heart of Bangalore. Thank you, Jhuma-di and Shampa.

Sudip and Niruj, my batchmates in JAP, need special mention: I always liked their unique sense of humour and their helpful nature in times of need. I was also lucky to have other equally helpful friends in IIsc : Abhikda, Ayan, Apratim, Anasuya and Sriparna. They, along with the Gym movies, the film society screenings, the weekly 'adda' at Ratna and the not-so-frequent cooking adventures made IISc a very happening and enjoyable place to spend the PhD years.

My attraction towards the academic world was result of my interactions with a number of people. It started with two great teachers in school: Brother Kyle and Prof. Dasgupta, the former short, stout and very Irish, the latter tall, thin, old and very much a Bengali. Together they taught us mathematics and science and geography. They also taught us everything about being self-respecting and confident. It was then that I first learnt that science can be fun. They were the best teachers I ever had.

After school, I spent my most enjoyable years in St. Xaviers college. I was lucky to be in a college which had the most invigorating academic atmosphere of all colleges in Kolkata. It boasted some of the best physics teachers: Profs. S. Bose, S. Bhanja, A. C. Gomes & D. Sengupta. I would be always indebted to the Dipankar-da and Prof. Gomes who helped me pull through hard times. They had more confidence in me that I had!

The M.Sc. years were, unfortunately, bleakest times in my academic career. It were, however, during these years that I found three fantastic friends: Rupa, Poonam and Sharmita. Distance has never been a barrier to the friendship we share. And then there were Indra, Rana, Kutush, Ruplekha, Kaushik, Shibaji, Subroto, Asmita and Sandhya; they made those dragging years so much more exiting.

During the PhD years I have been lucky to have come to know people like Bikram, Somnath-da, Sayan-da, Shiv, Varun Sahni, Charu, Nabila, Alain Blanchard, Sergio Colafrancesco, Luca Amendola and Amitabha-da. Although, all of them come from the academic world, I have come to realise that there are so many more interesting things outside academics, even for someone who is into academics. The two chance meetings that I had with Joe Silk have made a lasting impression on me. I wish I could have spent some more time with him.

This thesis would have been in this shape had it not been for Tirtha, Mama, Mamon and Suparna. A lot of the credit for the work completed in the last three years go to the motorbike I had :) It gave me unplugged joys of freedom.

Over all these years in IISc, my most special friends have been : Sanjib, Tirtha, Mamon, Mama, Raju,

Sonu and Shan :) I cannot imagine the last five years without them. Infact, I could not have done without them. Babua, Biplab, Sayan, Subha, Sankar and Rajat have always made me believe in the adage 'Old is Gold'. My first days of youth were spent with them and they were undoubtedly the best days. The famous five: Baju, Jishnu, Mou, Tumpa and me over the time grew up to secret seven with the addition of Mitu and Hemant. They, along with Rini, remain too dear to me to express anything at all in words.

This note remains unfinished without the mention of the 'small-ones', my favourites: Puchun, Mohor, Munai, Rudra, Tinni, Sayan, Paul and Aman. At times they have been sources of my sustenance.

Although, I spent many years alone in Kolkata away from my parents, Kanan-mashi never let me feel the absence of my mother. Along with 'Jethima', she was always there to take care of me. Let me take this opportunity to express my deep respect for 'Jethu' and my respect for all that 'Kakima' who has managed to so much against all the odds.

It's always the hardest to acknowledge your closest ones; anything said seems too little. It is impossible to think of this world without Mamu, Mami, Kutti-mashi, Dida and Dadi in it. I also cannot dream of this world without Moon in it; she has been a completely new world to me. I must say I am lucky. To my parents, I can only say like a child that 'you are the best:)'. They gave me the best that one can give to a son: belief, trust, freedom and respect. Ma, I only wish I could spend more time with you. I can say nothing more. Its useless to try to express all that I would like to and so I give up the idea completely.

I was brought up by my grand parents. The most beautiful period of my life was spent in their shadows. They were my first teachers who always taught by example. They laboured to give me deep roots when I was a child, but never lived to see me take my wings. Whatever I am, is because of them.

This thesis is dedicated to the memory of Dadun and Didun, my grand parents.

" *With them the Seed of Wisdom did I sow,*
And with my own hand labour'd it to grow
And this was all the Harvest that I reap'd
'I came like Water and like Wind I go'. "

Rubáiyát of Omar Khayyám

Contents

A Brief List of Abbreviations

Ω_o	Cosmological total density parameter
Ω_b	Cosmological baryon density parameter
Ω_Λ	Cosmological vacuum energy density parame
H_o	Hubble Constant
C(MB)	Cosmic (Microwave Background)
SZ(E)	Sunyaev-Zel'dovich (Effect)
TSZE	Thermal Sunyaev-Zel'dovich Effect
KSZE	Kinematic Sunyaev-Zel'dovich Effect
CDM	Cold Dark Matter
SCDM	Standard Cold Dark Matter
OCDM	Open Cold Dark Matter
ΛCDM	Lambda Cold Dark Matter
ICM	Intra-Cluster Medium
IGM	Inter-Galactic Medium

Chapter 1

Prologue

The Cosmic Microwave Background (CMB) radiation is now established, without doubt, to be the relic radiation of the early Universe (Srianand et al. 2000) and anisotropies of the CMB are thought to carry an imprint of the 'surface of last scattering'. These are called the primary anisotropies. The first detection of such anisotropies were reported almost a decade ago (Smoot et al. 1992), by the Cosmic Background Explorer (COBE) satellite. Ever since then, the study of the anisotropies of the CMB has grown by leaps and bounds to occupy a major place in our effort to understand the Universe we live in.

The primary anisotropy of the CMB gives us one of the best handles on the cosmological parameters that quantify any cosmological model. The amplitude of the temperature anisotropy of the CMB are, generally, expressed in terms of their multipole expansion, *i.e.*, $\Delta T_{\rm cmb}/T_{\rm cmb} = \Sigma_{\ell m} a_{\ell m}\, Y_{\ell m}\,(\theta\,,\phi)$. The angular power spectrum can then be expressed as $|a_\ell|^2 = \frac{1}{2\ell+1}\,\Sigma_m |a_{\ell m}|^2$. It is usually assumed that $a_{\ell m}$ obeys Gaussian statistics, and the ensemble of the values of $a_{\ell m}$ has a zero mean with a standard deviation that depends only on ℓ and phase that varies from 0 to 2π. The temperature field is completely specified by the two-point correlation function given by $C(\theta) = \langle \Delta T(\mathbf{n_1})\, \Delta T(\mathbf{n_2}) \rangle$, where θ is the angle between the two direction given by the units vectors $\mathbf{n_1}$ and $\mathbf{n_2}$. For a Gaussian random field, one then has $C(\theta) = \frac{1}{4\pi}\,\Sigma_\ell\,(2\ell+1)\,C_\ell\,P_\ell(\cos\,\theta)$, where $C_\ell = \langle |a_{\ell m}| \rangle$. The angular power spectrum, is then, the values of C_ℓ as a function of ℓ[1]. In general, the angular power spectrum of these anisotropies, as seen by observers in the present epoch, is found to depend sensitively on the parameters of the background cosmology — the Hubble constant $H_{\rm o}$, the mean matter density $\Omega_{\rm o}$, the composition of the matter (*i.e.*, the amount of baryonic matter, cold dark matter, hot dark matter etc.) and any cosmological constant Λ —

[1]Note that, $\ell \approx \frac{1}{\theta}$ and that one generally plots $\ell(\ell+1)C_\ell$ as a function of ℓ.

and on the magnitude and spectrum of primordial perturbations in the matter. Several authors have shown that the characteristic features in the CMB anisotropy spectrum have marginal and joint dependencies on the cosmological parameters. For example, at large and intermediate angular scales ($l \leq 500$), for $\Omega_0 < 1$, the Doppler peaks in the CMB anisotropy spectrum are shifted towards larger l values w.r.t. the case for a flat Universe with $\Omega_o = 1$. (see, for example, Kamionkowski & Spergel 1994 or Lineweaver & Barbosa 1998). The ionization history of the Universe also modifies the spectrum of the CMB. Primary anisotropies at small angular scales ($l \geq 500$) are expected to be relatively damped in most models of structure formation due to the thickness of the last scattering surface and the diffusion damping of sub-horizon scale baryon fluctuations in the pre-recombination era; anisotropies at even larger l may be critically dependent on the reionization history. The major portion of all the work on CMB distortion, till now, has been the study of these primary anisotropies.

Important modifications to CMB primary anisotropy can, however, occur even after decoupling. These are known as secondary anisotropies and are mainly caused by non-linear feedback where the small fraction of luminous matter injects significant energy into the intergalactic medium (or intra-cluster medium) to cause new distortions of the CMB. Arcmin-scale anisotropies may be generated due to coupling between density perturbations and bulk velocities (Vishniac 1987, Hu, Scott & Silk 1994, Persi et al. 1995). One can also have the so called Rees-Sciama effect (Rees & Sciama 1968), once non-linear structures form and the conformal time derivative of the gravitational potential is no more zero due to perturbations. Separately, decrements in the CMB sky may be generated by the inverse-Compton scattering of background photons as they pass through concentrations of hot gas associated with astrophysical entities along the line of sight; this phenomenon is referred to as the Sunyaev Zel'dovich effect (SZE) (Sunyaev & Zel'dovich, 1972). The main aim of this thesis is to use the secondary distortion due to SZE, in different astrophysical contexts, as a probe of our Universe. We will use it not only to study the background cosmology but also as a probe of astrophysical sites of hot plasma. In the next couple of sections we give a very brief introduction to SZE mainly focusing on that due to intra-cluster matter (ICM)) and keep detailed discussion of SZE for specific cases to be given at the beginning of each chapter.

1.1 The SZE as an observational tool

It has been long argued that since clusters of galaxies are, perhaps, the largest virialized objects containing a large chunk of observable matter (as well as dynamically estimated dark matter), observations of clusters can be taken to be a fair representation of observation of the Universe

around us. An added advantage of observing clusters has been the large angular radii subtended by clusters. The major disadvantage is that clusters rarely exist beyond redshifts of $z \sim 1$. To probe farther, one has to look at other objects like ordinary and active galaxies, cosmic explosions, etc. In this introductory note, however, we will focus only on clusters of galaxies and deal with other objects (which typically release energy to the inter-galactic matter (IGM), in later chapters.

Traditionally, optical observations have been the main probe of galaxy clusters and catalogs of them were made (*e.g.*, Abell 1958; Carlberg et al. 1997). Optical identification is, however, not trivial and becomes increasingly difficult for far away objects. Especially, for galaxy clusters, it is difficult to tell whether a galaxy at the edge of the cluster is bounded to the cluster or a field galaxy. Optical studies also suffer from projection effects. Spectral studies are time consuming and can only be done for the more luminous objects.

On the other hand, galaxy clusters are known to contain most of the baryonic matter in the Universe the form of X-Ray emitting hot gas bound to the cluster by its gravitational potential. The galaxy clusters can, thus, be observed in X-Ray. In this band, the whole of the cluster (now defined as the region within some radius called the virial radius) appears as a luminous source. This reduces some of the problems faced by optical observations. However, it is still difficult to look at far away ($z \gtrsim 1$) objects with X-Ray surveys, with the majority of the clusters detected below $z \sim 0.5$. One reason for this is that since X-Ray emission is proportional to the square of the electron density, regions having low densities become faint in emission. We note here, that for optical as well as the X-Ray observations, the observed flux declines as d_L^{-2}, where d_L is the luminosity distance. This selection function limits the redshift up to which one can observe.

A third probe of galaxy clusters is offered by the Sunyaev-Zel'dovich effect . The SZE arises in the galaxy clusters from the inverse Compton scattering of CMB photons when the photons pass through the hot ICM. Using SZE to probe galaxy clusters will be a major theme of this thesis. Indeed, any massive source of hot plasma (*e.g.*, ionized bubbles around quasars before cosmological re-ionization (Aghanim et al. 1996)) will distort the CMB through SZE. As already mentioned, one of the main purpose of this thesis is to probe our Universe by studying the SZE distortion of the CMB due to a variety of sources at different redshifts.

There are mainly two ways by which SZE can distort the CMB, namely, the thermal SZE (TSZE) and the kinematic SZE (KSZE). The first occurs due to scattering from the random motions of the hot gas whereas the second is due to the scattering of the CMB photons due to the bulk motion of the gas. The physics of both TSZE & KSZE are described in detail in the next chapter. The interesting point about TSZE is its spectrum: since scattering by the hot gas transfers some low energy photons to higher energies while at the same time conserving the total number of photons,

the net effect is a shift in the CMB spectrum up in energy which slightly distorts the blackbody curve. There is a decrement of photons at low energies and a resultant increment at higher energies with the crossover occurring at a frequency $\nu \sim 217$ GHz, at which the distortion from TSZE is zero. The SZ distortion appears as a decrement for wavelengths ≥ 1.44 mm and as an increment for wavelengths ≤ 1.44 mm. This results in a unique non-Blackbody spectrum of the CMB and experiments with good frequency coverage[2] will be able to distinguish it from the purely Blackbody spectrum. The promise of using TSZE as a probe depends heavily on this unique spectral shape.

The kinematic SZ effect is a simple doppler shift in the frequency of the CMB photons due to the bulk motion of the hot gas. Hence, it does not cause any deviation from the blackbody spectrum. This makes it impossible to separate out the KSZE distortion from the primary distortion of the CMB by spectral methods. It is, therefore, important to understand the *expected* KSZE contribution due to various astrophysical sources to the total observed CMB anisotropy, by modeling these sources. This is what we do in Chapter 6 of this thesis. An important point to be mentioned here is that due to the different spectral behaviour of TSZE and KSZE, the maximum contribution from KSZE occurs at the frequency where the TSZE is zero. This fact can, in fact, be used to estimate the peculiar velocity of a cluster (see *e.g.*, Birkinshaw 1999).

The TSZE, described above, provides a rather nice and complimentary approach to the traditional probes of our Universe. This probe has advantages which are unique to itself. First, the SZE flux is proportional to the the electron number density (and not its square as in X-Ray). Thus, low density regions can also be probed more easily than by X-Ray. Secondly, the integrated SZE flux declines as d_A^{-2}, where d_A is the angular diameter distance. Thus, SZE does not suffer from the cosmological $(1+z)^{-4}$ dimming. This is because the SZE is a fractional change in the brightness of the CMB and CMB energy density itself decreases as $(1+z)^4$. Also d_A, in general, grows more slowly than d_L and even decreases after a certain redshift ($z \sim 1$). This means that SZE flux from a cluster drops more slowly with distance than the X-Ray surface brightness of the cluster (and can even increase after a particular redshift). Finally, since the flux decrement from the integrated SZE due to an unresolved object (say, galaxy cluster at high z) is proportional to the total mass of the hot-gas times the particle-weighted temperature (explained in detail in Chapter 4 & 5), it is independent of any spatial distribution of the gas. If the observations can resolve the clusters through SZE, particularly at lower redshifts, the observed sky CMB temperature distribution will then be sensitive to the temperature structure within the clusters. This may be contrasted with X-ray emission images of cluster gas distributions which are sensitive mainly to the gas density

[2] *e.g.*, the future satellite mission Planck has a frequency coverage from 30-850 GHz and would be able to separate out the TSZE contributions to the temperature anisotropies

distribution and relatively insensitive to the temperature distribution. All these advantages make SZE a preferable tracer of clusters and other massive hot gaseous objects at cosmological distances. These have been the motivations behind a number of studies in the recent past (see, for example Blanchard & Bartlett 1998, Oukbir & Blanchard, 1992, 1997, Bartlett & Silk 1994, Barbosa et al. 1996 and Colafrancesco et al. 1997). All these studies have looked at SZE as a probe of the background cosmology, especially the cosmological matter density parameter Ω_o . Also, as pointed out first by Silk and White (1978) and later discussed by numerous authors (*e.g.*, Birkinshaw & Hughes 1994; Silverberg et al. 1997), one can combine the X-ray and radio observations for clusters to estimate the Hubble constant H_o (Birkinshaw, 1999)

The main disadvantage of using SZE as a probe is that the SZ signal is rather weak and difficult to detect. Recently, however, high signal to noise detections of SZE have been made over a wide range in wavelengths using single dish observations: at radio wavelengths (Herbig et al, 1995. Hughes & Birkinshaw 1998), millimeter wavelengths (Holzapfel et al. 1997, Pointecouteau et al. 1999) and sub-millimeter wavelengths (Komatsu et al. 1999). Interferometric observations have also been carried out to image the SZ effect (Jones et al. 1993, Saunders et al. 1999, Rees et al. 1999, Grego et al. 2000). Continuous developments in the technology of microwave background (MB) measurements give us reasons to expect that SZE will become a major observational tool in cosmology in the near future. Over the next few years one expects substantial improvements in the SZE work to emerge from spectral measurements and from interferometric observations of clusters and the CMB using optimized interferometers.

1.2 Galaxy clusters and SZ distortion : A rudimentary treatment

The basic physics behind SZ distortion by clusters of galaxies is quite simple. A fraction of the CMB photons after decoupling ($z \sim 1100$) can be inverse Compton scattered by hot electrons in the intracluster medium as they traverse through the cluster. This can then lead to to an apparent change in the temperature of the CMB in the direction of the cluster. Since, typically, only a small percent of the background photons passing through the cluster get scattered, there is only a fractional change in the CMB sky temperature due SZ effect from clusters. It is easy to obtain *an order of magnitude* estimate for such a distortion. Let us assume that a cluster of galaxy has a total mass $M = 5 \times 10^{14} M_\odot$ and extends up to an effective virial radius $R_{vir} = 2$ Mpc. Since the ICM sits in the gravitational potential of the total cluster mass, its electron temperature, T, is given by

$$k_B T \approx \frac{G M m_p}{2 R_{vir}} = 6.65\,\mathrm{KeV} \quad , \tag{1.1}$$

where G is the gravitational constant and m_p is the proton mass. From observations, it is known that about 10% to 20% of the total mass of the galaxy cluster is in the form of ICM (White & Fabian, 1995). The contribution by the galaxies to the total baryonic mass is negligible (White et al. 1993). The temperature of the ICM is hot enough to ionize the gas. The ionized electrons of the ICM inverse Compton scatter the CMB photons. Since, the scatterings are essentially non relativistic in nature (*i.e.*, $k_B T/m_e c^2 << 1$), one can take the scattering cross section to be Thompson cross section σ_T. The scattering optical depth, τ_e, for the above cluster can then be written as

$$\tau_e = n_e \sigma_T (2 R_{vir}) \approx 5.25 \times 10^{-3} \quad . \tag{1.2}$$

In a single scattering, the frequency of the photon is slightly shifted, with up-scattering more probable than down scattering , because of the higher temperature of the electrons relative to the photons. The mean change in photon energy, ϵ, due to single scattering can be written as (Rybicki & Lightman, 1980)

$$\frac{\Delta\epsilon}{\epsilon} \approx \frac{k_B T}{m_e c^2} \sim 1.33 \times 10^{-2} \tag{1.3}$$

where we have used Equation (1.1).

Thus, combining Equations (1.2) & (1.3), and using the fact that for small τ_e (*i.e.*, $\tau_e << 1$) the number of scatterings is equal to τ_e, one can get mean change in the CMB sky temperature due to SZE from the galaxy cluster to be $\approx 7 \times 10^{-5}$. The point to be noticed is that this distortion is almost an order of magnitude larger than that due to primary anisotropies. At the same time one should compare it with the COBE limit on the mean spectral distortion ($< y >= 1.5 \times 10^{-5}$).

Similarly, an order of magnitude estimate can be made for the kinematic SZ effect. In this case all the photons get doppler shifted in frequency by a factor v/c, where v is the line of sight component of the peculiar velocity of motion of the cluster. Bulk peculiar velocities are expected to be less than 1000 km/s. One can then multiply the temperature change due to the bulk motion with the scattering optical depth, to get

$$\frac{\Delta T_{\mathrm{cmb}}}{T_{\mathrm{cmb}}} \approx \frac{v}{c} \times (5.25 \times 10^{-3}) < 1.75 \times 10^{-5} \quad , \tag{1.4}$$

where T_{cmb} is the CMB temperature. Typically, peculiar velocities are $\sim$ 300 km/s. Hence, for clusters of galaxies TSZE dominates over KSZE by at least an order of magnitude.

Since the fractional change of CMB temperature due to SZE towards a cluster of galaxies comes out greater than the mean fractional change of the CMB temperature due primary anisotropies, one can look for it in pointed radio studies of clusters. This is routinely done and the number of observations of SZE from clusters has grown tremendously in the last decade (for a comprehensive list of such observations, see Birkinshaw 1999). The secondary anisotropies due to SZE are distinguishable from the primary anisotropies by their different spatial distribution and frequency dependence. The difference in spatial distribution is easy to understand: SZE anisotropies are *localized* and are seen towards clusters of galaxies. In contrast, primary anisotropies are *non-localized* and are randomly (assumed to be Gaussian) distributed over the sky, with almost constant correlation amplitude in different patches of the sky. A result of the above 'localized' property of SZE anisotropies is that the resulting sky brightness fluctuations are strongly non-Gaussian and asymmetrical (skewed).

1.3 The scope of this thesis: A synopsis

Our basic philosophy in probing our Universe with SZE is based on the concept of hierarchical structure formation in a cold dark matter dominated Universe where larger structures grow out of accretion of matter onto smaller structures and hence form later in time (or equivalently at lower redshifts). Thus, one has only to probe lower mass astrophysical structures in order to probe higher redshifts. This is seen from Figure (4.3) which shows that abundance for lower masses peaks at higher redshifts (although the Figure shows the abundance of objects in the mass range suitable for clusters, the same conclusions can be drawn for smaller masses as well). We cover a large range in redshift upto $z \sim 15$ (equivalently, back to a time when the Universe was $\sim 1\%$ of its present age) by making use of the following strategy :

- We study SZE from pointed observations of X-Ray selected clusters of galaxies to estimate H_o . In this way, we probe up the Universe to $z \sim 0.5$.
- We then look at non-targeted present and future observations of SZE from galaxy clusters. This can push back the maximum redshift to $z \sim 1$.
- To probe higher redshifts, we look at SZE distortions by cocoons of radio galaxies. This can effectively probe redshifts up to $z \sim 5$.
- Finally, to go to even higher redshifts, we look at SZE distortions due to galactic winds coming out of dwarf galaxies, which allows us to go to $z \leq 15$.

In the next chapter, we give a primer on SZE, expanding on and going beyond the rudimentary approach to the physics of SZE given in the present chapter. We look at the non-relativistic and relativistic Comptonization of the CMB by hot electrons, and derive the amplitude and spectral dependence of SZE (both TSZE and KSZE). We briefly discuss corrections to the simple non-relativistic formula for the SZE, and end the chapter with some comments on the observational aspects of SZE.

The main new work presented in this thesis begins in Chapter 3, where. we start by looking at SZE in the nearby Universe, before looking at the more distant Universe in the later chapters. In this chapter, we study the effects of cooling flows in galaxy clusters on the Sunyaev-Zel'dovich distortion of the CMB and their possible cosmological implications, especially in the determination of the Hubble constant. It is well known that SZE, along with X-ray observations of clusters, can be used to estimate H_o. It is also known that a significant fraction of clusters have cooling flows in them, which change the pressure profile of intracluster gas. Since the SZ decrement depends essentially on the pressure profile, it becomes important to study possible changes in the determination of cosmological parameters in the presence of cooling flows. To do so, we build several representative models of cooling flows and compare the results with the corresponding case of gas in hydrostatic equilibrium. We find that cooling flows can lead to an over-estimation of the Hubble constant. Specifically, we find that for realistic models of cooling flows with mass deposition, the deviation in the estimated value of the Hubble constant (as compared to that in absence of a cooling flow) can be of order $\sim$ 10% even after excluding $\sim$ 80% of the cooling flow region from the analysis. Since, expected determination of number counts of clusters based on SZE are planned as an interesting way to constrain other cosmological parameters, like Ω_0, we also discuss the implications of the presence of clusters with cooling flows for such estimates.

Using SZE from clusters of galaxies as a probe of cosmological parameters is the main aim of Chapter 4. In the context of cold dark matter (CDM) cosmological models, we simulate images of the brightness temperature fluctuations in the cosmic microwave background (CMB) sky owing to the Sunyaev Zel'dovich effect in a cosmological distribution of clusters. We compare the image statistics with recent Australia Telescope Compact Array (ATCA) limits on arcmin-scale CMB anisotropy. The SZE effect produces a generically non-Gaussian temperature field and we compute the variance in the simulated temperature-anisotropy images after convolution with the ATCA beam pattern, for different cosmological models. All the models are normalized to the 4-year *COBE* data. We find an increase in the simulated-sky temperature variance with increase in the cosmological density parameter Ω_0. Finally, we compare our results with the upper limits on the sky variance set by the ATCA, based on which we argue that closed Universe models are disfavoured

and that instead low-Ω_0 open-Universe models are preferred. This result follows irrespective of any present day observations of the mass variance in regions of size $8h^{-1}$Mpc (σ_8).

Chapter 5 is devoted to a detailed modeling of the power spectrum of SZE from clusters and groups of galaxies, taking both Poisson distribution as well as clustering of the clusters into account. We show how the power spectrum shape and amplitude differ as functions of various parameters and how one can use such information to probe the parameter space. As a specific example, we show how the power spectrum of the secondary CMB anisotropies due to the thermal Sunyaev-Zel'dovich Effect by clusters of galaxies can be studied to constrain cluster-specific properties (such as the gas mass fraction of the clusters). We show the SZE power spectrum from clusters to be a very sensitive probe of any possible evolution (or constancy) of the gas mass fraction. The position of the peak of the SZE power spectrum is shown to be a strong discriminatory signature of different gas mass fraction evolution models. As an example, for a flat Universe, we show that there can be a difference in the l values of the peak of the SZE spectra of as much as 3000 between a constant gas mass fraction model and an evolutionary one. Since observational determination of power spectrum from blank sky surveys is devoid of any selection effects that can possibly affect targeted X-ray or radio studies of gas mass fractions in galaxy clusters, the use of power spectrum as a discriminator is argued to be especially promising. We also show how one can use the power spectrum of SZE, in a complimentary approach to that described in Chapter 4. to constrain cosmological models.

Other than SZE from clusters of galaxies, any large reservoir of hot gas is capable of distorting the CMB through the SZE, and we look at one such case in Chapter 6. There, we consider the distortions in CMB due to galactic winds at high redshift. Winds flowing out from galaxies have been hypothesized to be possible sources of metals in the intergalactic medium, which is known to have been enriched to $\sim 10^{-2.5}$ $Z_\odot$ at $z \sim 3$, where $Z_\odot$ is the solar metallicity. Using the above fact as a motivation, we model these winds as functions of mass of the parent galaxy and redshift, assuming they initiate at a common initial redshift, z_{in}, and calculate the mean Compton y distortion and the angular power spectrum of the SZE distortion in the CMB. We find the thermal SZE due to the winds to be consistent with values estimated before. The distortion due to the kinetic SZE is, however, found to be more important than the thermal SZE. This makes the distortion due to galactic winds an important contributor to the power spectrum of CMB distortions at very small angular scales ($l \sim 10^4$). We also show that the power spectrum due to clustering dominates the Poisson power spectrum for $l \leq 4\text{-}5 \times 10^5$. Finally, we show explicitly how the combined power spectrum from galactic winds dominates over that of galaxy clusters at 217 GHz, a frequency relevant for planned space mission Planck. We also discuss how these constraints change when the efficiency of the winds is varied.

In the second last chapter, i.e Chapter 7, we consider the distortion in the CMB due to non-thermal electrons in the cocoons of radio galaxies, and due to thermal gas shocked by the cocoons. For the distortion from non-thermal electrons, it has been recently claimed that the integrated distortion from the population of radio galaxies is of order 10^{-5}. Later it was pointed out that this result suffers from an over-estimation of the energy input rate by the radio jets. We find that the above result also suffers from the neglect of energy loss mechanisms in the cocoons. In our calculation, we take into account the loss of energy of the cocoons due to the work done by them against the surrounding medium and due to radiation, and show that the mean Compton y-parameter of distortion is far less than it has been claimed, even when the same rate of energy input by radio galaxies is considered. In addition, we investigate the dependence of the distortion on the cosmological models, and find that the distortions are smaller in ΛCDM and OCDM models than in the SCDM case. In the standard ΛCDM cosmology, we find a mean y parameter of order 6×10^{-7}. We also calculate the angular power spectrum of distortion and find that the resulting distortion peaks at similar angular scales as that due to hot gas in clusters but with much lower amplitude. We also find that earlier calculations have over-estimated the of distortion due to the gas heated by the work done by cocoons has been overestimated. Although the heating rate by the cocoons is substantial, we find that the resulting distortion is $\sim 5 \times 10^{-8}$, since most of the heating takes place at low redshifts where the efficiency of energy loss due to inverse Compton scattering is small. For cocoons embedded in clusters, we found that the distortion from individual cocoons could be as large as $y \sim 10^{-4}$ and estimate a mean y distortion from the population of cocoons in clusters to be of order 5×10^{-6}. In view of these results, we conclude that the upper limits on the redshift of preheating for clusters, obtained with the earlier estimate of distortion, are weaker than previously thought.

Finally, in the last chapter (*i.e.*, Chapter 8), we conclude by summarizing the main issues dealt with in this thesis and pointing out the possibilities that studies of SZE hold for the future.

1.4 Post-Script

We have attempted to make the thesis as self contained as possible without being too voluminous. Other than Chapters 4 & 5, all the other chapters can, more or less, be read independently.

The main new results presented in this thesis are partially based on the following articles:

- Cosmology with Sunyaev-Zel'dovich effect,
  Subhabrata Majumdar,
  Indian Journal of Physics, **73B**, (1999), 835.

- On cooling flows and Sunyaev-Zel'dovich effect,
  Subhabrata Majumdar and Biman B. Nath,
  The Astrophysical Journal, **542**, (2000), 597.

- Constraints on Structure Formation Models from Sunyaev-Zel'dovich Effect,
  Subhabrata Majumdar and Ravi Subrahmanyan,
  Monthly Notices of the Royal Astronomical Society, **312**, (2000) 724.

- Sunyaev-Zel'dovich distortion from early galactic winds,
  Subhabrata Majumdar, Biman B. Nath and Masashi Chiba,
  Monthly Notices of the Royal Astronomical Society, in Press.

- Probing the evolution of gas mass fraction with Sunyaev-Zel'dovich effect,
  Subhabrata Majumdar,
  The Astrophysical Journal Letters, **324**, (2001), in Press.

- Microwave background distortion from radio galaxy cocoons,
  Biman B. Nath and Subhabrata Majumdar,
  Monthly Notices of the Royal Astronomical Society, submitted for publication.

- Constraining cosmological parameters with Sunyaev-Zeldovich surveys,
  Subhabrata Majumdar and Ravi Subrahmanyan,
  in Proceeding of "Workshop on Cosmology: Observations confront Theories" in IIT-Kharagpur
  Janauary, 1999
  Pramana, **53**, (1999) 971.

- Galactic winds at high redshifts and small scale CMB anisotropy,
  Subhabrata Majumdar, Biman B. Nath and Masashi Chiba,
  To be published in the proceedings of the international conference on "Cosmic Evolution",
  held in IAP, Paris, November 2000.

- Non-targeted studies of Sunyaev-Zel'dovich effect,
  Subhabrata Majumdar,
  To be submitted for publication.

Chapter 2

A primer on Sunyaev-Zel'dovich effect

In this chapter, we give a short review of the SZE. First, we take a cursory look at the Boltzmann equation and also at some rudiments of radiative transfer that would be needed for a proper treatment of SZE. We then proceed to the more mathematical aspects of of inverse Compton scattering. Towards the end of the chapter we look at the different possible kinds of SZE, and finally we focus on some observational issues related to the SZE. The material in this chapter draws heavily upon the excellent reviews by Birkinshaw (1999), Bernstein & Dodelson (1990) and Rephaeli (1995b). The emphasis is on the theoretical aspects of SZE. However, in the last section, we also briefly look at the observational aspects.

2.1 Preliminaries

2.1.1 Basics of radiation field

In this section, we look at the basic of the CMB radiation field as an example of an isotropic and thermal radiation background. The treatment closely follows that of Birkinshaw (1999), which is based on Shu (1991). In this chapter all the vectors are denoted by bold letters.

The distribution function, $f_\alpha(\mathbf{r},\mathbf{p}_\nu,t)$, of any radiation field is defined such that $f_\alpha d^3r d^3p_\nu$ is the number of photons in the real space volume d^3r about r and the momentum space volume d^3p_ν about $\mathbf{p}_\nu$ (ν being the frequency) at time t with polarization $\alpha = 1, 2$. This distribution can be related to the photon occupation number, $n_\alpha(\mathbf{r},\mathbf{p}_\nu,t)$, by

$$n_\alpha(\mathbf{r},\mathbf{p}_\nu,t) = h^3 f_\alpha(\mathbf{r},\mathbf{p}_\nu,t) \tag{2.1}$$

The energy crossing an area element dS in time dt from within solid angle $d\Omega$ about $\hat{\mathbf{k}}$ and with frequency in the range ν to $\nu + d\nu$ is given by $I_\nu\,(\hat{\mathbf{k}}.\mathbf{dS})\,d\Omega\,d\nu\,dt$, where $I_\nu(\hat{\mathbf{k}},\mathbf{r},t)$, is the specific intensity of radiation and is also related to the distribution function by

$$I_\nu(\hat{\mathbf{k}},\mathbf{r},t) = \sum_{\alpha=1}^{2}\left(\frac{h^3\,\nu^3}{c^2}\right) f_\alpha(\mathbf{r},\mathbf{p}_\nu,t) \quad . \tag{2.2}$$

Now, for CMB radiation, the occupation number has a Planckian distribution given by

$$n_\alpha = \left(e^{h\nu/k_B T_{\rm cmb}} - 1\right)^{-1} \quad \text{for } \alpha = 1,2 \quad , \tag{2.3}$$

where the $T_{\rm cmb}$ is the temperature of the CMB photons. So, the radiation field is given by

$$I(x) = I_\nu = \frac{2\,h\,\nu^3}{c^2}\left(e^{h\nu/k_B T_{\rm cmb}} - 1\right)^{-1} \tag{2.4}$$

The number density of CMB photons in the Universe is then given by

$$\begin{aligned} n_\gamma &= \sum_\alpha \int f_\alpha(\mathbf{p}_\nu)\,d^3p_\nu \\ &= \frac{8\pi}{h^3\,c^3\,\beta^3}\int_0^\infty \frac{x^2\,dx}{(e^x-1)} \\ &= 16\pi\,\zeta(3)\left(\frac{k_B T_{\rm cmb}}{hc}\right)^3 \\ &\approx (4.12)\times 10^8 \quad \text{photons}\,\text{m}^{-3} \end{aligned} \tag{2.5}$$

In (2.5) $\zeta(x)$ is the Riemann zeta function ($\zeta(3) \approx 1.202$) and $\beta = 1/k_B T_{\rm cmb}$. In a similar way, the energy density of CMB radiation field can be calculated as,

$$\begin{aligned} u_\gamma &= \sum_\alpha \int h\nu\, f_\alpha(\mathbf{p}_\nu)\,d^3p_\nu \\ &= \frac{8\pi}{h^3\,c^3\,\beta^4}\int_0^\infty \frac{x^3\,dx}{(e^x-1)} \\ &= \frac{8\pi^5\,h\,c}{15}\left(\frac{k_B T_{\rm cmb}}{h\,c}\right)^4 \\ &= (4.19)\times 10^{-14} \quad \text{J}\,\text{m}^{-3} \end{aligned} \tag{2.6}$$

We have taken $T_{\rm cmb}$ to be 2.725 K.

Commonly, the specific intensity is described in units of brightness temperature, $T_{\rm R-J}$, which is defined as the temperature of the thermal radiation field which in the Rayleigh-Jeans limit (*i.e.*,

low frequency) would have the same brightness as the radiation that is being described. In the limit of low frequency (2.4) is reduced to $I_\nu = 2k_B T_{cmb}\nu^2/c^2$, so that

$$T_{R-J}(\nu) = \frac{c^2 I_\nu}{2k_B \nu^2} \tag{2.7}$$

Thus, the brightness temperature (of a thermal spectrum) is frequency dependent, with peak value equal to the radiation temperature at low frequencies. T_{R-J} tends to zero in the Wien tail.

Finally, we need to look at the propagation of the background radiation and this can be done with the help of the transport equation. The transport equation, for a flat space time, in the presence of absorption, emission and scattering processes can be written as

$$\frac{1}{c}\frac{\partial I_\nu}{\partial t} + \hat{\mathbf{k}}.\nabla I_\nu = j_\nu - \alpha_{\nu,abs} I_\nu - \alpha_{\nu,sca} I_\nu + \alpha_{\nu,sca} \int q_\nu(\hat{\mathbf{k}}, \hat{\mathbf{k}}')\, I_\nu(\mathbf{k}') d\Omega' \tag{2.8}$$

In the above equation, j_ν is the emissivity along the path (the energy emitted per unit time per unit frequency per unit volume per unit solid angle), $\alpha_{\nu,abs}$ is the absorption coefficient (the fractional loss of intensity of the radiation per unit length of propagation because of absorption by material in the beam), $\alpha_{\nu,sca}$ is the scattering coefficient (the fractional loss of intensity of the radiation per unit length of propagation because of scattering by material in the beam), and $q_\nu(\hat{\mathbf{k}}, \hat{\mathbf{k}}')$ is the scattering redistribution function — the probability of a scattering from direction $\hat{\mathbf{k}}'$ to $\hat{\mathbf{k}}$. The absorption coefficient is regarded as containing both true absorption and stimulated emission. An important property of I_ν that follows from its definition is that it is conserved in flat space times in the absence of radiation sources or absorbers.

2.1.2 The Boltzman Equation

For an ensemble of particles, if the motion of one particle is completely independent of all other particles, then to describe the state of the particles, one can specify the single particle distribution function given by $f(\mathbf{x}, \mathbf{p}, t)\, d^3x\, d^3p$, which is the probability of finding a single particle in the phase space volume $d^3x\, d^3p$ around the point ($\mathbf{x}$, $\mathbf{p}$) at time t. Now, if there are no interactions between the particles and if they are non-relativistic, then the distribution obeys the Liouville equation

$$\frac{df}{dt} = \frac{\partial f}{\partial t} + \frac{\mathbf{p}}{m}.\frac{\partial f}{\partial \mathbf{x}} + F(\mathbf{x}, \mathbf{p}, t).\frac{\partial f}{\partial \mathbf{p}} = 0\,, \tag{2.9}$$

where $\mathbf{F}$ is any force that may be present, and m is the mass of a particle assumed same to for all particles.

In the case of interparticle interaction being random and statistical in nature, one cannot describe the system by a mean force F, but one has to consider instantaneous collisions between the particles (and this is the case for photon - electron interactions). These collisions will remove particles from (or add particles to) a cell in phase-space. The total rate of removal of particles from a phase-space cell $d^3x\,d^3p$ is given by

$$\int f(\mathbf{x},\mathbf{p})\,d^3\mathbf{p}_1\,2\pi\,s\,ds\,\frac{|\mathbf{p}-\mathbf{p}_1|}{m} \tag{2.10}$$

where it is assumed that collision took place between particles with momenta $\mathbf{p}$ and $\mathbf{p}_1$ and produced particles with momenta $\mathbf{p}'$ and $\mathbf{p}'_1$. The collisions take place with an impact parameter between s and $s+ds$ in time dt. The inverse process is described by removal of particles from the phase cell $d^3x'd^3p'$, the rate for which is given by

$$\int f(\mathbf{x},\mathbf{p}')\,f(\mathbf{x},\mathbf{p}'_1)\,d^3\mathbf{p}_1\,2\pi\,s'\,ds'\,\frac{|\mathbf{p}'-\mathbf{p}'_1|}{m} \tag{2.11}$$

For non-relativistic elastic collisions, we have $|\mathbf{p}-\mathbf{p}_1| = |\mathbf{p}'-\mathbf{p}'_1|$, $s\,ds = s'\,ds', d^3p_1 = d^3p'_1$, $d^3p = d^3p'$, and $d^3x = d^3x'$. Then one can combine Equations (2.9), (2.10) and (2.11) to get the Boltzman equation:

$$\begin{aligned}\frac{df}{dt} &= \frac{\partial f}{\partial t} + \frac{\mathbf{p}}{m}.\frac{\partial f}{\partial \mathbf{x}} + F(\mathbf{x},\mathbf{p},t).\frac{\partial f}{\partial \mathbf{p}} = 0 \\ &\int d^3\mathbf{p}_1\,\frac{|\mathbf{p}-\mathbf{p}_1|}{m}\,\frac{d\sigma}{d\Omega}\,d\Omega\,[f(\mathbf{p}'_1)\,f(\mathbf{p}') - f(\mathbf{p}_1)\,f(\mathbf{p})]\end{aligned} \tag{2.12}$$

The scattering solid angle $d\Omega$ is determined by the conservation of momentum and energy and $d\sigma = 2\pi\,s\,ds$. The Boltzman equation being integro-differential in nature is difficult to solve analytically. However, it can be tackled under some approximations (as in the next section) which can be made when $\mathbf{p}$ is close to $\mathbf{p}'$ and $\mathbf{p}_1$ is close to $\mathbf{p}'_1$. It can then be possible to expand the right hand side of Equation (2.12) in powers of $\Delta\mathbf{p} = \mathbf{p}' - \mathbf{p}$ and then carry out the integral. The result can be expressed in terms of a Taylor series giving what is known as k the Fokker-Planck equation. The Kompaneets equation, derived in the next section,which describes the interaction of photons and electrons through Compton scattering is a direct example of such a case.

2.2 Non relativistic treatment of thermal SZE

2.2.1 Building the Kompaneets Equation

This subsection is devoted to the derivation of the Kompaneets equation. In the next subsection, we solve the Kompaneets Equation to get the spectral distortion of CMB characterized by the non relativistic SZE. We begin this section with a brief overview of Comptonization.

"Comptonization is the name given to the process by which electron scattering brings a photon gas to equilibrium" (Katz (1987)). The term Comptonization is used if the electrons are in thermal equilibrium at some temperature T, and if both $k_{\rm B}T << m_{\rm e}c^2$ and $h\nu << m_{\rm e}c^2$, where ν is the frequency of the photon. This is what defines the non-relativistic nature of the problem. In the non-relativistic limit, a differential Fokker-Planck equation can be written to describe the time evolution of the photon occupation number $n(\nu)$, which is assumed to be isotropic. This equation is known as the Kompaneets Equation (Kompaneets (1956)). In the fully relativistic case, which we treat in the next section, a Fokker-Planck type equation cannot be written because the change in the photon frequency $\Delta\nu$ due to scattering is not negligible compared to its incident frequency ν. Due to scattering, the photon spectrum is changed and there is net energy transfer from the electrons to the photons (or vice versa). However, the total photon number is conserved. It is worth noting that in the case of the electron being infinitely massive ($i.e., m_{\rm e}c^2 >> h\nu$), there would have been no net gain in the photon energy and Comptonization would only have resulted in making the photon angular distribution isotropic.

Comptonization becomes important when the temperature of a low density electron gas becomes higher than the temperature of a Planck function with the same energy density, and the absorption optical depth is low enough that the photon spectrum falls below a Planck function at the same electron temperature. This is typically the situation in ionized regions (like ICM, accretion flows around compact objects, ionized bubbles around high redshift quasars, etc). This makes the absorption process, which is proportional to the square of the density, negligible compared to Compton scattering. Since, low energy photons are available, there can be energy transfer from the electrons to the photons. This is what is seen in the SZE observed for clusters of galaxies and predicted for other astrophysical sources of hot plasma.

To derive Kompaneets equation, one has to start with the elementary scattering process between an electron and a photon. We follow closely the treatment given in Rybicki & Lightman (1980) and Katz (1987). Let us label the electron by its momentum $\mathbf{p}$ and energy E. The incident photon is labeled by its frequency ν along the unit vector $\hat{\mathbf{n}}$ and the scattered photon by corresponding

frequency ν' along unit vector $\hat{\mathbf{n}}'$. The electron is scattered to $\mathbf{p}'$ and E'. The frequency change is given by $\Delta\nu = \nu' - \nu$. The equations for the conservation of energy and momentum are then given by

$$h\nu + \frac{\mathbf{p}^2}{2m_e} = h\nu' + \frac{\mathbf{p}'^2}{2m_e} \tag{2.13}$$

$$\frac{h\nu}{c}\hat{\mathbf{n}} + \mathbf{p} = \frac{h\nu'}{c}\hat{\mathbf{n}}' + \mathbf{p}' \tag{2.14}$$

Now, $\mathbf{p}'$ can be eliminated from the last two equations and ignoring higher order terms of $\Delta\nu$, one gets

$$h\Delta\nu = -\frac{h\nu c\mathbf{p}.(\hat{\mathbf{n}} - \hat{\mathbf{n}}') + h^2\nu^2(1 - \hat{\mathbf{n}}.\hat{\mathbf{n}}')}{m_e c^2 + h\nu(1 - \hat{\mathbf{n}}.\hat{\mathbf{n}}') - c\mathbf{p}.\hat{\mathbf{n}}} \tag{2.15}$$

Considering the leading term only, one gets

$$h\Delta\nu \approx -\frac{h\nu\mathbf{p}.(\hat{\mathbf{n}} - \hat{\mathbf{n}}')}{m_e c} \tag{2.16}$$

This can be understood as follows: In Equation (2.15) If we take $h\nu \sim k_B T \sim \mathcal{O}(m_e v^2)$, then in the numerator, the second term is an $\mathcal{O}(v/c)$ correction to the first term. In the denominator, the second term is an $\mathcal{O}(v^2/c^2)$ correction to the first term and the third term in the denominator is also an $\mathcal{O}(v/c)$ to the first term. Inclusion of higher orders in $h\Delta\nu$, would have resulted in $\mathcal{O}(v^3/c^3)$ corrections. These corrections are negligible in most cases that we consider. In a later section, we show how these corrections (and others) will modify the current non-relativistic treatment of SZE.

We start by writing down the Boltzman equation describing the evolution of the photon occupation number $n(\nu)$, where the *primed* quantities are after scattering whereas the *un-primed* ones are before scattering. For an infinite homogeneous volume $(\partial/\partial\mathbf{x}) = 0$ and $\mathbf{F} = 0$ and therefore we get $\frac{dn(\nu)}{dt} = \frac{\partial n(\nu)}{\partial t}$.

$$\frac{\partial n(\nu)}{\partial t} = -\int d^3p\, c\frac{d\sigma}{d\Omega}d\Omega\left[n(\nu)\left(1 + n(\nu')\right)N(E) - n(\nu')\left(1 + n(\nu)\right)N(E')\right] \quad , \tag{2.17}$$

and (2.18)

$$E' = E + h\nu - h\nu' \tag{2.19}$$

In (2.17), $N(E)$ is the electron distribution in unit phase-space and depends only on energy since the electrons are in thermal equilibrium. The differential scattering cross section is given by $\frac{d\sigma}{d\Omega}$. The first term in the square bracket represents the scattering of the photons from frequency ν to frequency ν' by the electrons of energy E. The second term represents the reverse process. The factors $(1 + n(\nu)$ and $(1 + n(\nu')$ are due to the bosonic character of photons, whereas, the

corresponding fermionic factor $(1 - N(E))$ and $(1 - N(E'))$ are ignored, since the electrons are assumed to be non-degenerate. Note that for a given ν and $\hat{\mathbf{n}}$, the electron momentum $\mathbf{p}$ and the scattering angle decide the scattered ν' and $\hat{\mathbf{n}}'$. Thus finally we have an integro-differential equation for $n(\nu)$, which can in general be solved numerically.

Now, for a Bose gas at temperature T, the distribution of occupation number is given by

$$n(\nu) = \frac{1}{\exp\,(a + h\nu/k_{\rm B}T) - 1} \tag{2.20}$$

where a is the chemical potential. When (2.20) is substituted in (2.17) and $N(E)$ is taken to be Maxwellian at the same temperature[1] T, then the right hand side of (2.17) goes to zero. Since Compton scattering conserves numbers of photons, one has to introduce the chemical potential $-ak_{\rm B}T$ in the B.E. distribution, so that equilibrium can be achieved.

To solve (2.17), we Taylor expand the energy gain in powers of $\Delta\nu$. This leads to:

$$n(\nu') = n(\nu) + \frac{h\Delta\nu}{k_{\rm B}T}\frac{\partial n}{\partial x} + \frac{1}{2}\left(\frac{h\Delta\nu}{k_{\rm B}T}\right)^2\frac{\partial^2 n}{\partial x^2} + \ldots \tag{2.21}$$

$$N(E') = N(E)\left[1 + \frac{h\Delta\nu}{k_{\rm B}T} + \frac{1}{2}\left(\frac{h\Delta\nu}{k_{\rm B}T}\right)^2 + \ldots\right]. \tag{2.22}$$

In the above expansion we have redefined $x = h\nu/k_{\rm B}T$. One can now substitute (2.21) and (2.22) into (2.17) and collect the terms to get

$$\begin{aligned}\frac{\partial n(\nu)}{\partial t} &= \frac{h}{k_{\rm B}T}\left(\frac{\partial n}{\partial x} + n + n^2\right)\mathcal{I}_1 \\ &+ \left(\frac{h}{k_{\rm B}T}\right)^2\left(\frac{\partial^2 n}{\partial x^2} + 2(1+n)\frac{\partial n}{\partial x} + n + n^2\right)\mathcal{I}_2 \\ &+ \left(\frac{h}{k_{\rm B}T}\right)^3\left(\frac{\partial^3 n}{\partial x^3} + 3(1+n)\frac{\partial^2 n}{\partial x^2} + 3(1+n)\frac{\partial n}{\partial x} + n(1+n)\right)\mathcal{I}_3 + \ldots\end{aligned} \tag{2.23}$$

where the integrals I_k are given by

$$\mathcal{I}_k \equiv \int d^3p\, d\sigma\, cN(E)\,(\Delta\nu)^k \tag{2.24}$$

Thus the integro-differential equation (2.17) has been reduced to a differential equation, the effect of the scattering being factored out in the integrals $\mathcal{I}_k$.

[1] the reason being that for time independent solution of the Kompaneets Equation, the electrons and photons are in thermal equilibrium with each other.

A few comments can be made at this point. Note that to lowest order in v/c, $\mathcal{I}_1 = 0$. This is because for the lowest order in v/c, for any $(\hat{\mathbf{n}} - \hat{\mathbf{n}}')$, the integral $\mathcal{I}_1$ is proportional to $\int d^3p\, \mathbf{p}.(\hat{\mathbf{n}} - \hat{\mathbf{n}}')N(E)$, which is zero since $N(E)$ is independent of direction. This term in fact corresponds to a systematic doppler shift of $\mathcal{O}(v/c)$ in each scattering. To have a non-zero value of $\mathcal{I}_1$, on would need a to consider the higher order terms neglected in (2.16). However, the lowest order approximation of Equation (2.16) gives a finite contribution to the integral $\mathcal{I}_2$, containing the $\Delta\nu^2$ term. If one substitutes (2.16) in (2.24), then one gets

$$\mathcal{I}_2 = \left(\frac{\nu}{m_e c}\right)^2 \int cd\sigma\, d^3p\, N(E)\, (\mathbf{p}.(\hat{\mathbf{n}} - \hat{\mathbf{n}}'))^2 \tag{2.25}$$

One can now replace $\mathbf{p}.(\hat{\mathbf{n}} - \hat{\mathbf{n}}')$ by $p|\hat{\mathbf{n}} - \hat{\mathbf{n}}'|cos\psi$, where ψ is the angle between the incident and the scattered directions. Note, that the factor $|\hat{\mathbf{n}} - \hat{\mathbf{n}}'|$ does not depend on $\mathbf{p}$ and so can be taken out of the integral over electron momentum space. Since $N(E)$ is isotropic the integral of the angular part gives the factor $4\pi/3$. Thus the above equation can be written as

$$I_2 = \frac{1}{3}\left(\frac{\nu}{m_e c}\right)^2 \int cd\sigma\, |\hat{\mathbf{n}} - \hat{\mathbf{n}}'|^2 \int 4\pi p^2 dp\, N(E) p^2 \tag{2.26}$$

The second integral in (2.26) is simply $n_e \times < p^2 >$, where n_e is the number density of electrons and $< p^2 >$ is the average value of p, which is $3k_B T m_e n_e$ for a Maxwellian distribution of $N(E)$. Thus we have

$$\mathcal{I}_2 = \left(\frac{\nu}{m_e c}\right)^2 k_B T m_e n_e c \int d\Omega \frac{d\sigma}{d\Omega}\, |\hat{\mathbf{n}} - \hat{\mathbf{n}}'|^2 \tag{2.27}$$

In the non-relativistic limit, the differential cross section is the Thomson cross section given by $d\sigma/d\Omega = \frac{1}{2}r_e^2\left(1 + (\hat{\mathbf{n}}.\hat{\mathbf{n}}')^2\right)$, where $r_e \equiv e^2/(m_e c^2)$ is the classical electron radius. Then, we have

$$\mathcal{I}_2 = \left(\frac{\nu}{m_e c}\right)^2 k_B T m_e n_e c \int d\Omega\, \frac{1}{2}r_e^2\left(1 + (\hat{\mathbf{n}}.\hat{\mathbf{n}}')^2\right)\, |\hat{\mathbf{n}} - \hat{\mathbf{n}}'|^2 \tag{2.28}$$

To simplify further, one has to substitute $|\hat{\mathbf{n}} - \hat{\mathbf{n}}'|^2 = 2 - 2\,(\hat{\mathbf{n}}.\hat{\mathbf{n}}')$. Integrating over $d\Omega$ one obtains the factor $4\pi/3$ once again. Finally, one gets

$$\mathcal{I}_2 = 2\left(\frac{\nu}{m_e c}\right)^2 k_B T m_e n_e c \sigma_T, \tag{2.29}$$

where $\sigma_T = \frac{8}{3}\pi r_e^2$ is the Thomson cross section. Substituting (2.29) into (2.23). one gets the term $x^2(\partial^2 n/\partial x^2)$ coming from the integral $\mathcal{I}_2$.

Now, since Compton scattering conserves photons, one can use the the continuity equation for 'photon current' j given by

$$\frac{\partial n}{\partial t} = -\frac{1}{x^2}\frac{\partial(x^2 j)}{\partial x} \tag{2.30}$$

Comparing Equations (2.30) and (2.23), one sees that j must have the form

$$j(n,x) = w(x)\left(\frac{\partial n}{\partial x} + u(x)\right), \tag{2.31}$$

where $w(x)$ and $u(x)$ are functions to be determined. We can determine these functions in the following way: For Bose-Einstein distribution function we must $\frac{\partial n}{\partial t} = 0$. We put $j = 0$ since there are no sources or sinks of photons. Thus, for Bose-Einstein distribution, one gets from Equation (2.23) the identity

$$\frac{\partial n}{\partial x} = -(\dot{n} + n^2). \tag{2.32}$$

Since the condition $j = 0$ is satisfied for all n and x, hence one can write

$$u(n,x) = n + n^2. \tag{2.33}$$

Moreover, comparing Equations (2.30), (2.31) and (2.23), one sees that $w(x) \propto x^2$, with the proportionality constant found from (2.29). Hence,

$$w(x) = -\frac{k_B T}{m_e c^2} n_e \sigma_T c x^2. \tag{2.34}$$

Defining a dimensionless scaled variable y given by

$$y \equiv t \frac{k_B T}{m_e c^2} n_e \sigma_T c \tag{2.35}$$

then one finally arrives at the Kompaneets equation by combining Equations (2.30), (2.31), (2.33) and (2.35)

$$\frac{\partial n}{\partial y} = \frac{1}{x^2}\frac{\partial}{\partial x}\left[x^4\left(\frac{\partial n}{\partial x} + n + n^2\right)\right]. \tag{2.36}$$

One can actually determine $\mathcal{I}_1$ explicitly, now, by comparing the coefficients of n or n^2 from (2.36) and (2.29) to give

$$\mathcal{I}_1 = \frac{k_B T}{m_e c^2} n_e \sigma_T x\,(4 - x). \tag{2.37}$$

2.2.2 Solving the Kompaneets Equation

The Kompaneets equation describes the change in the photon occupation number, $n(\nu)$, by a diffusion process. The dimensionless parameter y (defined in (2.35)) is generally known as the

'Comptonization parameter' or the 'Compton y-parameter'. One can use $ct = l$ and rewrite the 'y-parameter' as

$$y = \int n_e \sigma_T dl \frac{k_B T}{m_e c^2} \quad . \tag{2.38}$$

The stationary solution of the Kompaneets equation is given by the Bose-Einstein equilibrium distribution. In most astrophysical processes of interest (*e.g.*, SZE), we have $h\nu << k_B T$, and hence $x << 1$. Then, we have $\partial n/\partial x >> n$ and n^2. The Kompaneets equation then gets the form

$$\frac{\partial n}{\partial y} = \frac{1}{x^2} \frac{\partial}{\partial x} \left(x^4 \frac{\partial n}{\partial x} \right) \tag{2.39}$$

The homogeneity of right hand side of equation (2.39) allows us to substitute $x = \frac{h\nu}{k_B T}$ by $x = \frac{h\nu}{k_B T_{\rm cmb}}$.

The above equation has the formal solution

$$n(x,y) = \exp \left[\frac{y}{x^2} \frac{\partial}{\partial x} x^4 \frac{\partial}{\partial x} \right] n(x,0), \tag{2.40}$$

where $n(x,0) = (e^x - 1)^{-1}$, since in the absence of distortions (*i.e.*, $y = 0$), the photon spectrum is a black body. Now, if $x^2 y < 1$, then one can expand the exponential of the above equation as

$$n(x,y) \cong n(x,0) + \frac{y}{x^2} \frac{\partial}{\partial x} \left[x^4 \frac{\partial}{\partial x} n(x,0) \right]. \tag{2.41}$$

Using the identity:

$$\frac{1}{x^2} \frac{\partial}{\partial x} \left[x^4 \frac{\partial}{\partial x} \frac{1}{e^x - 1} \right] = \frac{x e^x}{(e^x - 1)^2} \left[x \coth(x/2) - 4 \right] \tag{2.42}$$

in Equation (2.41), we get for $x^2 y < 1$,

$$\frac{\Delta n}{n} = \frac{n(x,y) - n(x,0)}{n(x,0)} = y \frac{x e^x}{(e^x - 1)} \left[x \coth(x/2) - 4 \right] \quad . \tag{2.43}$$

Now, since the change in radiation spectrum $\Delta I(x)$ at frequency x is given by $\Delta I(x) = x^3 \Delta n(x) I_0$, where $I_0 = \frac{2h}{c^2} \left(\frac{k_B T_{\rm cmb}}{h} \right)^3$, we have

$$\Delta I(x) = I_0 \, y \frac{x^4 e^x}{(e^x - 1)^2} \left[x \coth(x/2) - 4 \right] \tag{2.44}$$

and

$$\frac{\Delta I(x)}{I(x)} = \frac{\Delta n}{n}. \tag{2.45}$$

Finally, the temperature anisotropy due to inverse Compton scattering of CMB photons by hot electrons in a plasma, known as the "thermal SZE " is given by:

$$\begin{aligned} \frac{\Delta T_{\rm cmb}}{T_{\rm cmb}} &= \frac{\Delta I(x)}{I(x)} \frac{d\ln I(x)}{d\ln T_{\rm cmb}} \\ &= y\,[x\coth(x/2) - 4] \\ &= y\,g(x)\ . \end{aligned} \tag{2.46}$$

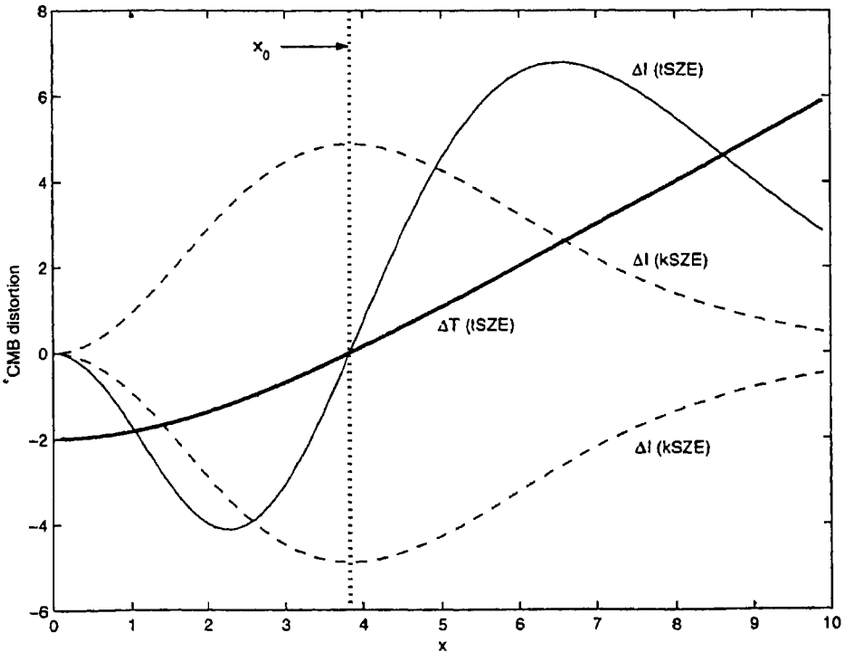

Figure 2.1: Frequency dependence of thermal and KSZE. The thick line shows the frequency dependence of $\frac{\Delta T}{T_{\rm cmb}}$ from TSZE, whereas the thin solid line shows the same for the change in spectral intensity $\Delta I(x)$. the thin dashed lines show the change in spectral intensity for KSZE, the upper one for a receding source of distortion and lower for a approaching one. The vertical dotted line shows the scaled frequency at which the TSZE is zero and KSZE is maximum. In the above plot y, I_0 and $T_{\rm cmb}$ are all scaled to unity.

In the Rayleigh-Jeans limit[2], *i.e.*,when $x \to 0$, we have

[2]Note, that our definition of $g(x)$ is different from that normally used, where $g(x)$ gives the spectral dependence

$$\frac{\Delta T_{\rm cmb}}{T_{\rm cmb}} = -2y\,. \tag{2.47}$$

Thus, we see that there would an apparent *decrease* in the sky brightness of the CMB sky towards any object (for example galaxy clusters)in the sky which is capable of scattering the microwave background photons. This has been sometimes referred to in the literature as 'holes in the sky' (Birkinshaw & Gull (1978)). In the Wien region, the distortion goes as $x^2\,y$. In most cases of interest in astrophysics (and in all the cases looked at in this thesis), the approximation $x^2\,y < 1$ is a valid assumption and we use Equations (2.46) & (2.47) in the analysis. However, when the condition $x^2\,y < 1$ is not satisfied, then one may make use of a change in variable from $(x\,,y) \rightarrow (\xi\,,y)$ given by $\xi = 3y + \ln x$ to reduce Equation (2.39) to the canonical form of the diffusion equation given by

$$\frac{\partial n}{\partial y} = \frac{\partial^2 n}{\partial \xi^2}\quad . \tag{2.48}$$

The solution to such an equation can be written as

$$I(x) = \int_{-\infty}^{\infty} P_k(s)\, I_0\, ds\,. \tag{2.49}$$

In the above equation, the energy shift due to scattering is denoted by $e^s = \frac{\nu'}{\nu}$ and the Kompaneets scattering kernel is given by (Sunyaev 1980, Bernstein & Dodelson 1990)

$$P_k(s) = \frac{1}{\sqrt{4\pi y}} \exp\left(-\frac{(s+3y)^2}{4\,y}\right). \tag{2.50}$$

With this we come to the end of non-relativistic treatment of the thermal SZE. Before going over to the next section, we briefly discuss a few features of the Equations (2.43) & (2.46). The usefulness of the form of the temperature distortion given by (2.46) is due to its simple analytic form. However, it must be emphasized once again that this is valid in the case of small optical depth of the scattering medium. As it stands, from Equation (2.46), we see that g(x) gives the frequency dependence of the distortion and it is characterized by three distinct frequencies : $x_0 = 3.83$, where the thermal SZE vanishes; $x_{min} = 2.26$ which gives the minimum decrement of the microwave background intensity and $x_{max} = 6.51$ which gives the maximum distortion due to this effect. In figure 2.1, we plot the frequency dependence of the temperature distortion and the spectral intensity from thermal SZE (and also KSZE, which we discuss later). For easy reference, the crossover frequency (*i.e.*,$x_0 = 3.83$) is shown with a vertical dotted line. It is clearly seen from the

of the intensity and not of the temperature distortion

thick solid line that at R-J limit, $\frac{\Delta T}{T} = -2y$ and at frequencies below the crossover frequency there is a dip in the temperature and the intensity for TSZE.

At first approximations, none of these spectral features depend on the temperature of the scattering medium. However, for very hot gas, one can no longer do a non-relativistic treatment and the final result would depend on the temperature of the gas. The relativistic treatment of thermal SZE is discussed in the next section. There can be other corrections to the simple expression given in (2.46) and these we treat in a later section. The amplitude y of the distortion, as in (2.35) and (2.46) depends only on the product $T\,\tau_e$ of the gas where τ_e is the optical depth along the line of sight through the scattering medium. This is essentially the integral of the gas pressure along the line of sight. For relativistic treatment, the expression for the amplitude would be proportional to τ_e for small τ_e and would also depend on T in a complicated manner.

2.3 Relativistic treatment of thermal SZE

In this section, we relax the assumption of low optical depth for the scattering medium. We also do not make the assumption $k_B T_e << m_e c^2$. Thus, we try to do a more exact treatment of the relativistic nature of thermal SZE which would be applicable if the plasma is very hot ($T_e \gtrsim 10$ keV). We, however, still ignore the Compton shift in scattering and so require $h\nu << m_e c^2$, and also take the electrons to have a Maxwellian distribution. In the rest of the section we closely follow the treatment given in Wright (1979), Taylor & Wright (1989) and Rephaeli (1995 a,b).

The distortion of the photon spectrum, due to Compton scattering by the electrons, is given by a convolution of the input photon spectrum with the frequency shift per scattering. To proceed. one must first look at the photon's frequency in the electron's rest frame which is given by

$$\tilde{\nu} = \frac{\nu}{\gamma\,(1 - \beta\mu)} \quad , \tag{2.51}$$

where ν is the incident photon frequency , $\beta = v/c$, v being the elctron's velocity, $\gamma = 1/\sqrt{1-\beta^2}$ and $\mu = \cos\theta$, θ being the angle between the photon direction and the electron velocity in the electron rest frame. The probability of collision with an angle θ is given by (Chandrasekhar (1950))

$$p(\mu)\,d\mu = \left[2\,\gamma^4\,(1 - \beta\mu)^3\right]^{-1} d\mu \tag{2.52}$$

The outgoing photon frequency is given by

$$\nu' = \nu(1 + \beta\mu')/(1 - \beta\mu') \tag{2.53}$$

with $\mu' = \cos\theta'$, θ' the outgoing photon angle w.r.t. the electron velocity direction in the electron rest frame. For a given μ, the probability of getting μ' is given by the scattering redistribution function:

$$q(\mu';\mu)\,d\mu' = \frac{3}{8}\left[1 + \mu^2\mu'^2 + \frac{1}{2}(1 - \mu^2)(1 - \mu'^2)\right] d\mu' \tag{2.54}$$

Conventionally, one describes the scattering in terms of the logarithmic frequency shift, s, caused by the scattering

$$s = \ln\left(\frac{\nu'}{\nu}\right) = \ln\left(\frac{1 + \beta\mu'}{1 - \beta\mu'}\right) . \tag{2.55}$$

Then the probability that a single scattering of the photon by an electron with speed βc causes a frequency shift s is given by

$$P(s;\beta)\,ds = \int\left[\left(\frac{d\mu'}{ds}\right) ds\right] q(\mu';\mu)\,p(\mu)\,d\mu \tag{2.56}$$

$$= \frac{3}{16\gamma^4\beta}\int_{\mu_1}^{\mu_2} \frac{(1 - \beta\mu')[1 + \mu^2\mu'^2 + \frac{1}{2}(1 - \mu^2)(1 - \mu'^2]}{(1 - \beta\mu)^3}\, d\mu \tag{2.57}$$

where μ' is expressed in terms of μ and s as

$$\mu' = \beta^{-1}\left[e^s\,(1 - \beta\mu) - 1\right] , \tag{2.58}$$

and the range of the integrals is over real angles only (*i.e.*,$-1 \leq \mu, \mu' \leq 1$).

To calculate the photon frequency spectrum on scattering by a population of electrons, one has to average over the electron velocity distribution, $p_\beta(\beta)\,d\beta$. One assumes the electron velocities to follow a relativistic Maxwellian distribution (Lahav et al. 1990), then the overall distribution in frequency shifts in a single scattering, $P_1(s)$, is given by

$$P_1(s) = \frac{\int \beta^2\gamma^5\, e^{-(\gamma-1)/\tilde{x}}\, P(s,\beta)\, d\beta}{\int \beta^2\gamma^5\, e^{-(\gamma-1)/\tilde{x}}} \tag{2.59}$$

where $\tilde{x} = \frac{k_B T_e}{m_e c^2}$ and the integration is from $\beta_m = (e^{|s|} - 1)/(e^{|s|} + 1)$ (which is the minimum value of β capable of causing a frequency shift s) to $\beta = 1$. The final distribution $P(s)$, is then the weighted sum of the probabilities for any number of scattering. If the optical depth to scattering through

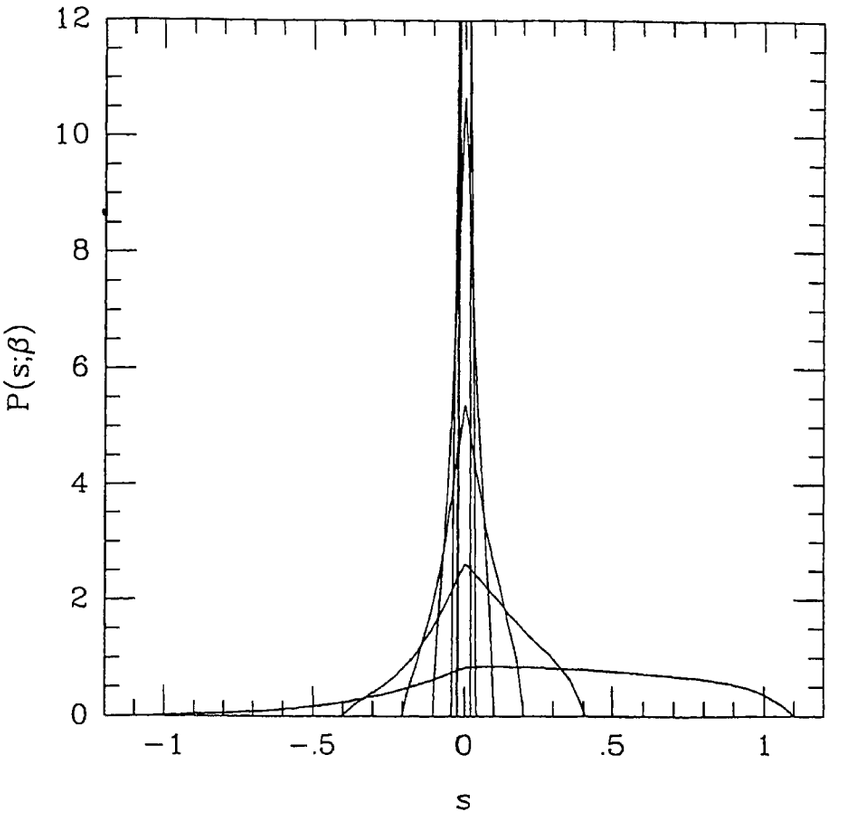

Figure 2.2: The scattering probability $P(s,\beta)$ as a function of s is plotted, for β = 0.01, 0.02, 0.05, 0.1, 0.2 and 0.5 As β increases the function becomes broader and asymmetric. (From Birkinshaw, 1999)

the plasma is τ_e, then the probability that the photon traverses the medium un-scattered is $e^{-\tau_e}$, the probability of one scattering is $\tau_e\, e^{-\tau_e}$ and the general probability of N scattering is then

$$p_N = \frac{{\tau_e}^N\, e^{-\tau_e}}{N!} \quad . \tag{2.60}$$

Thus we have

$$P(s) = e^{-\tau_e}\left[\delta(s) + \tau_e P_1(s) + \frac{1}{2}{\tau_e}^2\left(P_1(s) \bigotimes P_1(s)\right) + ...\right], \tag{2.61}$$

where $\delta(s)$ is the delta function and $\bigotimes$ denotes convolution.

The multiple scattering of the photon changes the incident Planck intensity photon spectrum $I_0(x)$ to $I(x)$, which is obtained by convolving $I_0(x)$ with $P(s)$. Here $I_0(x) = \frac{2h\nu^3}{c^2}(e^x - 1)^{-1}$ and

$$I(x) = e^{-\tau_e}\left[I_0(x) + \tau_e\, I_0(x) \bigotimes P_1(s) + \frac{1}{2}\tau_e{}^2\left(I_0(s) \bigotimes P_1(s) \bigotimes P_1(s)\right) + ...\right], \tag{2.62}$$

It has been noted by Taylor and Wright (1989), that the exact calculation of Equation (2.62) becomes simpler by going to the Fourier space $I(k)$ of $I(x)$. Then, we get

$$I(k) = e^{-\tau_e}\, I_0(k)\left[1 + \tau_e\, P(k) + \frac{1}{2}\tau_e{}^2\, P(k)^2 + ...\right], \tag{2.63}$$

which can be simply written as

$$I(k) = I_0(k)\, e^{\tau_e(P(k)-1)}. \tag{2.64}$$

This allows one to calculate the intensity change for any values of the temperature and optical depth of the scattering medium. However, for most cases of application in astronomy, one deals with regions of small optical depth (like in ICM) and then one can approximate $P(s)$ by

$$P(s) \simeq (1 - \tau_e)\,\delta(s) + \tau_e P_1(s). \tag{2.65}$$

Integrating the product $I_0(x)\,P(s)$, we obtain

$$\frac{\Delta I(x)}{I_0(x)} = \tau_e\,[\Phi(x,\tilde{x}) - 1]. \tag{2.66}$$

Then the fractional change in the CMB temperature is given by (following Equation (2.46))

$$\frac{\Delta T}{T_{\rm cmb}} = \frac{(e^x - 1)}{x\, e^x}\,\tau_e\,[\Phi(x,\tilde{x}) - 1]. \tag{2.67}$$

The function $\Phi(x,\tilde{x})$ comes from the integral over μ, β, s (given in Equation (2.71)). The limit on β has been given above and the angle integrals are between μ_1 and μ_2 given by

$$\mu_1 = \begin{cases} -1 & s \le 0\ , \\ \frac{1-e^{-s}(1+\beta)}{\beta} & s \ge 0\ , \end{cases} \tag{2.68}$$

$$\mu_2 = \begin{cases} \frac{1-e^{-s}(1-\beta)}{\beta} & s \le 0\ , \\ 1 & s \ge 0\ , \end{cases} \tag{2.69}$$

Using $w = \exp(-s)$, we obtain

$$\Phi(x,\tilde{x}) \;=\; A(\tilde{x})\,[\Phi_1(x,\,\tilde{x}) + \Phi_2(x,\tilde{x})]\,, \tag{2.70}$$

where

$$\begin{aligned}
\Phi_1(x,\,\tilde{x}) &= \int_0^1 \frac{w(e^x-1)dw}{e^{xw}-1}\int_{\beta_m}^1 \gamma e^{-(\gamma-1)/\tilde{x}}\,d\beta\int_{\mu_1}^1 q(w,\mu,\beta)d\mu \quad ,\\
\Phi_2(x,\,\tilde{x}) &= \int_0^1 \frac{w(e^x-1)dw}{w^3(e^{x/w}-1)}\int_{\beta_m}^1 \gamma e^{-(\gamma-1)/\tilde{x}}\,d\beta\int_{-1}^{\mu_2} q(w,\mu,\beta)d\mu \quad ,\\
q(w,\mu,\beta) &= \frac{\frac{1}{\beta^2}(3\mu^2-1)\left(\frac{1-\beta\mu}{w}-1\right)^2+(3-\mu^2)}{(1-\beta\mu)^2}\\
A(\tilde{x}) &= \frac{3}{32\int_0^1\beta^2\gamma^5 e^{-(\gamma-1)/\tilde{x}}d\beta} \quad .
\end{aligned} \tag{2.71}$$

where $\beta_m = (1-w)/(1+w)$ The above equations summarize the calculation of the relativistically correct Comptonization spectrum of the CMB in the limit of small optical depth and using the exact angular probability distribution for scattering. However, since the photon field is isotropic in nature and the electrons are, in general, only mildly relativistic, the scattering can be assumed to be isotropic in the electron rest frame. Under this assumption, one can average the scattering probability over the direction of the incident photon (Rybicki & Lightman 1980) to have

$$P_{iso}(s,\beta) \;=\; \frac{e^s}{(2\gamma\beta)^2}\begin{cases}(1-\beta)e^s-1+\beta, & \frac{1-\beta}{1+\beta}\le e^s\le 1\,,\\ 1+\beta-(1-\beta)e^s & 1<e^s\le\frac{1+\beta}{1-\beta}\,.\end{cases} \tag{2.72}$$

In this approximation, we then have

$$\Phi_{iso}(x\,,\tilde{x}) \;=\; B(\tilde{x})\,\Phi(x,\,\tilde{x}), \tag{2.73}$$

where

$$\Phi(x\,,\tilde{x}) \;=\; \int_0^1 (e^x-1)\left[\frac{1}{e^{xw}-1}+\frac{1}{w^3(e^{x/w}-)}\right]\zeta(x,\,\tilde{x})\,dw \tag{2.74}$$

$$\zeta(x,\,\tilde{x}) \;=\; \int_{\beta_m}^1 \gamma^3 e^{-(\gamma-1)/\tilde{x}}\,[(1+\beta)\,w-1+\beta]\,d\beta \tag{2.75}$$

$$B(\tilde{x}) \;=\; \frac{8}{3}A(\tilde{x}). \tag{2.76}$$

At this point, let us comment on the results of the fully relativistic calculations. The thing that is to be noted first is that the intensity change is no longer linear in T_e, as was the case for the

non-relativistic case. For the relativistic treatment, ΔI depends explicitly on x, $\tilde{x}$ and τ_e, whereas that of Equation (2.46) depends only on x and $y = \tau_e \tilde{x}$. Also at a given frequency , the intensity change can assume different values depending on different ratios of $y = \tau_e \tilde{x}$. Moreover, due to the exponential nature of the Planckian spectrum, a slight shift in scattering probability distribution to higher frequencies can cause distinguishable change between non-relativistic and relativistic results, near the cross-over frequency. Rephaeli (1995 a,b) has checked that the simplification of the relativistic case to the isotropic scattering does not lead to appreciable change in the final value of the intensity change. For the relativistic cases, the level of deviation starts becoming important for $k_B T_e > 5$ keV. At this temperature, the relative intensity change between the non-relativistic case to the relativistic case is greater than 20% in the range $3.7 < x < 4.2$ and at $x > 11.0$. the deviations are higher and over a wider range in x for higher temperatures and especially at higher frequencies. However, one must note that, we have neglected the higher order terms in τ_e (refer to Equation (2.65)) which means that the above results are only approximate. This is justified in all the cases (like ICM or inter-galactic medium) that we study in this thesis. As has been pointed out by Rephaeli (1995 a,b), the main characteristic of the relativistic solution w.r.t. to non-relativistic case is the general decrease of the intensity change for values of $x < 8 - 8.4$ for T_e between $1 - 15$ keV, and an increase at higher values of x. The higher the gas temperature, the higher is the Wien deviation from that in the Kompaneets case.

The non-relativistic nature is also manifest in the change in the cross-over frequency. The value of x_{zero} is pushed to higher values of x with increase in T_e for the relativistic case compared to the constant $x_{zero} = 3.83$ one gets from solving the Kompaneets Equation This deviation is linear in $k_B T_e / m_e c^2$ and as a first approximation can be written as

$$x_0 \sim 3.83\,(1 + k_B T_e / m_e c^2). \tag{2.77}$$

A more precise expression for this deviation would be given in a later section. The importance of this result cannot be over-emphasized. Recall that the cross-over frequency is the frequency where the thermal SZE is equal to zero. A precise knowledge of the cross-over frequency becomes important if one would like to disentangle the KSZE (discussed below) from the thermal one. Also, this becomes important if one has to separate out the secondary anisotropy due to thermal SZE from the primary anisotropies at angular scales dominated by the primary anisotropies.

To conclude this section, let us point out once again that the degree of Comptonization predicted by a solution of the Kompaneets equation is significantly different in the Wien side of the photon spectrum from a relativistic calculation taking into account near -relativistic electrons and low optical thickness. The difference between the two treatment is not significant for gas temperature

below $\sim$ 5 keV. Also, in the relativistic case x_0 becomes temperature dependent in contrast to the constant value of 3.83 predicted in the last section. A precise knowledge of this value becomes important if one needs to decouple the KSZE from the thermal SZE. Finally, we mention that while the above review is sufficient for the purpose of this thesis, for more details on the the relativistic treatment of Comptonization, see *e.g.*, Loeb, McKee & Lahav (1991).

2.4 The Kinematic Sunyaev-Zel'dovich effect

The KSZE occurs, along with thermal Sunyaev-Zel'dovich effect, if the scattering medium (like the ICM) has any bulk motion (*e.g.*, peculiar motion) relative to the CMB. Due to the relative motion the microwave background photons appear anisotropic in the reference frame of the scatterer and kSZ tries to isotropize the radiation. This, however, makes the radiation anisotropic in the reference frame of the observer, and there is a distortion towards the scatterer with amplitude proportional to $\tau_e \frac{v_z}{c}$, where v_z is the peculiar velocity of the scattering bulk (Sunyaev & Zel'dovich 1972, Repaheli & Lahav 1991). The KSZE is found to have a different spectral nature than the thermal SZE, and hence the two can be separated. This then brings out the interesting possibility of deducing an object's peculiar velocity at large distances by observation of the KSZE. Since, the peculiar velocities of clusters arise from the gravitational attraction of the large scale distribution of matter, observations of KSZE can be used to probe of this distribution.

To derive the expression for CMB temperature distortion due to KSZE, one can either start with the Boltzman equation (as done for the thermal SZE, for example, see Phillips 1995, Nozawa et al. 1998) or use the radiative transfer equation. We follow Birkinshaw (1999) closely and use the latter method. For the sake of simplicity, we shall assume that the kinematic and thermal effects are both small and only single scattering is appropriate to describe the situation. In this case, the thermal and the kinematic effects will decouple and we can derive the kinematic effect by taking the electrons to be at rest in the frame of the scattering medium. This also means that we are ignoring all cross terms like $\left(\frac{k_B T_e}{m_e c^2}\right)\left(\frac{v_z}{c}\right)$. This approximation is not valid for non-thermal electron population where the electron energies can be far greater than the rest mass and one would need a relativistic treatment (see for example, Nozawa et al. 1998).

In the rest frame of the CMB, the radiation spectrum is given by Equation (2.4) and the occupation number is given by Equation (2.3). In such a case, the occupation number in a frame moving at a speed v_z along the z-axis of the observer is given by

$$n_\alpha = \frac{1}{\exp\left(x_1 \gamma_z (1 - \beta_z \mu_1)\right) - 1}, \tag{2.78}$$

where $x_1 = \frac{h\nu_1}{k_B T_1}$ denoting the dimensionless photon frequency in the frame of the electrons. The radiation temperature as seen by an observer at rest in the Hubble flow near the electrons would be $T_1 = T_{\rm cmb}(1 + z_H)$, where z_H is the Hubble flow redshift and $\beta_z = \frac{v_z}{c}$ is a measure of the peculiar velocity; γ_z is the corresponding Lorentz factor. The direction cosine of the photons arriving at the scattering electron relative to the z axis and measured in the frame of the moving scattering medium is given by $\mu_1 = \cos\theta_1$. One can now use the relativistic transformation of frequencies to relate μ_1 to μ in the CMB rest frame by

$$\mu_1 = \gamma_z (1 + \beta_z)\mu. \tag{2.79}$$

The observer at rest sees the scattered photon along the z axis and so $\mu = \cos\theta = 1$.

We use the radiative transfer (Equation (2.8)) and scattering redistribution function (Equation (2.54)), to get the specific intensity as

$$\frac{dI_{\nu_1}(\mu)}{d\tau_{\rm e}} = \int_{-1}^{+1} d\mu_1\, q(\mu, \mu_1) \Big(I_{\nu_1}(\mu_1) - I_{\nu_1}(\mu) \Big) \quad , \tag{2.80}$$

where the optical depth is $\tau_{\rm e} = \int \alpha_{\nu,{\rm sca}} dz$. The above equation can be simplified for small optical depth to give

$$\frac{I_{\nu_1}(\tau_{\rm e};\mu) - I_{\nu_1}(0;\mu)}{\tau_{\rm e}} = \int_{-1}^{+1} d\mu_1\, q(\mu, \mu_1) \Big(I_{\nu_1}(0;\mu_1) - I_{\nu_1}(0;\mu) \Big). \tag{2.81}$$

Now for $\mu = 1$, the above equation can be simplified to give the fractional change in the specific intensity as

$$\frac{\Delta I_{\nu_1}}{I_{\nu_1}} = \tau_{\rm e} \int_{-1}^{+1} d\mu_1 \frac{3}{8}(1 + \mu_1^2) \left(\frac{I_{\nu_1}(0;\mu_1)}{I_{\nu_1}(0;1)} - 1 \right). \tag{2.82}$$

Now, since the L.H.S. of Equation (2.82) is a ratio of specific intensities, it is relativistically invariant (*i.e.* μ_1 is related to μ through a Lorentz transformation). Then, using the occupation number from Equation (2.78) and substituting ν_1 by ν, the frequency seen at redshift zero, we get

$$\frac{\Delta I_\nu}{I_\nu} = \tau_{\rm e} \int_{-1}^{+1} d\mu_1 \frac{3}{8}(1 + \mu_1^2) \left(\frac{e^x - 1}{e^{x_2} - 1} - 1 \right), \tag{2.83}$$

where $x_2 = x\gamma_z^2(1 + \beta_z)(1 - \beta_z\mu_1)$ and $x = \frac{h\nu}{k_B T_{\rm cmb}}$ To get the familiar expression for KSZE, we expand the integral in power of β_z for small β_z (*i.e.*non-relativistic) and due to the symmetry of the integrand, only terms having even powers of μ_1 remain. Thus we finally have

$$\frac{\Delta I_\nu}{I_\nu} = -\tau_e \beta_z \frac{x\, e^x}{e^x - 1} \tag{2.84}$$

$$\Delta I_\nu = -I_0 \tau_e \beta_z \frac{x^4\, e^x}{(e^x - 1)^2} \qquad \text{and} \tag{2.85}$$

$$\left(\frac{\Delta T}{T_{\rm cmb}}\right)_{kSZ} \approx -\frac{v_z}{c} \tau_e \tag{2.86}$$

At this point, let us make a few remarks on KSZE, before moving on to the next section:

- The spectral form of the KSZE is the same as that of the primary anisotropies and shows up as a simple decrease in radiation temperature. Thus, a precision measurement of the primary anisotropy must take into account any possible contamination from kSZ at lower redshifts.

- For clusters of galaxies, it is very difficult to measure the KSZE in presence of the thermal SZE. The ratio of the change in brightness temperatures caused by these two effects is

$$\frac{\Delta T_{\rm kinematic}}{\Delta T_{\rm thermal}} = \frac{1}{2}\frac{v_z}{c}\left(\frac{k_{\rm B}T_e}{m_e c^2}\right)^{-1} \approx 0.09\,(v_z/1000\ {\rm km\,s^{-1}})\,(k_{\rm B}T_e/10\ {\rm keV})^{-1} \tag{2.87}$$

  Since typical peculiar velocities are around a few hundred kilometers per second and typical temperature a few keV, hence the kinematic effect comes out to be at least an order of magnitude less than the thermal effect. However, the two effects differ in their spectral shape and so can be, in principle, separated. Infact, for non-relativistic cases, the kinematic effect attains the maximum distortion at the frequency where the thermal effect is zero (see Figure 2.1). However, to be precise, one has to take the exact value of the cross-over frequency which would, in general, depend on both the plasma temperature as well as the optical depth.

- There can be cases when the kinematic distortion is more than the corresponding thermal distortion. This is so when the plasma is either too tenuous or relatively cool or both and the peculiar velocity is larger. In chapter 4, we consider in detail an example, where the kinematic distortion from galactic winds at high redshifts overshadows the thermal distortion. To give another example, consider the case of an ionized bubble around a quasar at redshifts before cosmological reionization. (Aghanim et al. 1996).

- The distortion as given by Equation (2.86) can be used to measure the peculiar radial velocity. However, the tangential velocity of a galaxy cluster can be measured using the distortion caused by gravitational lensing (Birkinshaw & Gull 1983, Gurvits & Mitrofanov 1986, Pyne & Birkinshaw 1993). For typical clusters, this distortion (the moving gravitational lense

effect) comes out to be an order of magnitude less than the kinematic effect, and hence would be extremely difficult to detect at present.

- A moving scatterer that gives rise to the kinematic SZE would also give rise to polarization (Sunyaev & Zel'dovich 1980b, Itoh et al. 2000, Challinor et al. 2000) due to Thomson scattering of the anisotropic radiation field in the reference frame of the scatterer. The two largest contributions to the polarized intensity were found by Sunyaev & Zel'dovich (1980b) as a intensity component of about $0.1\,\tau_e\,(v_{xy}/c)^2$ of the CMBR intensity, due to single scatterings of the quadrupolar term in the anisotropic radiation field seen in the frame of the moving cluster, and a component of about $0.025\,\tau_e^2\,(v_{xy}/c)$ from repeated scatterings of the dipolar term in the radiation.

2.5 A short note on corrections to SZE

In this section, we briefly discuss corrections to the simple expressions of the thermal SZE (refer to Equation (2.46) and KSZE (refer to Equation (2.86)) derived in the previous sections and collect a few fitting functions from the literature which becomes important (and useful) when one deals with hotter and denser scattering systems.

The Sunyaev-Zel'dovich formula, in a previous section, was derived from the kinematic equation for the photon distribution function taking the Compton scattering by the electrons into account, *i.e.*, the Kompaneets equation. This gives us the formula (2.46) which is sufficiently accurate for clusters having temperatures less than 5 keV. However, observations show the presence of clusters having temperature up to 15 keV, and hence makes extension of the Kompaneets equation to relativistic regimes important. The SZE for relativistic cases has been discussed in the previous section, but no analytic extension of the simple SZE formula (*i.e.*, Equation (2.46)) was given. In practice, it is of use if one can get an analytic expression of sufficient accuracy for distortion of the CMB by mildly relativistic electrons. Furthermore, one would like to relax the assumption of low optical depth and allow for multiple scattering of the photons by the electrons. These issues have been addressed in a number of papers (Itoh et al. 1998,2000, Nozawa et al. 1998,2000, Challinor & Lasenby, 1998,1999, Challinor et al. 2000, Molnar & Birkinshaw, 1999). Over here we only give a collection of three main results from the references stated above.

We start by writing the Kompaneets equation as a power series in $\theta_e = k_B T_e/m_e c^2$, where T_e and m_e are the plasma temperature and the electron mass. The convergence of the power series in θ_e is slow. We start from Equation (2.23). An integration of of the generalized Equation (2.24)

is not possible other than doing a power series expansion of the integrand. This expansion can be done for many choices of parameters like $p/m, v \equiv E/p$ etc. However, the analytic expression I_k after the integration does not depend on the choice of the expansion parameters. More important is the fact that the expansion is only an asymptotic expansion. The details of these expansions can be found in (Challinor & Lasenby 1998, Itoh et al. 1998). In the rest of the section we use natural units and put $h/2\pi = c = 1$. Therefore, the corresponding x in Equation (2.23) for this section is given by $x = \frac{\omega}{k_B T_e}$ and $\Delta\nu = \frac{\omega' - \omega}{k_B T_e}$, with $\omega = 2\pi\nu$.

Taking these expansions and assuming a Planck spectrum for the photons with $T_{\rm cmb} << T_{\rm e}$, one gets the fractional distortion of the photon spectrum as

$$\frac{\Delta n(X)}{n_0(X)} = \frac{y X e^X}{e^X - 1} \theta_e \left[Y_0 + \theta_e Y_1 + \theta_e^2 Y_2 \right] \tag{2.88}$$

with

$$Y_0 = -4 + \tilde{X} \quad , \tag{2.89}$$

$$Y_1 = -10 + \frac{47}{2}\tilde{X} - \frac{42}{5}\tilde{X}^2 + \frac{7}{10}\tilde{X}^3 + \tilde{S}^2\left(-\frac{21}{5} + \frac{7}{5}\tilde{X}\right) \quad , \tag{2.90}$$

$$Y_2 = -\frac{15}{2} + \frac{1023}{8}\tilde{X} - \frac{868}{5}\tilde{X}^2 + \frac{329}{5}\tilde{X}^3 - \frac{44}{5}\tilde{X}^4 + \frac{11}{30}\tilde{X}^5 + \tilde{S}^2\left(-\frac{434}{5} + \frac{658}{5}\tilde{X} - \frac{242}{5}\tilde{X}^2 + \frac{143}{30}\tilde{X}^3\right) + \tilde{S}^4\left(-\frac{44}{5} + \frac{187}{60}\tilde{X}\right) \quad , \tag{2.91}$$

where we have kept terms only up to $O(\theta_e^3)$. Here $y \equiv \sigma_T \int dl\, n_e$ and

$$\tilde{X} \equiv X \coth\left(\frac{X}{2}\right) \quad , \tag{2.92}$$

$$\tilde{S} \equiv \frac{X}{\sinh\left(\frac{X}{2}\right)} \quad , \tag{2.93}$$

$$n_0(X) = \frac{1}{e^X - 1} \quad , \tag{2.94}$$

and (2.95)

$$X = \frac{\omega}{k_B T_{\rm cmb}} \quad . \tag{2.96}$$

The definitions of n and X remains unchanged for the rest of this section. Once we have the fractional change in the photon number due to scattering, the temperature anisotropy can be obtained following Equation (2.46).

Till date, most of the observations of SZE have been carried out in the Rayleigh-Jeans (R-J) region of the blackbody spectrum. Hence, it is instructive to see how the corrections behave in this region. In the R-J limit, i.e as $X \to 0$, we have

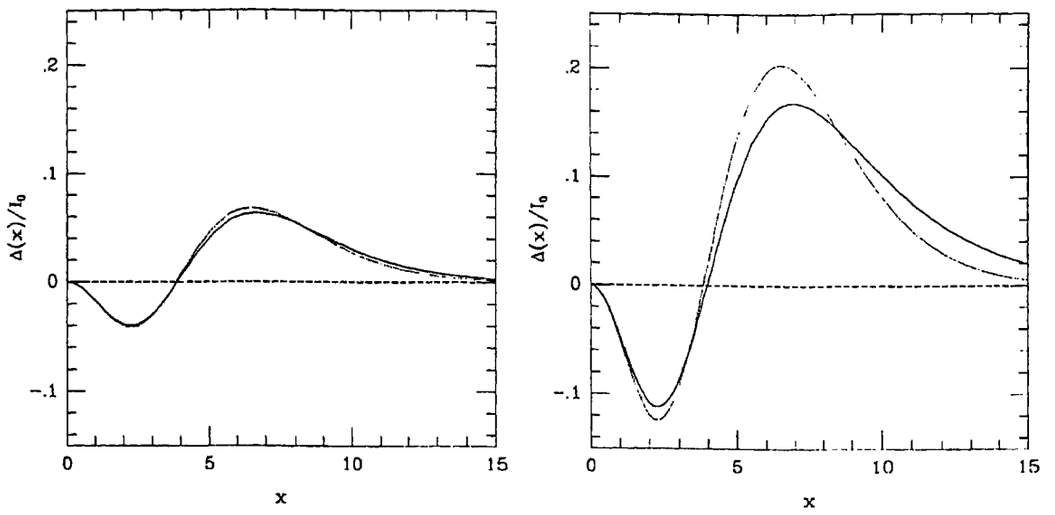

Figure 2.3: The spectral deformation $\Delta I/I_0$ is plotted against $x = h\nu/k_{\rm B}T_{\rm cmb}$ for the relativistic expression (from direct numerical integration) shown by the solid line, and that obtained from the corresponding Kompaneets kernel, shown by the dotted line. The left plot is for $k_{\rm B}T_{\rm e} = 5\,{\rm keV}$ and the right plot is for $k_{\rm B}T_{\rm e} = 15\,{\rm keV}$. (From Birkinshaw, 1999)

$$\frac{\Delta n(X)}{n_0(X)} \rightarrow -2y\,\theta_e \left[1 - \frac{17}{10}\theta_e + \frac{123}{40}\theta_e^2\right] \tag{2.97}$$

In the R-J limit, the convergence of the above series is very fast. This is, however, not the case in the Wien limit.

Before moving onto corrections to the KSZE, we look at the cross-over frequency in a little more details. A good fit to the cross-over frequency due to relativistic thermal SZE calculated from analytical expression and by direct numerical integration has been found by Itoh et al. (1998). The numerical result is well approximated as a linear function in θ_e for plasma temperatures below 20 keV and a quadratic in θ_e up to 50 keV. The numerical fit is given below:

$$X_0 = 3.830\left(1 + 1.1674\theta_e - 0.8533\theta_e^2\right). \tag{2.98}$$

Next, we come to the relativistic corrections to the KSZE. This can be done in a way similar to the one above, by starting once again from a generalized Kompaneets equation and applying a Lorentz boost to the direction of the peculiar velocity. One can assume the cluster to move with a

peculiar velocity $\vec{\beta}(\equiv \vec{v}/c)$ with respect to the CMB. The directions of the velocity is chosen to be in the $x-z$ plane, *i.e.*, $\vec{\beta} = (\beta_x, 0, \beta_z)$. The electron distribution functions are connected between the cluster frame and the microwave background frame by Lorentz transformations. One can then work out through the algebra in the same way as before by expanding the Kompaneets solution in powers of θ_e. However, this time, we will have cross terms like $\beta\theta_e, \beta\theta_e^2$ etc. The $\beta\theta_e$ term can give rise to a correction of the order of 10% for a typical electron temperature of 10 keV. The other higher order terms lead to negligible corrections for temperatures of interest. Without going into the details, we write down the relativistic correction in the R - J limit, which is

$$\frac{\Delta n(X)}{n_0(X)} \rightarrow -2y\,\theta_e \left[1 - \frac{17}{10}\theta_e + \frac{123}{40}\theta_e^2\right] + y\beta P_1(\hat{\beta}_z)\left[1 - \frac{2}{5}\theta_e + \frac{13}{5}\theta_e^2\right] . \qquad (2.99)$$

In the above expression we have neglected all β^2 and higher order terms. $P_1(\hat{\beta}_z) = \frac{\beta_z}{\beta} = \cos\theta_\gamma$, where θ_γ is the angle between the cluster peculiar velocity $(\vec{\beta})$ and and the photon momentum $\hat{n}$.

One can now look once again to the correction to the cross over frequency. The cross-over frequency is shifted toward higher (lower) frequency region by the kinematic Sunyaev-Zel'dovich contribution when the cluster is moving outward (inward) with respect to the observer. The shift is given by $\Delta X_0 \equiv X_0 - X_{0,\beta}$, where X_0 is given by Equation (2.98) and $X_{0,\beta}$ is the new cross-over frequency in the presence of the kinematic Sunyaev-Zel'dovich effect. The shift can be expressed in the form of a function, h, given by

$$h \equiv \Delta X_0 / \left(300\beta P_1(\hat{\beta}_z)\right) . \qquad (2.100)$$

For temperatures 5keV $\leq k_B T_e \leq$ 15keV, the function h can be well fitted by (Nozawa et al. 2000)

$$h = \frac{a_1}{\theta_e - \theta_{e,min}} + \frac{a_2}{(\theta_e - \theta_{e,min})^2} + a_3 + a_4\,\theta_e + a_5\,\theta_e^2 , \qquad (2.101)$$

where $\theta_{e,min}$ is the minimum value of θ_e which has a real solution for a given β. $\theta_{e,min} = 1.654\times10^{-3}$ and the other constants are $a_1 = 3.857\times10^{-3}$, $a_2 = -4.631 \times 10^{-6}$, $a_3 = 1.370\times10^{-2}$, $a_4 = 1.014\times10^{-2}$, and $a_5 = 1.000\times10^{-2}$. Nozawa et al. (1998) quote the errors of this fitting function to be less than 4% for $5 \leq k_B T_e \leq$ 15keV and $0.5/300 \leq \beta \leq 1.5/300$.

Finally, we relax our assumption of low optical depth and look at multiple scatterings of the incident photon spectrum. In general, multiple scattering contribution is found out to be rather small compared to single scattering. As an example for a 15 keV cluster, the multiple scattering affects the final result by -0.3% in the Wein region and -0.03% in the R - J region. The basic idea is as follows: Since $y << 1$ for all clusters, only first order perturbations to the photon spectrum

is sufficient, and one can write the initial photon distribution as

$$\begin{aligned} n(X) &\equiv n_0(X) + \Delta n(X)\,, \\ &= n_0(X)\left[1 + \frac{\Delta n(X)}{n_0(X)}\right]\,, \end{aligned} \tag{2.102}$$

where the second term in the last equation is given by Equation (2.97) (in the R - J limit). This then gives us the correction in R - J regime to be

$$\frac{\Delta n(X)}{n_0(X)} \rightarrow -2y\,\theta_e\left(1 - \frac{17}{10}\theta_e + \frac{123}{40}\theta_e^2\right) + 2y^2\,\theta_e^2\left(1 - \frac{17}{5}\theta_e + \frac{226}{25}\theta_e^2\right)\,. \tag{2.103}$$

In the Equation (2.103), we have taken terms only up to second order in y and have defined $y^2 = \frac{1}{2}(\sigma_T \int n_e dl)^2$.

The formulae (Equations (2.97), (2.98), (2.101) and (2.103)) are important and come in handy when one needs to get the value of temperature distortion due to SZE within an accuracy of $\sim 10\%$. For example, for assessing the uncertainties in the determination of the Hubble constant from observations of galaxy clusters in radio (SZE) and X-ray, one would like to use the approximations to the relativistic treatment of temperature distortions by SZE. Using the non-relativistic expression for TSZE can result in deviations of $\sim 5 - 10\%$ in the estimated value of H_o from the actual value. We will return to this issue in greater detail in Chapter 3.

2.6 Observational aspects of SZE

Till now, observations of SZE have mainly been carried out towards clusters of galaxies (see Birkinshaw 1999, for details) with the exception of a singular attempt made towards a radio jet lobe (McKinnon et al. 1990). There have also been two claims of detection of Sunyaev-Zel'dovich distortion towards blank fields in the sky (Jones et al. 1997, Richards et al. 1997), but other sensitive blank sky searches have only resulted in upper limits (Subrahmanyan et al. 1998,1999). In observing the secondary CMB distortions, three distinct techniques have been utilized, namely, 1) single dish radiometer observations, 2) bolometric observations and 3) interferometric observations. Till now no concerted effort of measuring the polarization has been made. However, with the coming up of 'Array for Microwave Background Anisotropy' $AMiBA$[13] in the future, one of the main aims will be to look at polarization signals at arc min scales. We briefly describe the three different observational techniques below:

[3]http://www.asiaa.sinica.edu.tw/amiba

- **Use of single dish radiometers**

  For clusters of galaxies at low redshifts having large angular sizes, it may be possible to observe the SZE using small single dish radiometers. For better results one must optimize the setup for microwave background observations. The major optimization necessity comes from requirement to have greater sensitivity for observing the Sunyaev-Zel'dovich distortion. Following Birkinshaw (1999) a simple estimate of the sensitivity of single observation can be given as follows: A good system might have a noise temperature of about 40 K (including noise from the atmosphere) and a bandwidth of 1 GHz. Then in 1 second, the radiometric accuracy of a simple measurement will be 0.9 mK, and a difference measurement, between the center of a cluster of galaxies and some reference region of blank sky, would have an error of 1.3 mK. Thus if problems with variations in the atmosphere are ignored, it would appear that a measurement with an accuracy of 10 μK could be made in 4.4 hours. However, this estimate is highly optimistic because of emission from the Earth's atmosphere. This unwanted contamination can be separated out by using some differencing schemes.

The simplest scheme for removing the atmospheric signal is simply to position-switch the beam of an antenna between the direction of interest (for example, the center of some cluster) and a reference direction well away from the cluster and then the radiometric signals measured in these two directions are subtracted from one another. An alternative strategy is to allow the sky to drift through the beam of the telescope or to drive the telescope so that the beam is moved across the position of the target. The time sequence of sky brightnesses produced by such a drift or driven scan is then converted to a scan in position, and fitted as the sum of a baseline signal and the Sunyaev-Zel'dovich effect signal associated with the target.Many scans are needed to average out the atmospheric noise, and this technique is often rather inefficient. Using this technique the first measurement of SZE was carried out towards the Coma cluster (Parijskijs 1972). However, more often a higher order differencing scheme is adopted. At cm wavelengths, it is common for the telescope to be equipped with multiple feeds so that two or more directions on the sky can be observed without moving the telescope. The difference between the signals entering through these two feeds is measured many times per second, to yield an "instantaneous" beam-switched sky signal. On a slower timescale the telescope is position-switched, so that the sky patch being observed is moved between one beam and the other. At mm wavelengths it is common for the beam switching to be provided not by two feeds, but by moving the secondary reflector, so that a single beam is moved rapidly between two positions on the sky. In general, most measurements have been made using a combination of beam-switching and position-switching, because this is relatively

efficient, with about half the observing time being spent on target. Two recent observations with single dish radiometers are by Tsuboi et al. (1998) and Myers et al. (1997).

- **Using Bolometers**

  Bolometric measurements of the SZE effects are now becoming more common, as the technology needed has become more widely available. The principal advantage of a bolometric system is the high sensitivity that is achieved, but these devices are also of interest because of their frequency range: at present they provide the best sensitivity for observing the microwave background outside the Rayleigh-Jeans part of the spectrum, and hence for separating the thermal and kinematic components of the SZE effect using their different spectral shapes. Moreover, for some systems, one can have simultaneous observations in several bands.

  Although the unprocessed sensitivity of bolometer systems is high because of the large bandpasses and sensitive detector elements, a problem with the technique is the extremely high sky brightness against which observations must be made. Coupled with the varying opacity of the sky, this implies that telescopes on high, dry, sites are essential for efficient observing, like in balloon operations. The CalTech Submillimeter Observatory (CSO) on Mauna Kea 'Sunyaev-Zel'dovich Infrared Experiment' (SuZIE) successfully running. The other possibilities are to have space borne missions or observations carried out in Antarctica.

- **Interferometric Measurements**

  Use of radio interferometry has, in the recent past, developed into a powerful tool for making detailed *images* of SZE. Such higher angular resolution images are desirable for making detailed comparisons with X-ray images, and can also measure accurate Sunyaev-Zel'dovich effects while avoiding some of the systematic difficulties of the other techniques described above. This has made this technique popular in recent times (Carlstrom et al. 1996, White et al. 1999, Reese et al. 2000, Patel et al. 2000, Holder et al. 2000) The extremely low systematics of interferometers and their two-dimensional imaging capability make them well suited to study the weak ($\lesssim 1$ mK) SZE signal in galaxy clusters. In this thesis, we have used interferometric measurements/limits of the CMB sky as probe in cosmology, and hence we look at this technique in little more details.

  An interferometer samples the Fourier transform of the sky brightness rather than the direct image of the sky. The final products from the interferometer are the amplitudes of the real and imaginary components of the Fourier transform of the cluster SZE distribution on the sky multiplied by the primary beam of the telescope. The SZE data files include the positions in the Fourier domain, which depend on the arrangement of the telescopes in the array, the real

and imaginary components of the Fourier signals, and a measure of the noise in the real and imaginary components. The Fourier conjugate variables to right ascension and declination are commonly called u and v (measured in wavelengths), respectively, and the Fourier domain is commonly referred to as the $u-v$ plane. The finite size of each telescope dish imposes an almost Gaussian attenuation across the field of view, known as the primary beam. The primary beams are constructed from holography data taken at each array. The main lobe of the primary beam can be approximated as a Gaussian. The primary beam sets the field of view. The effective resolution, called the synthesized beam, depends on the sampling of the $u-v$ plane of the observation and is therefore a function of the configuration of the telescopes. The cluster SZE signal is largest on the shortest baselines (largest angular scales). The shortest possible baseline is set by the diameter of the telescopes, D. Thus interferometers are not sensitive to angular scales larger than about $\lambda/2D$. Because of this spatial filtering by the interferometer, it is necessary to fit models directly to the data in the $u-v$ plane, rather than to the deconvolved image.

For "small" sources, observed with narrow bandwidths and short time constants, the measured source visibility is

$$\mathcal{V}(u,v) \propto \int_{-\infty}^{\infty} d\xi \int_{-\infty}^{\infty} d\zeta\, B(\xi,\zeta)\, G(\xi,\zeta)\, e^{-2\pi i(u\xi+v\zeta)} \quad , \tag{2.104}$$

where $B(\xi,\zeta)$ is the brightness distribution of the sky, $G(\xi,\zeta)$ represents the polar diagram of the antennas of the interferometer and (ξ,ζ) are direction cosines relative to the center of the field of view, and the constant of proportionality depends on the detailed properties of the interferometer An image of the sky brightness distribution, $B(\xi,\zeta)$, can be recovered from the measurements $\mathcal{V}(u,v)$ by a back Fourier transform and division by the polar diagram function: alternatively, estimation techniques can be used to measure $B(\xi,\zeta)$ directly from the $\mathcal{V}(u,v)$. The finiteness of interferometer measurements means that not all (u,v) values are sampled: in particular, the design for high resolution means that the antennas are usually placed so that their minimum separation is many wavelengths (and always exceeds the antenna diameter by a significant factor). The Fourier relationship (2.104) means that the short baselines contain information about the large angular scale structure of the source, and so there is some maximum angular scale of structure that is sampled and imaged by interferometers. The Sunyaev-Zel'dovich effects of clusters of galaxies have angular sizes of several arc minutes — most interferometers lose ("resolve out") signals on these or larger angular scales, and hence would find extreme difficulty in detecting Sunyaev-Zel'dovich effects. However, smaller interferometers would allow the Sunyaev-Zel'dovich effects to be measured. What is needed is an array of antennas whose individual beam-sizes are significantly larger than the angular

sizes of the cluster Sunyaev-Zel'dovich effects, so that many antenna-antenna baselines can be arranged to be sensitive to the effects (see Saunders 1995).

One major advantage of using an interferometer is that the effects of structures in the atmosphere are significantly reduced. Emission from the atmosphere is important only in its contribution to the total noise power entering the antennas, since this emission is uncorrelated over baselines longer than a few metres and does not enter into the (correlated) visibility data. Furthermore, there are no background level problems: an interferometer does not respond to a constant background level, and so a well-designed interferometer will not respond to constant atmospheric signals, the uniform component of the microwave background radiation, large-scale gradients in galactic continuum emission, or ground emission entering through the telescope side lobes.

Chapter 3

Uncertainties in the determination of H_o from SZE

3.1 Introduction

Having gone through the basic physics behind the SZE in the last chapter, we try to probe one of the fundamental parameters in cosmology, the Hubble constant (H_o), using SZE as our main tool. To do so, we look at observations of SZ distortions in clusters of galaxies, which have also been observed in X-ray. The distance to a cluster can be estimated from the two observations and along with a knowledge of the redshift of the cluster and plausible values for the other cosmological parameters (like Ω_o), one can estimate the value of the Hubble constant at the present epoch (for specific examples see Birkinshaw & Hughes 1994; Silverberg et.al. 1997).

In the radio band, a cluster can be observed in the Rayleigh-Jeans side of the cosmic microwave background spectrum as a dip in the brightness temperature. The SZ distortion appears as a decrement for wavelengths $\geq$ 1.44 mm (frequencies $\leq$ 218 GHz) and as an increment for wavelengths $\leq$ 1.44 mm (see Figure2.1). As noted in the introductory chapter, the SZE has the advantage that the SZ intensity, unlike that of the X-ray, does not suffer from the $(1+z)^{-4}$ cosmological dimming. The SZ signal is, however, weak and difficult to detect. Recent high signal-to-noise detections have been made over a wide range in wavelengths using single dish observations: at radio wavelengths (Herbig et al. 1995, Hughes & Birkinshaw 1998), millimeter wavelengths (Holzapfel et al. 1997, Pointecouteau et al. 1999) and sub millimeter wavelengths (Komatsu et al. 1999). Interferometric observations have also been carried out to image the SZ effect (Jones et al. 1993, Saunders et al.

1999, Reese et al. 1999, Grego et al. 2000). Most of these observations have been used to get an idea of the value of H_o .

These procedures generally assume the cluster gas to be spherical, unclumped and isothermal. Almost all clusters, however, show departures from these simplistic assumptions with some to a large extent. Departures from these simple assumptions can lead to systematic errors in the determination of the different cosmological parameters (Inagaki et al 1995). Observationally, the main handicap arises from the fact that the thermal structures of clusters is hard to measure. Similarly, the clumpiness of the ICM is hard to detect and to quantify. So, in general an isothermal, unclumped description of the cluster is taken (or sometimes a phenomenological temperature model based on the Coma cluster; for example, see Eq 73 of Birkinshaw 1999). The asphericity of the cluster may be easier (than temperature structure or clumpiness) to identify from observations. As we will see below, there can be a number of other errors that can creep in in using SZE to determine H_o . This chapter is devoted to a study of these uncertainties including those already discussed in the literature and a new and potentially major cause of error discussed here. We give a very brief review of the different systematic and random errors present in the estimation of H_o using this method, before going on to the physics of 'cooling flows' and its effect on the determination of H_o , which is the main topic of this chapter. We begin by describing the basic formalism used in estimating H_o using X-Ray and SZE.

3.2 Determining Hubble constant with Sunyaev-Zel'dovich effect

The method for the determination of Hubble constant using Sunyaev-Zel'dovich effect uses two observable quantities : 1) $\Delta T/T$ of the CMB due to SZ effect; 2) the X-ray surface brightness S_X of the cluster. These can be written as

$$\frac{\Delta T_{SZ}}{T}(r) = -2\int_{l_{min}}^{l_{max}} \frac{k_B T}{m_e c^2}\sigma_T n_e dl, \tag{3.1}$$

$$S_X(r) = \frac{1}{4\pi(1+z)^4}\int_{l_{min}}^{l_{max}} \frac{dL_X}{dV}dl, \tag{3.2}$$

where r is the distance to the line of sight from the cluster centre, l_{max} and l_{min} give the extension of the cluster along the line of sight, $\frac{dL_X}{dV}$ is the X-ray emissivity and dl the line element along the line of sight. All other symbols have their usual meanings as defined in Chapter 2.

The X-ray emissivity in the frequency band $\nu = \nu_1$ to ν_2 can be written as (Sarazin 1988)

$$\frac{dL_X}{dV} = {n_e}^2\alpha(T;\nu_1,\nu_2,z), \tag{3.3}$$

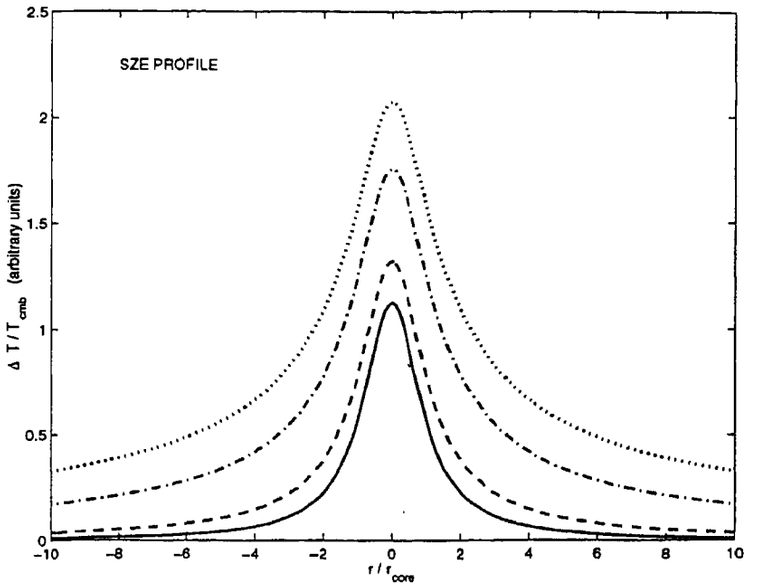

Figure 3.1: The SZ distortion for an *infinite* cluster having a β-model gas distribution is plotted for different β's. The normalization of the distortion is arbitrary, but constant for all the models. From top to bottom $\beta = 0.5,\ 0.67,\ 0.8$ and 1.

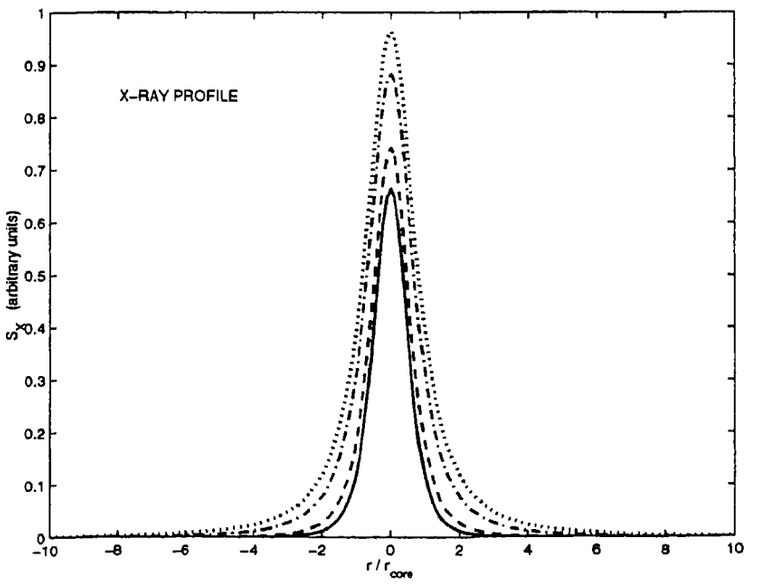

Figure 3.2: Same as above, but for the X-ray surface brightness.

where

$$\alpha(T;\nu_1,\nu_2,z) = \frac{2}{1+X}\left[\frac{2\pi}{3m_ec^2}\right]^{1/2}\frac{16e^6}{3\hbar m_ec^2}A(T;\nu_1,\nu_2,z), \tag{3.4}$$

where

$$A(T;\nu_1,\nu_2,z) = \int_{u_1(1+z)}^{u_2(1+z)}(k_BT)^{1/2}e^{-u}[Xg_{ff}(T,u,1)+(1-X)g_{ff}(T,u,2)]du. \tag{3.5}$$

In the above equations we have assumed primordial abundance of hydrogen and helium and have set $X = 0.76$, e is the electron charge, $\hbar = h/(2\pi)$, $u \equiv 2\pi\hbar\nu/k_BT$, and $g_{ff}(T,u,Z)$ is the velocity averaged Gaunt factor for the ion of charge Ze (Kellog et al. 1975).

Traditionally, to model the cluster gas distribution one takes the following density and temperature profiles (Cavaliere & Fusco-Femiano 1978)

$$n_e(r) = n_{e0}\left[1+\left(\frac{r}{r_{core}}\right)^2\right]^{-3\beta/2}, \tag{3.6}$$

$$T(r) = T_{iso} = constant, \tag{3.7}$$

where n_{e0} is the central electron density and r_{core} the core radius of the cluster. The above expressions are used as an empirical fitting model, and the parameter β is regarded as the fitting parameter. The equation holds for $0 < r < R_{cluster}$, where $R_{cluster}$ is the maximum 'effective' extension of the cluster. Conventionally, $R_{cluster} = \infty$, and then from Equations (3.1), (3.2), (3.6) and (3.7), we get

$$\frac{\Delta T_{SZ}}{T}(\theta) = -\frac{2\sqrt{\pi}\sigma_T k_B T_{iso}}{m_ec^2}n_{e0}r_{core}\frac{\Gamma(3\beta/2-1/2)}{\Gamma(3\beta/2)}\left[1+(\frac{d_A\theta}{r_{core}})^2\right]^{1/2-3\beta/2}, \tag{3.8}$$

$$S_X(\theta) = \frac{\sqrt{\pi}}{4\pi(1+z)^4}\alpha n_{e0}^2 r_{core}\frac{\Gamma(3\beta-1/2)}{\Gamma(3\beta)}\left[1+(\frac{d_A\theta}{r_{core}})^2\right]^{1/2-3\beta}, \tag{3.9}$$

where $\Gamma(x)$ is the gamma function and d_A and θ are the angular-diameter-distance and the angular distance from from the cluster centre. Since both the central CMB decrement and the X-ray surface brightness are observed, one can then combine equations (3.8) and (3.9) to estimate the core radius as

$$r_{c,est} = \left[\frac{\Delta T(\theta)}{T}\right]^2_{obs}\frac{\Gamma(3\beta-1/2)\Gamma(3\beta/2)^2}{S_X(\theta)_{obs}\,\Gamma(3\beta/2-1/2)^2\Gamma(3\beta)} \frac{m_e^2c^4\alpha}{16\pi^{3/2}(1+z)^4\sigma_T k_B T_{e,fit}^2}\left[1+(\frac{\theta}{\theta_{X,core}})^2\right]^{-1/2}. \tag{3.10}$$

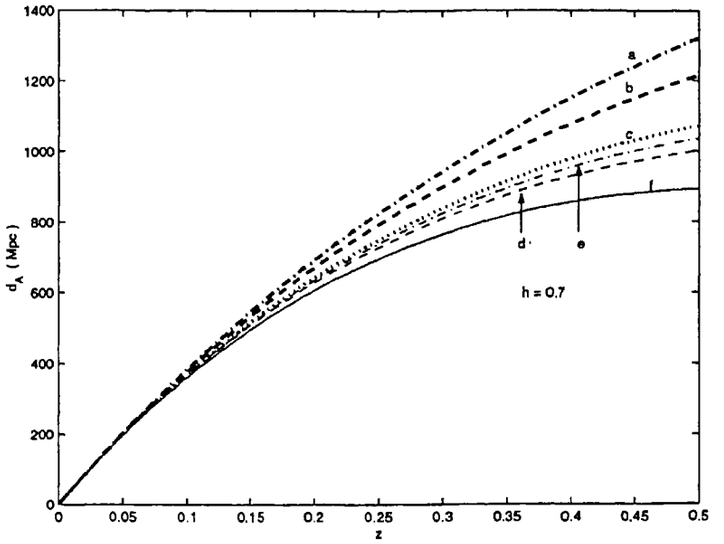

Figure 3.3: The angular-diameter distance vs redshift is plotted. The upper three lines are for a flat Universe and the lower three lines are for an open Universe. The labels are: $\Omega_o = 0.2$('a' & 'e'); $\Omega_o = 0.4$('b' & 'd'); $\Omega_o = 1$ ('f') and $\Omega_\Lambda = 1$('c'). For all cases, $h = 0.7$.

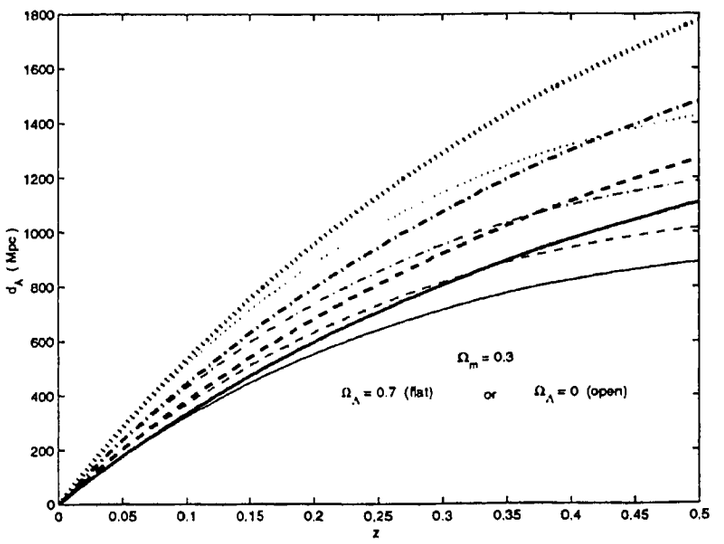

Figure 3.4: The angular-diameter distance vs redshift is plotted for different values of H_o , with $\Omega_o = 0.3$ and $\Omega_\Lambda = 1 - \Omega_o$ (thick lines) or zero (thin lines). In each case, from top to bottom, $h = 0.5, 0.6, 0.7, 0.8$.

In the above equation $\theta_{X,core}$ is the angular core radius observed in X-ray, and $T_{e,fit}$ is the X-ray flux averaged temperature (obtained from fitting the observed X-ray spectrum to the theoretical spectrum expected from isothermal case). This X-ray emission weighted temperature is given by

$$T_{iso} \equiv \frac{\int_0^{r_{vir}} T(r) \alpha {n_e}^2 r^2 dr}{\int_0^{r_{vir}} \alpha {n_e}^2 r^2 dr}. \tag{3.11}$$

The point to be noted is that r_{vir} is the virial radius of the cluster and its choice depends on the observer. If the gas temperature has a spatial structure then the T_{iso} inferred from such a procedure may have different values depending on how much of the cluster is taken in making the above average.

The angular diameter distance d_A can be approximated for nearby ($z \ll 1$) clusters in terms of the deceleration parameter $q_0 = \frac{\Omega_o}{2} - \Omega_\Lambda$ as (see Peacock 1999)

$$d_A = \frac{c}{H_o(1+z)} \left[z - \frac{1+q_0}{2} z^2 \right]. \tag{3.12}$$

Thus finally we have got an estimate of $d_A(z)$ as $r_{c,est}/\theta_{X,core}$. Now, if from other observations we know the cosmological parameters Ω_o and Λ, then one can estimate the Hubble constant.

As can be seen from the above equations, the value of H_o depends crucially on the assumptions of isothermality and β-model density distribution of the cluster. Cooling flow changes both these and so it can significantly affect the value of the Hubble constant.

3.3 Some uncertainties in the determination of H_o

The value of the H_o obtained using SZE is found to be systematically lower (a compilation of the estimated values of H_o is given in Birkinshaw 1999)than that found from other methods (for example, Cepheid distances). This has led to many investigations to the cause of such a decrease and to the reliability of obtaining H_o by this method. In particular, it has been found that non-isothermality, non-sphericity, clumpiness of intracluster medium and a host of other factors can give rise to either over or under estimation of the Hubble constant. In this section we take a quick look at these uncertainties, before going into another effect that can give rise to further uncertainty in the determination of H_o .

Basic error analysis: The major sources of error, till date, in the determination of H_o using SZE are observational in nature. They come from the uncertainty in determining the cluster parameters like β, r_{core} and T; the intracluster medium parameters like the central density $n_{e,0}$ and the metallicity $[Fe]/[H]$ and the central values of the $\frac{\Delta T}{T}$ and S_X. Errors are also introduced

due to contamination from point sources (specially near the cluster centre). If the sources have a flat spectra, then there can be an over estimation of H_o due to overestimation of the temperature of the cluster atmosphere. There can also be systematic errors due to overall flux and brightness temperature calibration uncertainties and from improper subtraction of zero level offset to SZ data. At present, the observational uncertainties are, perhaps, the biggest source of error in the determination of H_o using SZE. With time, however, these uncertainties will decrease and one has to look at other sources of error in greater detail. We begin by briefly summarizing a few of the other uncertainties :

- The first uncertainty in the determination of H_o comes from using Equations (3.8) and 3.9. These equations were derived under the assumption of the cluster being of infinite size. This is surely not the case, and the cluster can extend only up to some finite size given by R_{cl}, and $n_e = T = 0$ for $r > R_{cl}$. Integrating analytically, the Gamma functions in Equations (3.8) and 3.9 must then be changed to a combination of Beta and incomplete-Beta functions (see Inagaki et al. 1995, for details). As a result, the observed values of $\frac{\Delta T}{T}$ and S_X would be lower than their estimates based on the assumption of an infinite cluster. Due to the fact that the SZ profile is more extended than the X-Ray profile, (compare Figures 3.1 & 3.2), it is seen that that $\frac{\Delta T}{T}$ is lowered by $5 - 10\,\%$. However, the X-Ray surface brightness is almost unchanged. This gives rise to an underestimation of $r_{c,est}$ (from Equation3.11) and hence an over estimation of H_o .

- A major cause of uncertainty in the estimation of H_o is the assumption of isothermality for the intracluster medium . It has been seen (Yoshikawa et al. 1998) that this can lead to a substantial change in SZ effect and thus to the value H_o. There is some debate in the literature as to the temperature structure of the cluster gas. (Markevitch et al. 1998). Theoretical work shows the temperature structure in a cluster as the result of the shape of the gravitational potential (Navarro et al. 1997, Makino et al. 1998), or it can arise due to the fact that the initial falling gas in the cluster potential is less shock heated than the later falling gas (Evrard 1990). Recall that in obtaining Equations (3.8) and (3.9) one has assumed an isothermal temperature derived through Equation (3.11) applicable to the whole of the cluster. Hence, if there is a gradient in the temperature profile, then the estimation of the isothermal temperature would depend on the maximum radius up to which the temperature profile has been observed (*i.e.*, the upper limit in the integral of Equation (3.11)). Since, it is difficult to obtain spectroscopic temperatures up to large radial distance, the evaluation of Equation (3.11) is handicapped by our assumption of the temperature profile far away from the centre. Another source of error is the complicated dependence of S_X on T. However,

as has been pointed out by Inagaki et al. (1995), this dependence is rather weak (because the Gaunt factor is roughly proportional to $T^{-1/2}$ in most of the observational bands). Note, however, the X-Ray spectrum is dominated by photons from the outer region of the cluster. The uncertainty, once again, comes from the effect of the temperature profile on the SZ measurement. It is estimated that non-isothermality can lead to an under estimation of H_o by $\sim 20\,\%$, if the gas temperature in outer parts of the cluster is lower than that in the inner part (for example, in the Coma cluster; Hughes et al. 1988).

An unresolved temperature profile can also affect the measurement of H_o , in another way, namely by affecting the determination of the gas profile and the total mass derived using hydrostatic equilibrium. If a temperature gradient is present, then the gas mass obtained using a polytropic model of the temperature profile can be substantially different from that obtained using an isothermal profile. For example, in the case of A370, Grego et al. (2000) find the temperature profile to be well described with a polytropic index $\gamma = 1.2$. This can lead to relative error $\sim 30\,\%$ in the evaluation of H_o (see figure 3 of Puy et al. 2000).

- Asphericity of the cluster atmosphere can give rise to substantial deviation in the determination of value of the H_o (Birkinshaw et al. 1991; Puy et al. 2000). If one assumes that the atmosphere is prolate or oblate, rather than spheroidal, with the symmetry axis oriented along the line of sight, then it would be difficult to determine the asphericity from observations of the isophotes (due to circular symmetry). In such a case, let us assume that the core radius of the gas distribution is larger by a factor F_{asph} than the core radii in the other two directions. It can be easily shown that the value of H_o will be underestimated if the cluster is prolate (*i.e.*$F_{asph} > 1$), and overestimated if the cluster is oblate ($F_{asph} < 1$). Thus the projection effect of the cluster can be a cause of systematic error in SZ effect (Cooray 1998, Sulkanen 1999). Puy et al. (2000) do a thorough study of the effect of asphericity of galaxy clusters on the determination of H_o and find errors up to 30 % for specific cases. There remains the possibility that this effect can be averaged out in an ensemble of clusters selected on the basis of integrated X-Ray flux.

- Clumpiness of the intracluster medium can also be a source of error. The assumption that goes into interpreting the observations is that density variations on scales that are unresolved by the images are small. However, strong clumping can affect the X-Ray emissivity ($\propto n_e^2$) more than the SZ effect ($\propto n_e$). If one characterizes the clumping factor by $F_{clump} = < n_e^2 > / < n_e >^2$, then it can be shown that $d_A(\text{true})/d_A(\text{estimate}) = F_{clump}$. Hence if the ICM is significantly clumped ($F_{clump} > 1$), then H_o is overestimated. Unlike asphericity, clumping cannot be averaged out from cluster to cluster, since all clusters do have some varying degree

of clumpiness (Mathiesen et al. 1999, Mohr et al. 1995, 1999). From hydrodynamical simulations of clusters, Inagaki et al. (1995) find that clumpiness can lead to overestimation of the Hubble constant of about $10-15\,\%$ in a SCDM Universe and perhaps much lower in Universe with a low Ω_o.

A related factor that can be another source of error is the presence of large scale substructures of the intracluster medium . Hydrodynamic simulations (Yoshikawa et al. 1998; Roettiger et al. 1997) show that almost all clusters have some form of sub structure (for example, due to mergers). This can lead to error in fitting the cluster parameters by a single β model and also in the intensity distribution of S_X and SZ distortion, both of which are assumed to fall smoothly with distance from the cluster centre.

- Another source of uncertainty in the determination of H_o is the inaccurate knowledge of the X-ray Bremsstrahlung emissivity, where mostly non-relativistic expressions are used. For example the Raymond & Smith code normally used for X-ray emission uses the Gaunt factor evaluated by Karzas & Latter (1961) which uses non-relativistic physics for the plasma emission. Moreover, as seen in Chapter 2, the relativistic corrections to the SZ decrement can be important for clusters with $T > 5$ keV. Hence, corrections to both S_X (Nozawa et al. 1998b) and $\frac{\Delta T}{T}$ should be incorporated for a more reliable evaluation of the H_o . However, as pointed out in Hughes & Birkinshaw (1998), the inclusion of relativistic corrections lead to a small change in the final value of the H_o of the order of $\sim 1-2\,\%$ only.

- Measurements of thermal SZE from galaxy clusters are always contaminated by the presence of the kinematic SZE. As long as they are not separated out using multi frequency observations, the KSZE acts as an additional source of temperature distortion. Typically $\frac{\Delta T(\mathrm{kin})}{\Delta T(\mathrm{thermal})} \sim 0.05\left(\frac{v_r}{300\mathrm{kms}^{-1}}\right)\left(\frac{5\mathrm{keV}}{T}\right)$, where v_r is the peculiar velocity of the cluster. The total distortion $\Delta T = \Delta T(\mathrm{kin}) + \Delta T(\mathrm{thermal})$. This can be over or underestimated according to the relative sign of v_r. In CDM Universes, v_r can have a range of values between $300-400$ km s^{-1}, and hence the error due to the presence of KSZE is generally less than $5\,\%$.

- It is evident from Equation (3.12), that the derived value of the Hubble constant would depend on our knowledge of the other cosmological parameters, Ω_o and Ω_Λ. As long as the redshift of the cluster is less that 0.2, d_A doesn't change significantly with small variation in the presently acceptable values of the the cosmological parameters (see Figure 3.3). For example, changing q_0 from 0 to 0.5 for clusters A665 or A2218 (having $z \sim 0.17-0.18$) would lead to a change in H_o by $\sim 3\,\%$. For a high redshift cluster like CL 0016+16, the changes in H_o due to different cosmology can be higher (by $\sim 5-10\,\%$). This issue has been dealt with

in the work by Kobayashi et al. (1996)

- An interesting effect called the Loeb-Refregier effect (Loeb & Refregier 1996) can lead to underestimation of the H_o inferred from SZE. This occurs due to the following reason: measurement of SZE takes into account the subtraction of background radio sources from the cluster field. The gravitational lensing by the cluster can, however, lead to a systematic deficit in the residual intensity of unresolved sources behind the cluster relative to a field far from the cluster centre, resulting in the over estimation of the R-J temperature of the microwave background . This gives rise to a systematic bias and can lead to under estimation of H_o by $\sim 5 - 10\,\%$. The ratio of lensing to SZ decrement depends on the relative dark matter density to gas density profiles. This ratio increases if the decline of gas pressure with radius is steeper than that of the dark matter density.

- Finally, we briefly mention two other probable sources of error. The first comes from the possible presence of a non-thermal component of electron population (cosmic rays). Large scale hydrodynamic simulations of clusters (Miniati et al. 2001) show that it may be possible to have non-thermal pressure, close to the cluster centre, to be a significant fraction of the thermal gas pressure. If this is the case, then it would affect the determination of the dynamical mass and the cluster gas profile β and would also add a non-thermal SZE component to the already present thermal distortion. Any estimation which neglects this new component would lead to an error in the determination of H_o . As will be seen in Chapter 7, (Figures 7.9 & 7.4), radio cocoons embedded in clusters of galaxies or as field radio galaxies can produce substantial SZ decrement. Presence of such cocoons in the line of sight of a cluster for which SZ decrement is measured will lead to a positive bias to the total SZ distortion and hence can affect the estimation of H_o . An example of a cluster containing such a radio source is RX J1347 - 1145 (Pointecouteau et al. 2001)

Now that we have an idea of the many different sources of uncertainties in the determination of the Hubble constant using the SZE, we turn to a detailed study of another important phenomenon that can substantially change the temperature structure in the innermost regions of a cluster, *viz.* a cooling flow, and thus be another source of uncertainty. Cooling flows in clusters of galaxies (for an introduction, see Fabian et al. 1984) is claimed to be well established fact by now. The idealized picture of a cooling flow is as follows: Initially when the cluster forms, the infalling gas is heated due to gravitational collapse. With time this gas cools slowly and a quasi hydrostatic state emerges. However in the central region, where energy is lost due to radiation faster than elsewhere, an inward 'cooling flow' initially arises due to the pressure gradient (Fabian 1994). This can modify

the SZ decrement and act as a systematic source of error in the determination of the cosmological parameters.

Schlickeiser (1991) has shown that free-free emission from cold gas in the cooling flow can actually lead to an apparent decrease of the SZ effect at the centre. Since the central cooling flow region is generally very small, the isothermal β-model of cluster gas can still be used for the majority of cluster region even for cooling flow cluster, with the extra precaution of excluding the central X-ray spike from the X-ray fit, and a corresponding change made in the fitting of the SZ decrement. This is only possible, however, for nearby clusters with well resolved cluster cores.

3.4 Cooling flows in clusters

3.4.1 Preliminaries

The motivation for considering cooling flows come from X-Ray observations of galaxies and clusters of galaxies. It is generally found that a significant number of clusters have a sharply peaked X-Ray surface brightness distribution. This is indicative of enhanced gas density and has been explained as due to the presence of a cooling flow. This shows that the gas density has increased near the centre and since the luminosity goes as the square of the density, the luminosity is highly peaked near the center. One can then calculate the cooling time near the centre to check if it is smaller than the age of the cluster. The cooling flow can then be characterized by $\dot{M}$, the flux of mass flowing in. Observationally, it is seen that around $60-90\%$ of clusters exhibit cooling flows in their core with $\approx 40\%$ of them having cooling flows of more than $100 M_{\odot}\ yr^{-1}$ (Markevitch et al. 1998, Peres et al. 1998, Allen et al. 1999). In the largest systems, the mass deposition rate can be as high as $1000 M_{\odot}\ \mathrm{yr}^{-1}$ (Allen 2000). In particular, three arguments can be given in favour of cooling flow:

- **X-Ray surface brightness profiles:** are sharply peaked showing enhanced density near the centre. However, the material seem to deposited near the very centre (few tens of kpc) as it flows in (Fabian 1994).
- **X-ray spectral data:** Observations of emission lines from gas temperature of $\sim 10^6$ K.

Excess X-Ray absorption has been found (for example, Ginga and Einstein Observatory data of A478, see Johnstone et al. 1992) for clusters having cooling flows inferred from peaked X-Ray surface brightness. This excess absorption is not present in non cooling flow clusters. The excess absorption gives credence to the theory that the cooling flow material drops out from the flow to form chunks of cooled gas (and probably lead to star formation at a later time).

One must stress that the arguments given above in favour of cooling flows only indicate the presence of cool gas in the cores of the clusters, but there is no direct evidence gas flowing into the core. The motion of the gas has not yet been directly detected, since the Doppler shifts due to the motion are too small to be resolved using X-Ray observations.

The basic physics of cooling flow is simple: The ICM, with a typical density of $10^{-4} - 10^{-2}\,\mathrm{cm}^{-2}$ sitting in the gravitational field (which in this case is mainly provided by the total dark matter in the cluster) has its sound speed similar to the typical velocity of a cluster galaxy. The velocity dispersion of cluster galaxies is around $500 - 1200\,\mathrm{km/s}$, and this requires a gas temperature of around $T_{\mathrm{ICM}} \sim 10^7 - 10^8\,\mathrm{K}$. The main energy loss for ICM, for this temperature range, is that from thermal Bremsstrahlung which is $\sim 10^{43} - 3 \times 10^{45}\,\mathrm{ergs/s}$. The intra-cluster gas is densest in the core of the cluster and hence the cooling time, t_{cool}, due to X-Ray emission is the shortest there. This can then result in a '*cooling flow*' if t_{cool} becomes less than the age of the system, $t_a \equiv t_{Hubble} \sim \mathrm{H_o}^{-1}$. Also, for most of the cluster gas, the cooling timescale is larger than the gravitational free-fall timescale, t_{grav}. Thus, for the innermost regions

$$t_a > t_{cool} > t_{grav} \,. \tag{3.13}$$

Due to the cooling of the gas, the pressure in the innermost parts drops, and to support the weight of the overlaying material above some radius, r_{cool}, an inflow takes place to increase the density and pressure of the innermost regions, giving rise to the cooling flow. A cooling flow is thus essentially pressure driven. However, the underlying gravitational potential can influence the flow to a large extent and at times even makes it gravity driven. We will come back to this point later in this chapter.

The gas continues to cool as it flows inwards until the adiabatic compression of the inflowing gas can counterbalance the radiative loss. Compression can even give a rise in the gas temperature. Finally, the gas temperature can plunge in the core of the central galaxy. As a net result, the gas within r_{cool} radiates its thermal energy as well as the pdV work done on it. This scenario describes a gas which has an unique temperature and density at each radial distance from the centre. Observations point out that the gas must be inhomogeneous. However, homogeneous flows (Cowie &Binney 1977) are still a good approximation and in this chapter we stick to homogeneous cooling flow models. This means 1) there is a single temperature and density at each r, and 2) the gas density rises inwards and the gas temperature drops so that an approximate pressure equilibrium exists. However, this simplistic picture cannot explain all the observations of cooling flows and one must finally consider an inhomogeneous multi phase model (see Nulsen 1986). Finally, as the flow

cools, cold clouds form which fall out of the flow and at some point of time the cloud drops out of pressure and ionization equilibrium. Further collapse can be supported by the amplification of magnetic field pressure. However, as cooling goes on, the magnetic fields can be expelled through ambipolar diffusion and the gas temperature can drop further giving rise to molecular clumps which can, in turn, form low mass stars or brown dwarfs.

Before going into the physics of cooling flows in some detail, we mention here a few problems and their possible solutions discussed in the literature. As mentioned earlier, strong evidence for cooling flows has been found in low resolution X-ray imaging and spectra of many galaxy clusters. However, recent high resolution X-Ray spectra from the Reflection Grating Spectrometer (RGS) on XMM-Newton show soft X-Ray spectrum inconsistent with cooling flow (Brinkman et al. 2000). Although, the spectra shows strong temperature decrease towards the centre, there is no evidence of emission lines (particularly Fe-XVII) from gas at 1 keV or below. Lines from the gas at $2-3$ keV are, however, observed. This has lead to some doubt on the credibility of the simple cooling flow models of galaxy clusters. Various explanations have been given to resolve this discrepancy (Peterson et al. 2000; Fabian et al. 2000). These include heating, mixing, differential absorption and inhomogeneous metallicity. Finally, recently there has been detection of the O VI doublet in the galaxy NGC 4636, showing that the gas can indeed cool to a temperature of around 3×10^5 K, leading support to the existence of cooling flows in astrophysical objects (Bregman et al. 2001).

3.4.2 More on cooling flows

In this subsection, we set up the equations for a cooling flow and study their solutions. The basic equations of cooling flow are:

$$\begin{aligned} \frac{du}{dr} &= -\frac{u}{\rho_b}\frac{d\rho_b}{dr} - \frac{2u}{r} - \frac{\dot{\rho}_b}{\rho_b}, \\ u\frac{du}{dr} + \frac{1}{\rho_b}\frac{d(\rho_b\theta)}{dr} &= -\frac{GM_t(r)}{r^2}, \\ u\frac{d}{dr}\left(\frac{3\theta}{2}\right) - \frac{\theta u}{\rho_b}\frac{d\rho_b}{dr} &= \frac{\rho\Lambda(\theta)}{(\mu m_p)^2}, \end{aligned} \tag{3.14}$$

where $\theta = 2k_BT/\mu m_p$, μ is the mean molecular weight, and m_p is the proton mass, u is the fluid velocity, ρ_b's is the gas density, r is the radial distance from the centre and time derivatives are indicated by a dot. For steady flows with constant mass flux, $\dot{\rho} = 0$. This implies $u = \dot{m}/4\pi\rho r^2$ for steady flows. (Note that in cooling flows both u and $\dot{m}$ are negative. The subscripts b refers to baryons and t refers to total i.e baryons + dark matter. However, we assume the baryonic contribution to the total mass negligible w.r.t to the dark matter contribution.)

$M(r)$ describes the distribution of the total mass and depends on the details of dark matter density profiles (see below). $\Lambda(\theta)$ is the cooling function defined so that $n_e n_p \Lambda(\theta)$ is the rate of cooling per unit volume, n_e and n_p being the number densities of electrons and protons, respectively. We use an analytical fit to the optically thin cooling function as given by Sarazin & White (1987),

$$\begin{aligned}\left(\frac{\Lambda(\theta)}{10^{-22}\,\mathrm{erg\,cm^3\,s^{-1}}}\right) &= 4.7 \times \exp\left[-\left(\frac{T}{3.5\times10^5\mathrm{K}}\right)^{4.5}\right] \\ &+ 0.313 \times T^{0.08} \exp\left[-\left(\frac{T}{3.0\times10^6\mathrm{K}}\right)^{4.4}\right] \\ &+ 6.42 \times T^{-0.2} \exp\left[-\left(\frac{T}{2.1\times10^7\mathrm{K}}\right)^{4.0}\right] \\ &+ 0.000439 \times T^{0.35} . \end{aligned} \tag{3.15}$$

This fit is accurate to within 4%, for a plasma with solar metallicity and for $10^5 \leq T \leq 10^8$ K. For $10^8 \leq T < 10^9$ K, it underestimates cooling by a factor of order unity (compared to the exact cooling function, as in, e.g., Schmutzler & Tscharnuter 1993) , and therefore is a conservative fit to use, as far as the effect of cooling is concerned.

For non-steady flows, we adopt the formalism of White & Sarazin (1987), where the mass deposition rate, $\dot{\rho}$, is characterized by a 'gas-loss efficiency' parameter q. One writes $\dot{\rho} = q(\rho/t_{cool})$ where t_{cool} is the local isobaric cooling rate ($t_{cool} = 5k_B T\mu m_p/\rho\Lambda$). It has been found that $q \sim 3$ models can reproduce the observed variation of mass flux ($\dot{m} \propto r$) (Sarazin & Graney 1991). Fabian (1994) has noted that these models of White & Sarazin (1987) yield good approximations to the emission weighted mean temperature and density profiles for cooling flow clusters. Rizza et al. (2000) have used the steady flow models of White & Sarazin (1987) to simulate cooling flows.

We first discuss cooling flows with $\dot{m}$ =constant. With $q = 0$, one can eliminate the density from Eq. 3.14 to get two differential equations:

$$\begin{aligned}\frac{du}{dr} &= \frac{u}{[r^2(5\theta - 3u^2)]}\left[3GM - 10r\theta + \frac{\dot{m}}{2\pi}\frac{\Lambda(\theta)}{uM^2}\right] , \\ \frac{d\theta}{dr} &= \frac{2}{[r^2(5\theta - 3u^2)]}\left[\theta(2u^2 r - GM) - (u^2 - \theta)\frac{\dot{m}}{4\pi}\frac{\Lambda(\theta)}{uM^2}\right] . \end{aligned} \tag{3.16}$$

These equations have singularities at the sonic radius r_s where $5\theta_s = 3u_s$. A necessary condition of singularity is that the denominators of Eq. 3.16 vanish at the sonic radius. Therefore (Mathews & Bregman 1978),

$$r_s = (3/10\theta_s)\left[GM(r) + \frac{\dot{m}\Lambda(\theta_s)}{10\pi\theta_s M^2}\right] . \tag{3.17}$$

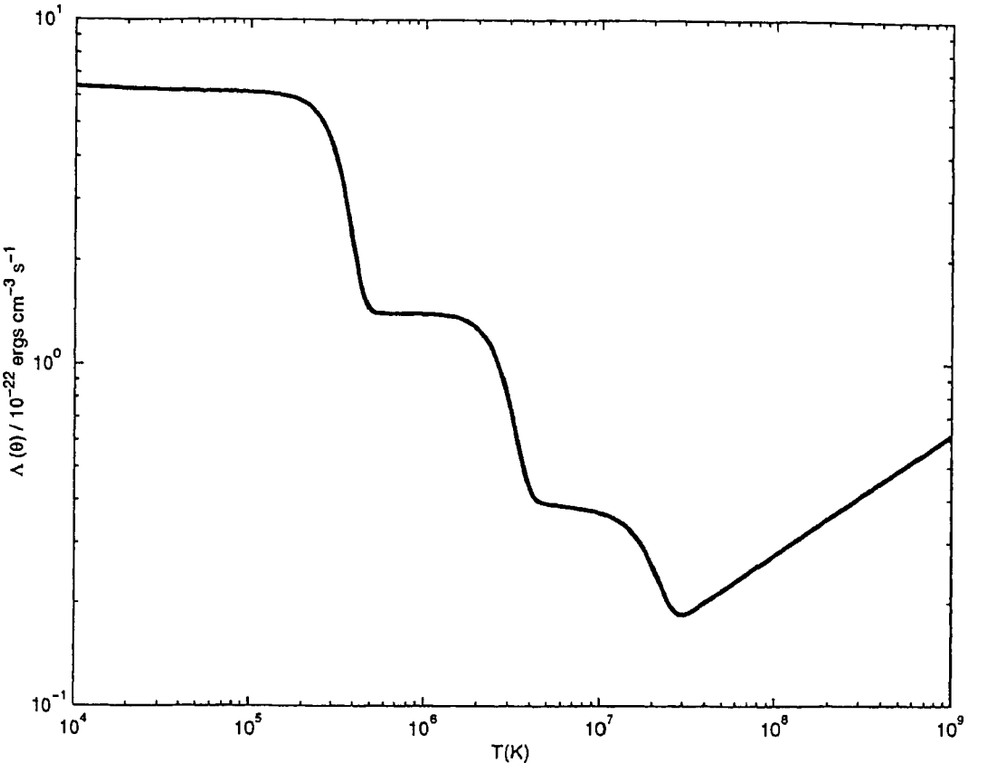

Figure 3.5: Plot of the cooling function used in our analysis.

We have used two different dark matter profiles for the cluster. The first model (Model A) has been discussed earlier in the literature in the context of cooling flows in cluster (White & Sarazin 1987, Wise & Sarazin 1993) with a density profile,

$$\rho_d = \begin{cases} \frac{\rho_o}{1+(r/r_{core})^2} + \frac{\rho_{o,g}}{1+(r/r_{c,g})^2} & \text{if } r < 237 \text{ kpc} \ , \\ \frac{\rho_o}{1+(r/r_{core})^2} & \text{if } r > 237 \text{ kpc} \ . \end{cases} \tag{3.18}$$

Here $\rho_o = 1.8 \times 10^{-25}$ gm cm^{-3} and $r_{core} = 250$ kpc describe the profile of the cluster mass, and $\rho_{o,g} = 4.1 \times 10^{-22}$ gm cm^{-3} and $r_{c,g} = 1.69$ kpc describe the profile of the galaxy in the centre of the cluster.

Model B does not have the galaxy in the center, and so it is described simply by $\rho = \rho_0/[1 + (r/r_{core})^2]$.

With these assumptions, the solutions for steady cooling flows, ($\dot{m}$ = constant) are fully char-

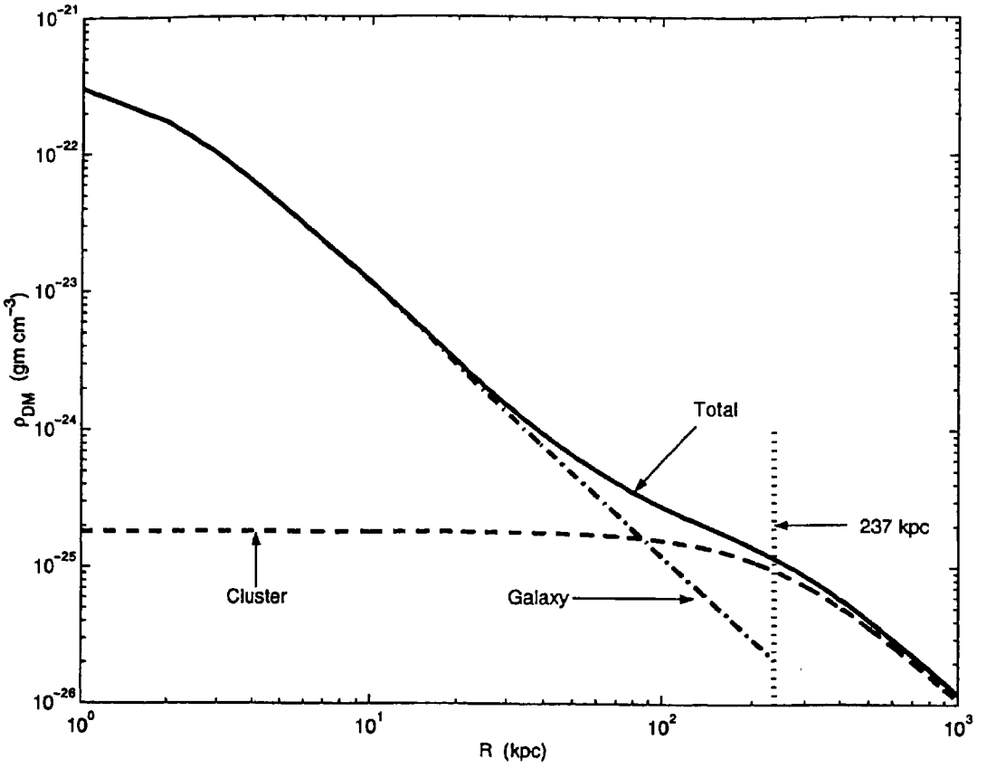

Figure 3.6: The underlying total dark matter density profile is shown, as well as, the individual central galaxy and the cluster dark matter density profiles. The vertical dotted line is at 237 kpc which is the extension of the galactic density profile.

acterized by (1) the inflow rate, $\dot{m}$, and (2) the temperature of the gas T_s at the sonic radius r_s. Obviously, the cooling flow solutions are only valid within the cooling radius r_{cool} where $t_{cool} = t_a$. We assume a value of $t_{age} = 10$ Gyr for all models. We assume that outside the cooling radius, gas obeys quasi-hydrostatic equilibrium (Sarazin 1986). Although this means matching the cooling flow solutions with nonzero u to $u = 0$ solutions outside, in reality the velocity of gas at the cooling radius is very small; for example $\dot{m} = 100$ M$_\odot$ yr^{-1} with $\rho \sim 10^{-26}$ gm cm^{-3} at $r = 250$ kpc implies a velocity of 30 km s^{-1}, which is close to the limit of turbulence in the cluster gas (Jaffe 1980), and smaller than the sound velocity ($\sim 1.5 \times 10^3\,(T/10^8\,K)^{1/2}$ km s^{-1}). The velocity of the flow at the cooling radius is, therefore, for all practical purposes, sufficiently small to be matched to the solution of hydrostatic equilibrium outside. (In this approach, we avoid the time consuming search for the critical value of $\dot{m}$ for which the flow solutions behave iso-thermally at $r \to \infty$.

As in the usual assumptions for the interpretation of SZ effect, we assume that the gas outside the cooling radius is isothermal, with a constant temperature profile. The density, therefore, obeys $\rho \propto [1 + (r/r_{core})^2]^{-3\beta/2}$, where $\beta = \mu m_p \sigma^2 / k_B T_{iso}$, and T_{iso} is the temperature of the gas at and outside the cooling radius.

For models with non-zero q, the solutions are characterized by T_s and the value of $\dot{m}$ at the cooling radius, $\dot{m}_{cool}$. Since a fraction of mass drops out of the flow in this case, the inflow velocity need not rise fast and so it is possible to find completely subsonic solutions.

3.4.3 Cooling flow solutions

We solved the flow equations, numerically, for the parameters listed in Table 1. The density, temperature and pressure profiles for three cases are presented in Figures 1, 2 & 3. We mark the position of r_{cool} in each case and we mark r_s for the cases of transonic flows (when $\dot{m}$ = constant). Beyond r_{cool} we match a hydrostatic solution. We also present, for comparison, the behaviour of the solutions if the solutions outside r_{cool} are assumed to extend inwards (that is, if no cooling flow is assumed). We will postpone the discussion on the effect of these profiles on the SZ decrement to a later section, and only discuss the qualitative aspects of the solutions here.

First, let us compare our solutions to the ones already existing in the literature. The solution A1 is similar to that presented by Wise & Sarazin (1993) (their Figure 1; although they chose to characterize the solutions by the temperature at r_{cool} and not T_s as we have done here). It is also similar (qualitatively) to the solution for A262 presented by Sulkanen et al. (1989). As the latter authors have noted, the effect of having a galactic potential in the center is to have a flatter temperature profile for $r > r_s$, than in the case of no galactic potential. This aspect is clearly seen while comparing our solutions with and without galactic potentials in the center. Our calculations for the case without the central galaxy are admittedly flawed in the very inner regions where the gas density is larger than the dark matter density, which results in an incorrect determination of the gravitational potential in the inner region. However, this happens only inside a region $\sim$ 25 kpc from the centre, and should not influence our final results by a large extent.

A word of explanation for the pressure profiles is in order here. Naively, it would appear that the pressure inside the cooling radius should have lower values than the corresponding case of hydrostatic equilibrium. The fact that it is not always so has been noted in the literature (e.g., Soker & Sarazin 1988, Figure 1 of Sulkanen et al. 1989). The reason for the pressure bump just outside of the sonic radius is that the flow in this inner region is not pressure driven, but rather by gravity (see also Soker & Sarazin 1988). This is why the bump in the profile depends on the

Table 3.1: Parameters for cooling flow solutions

Solution	Mass Model	q	$\dot{m}(r_{cool})$	T_s	r_s	r_{cool}	T_{iso}
			($M_\odot$ yr^{-1})	(K)	(kpc)	(kpc)	(K)
A1	Model A	0	100	6.5×10^6	0.688	127.5	1.2×10^8
A2	Model A	0	200	6.5×10^6	0.462	96.1	7.7×10^8
A3	Model A	0	300	6.5×10^6	0.712	132.2	7.7×10^8
B1	Model B	0	100	4.0×10^6	0.688	85.7	1.14×10^9
B2	Model B	0	200	6.5×10^6	0.462	89.6	1.9×10^9
B3	Model B	0	300	6.5×10^6	0.712	110.3	1.9×10^9
C1	Model A	3	200			111.6	1.1×10^8
C2	Model A	3	300			132.2	1.1×10^8

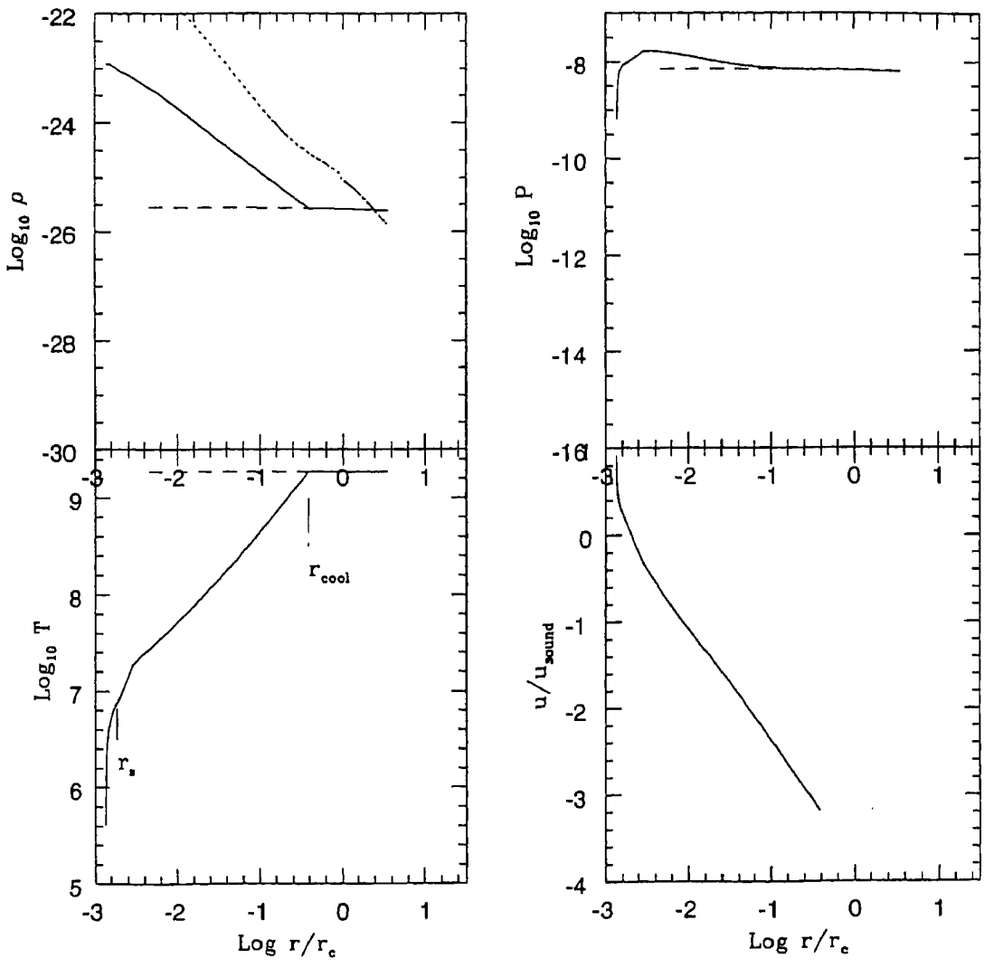

Figure 3.7: Cooling flow solution A2. The upper left panel shows the dark matter density profile (dotted line), the gas density profile for the cooling flow (solid line) and the corresponding case of gas in hydrostatic equilibrium. The lower left panel shows the temperature profiles for the same cases. The position of r_s and r_{cool} are shown. The upper right panel shows the pressure profiles and the lower right panel plots the Mach number of the cooling flow gas as a function of the radius.

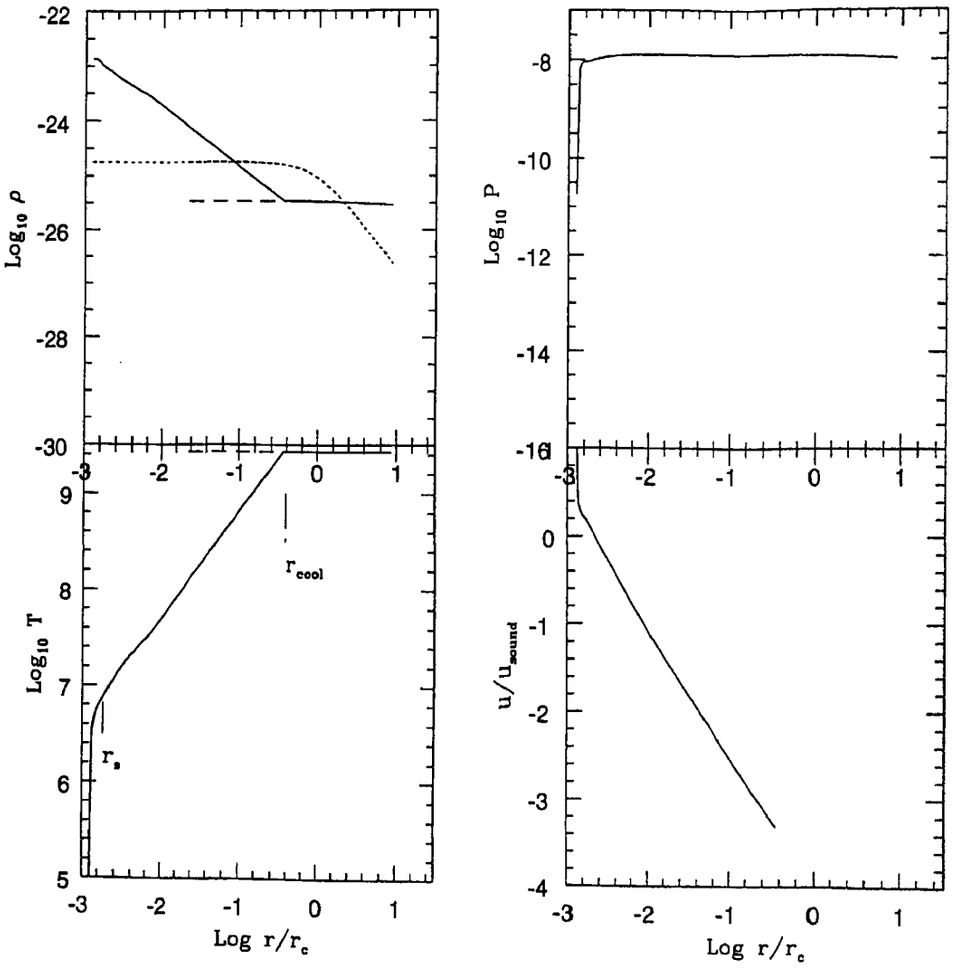

Figure 3.8: Same as figure 3.7, for cooling flow solution B2.

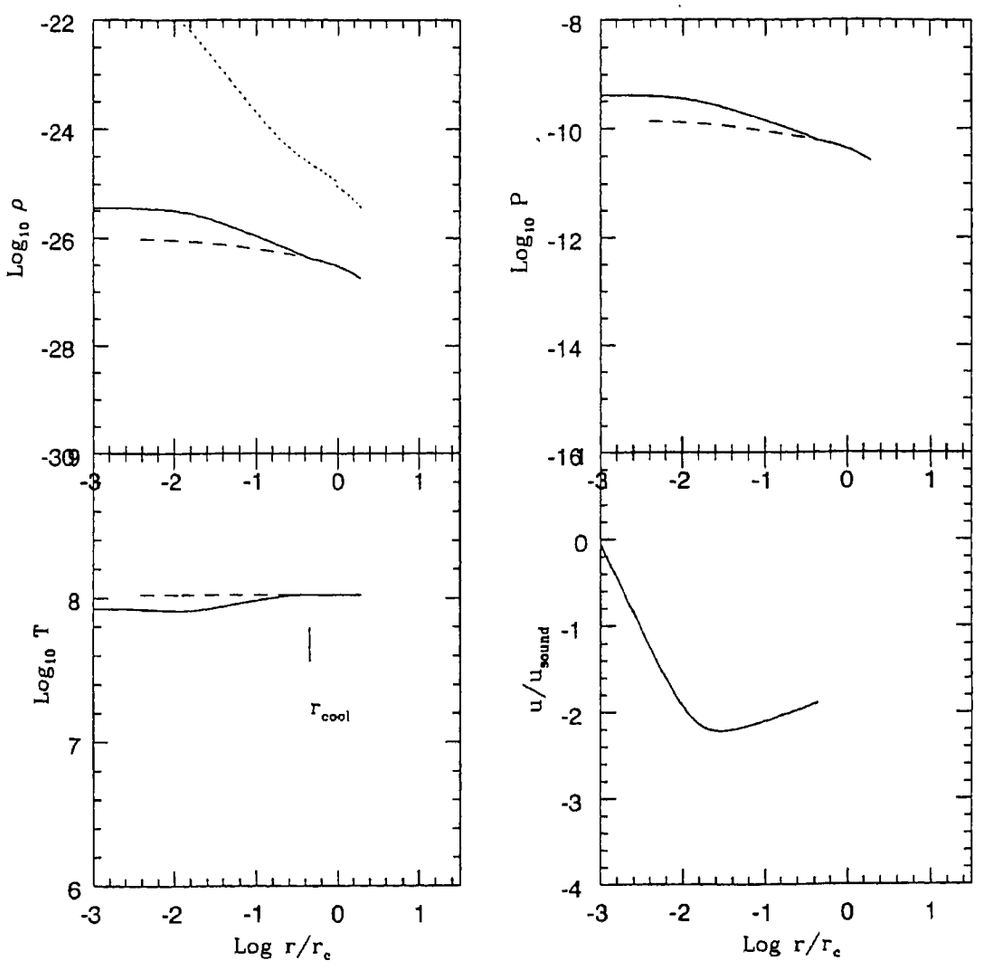

Figure 3.9: Same as figure 3.7, for cooling flow solution C1.

presence and absence of the galaxy in the centre. And this profile leads to the curious result that the presence of cooling flow can lead to the over estimation of the Hubble constant as discussed in the next section

The model with mass deposition (C1) is shown in Figure 3. The local mass flux is found to be almost proportional to the radius, consistent with various observations (Fabian, Nulsen & Canizares 1984, Thomas et al. 1987), and, therefore, is probably a realistic model for cooling flow clusters. In this case the temperature drops gradually all the way through, since the velocity does not rise too fast. The deposited mass is assumed to impart negligible pressure and the pressure refers only to that of gas taking part in the flow.

3.5 Determination of Hubble constant

Naively, the change in the central SZ decrement $y(0)$ in the presence of cooling flows can be seen as follows : For a non cooling flow cluster, the central decrement is given by the line of sight integral of the electron pressure through the cluster centre along the full extent of the cluster. If the cluster has a maximum radius r_{cl}, then the central SZ decrement at R-J wavelengths can be written as $y(0) = -4\frac{\sigma_T}{m_e c^2}\int_0^{r_{cl}} p_e dl$. For a cluster with a cooling flow, let us suppose that the electron pressure p_e drastically falls below a certain radius r_s, which is typically well inside the core of the cluster. The resulting central decrement is then $y(0) \approx -4\frac{\sigma_T}{m_e c^2}\int_{r_s}^{r_{cl}} p_e dl$. Depending on the distance of r_s from the cluster centre [$r_s \approx$ (0.1 to 0.3)r_{core}],there will be a change in the value of $y(0)$ by $\approx 5\% - 25\%$. However, this simplistic view may not be correct. This estimate assumes that the pressure profile remains a β profile outside the radius r_s. The pressure profile, however, need not follow the β profile once cooling flow starts and it can deviate from it substantially even for radii much larger than r_s. As a matter of fact, there can actually be an increase in the pressure for a large region inside the cooling flow, before a sudden drop inside r_s. Since the usual procedure for estimating the Hubble constant depends on fitting β profiles to the SZ and X-ray profiles, to estimate r_{core}, this change in the pressure profile due to cooling flow can distort the estimation of r_{core} and hence, the value of H_o in a non-trivial way. We study this effect in detail in later sections.

In this section we discuss the SZ and X-ray profiles of clusters with cooling flows. We compare these with profiles from cluster having gas in hydrostatic equilibrium, and comment on the reliability of measuring Hubble constant. The effect of cooling flow and the subsequent increased Bremsstrahlung emission is seen in the sudden increase in the X-ray flux in the innermost region of the cluster (Figure 5). The signature of the cooling flow is seen in the form of the central spike in the X-ray profile. The X-ray profile is more sensitive to the gas density profile but is affected

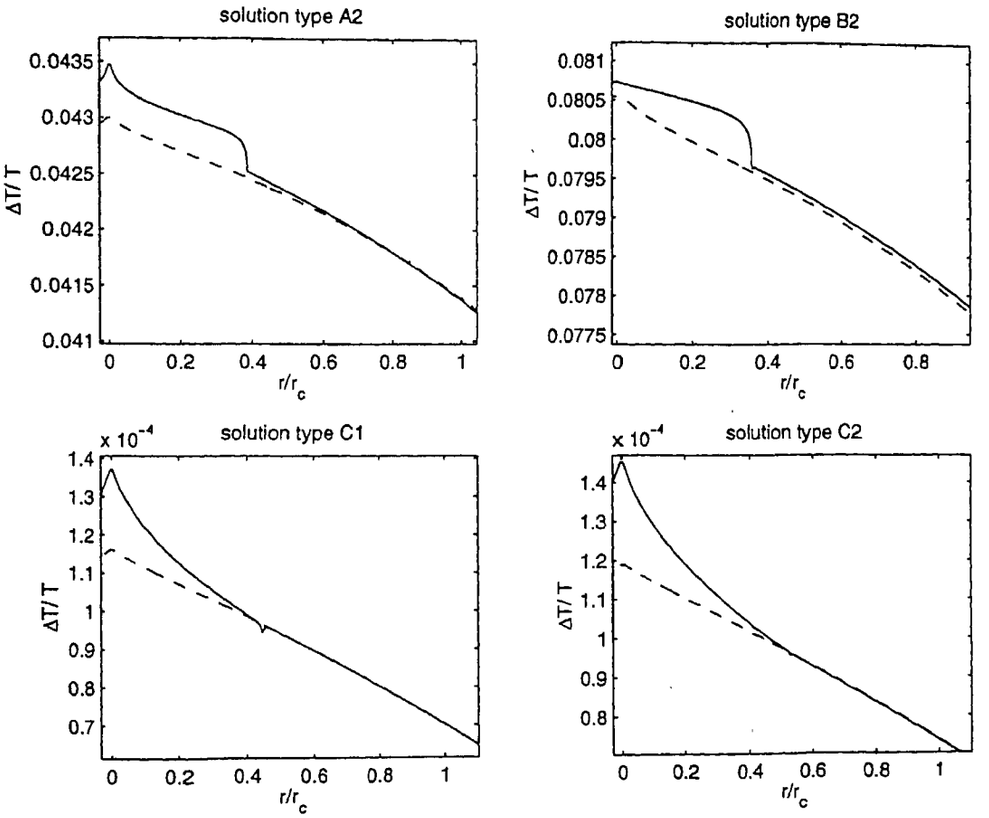

Figure 3.10: Unconvolved SZ profiles, for the solution types A2 (upper left), B2 (upper right), C1 (lower left) and C2 (lower right), for cooling flow (solid line) and the corresponding cases of gas in hydrostatic equilibrium (dashed line). $\frac{\Delta T_{R-J}}{T_{cmb}}$ is plotted against $\frac{r}{r_{core}}$. Individual plots have been magnified to highlight the differences between cooling flow and hydrostatic cases.

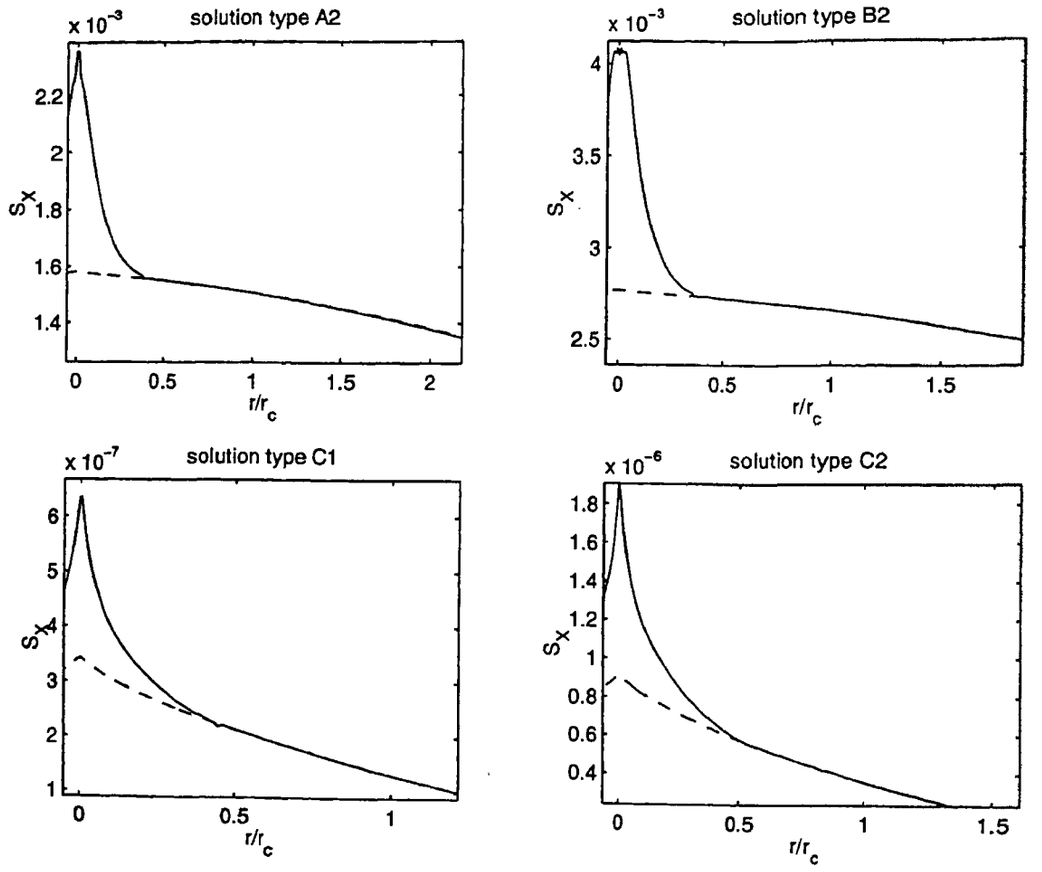

Figure 3.11: Unconvolved X-ray profiles for the solution types A2 (upper left), B2 (upper right), C1 (lower left) and C2 (lower right), for cooling flow (solid line) and the corresponding cases of gas in hydrostatic equilibrium (dashed line). X-ray surface brightness in units of ergs s^{-1} cm^{-2} $ster^{-1}$ is plotted against $\frac{r}{r_{core}}$. Individual plots have been magnified to highlight the differences between cooling flow and hydrostatic cases.

slightly by the drop in temperature. The temperature dependence becomes important only near the sonic point. Outside r_{cool}, the X-ray profile is the same as that in the hydrostatic cases.

The SZ distortion is proportional to the line of sight integral of the pressure, and the sudden increase of the gas density inside the cooling radius is moderated by the decrease of the gas temperature. As a result there is a gradual increase in the gas pressure. Near the sonic point the temperature drops drastically by orders of magnitude, and results in sudden decrease in pressure. However, since this change in pressure becomes acute only within $\approx$ 5% of the core radius, it contributes negligibly to the line-of-sight integral of the gas pressure, and leads to an increase in the SZ distortion inside the cooling radius for all models considered (see Figure 4). Like the X-ray profiles, the SZ profiles outside r_{cool} is the same as that for the corresponding hydrostatic cases.

The SZ profiles have been calculated in the Rayleigh-Jeans limit. In general, however, the profiles should be calculated using full frequency dependence. Our results below are, however, independent of the observational frequency, since the profiles at different frequencies have similar shapes, with the amplitude of the SZ distortion scaled either up or down.

Once both profiles are known, one can determine the deviation in the value of the Hubble constant using Equations(14) & (16). The deviation from the idealistic case can be parametrized as

$$f_H \equiv \frac{r_{core,true}}{r_{core,est,fit}} = \frac{H_{0,est}}{H_{0,true}} \tag{3.19}$$

where the subscripts $(true)$ and est, fit refers to the actual value of H_o and the value estimated using model fitting to the SZE and X-Ray profiles, respectively. The above formula has been used to determine the deviation of the estimated value of H_o from the actual value, for models listed in Table-1. The effect of cooling flow on the determination of the cosmological parameters are summarized in Table-2.

To begin with, one has to get best fitted values for r_{core} (or θ_c) and β from different profiles. Since the estimation of the Hubble constant depends on the determination of these parameters from the profiles, we look at this issue in more detail. We must keep in mind that the best fitted values of r_{core} (or θ_c) and β depend on whether one decides to fit the X-ray or the SZ profiles, and the choice can lead to significant differences in the estimated value of H_o. One of the reasons for the strong dependence on the nature of the profile can be the non-isothermality of the cluster gas. Recent observations indicate that intracluster gas has a temperature structure, see Markevitch et al. 1998. This is because the y-parameter depends on the integral over T, while emissivity of thermal Bremsstrahlung depends on $\sqrt{T}$. The dependence of the Gaunt factor on T is indirect

and weak. Yoshikawa et al. 1998 have shown that gas temperature drop in the central regions (their Figure 3), should increase both r_{core} and β fitted to $y(\theta)$, and to a lesser extent to $S_X(\theta)$, as compared to those compared to $n_e(r)$. This discrepancy increases at higher redshifts. However, in their case, there is little change in the gas density profile. Clumpiness can also give rise to different fits, resulting in an over estimation of the Hubble constant (Inagaki et al. 1995).

There are two other important points that have to be kept in mind while fitting the profiles. First, we must remember that we are trying to fit a cluster having a finite profile with the formulae (Equations 12 & 13) for isothermal β profiles which is derived assuming the cluster to be of infinite extent. This can, by itself, lead to an over estimation of H_o (Inagaki et al. 1995). Thus to have a good fit one must choose a segment of the profile such that, within that segment, the profiles (SZ or X-ray) for a finite cluster do not differ much from those of a *hypothetical* cluster of infinite extent. We found that SZ and X-ray profiles of clusters start differing from those of infinite size at radii greater than 1.5 times the core radius. Hence, we have restricted our fitting to radii within $1.5r_{core}$.

Next, one must also be careful to exclude the region close to the sonic point, so that the X-ray spike is excluded from the fit. Also, the central portion in the SZ profile should be avoided as its inclusion can give an *apparent* central decrement less than its neighbouring points (see Schlickeiser 1991). We have fitted the SZ and X-ray profiles varying the inner cutoff radius and the results for a representative solution for each class of model are tabulated in Tables 3 & 4. Thus, all fittings were done for profiles extending from $r = r_{min}$ to $r = 1.5r_{core}$.

As can be seen from Table-2, cooling flows can lead to an over estimation of the Hubble constant. However, we must emphasize, that it may not be possible to *a priori* estimate the amount of bias introduced in the measurement of the Hubble constant due to cooling flows. There is no simple correlation between the amount of cooling (i.e $\dot{m}$) and the change in the estimated H_o from the actual value. The total change depends not only on $\dot{m}$, but also on the position of cooling radius, sonic radius, temperature at the sonic point and the isothermal temperature characterizing the hydrostatic cases, with which comparisons are made. Specifically, the fitted values of $r_{core}(\theta_c)$ and β for cooling flow models differ from hydrostatic models according to shape of underlying profiles, which is marked by two important features, firstly the central excess of X-ray flux (or excess decrement of SZ flux), and secondly the deviation from the smooth hydrostatic profile inside r_{cool}, the amount of over estimation mainly depends on these factors. For models with a central galaxy potential, there is always an over-estimation of H_o, which is greater than the models without the central galaxy.

For the realistic cases of models C1 and C2, where we have a variable $\dot{m}$ with r inside the cooling

Table 3.2: The effect on central decrement and H_o for $r_{min} = 0.1 r_{core}$

Solution Type	$\frac{H_{est}}{H_{true}}$	Δy_0
		(% change)
A1	1.91	35
A2	1.18	11.5
A3	2.6	25
B1	1.36	12.0
B2	1.19	9.0
B3	1.13	8.5
C1	2.6	14.0
C2	2.7	11.3

radius, the deviation of estimated Hubble constant from its actual value is almost the same. They are also greater than that of models A and B, having similar mass flow rates. This may be due to the fact that the maximum deviation in pressure from the hydrostatic cases is more in non steady cases, than in steady flows. Also non-steady cases are marked by the absence of the sonic radii and the subsequent drop in temperature.

Table 3.3: Fitting of SZ profile and deviation of H_o for $\dot{m} = 200 m_\odot/yr$

Solution Type	$r_{min} = 0.2 r_{cool}$	$r_{min} = 0.5 r_{cool}$	$r_{min} = 0.8 r_{cool}$
	H/H_{true}	H/H_{true}	H/H_{true}
A2	1.57	1.74	2.18
B2	1.44	1.58	2.06
C1	2.20	1.18	1.07

Table 3.4: Fitting of X-ray profile and deviation of H_o for $\dot{m} = 200 m_\odot/yr$

Solution Type	$r_{min} = 0.5 r_{cool}$	$r_{min} = 0.8 r_{cool}$	$r_{min} = 0.9 r_{cool}$	$r_{min} = 0.95 r_{cool}$
	H/H_{true}	H/H_{true}	H/H_{true}	H/H_{true}
A2	-	4.7	2.7	1.7
B2	-	4.9	2.24	1.6
C1	1.69	1.12	1.02	≈ 1.0

We note that although the different choice of fitting may change the absolute determination of cosmological parameters, the trend i.e deviation from the correct value remains more or less unaffected. It is interesting to note that for model C1, which include mass deposition in cooling flows, the deviations decrease as one excludes a greater part of the cooling flow region (Table 3.3 and 3.4). The other models show an increase instead. Here, we remind ourselves that models

with mass deposition i.e C-type models are more realistic (Fabian 1994). It is possible that the unusually high value of deviation (Table 4) and the counter-intuitive trend of increasing deviation with decreasing portion of cooling flow region used for fitting (Table 4 & 5), arise because of the unrealistic modeling of cooling flows. If we take the model C1 as a realistic one, then Table 4 & 5 show that to obtain a value of the Hubble constant within an accuracy of $\sim 10\%$, one should have $r_{min} \sim 0.8 r_{cool}$. In most cases, $r_{cool} < r_{core}$ (Fabian et al. 1984). However, as r_{cool} cannot be determined without actually detecting a cooling flow in a cluster, we suggest that *a significant portion of the profile within r_{core} should be excluded as a precaution.* The SZ and the X-ray profiles for the different models are shown in Figures 4 & 5.

3.6 Discussions and Conclusion

Our work on the effect of temperature structure of clusters and its effect on SZ decrement differs from other previous work of this nature in following way: this work takes into account the change in density profile as well as the temperature profile since both become important in the central region of the cluster. Also, previous authors have looked at the issue of non-isothermality of a cluster at radii greater than the core radius of the cluster, whereas we look at temperature change at regions inside the core radius. For them the density profile can still be well approximated by a β profile, whereas for cooling flow solutions, density profile is vastly different. Further, they have neglected radiative cooling in their work. We for the first time look at SZ effect in presence of radiative cooling, by first solving the cooling flow equations for reasonable and physical solutions.

In summary, we find that the presence of a cooling flow in a cluster can lead to an over estimation of the Hubble constant determined from the Sunyaev-Zel'dovich decrement. We have used different models of cooling flows, with and without mass deposition, and found the deviation in the estimated value of the Hubble constant in the case of a cooling flow from that of hydrostatic equilibrium. We have used the usual procedure of fitting the SZ and X-ray profile with a β profile to get an estimated value of r_{core}, and then compared with that for the case of gas in hydrostatic equilibrium in order to estimate the deviation in the Hubble constant. For the more realistic models with mass deposition (varying $\dot{m}$ with radius), we found that the deviation decreases with the exclusion of greater portions of the cooling flow region. Quantitatively, we found that for the deviation to be less than $\sim 10\%$, one should exclude a portion of the profile up to $\sim 0.8 r_{cool}$. Since r_{cool} is difficult to estimate without actually detecting a cooling flow, we have suggested that a significant portion of the profile inside r_{core} should be excluded, to be safe.

There can be another important implication of the effect of cooling flows. With the upcoming

satellite missions (MAP & Planck), we have come to the point where there are efforts to constrain Ω_0 with surveys of blank SZ fields (Bartlett et al. 1998, Bartlett 2000), ultimately giving rise to SZ-selected catalog of clusters (Aghanim et al. 1997). This method relies on estimating the number of SZ sources brighter than a given threshold flux (Barbosa et al. 1996). The point to be noted is that since these surveys are essentially flux limited in nature, the validity of the analysis to determine Ω_0 depends crucially on the *one-to-one* association of flux-limits to corresponding mass limits of clusters. From our analysis above, it seems that it may not be possible to associate a unique cluster mass to a given SZ distortion, given the uncertainty due to the presence of cooling flows. This might lead to contamination in SZ cluster catalogs and the inference of Ω_0. Recently, attempts have been made to constrain Ω_o from variance measurement of brightness temperature in blank fields (Subrahmanyan et al. 1998) and comparing them to simulated fields (see next Chapter, also Majumdar & Subrahmanyan 2000) of cumulative SZ distortions from a cosmological distribution of clusters. These results may also be systematically affected due to the presence of clusters having cooling flows.

The estimations made in this chapter strictly apply to cases where the image of the SZ effect is directly obtained by single dish observations. For interferometric observations, the interferometer samples the Fourier transform of the sky brightness rather than the direct image of the sky. The Fourier conjugate variables to the right ascension and declination form the $u-v$ plane in the Fourier domain. Due to spatial filtering by an interferometer, it is necessary that models be fitted directly to the data in the $u-v$ plane, rather than to the image after deconvolution. We do not forsee drastic change from our inferences in such cases since the result mainly depends on the deviation of the SZ and X-ray profile in case of a cooling flow from those in hydrostatic equilibrium. This, however, should be worked out in greater detail in future. We also note that with the growing number of high quality images of the SZ effect with interferometers, which have greater resolution than single dish antennas, the shape parameters of the clusters can be directly determined from the SZ data set rather than from an X-ray image (Grego et al. 2000).

Finally, we would like to add that though the calculations presented in this chapter were done using the dark matter profile (Equation 21), which is "commonly used" for calculating cooling flow solutions, it is inconsistent with the dark matter profile (Navarro et al. 1997) found in numerical simulations. (For a comparison of mass and gas distribution in clusters having cooling flows with different dark matter profiles, see Waxman & Miralda-Escude, 1995). However, it has been seen by Koch (1999) that there is little difference in cooling flow solutions by changing the underlying cluster dark matter density profiles. The main reason is that cooling flows are confined to the innermost parts of the clusters ($r < 100$kpc) where the the integrated mass of the dark matter are

almost identical for the different profiles. We have also neglected the self gravity of the gas. Suto et al. (1998) have calculated the effect of including the self gravity of the gas in determining the gas density profile. To make strong conclusions about the effect of cooling flows in the determination of the Hubble constant, one should take this into account.

Finally, let us comment on the inclusion of magnetic fields. Let the magnetic and thermal pressure become equal at a radius, r_B. It can be shown that $r_B > r_s$, and hence magnetic fields become important even before sonic point is reached. The magnetic field pressure, however, influences the cooling flow for small mass deposition rates. For the same flow velocity at the cooling radius, $v(r_{cool})$, the sonic radius is pushed outwards due to magnetic pressure. An interesting result is that magnetic pressure seems to keep the sound speed constant until a sudden drop at r_s. These details can be found in Koch (1999).

3.7 Summary

We have, in this chapter, looked at a novel method of estimating the Hubble constant using radio observations of SZE from galaxy clusters coupled with X-ray observations of the same. It has been found, however, that there can be a number of sources of uncertainties in the estimated value of the H_o . We have briefly reviewed the different sources of error before looking at cooling flows in clusters of galaxies to be another additional and important source of uncertainty. To give a bird's eye view, we have summarized the basic uncertainties and have tried to categorize them in Table 3.5. In the Table, uncertainties leading to error in the estimation of H_o greater than 10 % have been termed 'major' and all others are termed 'non-major'.

Other than estimating H_o combining SZ and X-ray data, SZ effect alone can also be used to determine the cosmological mass density Ω_o of the Universe (Bartlett & Silk 1994, Oukbir & Blanchard 1992,1997, Blanchard & Bartlett 1998, Majumdar & Subrahmanyan, 2000). Although a precise determination of the other cosmological parameters are, perhaps, almost impossible using only SZ studies, one can still go put constraints (limits) on such parameters and/or confirm the more precise predictions that can be made from the study of primary anisotropies. Moreover, once primary anisotropies give us the cosmological parameters to a high degree of accuracy, one can invert the role of the SZE to study the intracluster medium and other cluster specific physics. These are the issues that we look at in the next couple of chapters. Especially, in the next chapter, we look at an example of using SZ distortions from clusters to constrain the matter density parameter , Ω_o.

Table 3.5: Uncertainties in the determination of H_o using SZE.

Uncertainty	Importance
Observational	Major
Finite Extension	can be Major
Non-isothermality	Major
Non-sphericity	Major
Clumpiness	Not Major
Sub-structure	Not Major
Proper Cosmology	Not Major
Point sources	Not Major
Relativistic corrections	Not Major
kinematic SZE	Not Major
Gravitational Lensing	Not Major
Non-thermal electrons	Not Major
Radio Cocoons	Not Major
Cooling Flow	**Major**

Chapter 4

Constraining the matter density parameter using SZE

4.1 Introduction

A key problem in modern cosmology is the determination of the geometry of the universe. This mean determining the cosmological parameters that determine this geometry. Some of the classical methods of deriving the cosmological parameters involve measurements of the redshift dependence of apparent luminosities of 'standard candles', or the angular sizes of 'standard rulers', or the number densities of non-evolving objects. Many of these classical approaches are limited by difficulties in identifying objects, distributed over cosmic timescales, that are untouched by astrophysical evolution.

The formation of structure is dependent on the background cosmology. Attempts have been made to exploit this coupling by examining the parameter space allowed for the cosmological constants by favoured models of structure formation. Since the COBE discovery of anisotropy in the CMB, progress in the understanding of physical mechanisms responsible for the anisotropy spectrum and the influence of the background cosmology in the generation of these anisotropies have led to attempts at deriving constraints on the cosmological parameters from the shape of the CMB anisotropy spectrum (Bond et al. 1994) The density fluctuations that are hypothesized to have been generated in the very early universe are believed to grow via gravitational instabilities and give rise to the large scale structures we see in the present day universe. The CMB temperature fluctuations seen today on large angular scales exceeding about a degree are believed to be a direct

consequence of matter inhomogeneities on scales exceeding $\approx$ 100 Mpc at the recombination epoch. The gravitational and astrophysical evolution, in the post-recombination universe, which led to the formation of galaxies and their clustering, alter these primary radiation anisotropies and may have given rise to the dominant CMB fluctuations on small angular scales. At angular scales where the primary fluctuations become exponentially damped, and the secondary fluctuations take over, the SZE from galaxy clusters happens to be the major source of anisotropy. The generation of the CMB anisotropies (both primary and secondary) and their appearance on the sky are intimately linked with the background cosmology and/or the physics of astrophysical objects (for the case of the secondaries). Hence, the study of CMB anisotropies on different scales gives constraints on theories of structure formation and also on the parameters of cosmological models. Motivated by this link between the temperature anisotropy and the cosmological parameters, in this chapter, we focus on using SZ distortions by galaxy clusters as a probe of the cosmological matter density parameter. This is done by simulating the CMB anisotropy on small angular scales for specific models of structure formation. The results of simulations of sky temperature anisotropy are compared with ATCA limits on arc min-scale anisotropy to derive constraints on the cosmological density parameter Ω_o.

4.2 From the Cosmic Microwave Background to the Large Scale Structure

In this section, we give a brief overview of the intimate connection between the CMB distortions and the large scale structure seen around us. One can then pass smoothly from the very linear regimes (the largest scales which are probed by the primary CMB anisotropies) to the non-linear regimes (like cluster scales probed by secondary CMB anisotropies or by other traditional methods like cluster surveys). One can combine these complimentary approaches to yield important astrophysical and cosmological informations (*e.g.*, the normalization of the matter density power spectrum of large structures in hierarchical models of structure formation).

As discussed earlier, large-angle anisotropies in the microwave background radiation may be traced back to its generation from small-amplitude primordial density fluctuations in the early universe. Hence, from a study of these anisotropies we hope to learn a number of things : the cause behind the fluctuations (quantum or cosmic defects); the statistics of the fluctuation (Gaussian or non-Gaussian); the mode (adiabatic or isocurvature); ratio of scalar to tensor component etc. These will have their own power spectra (*e.g.*, $P_{ad}(k)$, $P_{grav.wave}(k)$ as a function of the comoving wave number $k = 2\pi a/\lambda$, with a as the scale factor. Analysis of the primary anisotropies can

help in determining these power spectrum amplitudes and in identifying any probable tilt ($n \neq 1$) of the initial primordial power spectrum. In what follows we have adopted the more popular adiabatic power spectrum with no contribution from gravitational waves, and denote it by $P_p(k)$, the primordial power spectrum. This then gives us Gaussian distribution of primordial fluctuations which we chose to be of the Harrison-Zel'dovich form given by $P_p(k) = Ak^n$. Once we know the power spectrum, we can compute all the relevant observable quantities (CMB & LSS), since for an isotropic, homogeneous, Gaussian random field, the power spectrum contains all the information.

The matter perturbations grow due to gravitational instabilities into the large scale structure we see at the present epoch. In addition, as the primeval CMB radiation propagated to us through growing matter inhomogeneities, astrophysical couplings give rise to secondary anisotropies on predominantly small angular scales. The power spectrum $P(k, z_f)$ of the fractional density fluctuations, at the redshift $z = z_f$ may be related to $P_p(k, z_i)$ by:

$$P(k, z_f) = \left[\frac{D_g(z_i)}{D_g(z_f)}\right]^2 T^2(k, z_f)\, P_p(k, z_i) \quad , \tag{4.1}$$

where D_g is the linear growth of perturbations and the matter transfer function $T(k, z_f)$ describes the processing of the initial density perturbations during the radiation dominated era (Padmanabhan 1993). $T(k, z_f)$ for linear perturbations modifies the initial Fourier components of the density $F(k, z_i)$ at some very early redshift z_i to the final ones $F(k, z_f)$ at some later redshift z_f by

$$T(K, z_f) = \frac{D_g(z_i)}{D_g(z_f)} \frac{F(k, z_f)}{F(k, z_i)} \quad . \tag{4.2}$$

The modifications to the shape of the perturbations would depend on the nature of the perturbations, cosmological models and the dark matter. During the matter-dominated era, the dominant dark matter (DM) perturbations experience equal growth on all scales and $P(k, z)$ grows retaining its shape. The growth rate, described below by the growth function, varies with cosmic time and depends on the mean matter density Ω_o. Models of structure formation are usually characterized by specific shape and normalization of $P(k, z_{eq})$, the power spectrum at the redshift of matter-radiation equality. Note, that for most cosmological models $T(k, z)$ is almost similar below a redshift $z \sim 100$. The choice of our transfer function is given in 4.4.2.

Along with the processed power spectrum, the final result of any calculation also depends on a large number of free parameters of the theory. These include the Hubble parameter H_o , the various mean energy densities (Ω_{tot}, Ω_o , Ω_Λ , Ω_{CDM}, Ω_{HDM}, Ω_b) and parameters characterizing the reionization of the universe (like z_{reion}). The number of independent parameters can be as large as 17 (see Bond & Jaffe 1998), and many more if one does not restrict the shape of the

$P_p(k)$. In these zoo of parameters, the relatively more important ones are H_o , Ω_o (defined in Chapter 1), the cosmological constant Ω_Λ and cosmological baryon density Ω_b . Also, since in this thesis, we are interested in secondary anisotropies caused due to the SZ scattering of primary radiation, we restrict ourselves to these four parameters that matter most in our case: H_o , Ω_b and the cosmological constant Ω_Λ through their direct effect on structure formation and size-angle relationship, and Ω_b through the amplitude of the secondary distortion caused by individual structures. One can reduce this parameter set further by taking recourse to measurement of H_o and Ω_b from other observations (like BBN). Finally, we are left with only two parameters, Ω_o and Ω_Λ . In this chapter, we concentrate only on Ω_o and look at models without a cosmological constant. Using a complimentary approach, we look at models including a cosmological constant, in the next chapter. Interestingly, both the approaches give very similar final results.

4.3 Cosmology with SZE from Galaxy Clusters: 'Blank Sky Surveys'

In the last chapter we have tried to probe the universe (via the Hubble constant) from targeted observations of SZE from galaxy clusters. However, with the upcoming satellite missions (like the Microwave Anisotropy Probe (MAP) and PLANCK) and ongoing/upcoming ground based missions, observations are reaching sensitivities when one can look for SZE in 'blank fields' in the sky. This would open up the possibility of detecting thousands of SZ sources in the sky from non-targeted observations along with detection (or upper limits) on the diffuse microwave background distortion due to SZE. These can then be used as powerful probes of the underlying cosmological models. In this chapter and the next we take a look at the possibilities that exist for such studies. Especially, we look at constraints on structure formation that can be put at present from recent observations of 'blank fields' (this chapter) and the possibility of using the SZ power spectrum as a tool in cosmology and astrophysics (next chapter). This chapter is devoted to simulating 'blank fields' of SZ distortion, whereas we take an analytic approach in the next chapter. Most of the basic materials (like normalization, number densities and cluster physics) discussed in this chapter have significant overlap with the next chapter and hence are described in some detail. We begin by brief overview of SZ number counts that will be possible in the near future.

As discussed in Chapters 1 & 2, clusters of galaxies may be 'visible', owing to the SZ effect (the 'holes-in-the-sky' phenomenon), as sources in the sky with a negative flux density (w.r.t. the flux at a position far from the cluster) at wavelengths longward of 1.35 mm and with a positive flux

density at shorter wavelengths. This SZ effect has been imaged to-date towards several clusters (see Birkinshaw 1999 for a recent review). We may consider distant cosmological clusters — observed at wavelengths longward of 1.35 mm — as a sky distribution of sources with negative flux density. Observational sensitivity in modern radio telescopes is reaching values close to that required for detecting the SZ effect from cosmological clusters towards 'blank fields' where no obvious clusters are seen in either their optical or X-ray emission. There have been claims in the literature of the detection of radio decrements (thought to be due to the SZ effect) in sensitive images made of 'blank' sky fields (Jones et al. 1996, Richards et al. 1997); however, sensitive observations of several other blank fields with arc min resolution have failed to detect any decrements or CMB anisotropies (Subrahmanyan et al. 1998,1999). However, rapid progress is being made in this field, and in the near future ground based surveys will be able to detect and possibly resolve a large fraction of cluster population. Modeling clusters as a simple self similar population, studies show that one would be able to discover $\sim$ 100 clusters per square degree at a wavelength of 2 mm and $\sim$ 10 per square degree at $\lambda \sim 1$ cm (Bartlett, 2000). One can then use the number counts as a cosmological test.

At wavelengths longward of 1.35 mm, a cluster appears as a negative source on the sky with respect to the mean CMB background intensity: the flux density S_ν due to the integrated SZ effect over the sky area of a cluster is

$$\begin{aligned} S_\nu(x) &= \frac{j_\nu(x)}{d_A^2(z)} \int dV \frac{kT}{m_e c^2} n_e \sigma_T. \\ &\propto M_{gas} \langle T_e \rangle \ . \end{aligned} \tag{4.3}$$

where $j_\nu(x)$ contains the frequency dependence of the SZ flux and the other symbols have their usual meanings as defined in the previous chapters. We have assumed that $T \gg T_{cmb}$. The integral extends over the cluster volume and $d_A(z)$ is the angular-size distance to the cluster. S_ν has units of erg s^{-1} cm^2 Hz^{-1}: this flux density is usually expressed in Jansky (Jy), defined as 1 Jy = 10^{-23} erg s^{-1} cm^2 Hz^{-1}. It is clear from the equation above that the net SZ effect due to a cluster is dependent only on the total mass of hot gas in the cluster and a density-weighted mean temperature. This means that for unresolved clusters the SZ flux is insensitive to the spatial distribution of the ICM or its temperature structure. The SZ flux density from a cluster diminishes as the square of its angular-size distance: because the angular-size distance of objects at cosmological distances, $z \gtrsim 1$, saturates to a limiting value or even decreases with increasing redshift, the SZ flux from a cluster does not rapidly diminish with increasing cosmological distance. However, the distributions of cluster gas temperature and electron density may be functions of redshift; therefore, the expected

SZ flux density from a cluster may be redshift dependent. Now, using scaling arguments for clusters *i.e.*$\left(T_{virial} \propto M^{2/3}\,(1+z)\right)$ and normalization from Evrard et al. (1996), one can express the total flux density of a cluster in terms of the total mass and the underlying cosmology only. If the cluster mass is supposed to follow the Press-Schecter mass function, then detection of clusters above a cutoff in S_ν would act as a probe of the cosmological model. This is the basic philosophy behind using SZ cluster counts from blank sky surveys to probe cosmological models.

Other than number counts, blank sky surveys of SZE from galaxy clusters can be used in other complimentary ways to probe our universe: 1) The power spectrum of secondary anisotropy can be used as a probe of the cosmology (analogous to that from primary anisotropies) and of the astrophysical phenomena/source causing the distortion. The TSZE power spectrum can be recovered from multi frequency non-targeted observations of the CMB sky. Chapters 5, 6 & 7 look at the power spectrum of SZE from different sources. Especially, in the next chapter, we take a detailed look at the SZE power spectrum from cluster of galaxies. 2) The other option is to use limits on the microwave background anisotropy from arc-min scale surveys of blank fields to put constraints on the background cosmology under the assumption that SZE of clusters are the dominant contributor of microwave background anisotropy at arc-min scales. This chapter is dedicated to such an approach.

It may be noted here that because the SZ effect has a generic non-Gaussian temperature distribution, it could be detected in a sky image by estimators sensitive to skewed variance. Many other secondary contributors to the temperature anisotropy have a Gaussian distribution in amplitudes; therefore, the negative-skewed-nature of the SZ effect may be useful in distinguishing it from other sources, foregrounds and instrument noise (Cooray, 2001b)

Finally, let us mention that though the large scale structure around us are in the form of web and filaments of tenuous matter with high density structures sitting at their junctions, it is the high density structures that mainly influence the microwave background photons. Hence, a halo based approach is sufficiently suited to look at the impact of LSS on the CMB. More justifications to this claim can be found in Cooray (2001a).

4.4 The cosmological distribution of clusters of galaxies

4.4.1 The Press-Schecter approach

For the purpose of our simulations, we wish to relate the number density of collapsed objects of different masses, at different cosmic epochs, to the initial density contrast on different scales,

i.e., the initial matter spectrum $P(k, z_{eq})$. It is assumed, in most theories of structure formation, that the initial small-amplitude density fluctuations are Gaussian random, *i.e.*, the amplitudes are Gaussian distributed and that the fluctuations on different scales are uncorrelated (random phase fluctuations). Structure is believed to form from the growing perturbations hierarchically, with smaller-scale fluctuations collapsing first and larger scales later. The mass and redshift distribution of the number density $n(M, z)$ of collapsed objects may then be computed using the Press-Schechter (PS) formalism (Press & Schechter 1974; see Padmanabhan & Subramanian 1992 for a tutorial):

$$n(M,z)dM = \sqrt{\frac{2}{\pi}}\frac{\langle\rho\rangle}{M}\nu_c \left|\frac{d\ln\sigma(M,z)}{d\ln M}\right| e^{-\nu_c^2/2}\frac{dM}{M}, \tag{4.4}$$

where

$$\nu_c(M,z) = \frac{\delta_c}{\sigma(M,z)} = \frac{\delta_c D_g(0)}{\sigma_0(M)D_g(z)}. \tag{4.5}$$

In these equations, $\langle\rho\rangle$ denotes the mean co-moving matter density in the universe: $\langle\rho\rangle = \frac{3\Omega_o H_o^2}{(8\pi G)}$, where Ω_o is the density parameter, $H_o = 100h$ km s^{-1} Mpc^{-1} is the Hubble constant and G is the gravitational constant. $\sigma(M, z)$ denotes the rms fluctuations, at redshift z, in the fractional density contrast in the matter when smoothed to a mass scale $M = \frac{4}{3}\pi R^3\langle\rho\rangle$, where R is the comoving radial length scale of the smoothing function. $\sigma_o(M)$ is the rms density contrast at the present epoch and δ_c is he density contrast in an overdensity, computed using linear theory, at the epoch when the collapsed object is deemed to have formed. We adopt the collapse of a spherical top-hat overdensity (Peebles 1980) as a valid model for the description of the dynamical evolution of the peaks in the Gaussian density distribution; the collapsed object is deemed to have 'formed' at the cosmic time t_c, which is approximately twice the cosmic time t_m at which the over dense region attains maximum expansion radius. In a universe with $\Omega_o = 1.0$, $\delta_c = 1.68$. It has been shown that δ_c varies by at most ~ 4 per cent for a range of Ω_o from 0.1 to 1 (Lacey & Cole 1993). Therefore, we have chosen to adopt a constant value 1.68 for δ_c. However, in the next chapter, we use the SZE to probe specific cluster physics. Thus we must be careful about the influence of the cosmological parameters and hence use a changing value of δ_c for different models. The more exact forms can be written in terms of the conformal time η as

$$\delta_c(\Omega_o, z) = \begin{cases} \frac{3}{2}D_g(\Omega_o,0)\left[\left(\frac{2\pi}{\sinh\eta-\eta}\right)^{2/3}+1\right] & \Omega_o < 1,\ \Lambda = 0 \\ 0.15(12\pi)^{2/3}\Omega_m^{0.0055}D_g(\Omega_o,0)/D_g(\Omega_o,z) & \Omega_o < 1,\ \Lambda = 1-\Omega_o, \end{cases} \tag{4.6}$$

where

$$\eta = \cosh^{-1}\left[\frac{2}{\Omega_m(z)} - 1\right] \tag{4.7}$$

In this Press-Schechter formalism, collapsed objects are identified on the basis of their overdensity assuming linear growth of perturbations. D_g, in Equation (4.6), quantifies the growth factor of the density perturbations from the epoch of matter-radiation density equality ($z = z_{eq}$) to any later epoch z in the matter dominated era. In the absence of free streaming, the growth function is given by (Peebles 1980, Heath 1977)

$$D_g(z) = \frac{5\Omega_o}{2}(1+z_{eq})\, g(z) \int_z^\infty \frac{1+z'}{g(z')^3} dz', \tag{4.8}$$

where

$$g^2(z) = \Omega_o(1+z)^3 + (1-\Omega_o-\Omega_\Lambda)(1+z)^2 + \Omega_\Lambda. \tag{4.9}$$

Closed form expressions are available in Weinberg (1972), Groth & Peebles (1975) and Edwards & Heath (1976) for universes with and without a cosmological constant Λ.

For open universe, the growth function can be written as (Peebles, 1980)

$$D_g(\Omega_o, z) = 1 + \frac{3}{w} + \frac{3(1+w)^{1/2}}{w^{3/2}} \ln\left((1+w)^{1/2} - w^{1/2}\right) \ , \tag{4.10}$$

where $w(\Omega_o, z) = \Omega_o{}^{-1}(z) - 1$ The redshift dependence of the density parameter Ω_o is given by

$$\Omega_o(z) = \frac{\Omega_o(1+z)}{\Omega_o(1+z) + (1-\Omega_o)} \ . \tag{4.11}$$

For flat universe with a cosmological constant, the integral of the growth function cannot be done analytically. Useful approximate expression are given by Lahav et al. (1991) and Caroll et al. (1992), which is

$$D_g(\Omega_o, z) = (1+z)^{-1} \frac{5\Omega_o(z)}{2} \left\{ \Omega_o(z)^{4/7} - \Omega_\Lambda(z) + \left[1 + \frac{\Omega_o(z)}{2}\right]\left[1 + \frac{\Omega_\Lambda(z)}{70}\right] \right\}^{-1} \ , \tag{4.12}$$

where

$$\Omega_o(z) = \frac{\Omega_o(1+z)^3}{\Omega_o(1+z)^3 + 1 - \Omega_o} \tag{4.13}$$

$$\Omega_\Lambda(z) = \frac{1-\Omega_o}{\Omega_o(1+z)^3 + 1 - \Omega_o} \ . \tag{4.14}$$

The rms amplitude of the mass fluctuations at any redshift z, $\sigma(M, z)$, when smoothed with a spherically symmetric window function of characteristic co-moving radius R, may be computed from the matter power spectrum $P(k, z)$ using the relation:

$$\sigma^2(M,z) = \int_0^\infty \frac{dk}{k}\frac{k^3}{2\pi^2}P(k,z)\left|\tilde{W}_R(k)\right|^2, \tag{4.15}$$

where $\tilde{W}_R(k)$ is the Fourier transform of the corresponding real space window function and, as before, $M = \frac{4}{3}\pi R^3\langle\rho\rangle$. A spherical top-hat form with radius R is usually adopted for the window function and this corresponds to a Fourier-space window function:

$$\tilde{W}_R(k) = \frac{3}{kR^3}(\sin(kR) - kR\cos(kR)). \tag{4.16}$$

We have plotted the rms mass fluctuations σ against the mass M or size R in Figure 4.1. In the upper panels, we show the variation of σ with mass (or size) for three different cosmological models: critical density model ($\Omega_o = 1$), open model (OCDM) and flat models (ΛCDM) both with $\Omega_o = 0.3$. For each set of models, $h = 0.7, 0.65, 0.6$ from top to bottom. We see that σ for the critical density models are far higher than OCDM or ΛCDM models, rendering it incompatible with observations. In the lower left panel, we show the variation of σ with M for four values of: Ω_o = 0.2 (dotted line), 0.4 (dot-dashed line), 0.6 (dashed line) and 0.8 (solid) line. Cases are shown for flat and open universes and the critical density model is also shown for reference. In the lower right panel, we show the effect of increasing the baryon fraction on σ. As is evident from the figure, increasing the value of Ω_b (to 1.5 times the BBN value) lowers the values of σ. Interestingly, one can see a degeneracy between a high Ω_b universe and a low h universe.

The Press-Schechter formalism has been verified by Tozzi & Governato (1998) against the results from numerical n-body dynamical simulations, particularly for the mass range encompassing clusters of galaxies.

4.4.2 COBE normalization of matter power spectrum

There are two independent ways to constrain models of LSS with COBE data. One can either use the shape of the power spectrum or the normalization. The first one turns out to be rather weak for the more popular models and so we use COBE to normalize our power spectrum by normalizing the small scale density fluctuation amplitude σ_8, which is the rms mass fluctuations smoothed using a window function with a radius $R = 8h^{-1}$ Mpc in the present day universe.

Normalization of the matter power spectrum can be obtained from cluster abundance studies (White et al. 1993, Bond & Myers 1996, Viana & Liddle 1996). The resulting σ_8 ranges between $0.5 - 0.8$. Specifically, one can approximately write σ_8 as

$$\sigma_8 \approx (0.6 \pm 0.1)\,\Omega_o^{-c}\ , \tag{4.17}$$

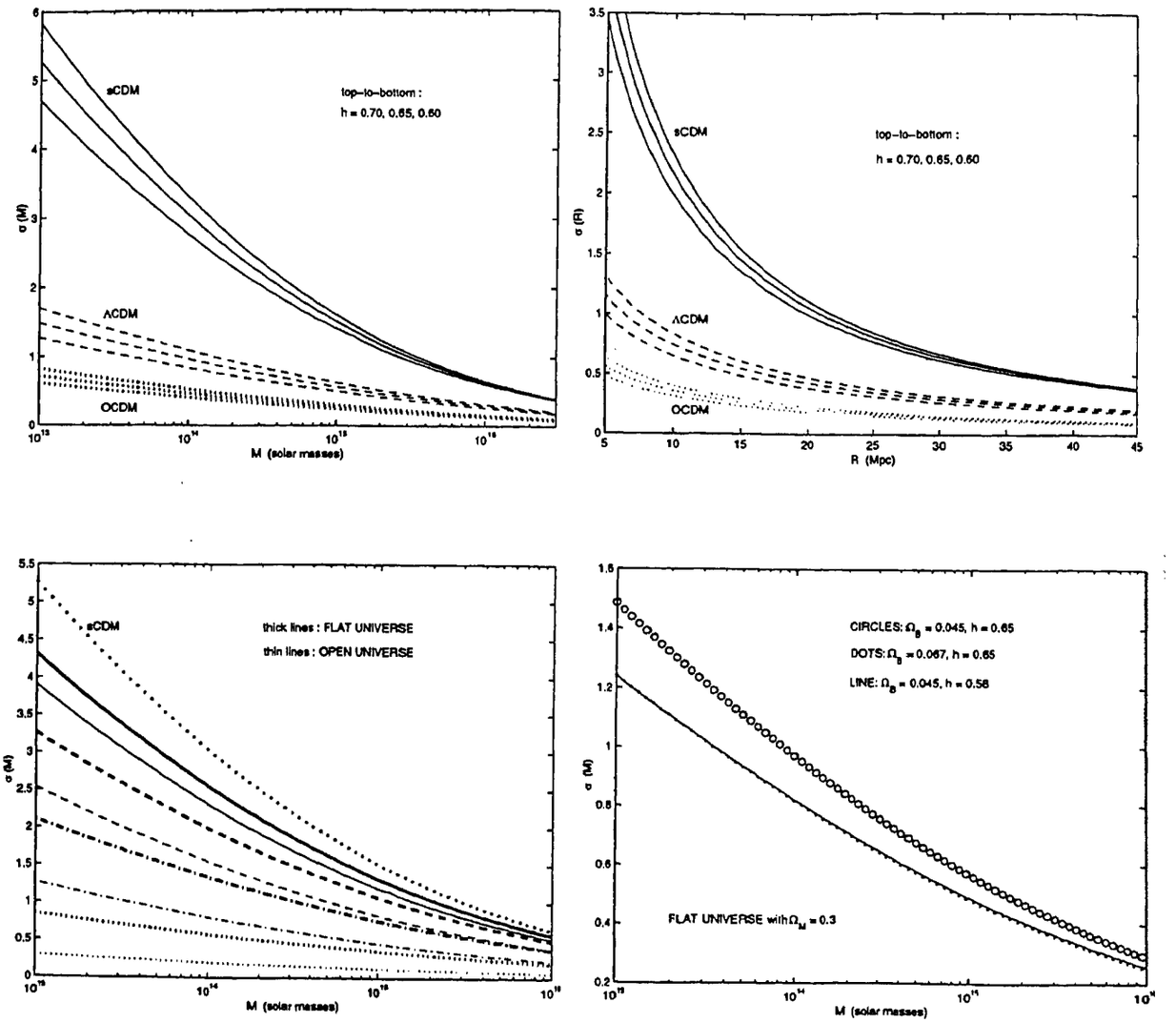

Figure 4.1: COBE normalized $\sigma(M)$ (or equivalently $\sigma(R)$) are plotted as function of Mass (or radius) for different cosmological models. The detailed explanation can be found in the text.

where $c = 0.4$ for OCDM and $c = 0.54$ for ΛCDM. However, such normalization can be affected by selection effects and other cluster physics. On the other hand, the large-angle CMB anisotropies discovered by COBE (Smoot et al. 1992) are believed to have been generated by processes at the last scattering surface. Since the matter fluctuations that generated these anisotropies were of small fractional amplitudes at the epoch t, and because the scale length of the perturbation modes

well exceeded ct, the coupling physics between the matter perturbations and radiation was linear and did not involve any astrophysical interactions. The CMB anisotropies detected by COBE may, therefore, be related to the primordial matter spectrum fairly exactly without all the uncertainties associated with the astrophysics involved in the formation of collapsed baryonic objects at late epochs. For this reason, we have chosen to normalize the $P(k)$ with the COBE results.

For the matter density perturbations, the LSS data are usually expressed in terms of the power spectrum $P(k) \equiv |\delta_k|^2$, where δ_k is the Fourier transform of the fractional density perturbations $(\delta\rho/\rho)$. The power spectrum is often expressed as the dimensionless mass variance per unit interval in $\ln k$, denoted by $\Delta^2(k)$, *i.e.*

$$\Delta^2(k) = \frac{d\sigma^2}{d\ln k} = \frac{k^3}{2\pi^2} P(k) \tag{4.18}$$

Equation (4.18) can then be used in terms of $\Delta^2(k)$ to give the normalization of $P(k)$, where one puts $r = 8h^{-1}$ Mpc. In Table 4.1, we list the COBE normalized σ_8 for the different models studied in this chapter.

We have adopted a power-law form for the initial primordial matter spectrum with $P_p(k) \propto k^n$, where n is the index of the primordial power spectrum; this index n equals unity for Harrison-Zel'dovich scale-invariant spectra. The power spectrum at any redshift z in the matter dominated era may then be written in the form

$$\frac{k^3}{2\pi^2} P(k,z) = \left(\frac{ck}{H_0}\right)^{3+n} \delta_H^2 T^2(k) D_g^2(z)/D_g^2(0), \tag{4.19}$$

where the D_g's are the growth factors defined in Section 4.4.1. δ_H represents the amplitude normalization of $P(k,z)$ and is defined as the amplitude of perturbations on the horizon scale at the present epoch $z = 0$. To a good approximation, δ_H as normalized to COBE is relatively insensitive to both h and Ω_b (see Bunn & White 1997, their figures 13 & 14). However, σ_8 depends on the parameters n, Ω_o, Ω_Λ and Ω_b.

We have used the fitting formulae of Bunn & White (1997) to normalize the power spectrum to the COBE-DMR measurements. For an open universe with vanishing cosmological constant, with no CMB anisotropies coming from gravitational waves, we use the normalization

$$\delta_H = 1.95 \times 10^{-5} \Omega_o^{-0.35-0.19\ln\Omega_o - 0.17\tilde{n}} e^{-\tilde{n}-0.14\tilde{n}^2} \tag{4.20}$$

and for a flat universe with a cosmological constant (used in the following chapters), the normalization with no gravitational waves is given by

$$\delta_H = 1.94 \times 10^{-5} \Omega_o^{-0.785 - 0.05 \ln \Omega_o} e^{(-0.95\tilde{n} - 0.169\tilde{n}^2)^2} \tag{4.21}$$

In the above equation, $\tilde{n} = n - 1$, and the normalizations are valid for $0.7 \leq n \leq 1.2$. and over the range 0.2–1.0 in Ω_o.

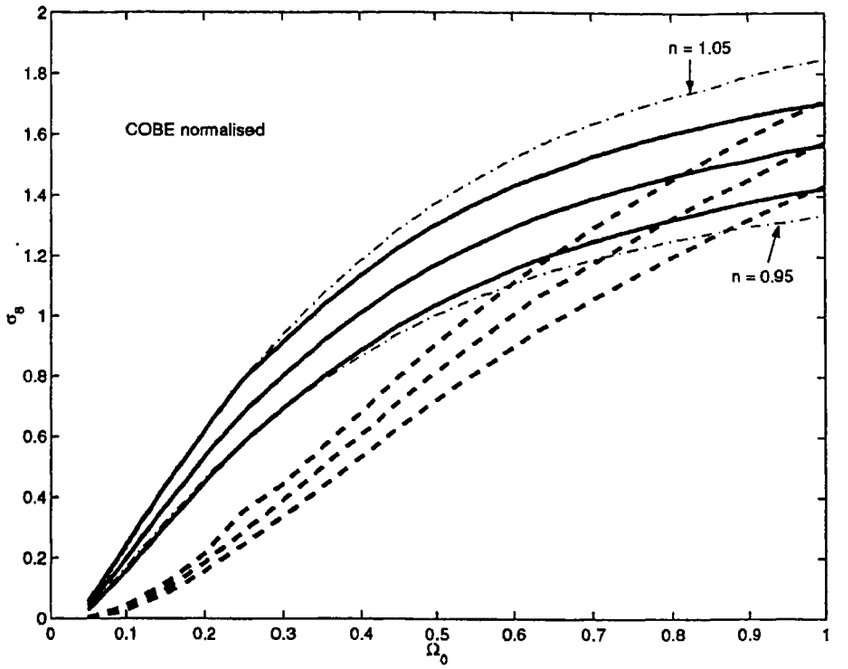

Figure 4.2: COBE normalized σ_8 is plotted against Ω_o . The thick solid lines are for a flat universe and the thick dashed lines for an open universe. The thick dash-dotted lines are for a critical density universe with tilted power spectrum. Note, the values of σ_8 for $\Omega_o < 0.2$ are only approximate.

As mentioned earlier, the shape of $P(k, z)$ in the matter dominated era is completely determined by the transfer function $T(k)$ and the assumed form for the primordial spectrum. With the choice of a power-law form for $P_p(k)$, the transfer function is critical relates the power on small wavenumber modes — which is fixed by the adopted COBE normalization — to those on large k modes at which we have clusters of galaxies. There are several fitting forms available for $T(k)$ in the literature in the context of the cold dark matter (CDM) dominated universes. However, different parametrizations of transfer functions can differ by large amounts (Peacock & Dodds 1994) and, moreover, to obtain better accuracy the effect of baryon damping must be included (Hu & Sugiyama 1996, Ma 1996, Eisenstein & Hu 1999). We, however, work within the context of low-baryon-density universes and,

therefore, include the effect of non-zero baryon content by adopting a modified 'shape factor' Γ. In this work, we have adopted the fitting function provided by Bardeen et al. (1986):

$$T_{CDM}(q) = \frac{\ln(1+2.34q)}{2.34q} \times$$

$$\left[1 + 3.89q + (16.1q)^2 + (5.46q)^3 + (6.71q)^4\right]^{-1/4} \tag{4.22}$$

where $q = k/h\Gamma$, $\Gamma = \Omega_o h \exp(-\Omega_B - \Omega_B/\Omega_o)$ and Ω_B is the baryon density parameter which is the ratio of the mean density of baryons in the universe to the critical density $\rho_c = 3H_o^2/(8\pi G)$.

From Table 4.1 and Figure 4.2, it is clear that a low Ω_o has a lower value of σ_8, with the flat $\Omega_o = 1$ having the highest value. The reason for such a behaviour is as follows: In a ΛCDM universe the fluctuations stop growing when $z \sim (\Omega_o{}^{-1} - 1)^{1/3}$ for $\Omega_o < 1$ and so the overall growth from $z \sim 1000$ to present is suppressed relative to a flat $\Omega_o = 1$ universe. Also, in addition the potential fluctuations are reduced by Ω_o . Thus for a fixed COBE normalization, one expects $P(k) \propto (D_g/\Omega_o)^2 \sim \Omega_o{}^{-1.54}$ (see Peebles 1984, Efstathiou et al. 1992). Hence for a COBE fixed normalization, the present day matter fluctuations are larger for low density universe (with or without a cosmological constant) than a critical density model. Another effect that influences this normalization is the integrated Sach-Wolfe effect, which becomes important for a low density open universe. Finally, two important features emerge from Figure 4.2: 1) for the same value of Ω_o , a flat universe has a higher σ_8. Cluster abundance studies give the value of $\sigma_8 \sim 0.9 - 1$. This corresponds to $\Omega_o \sim 0.3$ for a flat universe and $\Omega_o \sim 0.7$ for the open case. 2) Also notice that adding a tilt (say, $n = 0.95, 1.05$ can change the normalization by a large amount, specially at higher Ω_o values. Thus, a critical density universe can be brought to agreement with observations by the introduction of a small tilt ($n \sim 0.9$).

The Press-Schechter formalism described in section 4.1, along with the COBE-normalized $P(k)$ defined above, have been used to calculate the number densities of collapsed objects. We choose to identify the condensates as groups/clusters of galaxies and have computed their abundances as a function of cluster mass and redshift for a set of CDM cosmologies differing in their Ω_o. We have not considered the effect of including a cosmological constant in this work and have put $\Lambda = 0$. The computations of cluster distributions $n(M, z)$ have been carried out over logarithmic bins in the mass range 10^{13}–$10^{16} M_\odot$. The distribution in mass is computed at redshifts spaced at intervals of $\Delta z = 0.1$. Plots of $n(M, z)$ distributions are shown in Figure 4.3.

The theory predicts that the cosmic abundance of massive collapsed objects are extremely sensitive to the amplitude and slope of the primordial power spectrum and also on the growth factor. In a flat cosmology with $\Omega_o = 1$, $P(k)$ would grow as $(1+z)^{-2}$; in an open universe

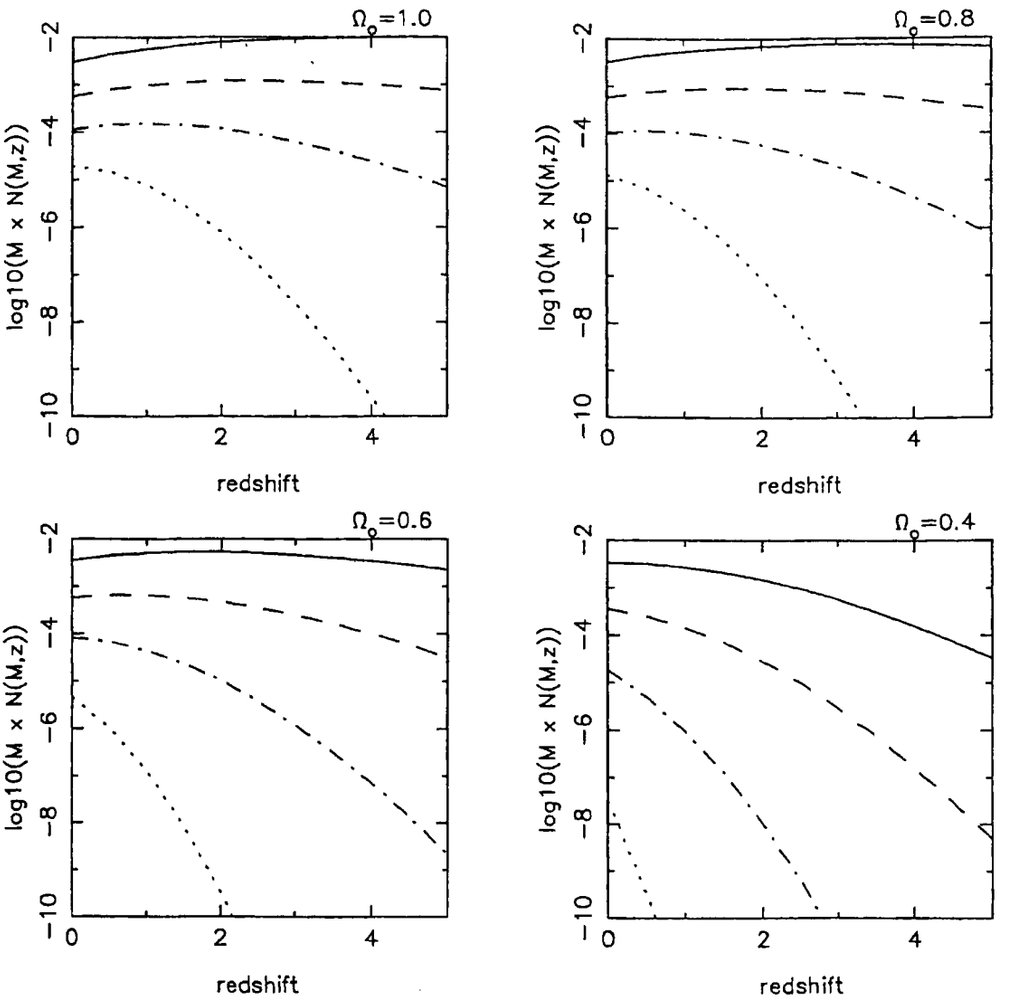

Figure 4.3: Abundance of objects with mass $M = 10^{12}$ $M_\odot$ (continuous line), $M = 10^{13}$ $M_\odot$ (dashed line), $M = 10^{14}$ $M_\odot$ (dot-dashed line) and $M = 10^{15}$ $M_\odot$ (dotted line). A CDM cosmology with $h = 0.65$, $\Lambda = 0$ and $\Omega_B = 0.019h^{-2}$ is adopted; the four plots are labeled with the assumed values of Ω_o. The abundance $n(M, z)$ is expressed as the number of objects per Mpc^3 and $\log_{10}(M \times n(M, z))$ is plotted versus redshift z.

the growth approximately follows this evolution down to redshift $z \approx (\Omega_o^{-1} - 1)$ and is stunted thereafter. Therefore, in these models, which are all COBE normalized, the total growth up to the present time will be greater in models with larger Ω_o. Consistent with this reasoning, it may

Table 4.1: COBE normalization for different models

Model[1]	Ω_o	h	σ_8
SCDM	1.0	0.50	1.128
SCDM(high h)	1.0	0.65	1.567
OCDM1	0.8	0.65	1.326
OCDM2	0.6	0.65	1.004
OCDM3	0.4	0.65	0.605
SCDM(variant1)	1.0	0.50	1.128
SCDM(variant2)	1.0	0.50	1.128

be seen in Figure 4.3 that the larger Ω_o models are dynamically more evolved: they have larger numbers of 10^{15} $M_\odot$ objects at $z = 0$ and in these models the abundances of lower mass objects are declining with cosmic time as they are incorporated into larger mass objects.

It may be seen from Figure 4.3 that the decline, with redshift, in the abundance of high-mass (10^{15} $M_\odot$) collapsed objects relative to the abundance at $z = 0$ is steepest in the case of models with lower Ω_o. This is the opposite of the expectations for models which are normalized at the present time to, for example, a specific value of σ_8. Although the growth function evolves slower at low redshifts in models with low Ω_o, the abundance of massive collapsed objects evolves more strongly in the case of the low Ω_o models because in these models the rms mass fluctuation $\sigma(M, z)$ is itself low at $z = 0$.

The Gaussian characteristic of the Press-Schechter mass function is evident in the distributions: at any redshift, there is a rapid exponential decline in the number density of objects in larger mass bins.

4.5 SZ distortion from a single cluster

In order to model the spatial distribution of the intra-cluster gas, the isothermal β model has been adopted, in which the cluster gas is modeled as being spherically symmetric, centred in the gravitational potential of the cluster and shock heated to a temperature corresponding to the potential energy. The variation in gas density with radial distance r is assumed to be given by

$$\rho(r) = \rho_0[1 + (r/r_c)^2]^{-3\beta/2}, \tag{4.23}$$

where ρ_o is the central density and r_c is the core radius. The value of β, inferred from the X-ray surface-brightness profiles observed in clusters of galaxies, is believed to be in the range 0.5–0.9 (Markevitch et al. 1998). Especially, isothermal β model fits to X-ray images give $\beta = 0.67$ (Jones & Forman 1984). Spectroscopically determined β comes out to be ≈ 1 (Girardi et al. 1996, Lubin & Bahcall, 1993). Numerical simulations give $\beta \approx 1$–1.3 (Evrard et al. 1996, Bryan & Norman 1998). Here, for simplicity, we adopt a value of $\frac{2}{3}$ for β. Since SZE, as compared to X-ray emission, is more sensitive to the outer regions, it is important to pay careful attention to the underlying density profile: a profile with a higher β is more strongly spiked towards the centre. Although β models describe the ICM well, for more accurate work an improved model is needed (for example see Cooray, 2001a for a gas model based on hydrostatic equilibrium with the total dark matter).

Assuming that the dynamical collapse of the cluster is self similar, the scaling of the core radius r_c of collapsed objects with mass and redshift has been derived to have the form (Colafrancesco et al. 1997, Kaiser 1986):

$$r_c(\Omega_o, M, z) = \frac{1.3h^{-1}\mathrm{Mpc}}{p}\frac{1}{(1+z)} \times \left[\frac{M}{10^{15}h^{-1}M_\odot}\frac{\Delta\,(\Omega_0 = 1, z = 0)}{\Omega_o\Delta(\Omega_o, z)}\right]^{1/3}, \tag{4.24}$$

where the non-linear density contrast at the epoch of virialisation is $\Delta = \tilde{\rho}/\rho$ where $\tilde{\rho}$ is the density contrast and ρ is the mean background density. In the above parametrization, $p = r_{vir}/r_c$, is a measure of the concentration of the cluster mass: small values of p model the cluster gas as centrally concentrated where as larger values of p spread the gas mass away from the core. Sometimes it is used as an adjustable free parameter that may be selected to fit observations of nearby clusters. Values of $p \approx 6$ appear to better model the parameters of nearby clusters; a comparison of the model with the observed parameters for the Coma cluster is given below. It may be noted that sensitive X-ray imaging of the gas in nearby clusters has shown gas extending out to at least eight core radii.

For the case of an open universe,

$$\Delta = \frac{18\pi^2}{\Omega_o H_0^2 t_v^2} \frac{1}{(1+z_v)^3}, \tag{4.25}$$

where t_v and z_v are the cosmic time and redshift corresponding to the epoch of virialisation. For OCDM and SCDM models, the overdensity can be parametrized as

$$\Delta(\Omega, z) = 4\pi^2 Q^2 \Big[(Q^2+2Q)^{1/2} - \ln(1+Q+(Q^2+2Q)^{1/2})\Big], \tag{4.26}$$

where $Q = 2(1-\Omega_o)/(\Omega_o(1+z))$ (Oukbir & Blanchard 1997).

In the case of a flat universe, $\Delta \approx 178$ (Peebles 1980; Colafransesco et al. 1997). For flat universe, it can be parametrized as (Kitayama & Suto 1996)

$$\Delta(\Omega, z) = 18\pi^2 \Big[1 + 0.4093(\Omega_f(z)^{-1} - 1)^{0.9052}\Big]. \tag{4.27}$$

If r_m denotes the maximum radial extent of the cluster, $p = (r_m/r_c)$ and is

Although recent observations indicate that intracluster gas has temperature structure (Markevitch et al. 1998), we have modeled the clusters as being isothermal. From the assumption that clusters form from self-similar collapse, it follows that the temperature $T \propto \frac{M}{R}$ and a good approximation for the temperature of the intra-cluster gas in clusters is (Colafrancesco et al. 1997)

$$T = 6.7 \times 10^7 (1+z) \left[\frac{M}{10^{15} h^{-1} M_\odot}\right]^{2/3} \times \left[\frac{\Omega_o \Delta(\Omega_o, z)}{\Delta(\Omega_0 = 1, z = 0)}\right]^{1/3} \text{K}. \tag{4.28}$$

The relation between the mass and the temperature in Equation (4.28) agrees well with the recent M-T parametrization as suggested by Bryan & Norman (1998). We have assumed that the hot gas detected in its X-ray emission is responsible for any SZ effect (Colafrancesco et al. 1994, Blanchard et al. 1992, Vittorio et al. 1997, Kaiser 1986). The use of Equation (4.28), assumes the cluster to form at recent times, which is however only an approximation for a low Ω_o universe. Voit & Donahue (1998) have given an expression valid for a low Ω_o universe which takes accretion during the evolution of the cluster into account. We, however, find that the final result is not much different if one uses the more exact expression.

Only the baryonic matter in collapsed clusters gives the SZ effect. White et al. (1993) have estimated the baryon content in clusters to be

$$\frac{M_b}{M_{tot}} \geq 0.009 + 0.050 h^{-3/2}, \tag{4.29}$$

where the first contribution is due to the galaxies and the second is due to the intra-cluster gas. Primordial nucleosynthesis predicts a universal baryon abundance $\Omega_b \simeq 0.019h^{-2}$ (Burles et al. 1999). Adopting the Hubble parameter $h = 0.65$, it is seen that the baryon gas-mass fraction in nearby clusters is about 0.1 and is a factor of two greater than the universal baryon abundance. The *Einstein* Medium Sensitivity Survey (EMSS) data appear to indicate a decline in the abundance of X-ray luminous clusters with redshift (Henry et al. 1992); this may be parametrized as a hot-gas fraction that evolves as $t^{1.4}$ with cosmic epoch. It may be noted that adopting a gas fraction that declines with redshift is a conservative assumption because it reduces the predicted SZ effect. We have adopted a parametrization

$$\frac{M_{gas}}{M_{tot}} = 0.050h^{-3/2}\left[\frac{M_{tot}}{10^{15}h^{-1}\ \mathrm{M}_\odot}\right]^{0.2}\left[\frac{t}{t_\circ}\right]^q, \tag{4.30}$$

with $q = 1.4$. M_{gas} represents the hot gas mass in the cluster and M_{tot} represents the total mass in the collapsed object. The exponent 0.2 in Equation (4.30) is from a fit in Colafrancesco et al. (1997). We have assumed that the intra-cluster gas has a primordial composition, with helium and hydrogen atoms in the number ratio 1:10, and is fully ionized. Interestingly, this parametrization can be cleverly used in future SZ surveys to look for any evolution of the gas mass fraction. We will come to this point in a greater detail in the next chapter.

The cluster mass distribution, as also the intra-cluster gas, are modeled as truncated at a maximum radius $r_m = p \times r_c$. We define the 'impact parameter' b as the projected distance between the cluster centre and any line of sight through the cluster. It follows that the SZ decrement in the Rayleigh-Jeans portion of the spectrum, in units of temperature, expected at any sky position $b \lesssim r_{max}$ is given by

$$\Delta T = -T_{cmb}\frac{2k_\mathrm{B}T}{m_e c^2} \times \int_b n_e \sigma_T dl, \tag{4.31}$$

where T_{cmb} is the average brightness temperature of the CMB. The integral is computed along the line of sight through the cluster at the impact parameter b.

The assumption that the cluster gas is of primordial composition implies that the total number of hot electrons in the cluster is $N_e = (18/14)(M_{gas}/a.m.u)$. Using the isothermal β-model for the cluster, the SZ decrement may be written in the form

$$\frac{\Delta T}{T_{cmb}} = -\frac{2k_\mathrm{B}T}{m_e c^2}\sigma_T \times \frac{1}{4\pi}\frac{\tan^{-1}\left(\frac{\sqrt{r_{max}^2 - b^2}}{\sqrt{r_c^2 + b^2}}\right) N_e r_c}{\sqrt{r_c^2 + b^2}\left[r_c r_{max} - r_c^2 \tan^{-1}\left(\frac{r_{max}}{r_c}\right)\right]}\ . \tag{4.32}$$

The Coma cluster at a redshift 0.0235, with a total mass about 2×10^{15} $\mathrm{M}_\odot$, is observed to have X-ray gas with a temperature 8-9 keV and a core radial size of 10.5 arc min (Silverberg et al.

Table 4.2: Statistics for different cosmological models.

Model	gas fraction	mean y $\times 10^{-5}$	Image rms before convolution (μK)	Image rms after convolution (μJy beam^{-1})
SCDM	parametrized	0.61	81	28
SCDM(high h)	parametrized	1.9	313	58
OCDM1	parametrized	0.46	60	23
OCDM2	parametrized	0.18	38	15
OCDM3	parametrized	0.05	9	3
SCDM(variant1)	no evolution	1.9	207	72
SCDM(variant2)	$\frac{M_{gas}}{M_{tot}} = \Omega_B$	2.4	245	79

1997, Herbig et al. 1995). The Compton-y parameter has been measured to be 9×10^{-5} towards its centre (Herbig et al. 1995). In our simulations, for the choice $p = 6$ and adopting a value of 0.096 as the baryon gas fraction, we find that a collapsed object of mass 2×10^{15} $M_\odot$ at redshift $z = 0.0235$ — corresponding to the Coma cluster parameters — yields values of 10.3–11.0 arcmin for the core size, $8\text{-}9 \times 10^7$ K for the gas temperature and the central SZ Compton-y decrement is in the range $7\text{-}8.5 \times 10^{-5}$.

4.6 Simulations

Our simulation codes compute the abundances $n(M, z)$ in redshift slices in the redshift range $z = 0$–5. We make the conservative assumption that only collapsed objects in the restricted range 10^{13}–10^{16} $M_\odot$ represent clusters of galaxies containing hot gas. Adopting a model, described below, for the spatial distribution of hot gas in the potential wells of these clusters, we simulate sky images

of the SZ effect expected owing to these clusters. The sky was simulated by separately computing the contributions from different redshift slices along the line of sight. In any redshift slice, the clusters are assumed to be Poisson-random distributed on the sky. We have simulated square patches of sky consisting of 256 pixels along each side: the pixels were chosen to be 10 arc sec square making the total image size 42′40″. The redshift slices were of size $\Delta z = 0.1$.

The mean number of clusters, λ, with mass in the range M–$(M + \delta M)$, is related to the Press-Schechter number density by:

$$\lambda = n(M, z) \times \delta M \times \text{volume corresponding to a pixel.} \tag{4.33}$$

The comoving volume of any pixel in a slice at redshift z is calculated as the product of the comoving area $(\Delta l)^2$ covered by the square pixels of angular size $\Delta\theta = 10$ arc sec and the comoving line-of-sight distance Δs corresponding to the redshift slice Δz. These are given by:

$$\Delta s = \frac{c}{H_0} \frac{dz}{(1+z)\sqrt{1+\Omega_o z}}, \tag{4.34}$$

and

$$\Delta l = \frac{2c\Delta\theta}{H_o \Omega_o^2 (1+z)} \left\{ \Omega_o z + (\Omega_o - 2) \left[\sqrt{\Omega_o + 1} - 1 \right] \right\}. \tag{4.35}$$

We have associated every collapsed massive object with mass exceeding $10^{13}\ M_\odot$ with cluster gas.

We use the simulations for the purpose of predicting the sky variance as observed by the ATCA; these observations are made with arc min resolution and will be less sensitive to SZ effects from clusters whose gas distribution is extended. The ATCA observations couple somewhat better to models with smaller p; therefore, we have adopted the conservative choice of $p = 8$.

We have accumulated the SZ effect from clusters in redshift slices up to a maximum redshift of 5. In each redshift slice, the pixels were populated by collapsed point masses in a Poisson random fashion; the expectation that any pixel was populated by objects in any mass bin was governed by Equation (4.32). We then substituted our cluster gas model for every mass point: the SZ effect owing to each cluster is distributed over several pixels surrounding that at which the point mass was located. The variance of the temperature fluctuations in the cumulative SZ effect images was then computed.

We have compared the results of the simulations with the observational limits on arc min-scale CMB anisotropy set by the ATCA experiment at 8.7 GHz (Subrahmanyan et al. 1993,1998,1999). These observations have been made with a Fourier synthesis array. The sky is viewed by the telescope as attenuated by a primary beam that has a full width at half maximum of about 6 arc min

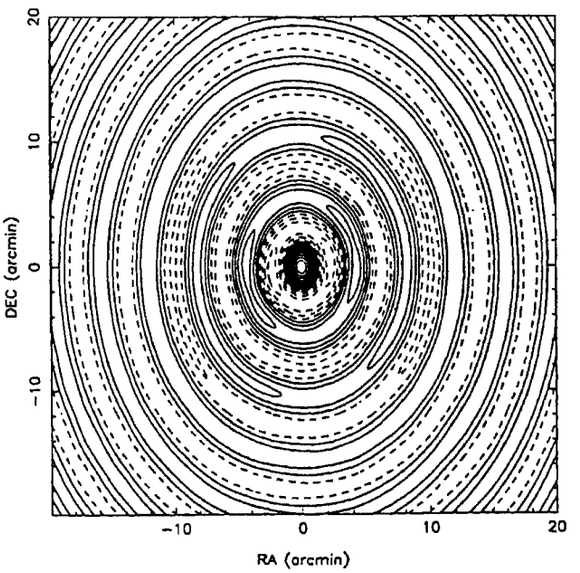

Figure 4.4: The synthesized *ATCA* beam at 8.7 GHz

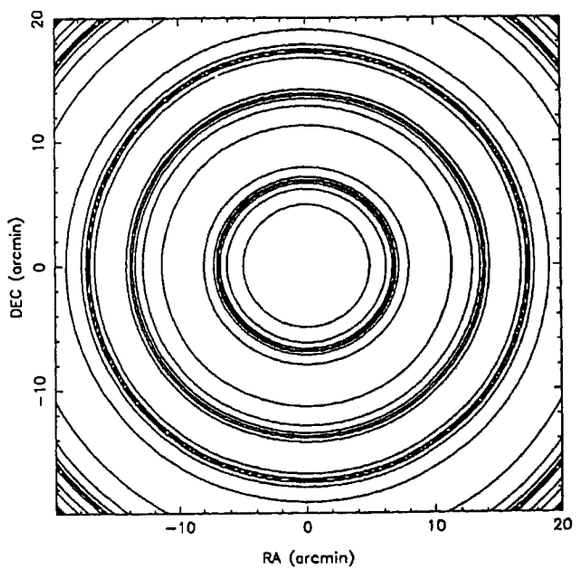

Figure 4.5: The primary *ATCA* beam at 8.7 GHz

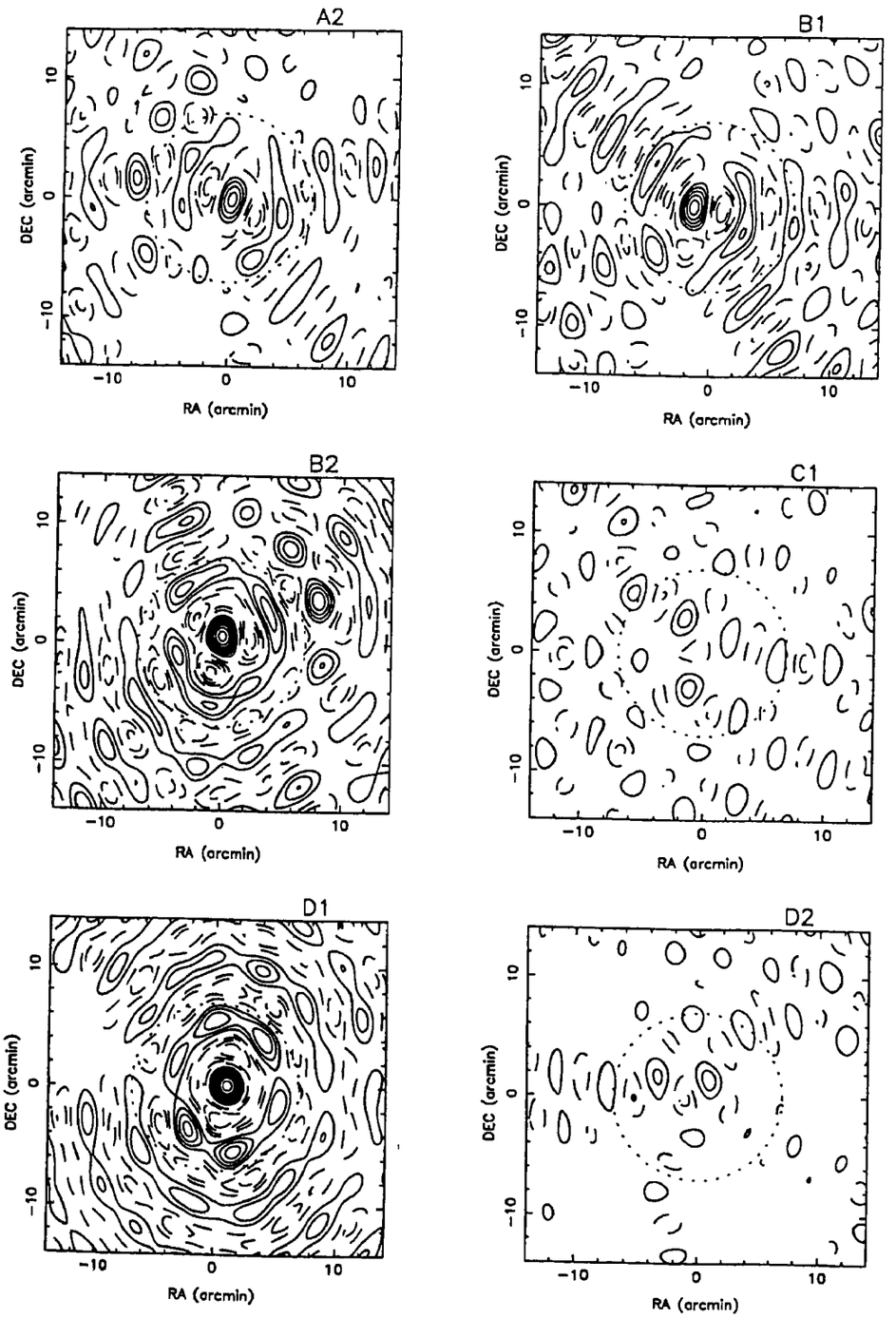

Figure 4.6: Images of the six fields in Stokes I made using visibilities in the 0-1 kλ range. Contours are shown for 24.2 μJy beam^{-1} $\times$ (-10, -8, -6, -4, -2, 2, 4, 6, 8, 10, 12, 14, 16). The locus of the first null in the primary beam pattern is shown as a dotted circle with a 7 arc min radius. Figure taken from Subrahmanyan et al. 1999.

and the synthetic images represent the convolution of the visible sky with a synthetic beam pattern. The ATCA synthesized and primary beams are shown in Figure 4.4 & 4.5. The ATCA experiment sets upper limits on any residual sky fluctuations apart from the instrument noise and confusing foreground sources. Assuming 'flat-band' CMB fluctuations, the ATCA limit corresponds to a flat band power $Q_{flat} \lesssim 25$ μK and, for their telescope filter function, this corresponds to an upper limit of 21 μJy beam^{-1} on the flux-density fluctuations on the sky. Sample observational images from the ATCA observations are shown in Figure 4.6 We have convolved the images resulting from our simulations by a beam that is the product of the ATCA synthetic beam and primary beam. Sample images are shown in Figure 4.7 corresponding to ΛCDM models with $\Omega_o = 1.0$ and 0.6. Images are displayed using a 1-arc min Gaussian (normalized to unit volume) as the convolving beam and separately using the ATCA product beam (normalized to a peak value of unity) as the convolving function. It is seen that the extended clusters seen in the $\Omega_o = 1.0$ simulation are resolved by the ATCA beam: the extended SZ structures will not be detectable by the ATCA imaging. It may be noted that before the convolution, the image pixels are in units of temperature (K); following the convolution, the pixel intensities are in units of flux density (Jy beam^{-1}). The predictions for the image variance have been made for different plausible cosmological models.

4.7 Results and Discussion

Results of the simulations are given in Table 4.2 for a range of model parameters. The image variances have been listed both before and after convolving with the ATCA product beam. The standard CDM model with $h = 0.5$, $\Omega_o = 1.0$ and with the hot gas fraction parametrized as described in Equation (4.30), is expected to result in an image rms which exceeds the ATCA limit. Increasing the Hubble parameter to a more likely value of $h = 0.65$ increases the expectations for the image rms and this 'high-h' CDM model is rejected with greater confidence. Considering open universe CDM models with $\Omega_o < 1$, the expected image variance decreases with decreasing Ω_o. Low $\Omega_o < 0.8$ open-universe models are allowed by the ATCA limits.

If we assume that $q = 0$ and that the cluster gas fraction does not diminish with redshift, high-redshift clusters contribute to the net SZ sky fluctuations. This is seen in the Table 4.2 where the image rms rises from 28 to 72 μJy beam^{-1} when the no-evolution assumption is made for the standard CDM model. We have also simulated images corresponding to the case where the gas fraction is a constant and equal to the mean baryon density predicted by nucleosynthesis. This gas model leads to predicted rms values which are not very different from that given by the $q = 0$ parametrized model; this indicates that the lower mass ($M_{tot} \approx 10^{13-14}$ M$_\odot$) objects dominate the

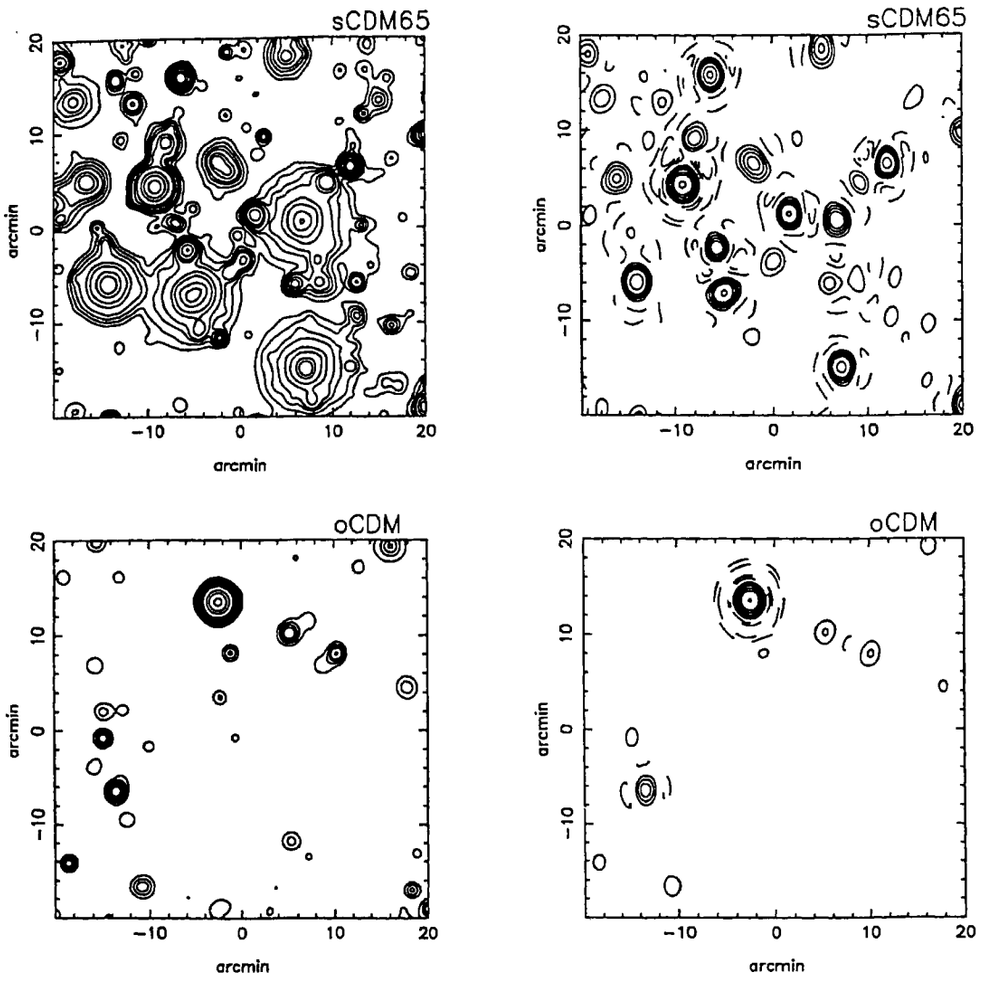

Figure 4.7: Simulated images. The upper pair of images corresponds to CDM cosmology with $\Omega_o = 1.0$; the lower pair corresponds to $\Omega_o = 0.6$. The cluster gas distribution has been parametrized with $p = 8$ and the baryon gas fraction is assumed to evolve with redshift as described by Equation (4.30); the Hubble parameter $h = 0.65$ has been adopted. The images on the left have been convolved with a Gaussian beam of FWHM 1 arc min; the images on the right have been convolved by the ATCA product beam. Contours are for $(-3, -2, -1, 1, 2, 3, 4, 6, 8, 12, 16, 24) \times -30\ \mu$K for the images on the left and $-30\ \mu$Jy beam^{-1} for the images on the right.

variance contribution in the no-evolution case.

We have computed the mean Compton-y parameter from the images for the different models and these are also listed in Table 1. The COBE-FIRAS experiment has set an upper limit of $y < 1.5 \times 10^{-5}$ (Fixsen et al. 1996). It may be noted that our SCDM model with $h = 0.65$ is independently rejected by these limits. Likewise, the models with no evolution in gas fraction are also disallowed by the FIRAS results.

The value of σ_8 has also been computed for each model and listed in Table 4.1. The standard CDM models normalized to COBE are known to be incompatible with estimates of σ_8 derived from the local X-ray luminosity function or other local measures of galaxy clustering (which prefer low values of σ_8 about 0.6). The ATCA results independently provide evidence in favour of a low-Ω_o universe. It must be emphasized once again that the sky fluctuations due to SZE is generically non-Gaussian in nature and a precise elimination of models have to take this into account.

An important difference between this work as compared to previous predictions for CMB anisotropies from SZ effects is that we have normalized our matter power spectrum to the COBE anisotropy results. All the previous predictions that we are aware of have normalized their models to observations of the present day clustering in galaxies or to X-ray luminosity functions; consequently, other workers have essentially normalized their matter power spectra to σ_8. This makes it possible for all the models to be consistent with the observational estimates of present day cluster abundances. Our choice of COBE normalization results in a σ_8 that varies across the models. This results in a dependence on Ω_o which is opposite to what is usually found. The difference may be understood in the following way : if the σ_8 is held constant across cosmological models, as previous workers have done, varying Ω_o changes the growth function and consequently the abundance of clusters at redsifts $z > 0$ will decrease with increasing Ω_o. On the other hand, when the matter power spectrum is normalized to COBE-DMR data, varying Ω_o across models alters the shape of the matter spectrum and the normalization in addition to the growth function. In this case, increasing Ω_o results in an increase in cluster abundances at all redshifts.

In the last chapter we pointed out that a significant fraction of clusters have cooling flows in them. We have, however, only considered isothermal clusters for simplicity. Since the majority of clusters will not be resolved by the *ATCA* beam, the SZ contribution to the rms will only dependent on the temperature weighted total gas mass of these clusters and not on their detail density and temperature profiles.

4.8 Conclusion

We have considered cosmological models composed of cold dark matter and baryons (and no cosmological constant), having an initial scale-invariant spectrum of adiabatic perturbations. We have used the Press-Schechter formalism to generate the distribution of clusters. We have normalized the rms mass fluctuations to COBE-DMR data. The Sunyaev-Zel'dovich decrement is calculated for each cluster adopting a model for the density profile of the cluster gas. We have simulated blank sky surveys for the SZ effect owing to a cosmological distribution of clusters. Finally, we have predicted the expectations for the variance in the background sky both before and after convolving with the ATCA beam. Based on a comparison with the upper limits set by the ATCA on CMB anisotropies on arc min scales, we conclude that COBE-normalized CDM models of the universe with a high density parameter ($\Omega_o > 0.8$) are rejected. This result is independent of any present epoch measures of σ_8. Thus, in this chapter, we have used 'blank sky' observations of SZE as a probe of our universe, through the matter density parameter Ω_o . In the next chapter, we continue to use Sunyaev-Zel'dovich effect as probe in cosmology, but also as a probe of specific cluster physics. This we do by looking at the variation of the power spectrum of SZ distortion from clusters of galaxies and linking it to the background cosmological model and astrophysics.

Chapter 5

A study of the power spectrum of Sunyaev-Zel'dovich effect

5.1 Introduction

An unbiased and statistical description of SZE requires wide field surveys. 'Blank' sky surveys of SZE have been envisaged to contribute to our understanding of our universe in three different ways: 1) using number counts of massive objects (clusters) to constrain the underlying cosmology, 2) using rms limits on arc min scale observations to put limits on cosmological parameters and 3) using the power spectrum of temperature fluctuations from SZE to constrain cosmological as well as astrophysical models. This chapter is devoted to the study of the SZE power spectrum, especially its shape, amplitude and peak position, and to use these probable observables as probes of our universe.

The statistics (mainly the power spectrum) of SZ distortions has been studied by many : Scaramella et al. (1993), da Silva et al. (1999, 2000), Springel et al. (2000) and Seljak et al. (2000) have used numerical simulations of SZE maps to study the power spectrum, whereas Persi et al. (1995)and Refregier et al. (2000) used a semi-analytic approach to compute the angular power spectrum from a projection of the 3-dimensional power spectrum of gas pressure on the sky. The Press-Schecter formalism has been used by Atrio-Barandela & Mucket (1999), Aghanim et al. (1997), Komatsu & Kitayama (1999) and Cooray (2000). Zhang & Pen (2000) has used non-linear perturbation theory to calculate the SZ power spectrum. Figure 5.1 shows the results of these works for comparison. It is clear that there is much discrepancy among these results. The reason

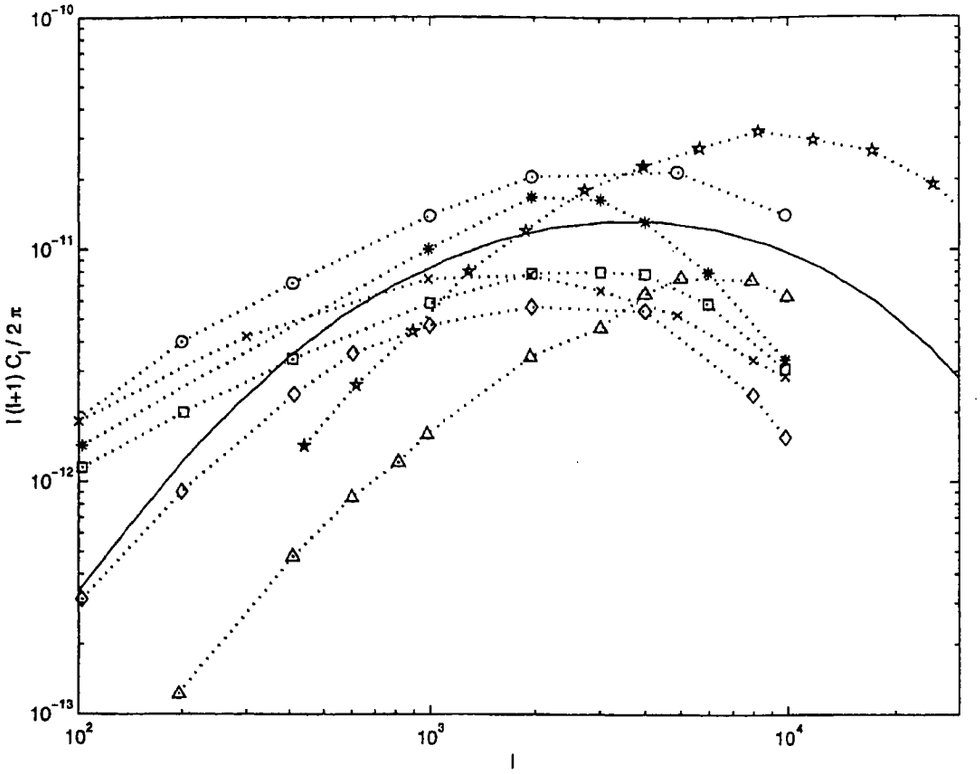

Figure 5.1: Comparison of published estimates of thermal SZ power spectrum. The symbols represent the following: circles (Komatsu & Kitayama 1999); cross (Molnar & Birkinshaw 2000); star (Cooray 2000); square (Zhang & Pen, 2000); diamond (Refregier et al. 2000); triangle (Seljak et al. 2000) and pentagon (Springel et al. 2000). The solid line is from the work presented in this Chapter. Note, that the maximum difference between the curves falls within an order of magnitude in amplitude.

being that slight differences in cosmological parameters or gas physics can change the conclusions. All of these approaches have their inherent advantages as well as disadvantages: the simulations are mainly limited by lack of dynamical range, enormous CPU time but have the advantage that they can incorporate the effects of non-linear feedback. The analytical approaches are simplistic to incorporate all the relevant physics but have the advantage of being easy to handle and less time consuming. In a recent study, Refregier and Teyssier (2000) have combined and compared both of these basic approaches. They conclude that the halo based (Press- Schecter) approach can give

sufficiently reliable results for the study of the SZE from clusters of galaxies. Encouraged by this result we study, analytically, the power spectrum of SZ distortion over a large parameter range. The main idea of this chapter is to look for some 'signatures' in the SZE power spectrum, which can be used to probe specific issues in astrophysics.

Throughout this chapter we concentrate mainly on thermal SZE since it is at least an order of magnitude more than the kinematic SZE for clusters of galaxies; see Molnar & Birkinshaw (2000). We mainly consider three different cosmological models: SCDM ($\Omega_o = 1.0$, $\Omega_\Lambda = 0$, h = 0.65), ΛCDM ($\Omega_o = 0.35$, $\Omega_\Lambda = 0.65$, h = 0.65) and OCDM ($\Omega_o = 0.35$, $\Omega_\Lambda = 0$, h = 0.65). All the models have $\Omega_b = 0.05$ and are COBE-normalized. Also, unless otherwise specified, all the power spectra shown are independent of frequency (*i.e.*,, the frequency dependent part of SZE is taken out) for easy comparison between them.

5.2 The SZE power spectrum

The fluctuations in the temperature background due to SZE from clusters of galaxies can be quantified in terms of correlations between the fluctuations along two lines of sight separated by an angle: this gives us the angular power spectrum of SZ distortion. The fluctuations of the CMB temperature produced by SZE can be quantified by their spherical harmonic coefficients a_{lm}, which can be defined as $\Delta T(\mathbf{n}) = T_0^{-1} \sum_{lm} a_{lm} Y_{lm}(\mathbf{n})$. The angular power spectrum of SZE is then given by $C_l =< |a_{lm}|^2 >$, the brackets denoting an ensemble average. These effects can be quantified if the cross correlation function of the clusters can be known (for details see Peebles 1980, section 41; Cole & Kaiser 1988). The pattern of temperature anisotropy on the sky is found by the convolution of the temperature anisotropy due a single 'template' cluster of mass M at redshift z with the angular distribution of the clusters and then integrating over their mass and redshift distribution. If one the takes an ensemble average and further assumes that $n(M, z)$ is constant over the range of comoving separation for which the cross-correlation function $\xi(M_1, M_2, z, \delta r)$ is non zero, then the angular temperature power spectrum C_l can be written as the sum of two terms

$$C_l = C_l^{Poisson} + C_l^{Clustering} \tag{5.1}$$

The power spectrum for the Poisson distribution of objects can then be written as (Cole & Kaiser 1988, Peebles 1980)

$$C_l^{Poisson} = \int_0^{z_{max}} dz \frac{dV(z)}{dz} \int_{M_{min}}^{M_{max}} dM \frac{dn(M, z_{in})}{dM} |y_l(M, z)|^2, \tag{5.2}$$

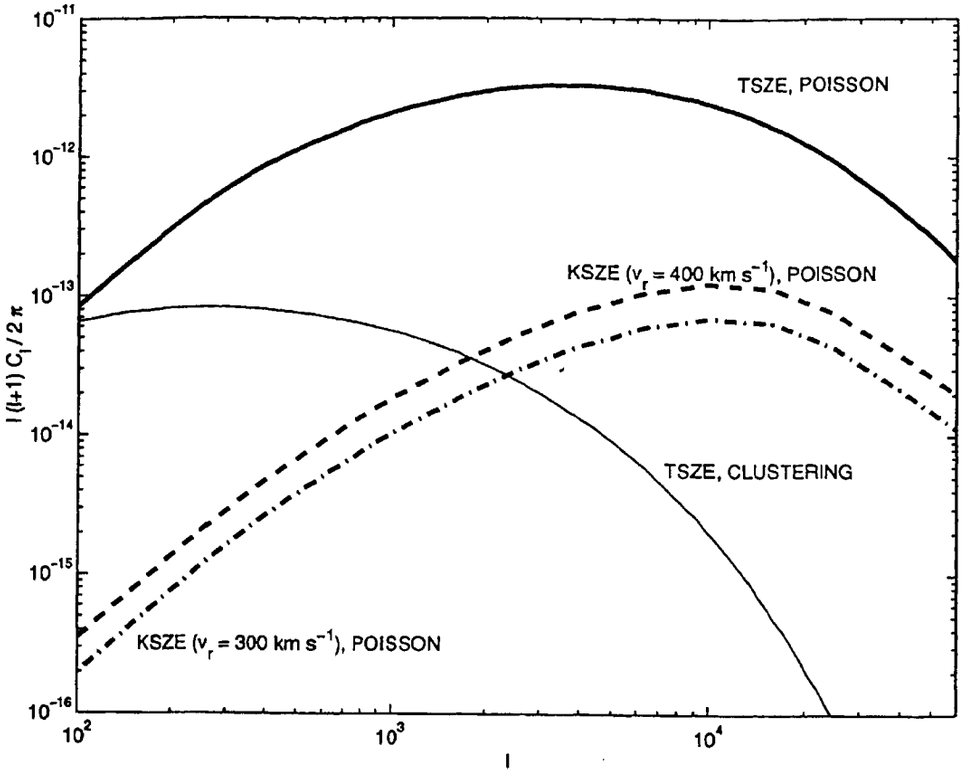

Figure 5.2: The SZE Poisson power spectra (thick lines) and the clustering spectrum from galaxy clusters are shown for ΛCDM cosmology. The solid lines are for the thermal SZE, the dashed line is for kinematic SZE with $v_r(z=0) = 400$ km s^{-1} and the dash-dotted line is for the same with $v_r(z=0) = 300$ km s^{-1}. We have a constant $f_g = \Omega_b/\Omega_o$.

where $dV(z)/dz$ is the differential comoving volume and dn/dM is the number density of objects. For the number density, we use the Press-Schecter formalism (see Chapter 4) and the volume element is given by

$$\frac{dV}{dz} = r(z)^2 \frac{4\pi c}{H_0}\left[\Omega_0(1+z)^3 + (1-\Omega_0-\Lambda)(1+z)^2 + \Lambda\right]^{-1/2} \quad , \tag{5.3}$$

where the comoving distance $r(z)$ is

$$r(z) = \begin{cases} \frac{2c}{H_0}\left[\frac{\Omega_0 z + (\Omega_0-2)(\sqrt{1+\Omega_0 z}-1)}{\Omega_0^2(1+z)}\right] & \Lambda = 0 \ , \\ \frac{c}{H_0}\int_0^z dx[\Omega_0(1+x)^3 + 1 - \Omega_0]^{-1/2} & \Lambda = 1-\Omega_0 \end{cases} \tag{5.4}$$

Since these fluctuations occur at very small angular scales, we can use the small angle approximation of Legendre transformation and write y_l as the angular Fourier transform of $y(\theta)$ as $y_l = 2\pi \int y(\theta) J_0[(l+1/2])\theta]\theta d\theta$ (Peebles 1980, Molnar & Birkinshaw 2000), where J_0 is the Bessel function of first kind and zero order.

In addition to Poisson power spectra, one would expect contribution to a 'correlation power spectrum' from the clustering of the galaxy clusters. Following Komatsu and Kitayama (1999), we estimate the clustering angular power spectrum as

$$C_l^{Clustering} = \int_0^{z_{max}} dz \frac{dV(z)}{dz} P_m \times \left[\int_{M_{min}}^{M_{max}} dM \frac{dn(M, z_{in})}{dM} b(M, z_{in}) y_l(M, z) \right]^2, \qquad (5.5)$$

where $b(M,z)$ is the time dependent linear bias factor. The matter power spectrum, $P_m(k,z)$, is related to the power spectrum of cluster correlation function $P_c(k, M1, M2, z)$ through the bias, *i.e.*, $P_c(k, M1, M2, z) = b(M1, z) b(M2, z) D^2(z) P_m(k, z = 0)$ where we adopt $b(M,z) = (1 + 0.5/\nu^4)^{0.06-0.02n}(1 + (\nu^2 - 1)/\delta_c)$ (Jing 1999 for details). This expression for the bias factor matches accurately the results of N-body simulations for a wide range in mass. In the above equation $D(z)$ is the linear growth factor of density fluctuation, $\delta_c = 1.68$ and $\nu = \delta_c/\sigma(M)$. These quantities have the same meaning as discussed in the previous chapter.

If one calculates the variance in beams of fixed size, the Poissonian model is a good approximation if the probability that a cluster has a neighbour is small inside the beam. (This is the justification for our use of only Poisson distributed objects in the simulations described in the last chapter). This probability is the product of the number density and the volume integral of the cross-correlation function over the region probed by the beam. It can be shown that for beams comparable to the size of rich clusters ($R \sim 1.5h^{-1}$ Mpc), the Poissonian approach to variance is a valid approximation. Only for very large beams, the variance will increase due to positive correlation of the clusters.

The statements made in the last paragraph are clearly illustrated in Figure 5.2, where we have plotted the Poisson as well as clustering power spectra for our ΛCDM model. It is seen that the clustering power spectrum is much less than the Poisson case and also falls off faster as one goes to smaller angular scales (smaller beam sizes). As has been pointed out by Komatsu & Kitayama (1999), the Poisson power spectrum dominates at all ℓ values greater than 100. However, by subtracting X-Ray selected clusters of galaxies over a certain flux (say $S_x > 10^{-13}$ erg cm^{-2} s^{-1}), from both the power spectra, one can make the clustering spectra dominate at around $\ell \sim 700$. The main features to be noticed from this figure are: 1)the power spectrum rises and falls with ℓ producing a peak at some ℓ_{peak}, which is around 4000 for the model shown (ΛCDM with $f_g =$

Ω_b/Ω_o = constant); 2) the main contribution of SZE to CMB anisotropy occurs at $1000 \lesssim \ell \lesssim 20000$ (*i.e.*,, after the CMB primary anisotropy becomes negligible) and 3) the amplitude of the kinematic SZE power spectrum is more than an order of magnitude smaller than that of thermal SZE spectrum and also peaks at a higher ℓ value. We thus have a basic idea of the 'shape and size' of the the power spectrum of SZE from galaxy clusters. In the next section we look at the nature of the power spectrum in more details.

5.3 The nature of the power spectrum

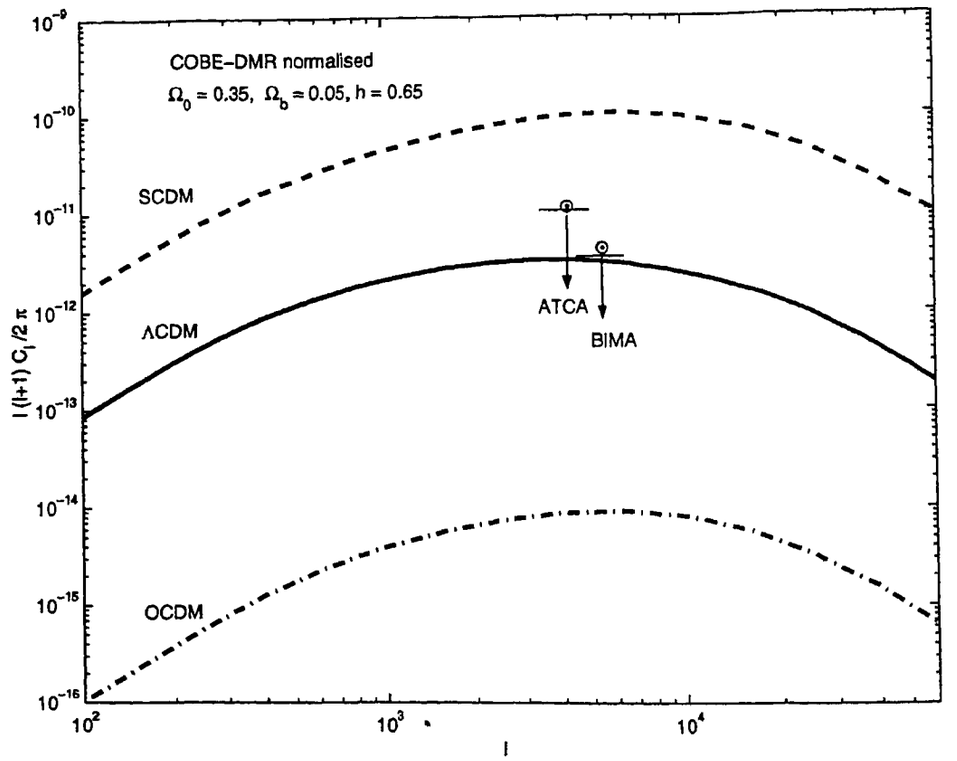

Figure 5.3: The SZE Poisson power spectra for different cosmological models are shown: ΛCDM (solid), SCDM (dashed) and OCDM (dot-dashed). The observational upper limits on arc minute temperature fluctuation seen by ATCA and BIMA are also shown with filled circles.

The basic nature of the power spectrum is governed by the the underlying cosmology, which not

only determines the peak position (*i.e.*,, ℓ_{peak}) but also fixes the the amplitude of the distortion. In fact, within accepted gas models of galaxy clusters (with *e.g.*, $n_e \sim 10^{-3}, T \sim 10^7 K$), the cosmology is the sole discriminatory factor as far as the overall amplitude of the power spectrum is concerned. This is easily seen from Figure 5.3. In this figure, we plot the power spectra for three different cosmological models (SCDM, ΛCDM and OCDM), all normalized to COBE-DMR data following Bunn & White (1997). Since the COBE normalized SCDM has the highest amplitude ($\sigma_8 = 1.57$), the resultant power is also large at all angular scales. In contrast, the ΛCDM and the OCDM model have lesser power.

Note is that this scaling (of the power with that of the mass variance) is insensitive to the details of the individual gas physics, and hence if one can have 'ideal' clusters, the one can, in principle, use the TSZE power spectrum to measure the cosmological parameters. Unfortunately, the gas physics of individual clusters are not yet known with precision, and so one cannot use SZE to precisely determine the cosmological model. One can, however, use the SZE power spectrum to *constrain* cosmological models (as done in the last chapter). The way to do this is also straight-forward and is illustrated in Figure 5.3. In this figure, we have also marked the observational upper limits given by ATCA (Subrahmanyan et al. 1998)and the Berkeley-Illinois-Maryland Array (BIMA) (Holzapfel et al. 2000) along with the various power spectra. The ATCA and BIMA observations put upper limits of 23μK and 14.1μK respectively at effective ℓ of 4200 and 5470. One can immediately see that the SCDM model is ruled out and the ΛCDM model is barely consistent with the BIMA limits. Thus, it is difficult to have Ω_o much greater than 0.35 in a flat universe without violating observations. One has, thus, been able to constrain the cosmological matter density parameter with a power spectrum analysis of SZE. This is consistent with the results presented in Chapter 4.

Another point to be noticed from Figure 5.3 is that the peak positions are different for different cosmologies, with the peak being at the highest ℓ for an OCDM universe. This is easy to understand since an object would subtend a smaller angle in an open universe than in a flat one. The reason for the small difference in the peak position between the SCDM and the ΛCDM models is more subtle and depends on the exact nature of the size angular-diameter relation and the distribution of the objects.

To understand these in a little more detail, let us concentrate on a particular model (say, the ΛCDM model) and see the effect of mass and redshift cutoff on the power spectrum . These are shown in Figures 5.4, 5.5, 5.6, 5.7, 5.8 and 5.9. In Figure 5.4, we have shown the effect of having different z_{max} the maximum redshift up to which we assume there are clusters capable of distorting the CMB. It is seen that the contribution to the distortion from redshifts beyond 3 is negligible. As one comes down in redshift, the power at high ℓ decreases. However, the power at

$\ell \lesssim 1000$ starts differing as a function of z only for $z \lesssim 1$. This is because lower masses are present at higher redshifts and thus their contributions get cutoff when one forces $z_{max} \lesssim 2$, whereas the more massive clusters are present mainly below $z \sim 1$.

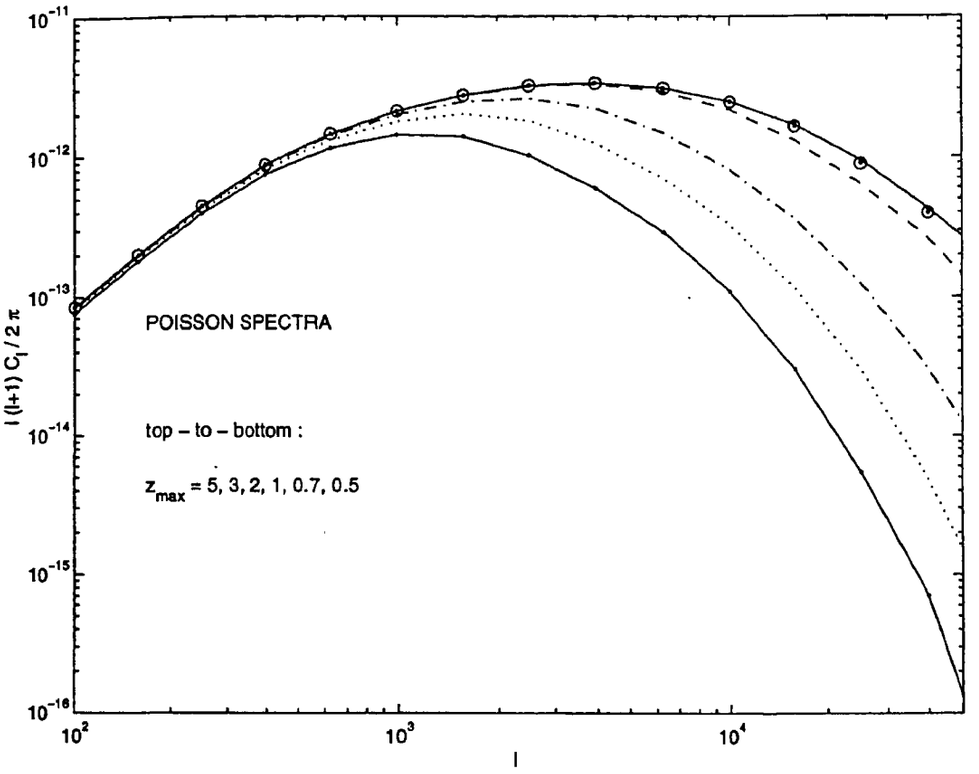

Figure 5.4: The SZE Poisson power spectra is plotted for different maximum redshifts : from top to bottom the z_{max} are 5 (circle), 3 (thick solid line with dots), 2 (dash), 1 (dash-dot), 0.7 (dotted) and 0.5 (solid line).

To see the effect of z_{max} more clearly, let us define the quantity C_ℓ^{**} as

$$C_\ell^{**} = \frac{\ell(\ell+1)C_l/2\pi}{<y>^2} \tag{5.6}$$

We have plotted C_ℓ^{**} vs ℓ for different z_{max} in Figure 5.5. We see that there is a cross-over of different curves at $\ell \sim 7000$, above which the behaviour of the different spectra are similar to that in Figure 5.4. However, below this crossover point, the trend is reversed and C_ℓ^{**} is larger for a lower value of z_{max}. There is also a trend in the peak position of the individual clusters, which moves to

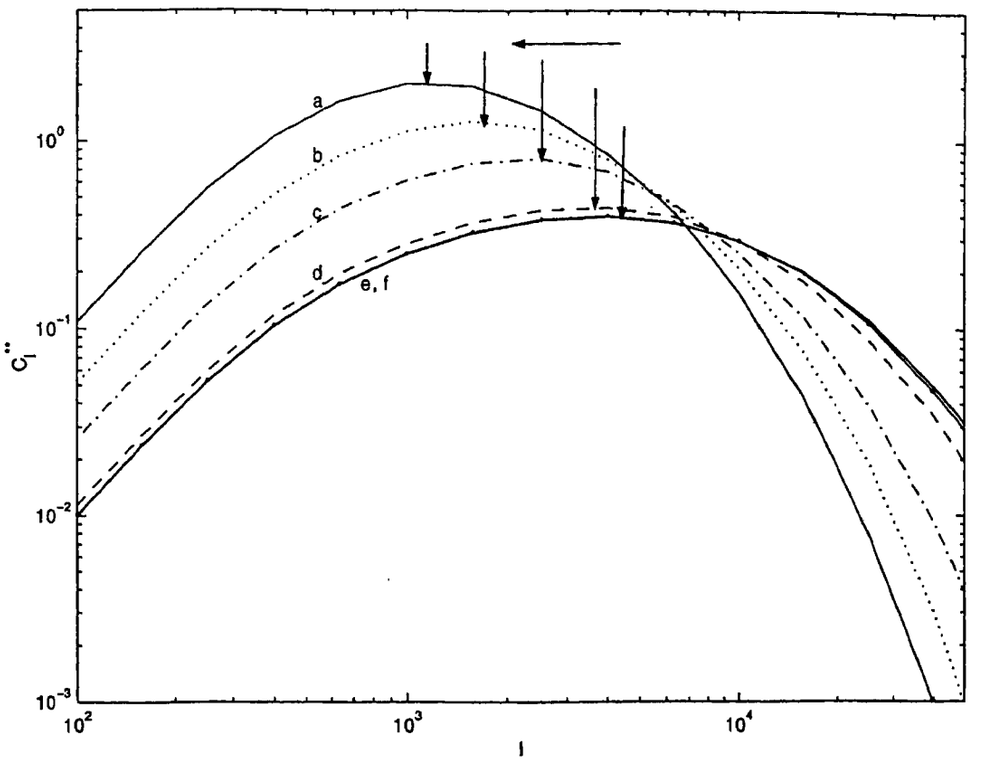

Figure 5.5: C_ℓ^{**} is plotted for different maximum redshifts z_{max} = 0.5 ('a'), 0.7 ('b'), 1 ('c'), 2 ('d'), 3 ('e') and 5 ('f').

lower ℓ values as one lowers the value of z_{max}. It is interesting to speculate on the possibility of using this plot to determine the maximum redshift up to which clusters can effectively contribute to the SZ power spectrum. In particular, it is easily seen that the ratio $C_\ell^{**}(\ell \simeq 10^4)/C_\ell^{**}(\ell \simeq 10^3)$ is a decreasing function of z_{max}. Thus, if it is possible to determine the background cosmology (from observations) and the gas physics (from simulations), then one can make use of Figure 5.5 to determine z_{max}.

In Figure 5.6, we show the effect of different values of z_{max} on the clustering spectrum. Compared to the Poisson case, the peak position remains almost the same. This is because the clustering spectrum depends mainly on the inter-cluster distance and the major contributions to the clustering power spectrum come from small redshifts.

At any epoch, one expects the temperature fluctuations to be dominated by very rare massive

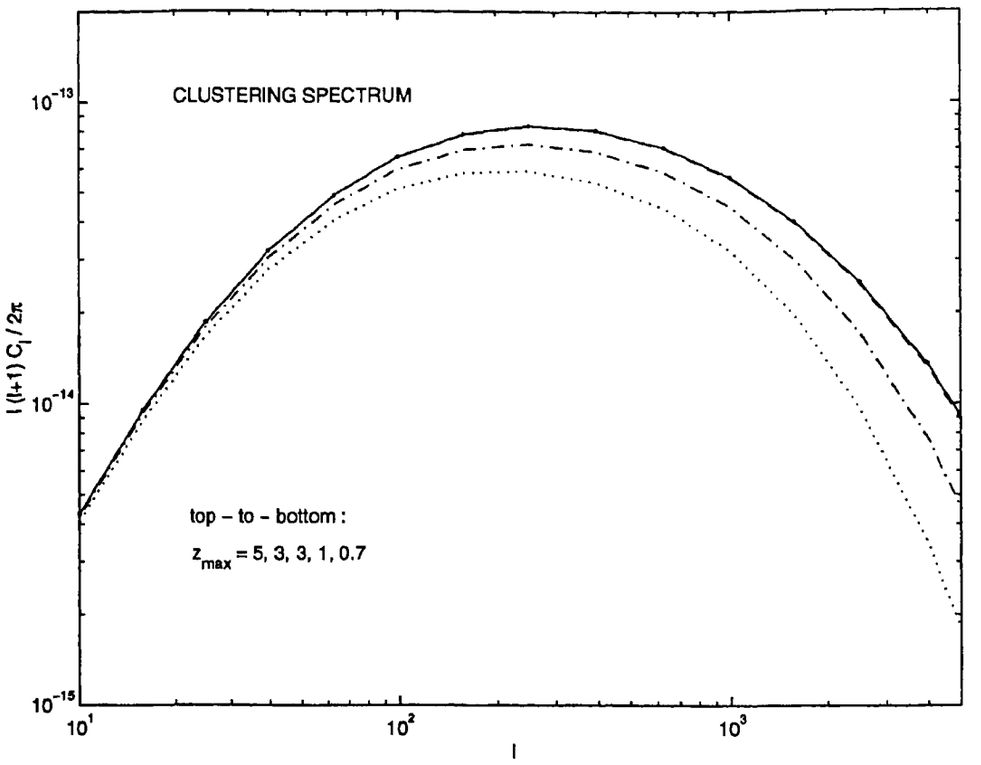

Figure 5.6: The SZE clustering power spectra is plotted for different maximum redshifts : from top to bottom the z_{max} are 5 (circle), 3 (thick solid line with dots), 2 (dash), 1 (dash-dot), 0.7 (dotted).

clusters (see Figure 5.7). It is clear from the figure that the main contribution to the Poisson power spectrum comes from clusters in the mass range of $10^{14-15}M_{\odot}$. The higher masses clusters (*i.e.*,, $M > 10^{15}M_{\odot}$) contribute less due to their dwindling number densities and the lower mass one (*i.e.*,, $M < 10^{14}M_{\odot}$) contribute less because their individual SZE distortion is less due to lower T and smaller sizes. Similar trends are seen in the clustering power spectrum as well. Another feature that is immediately noticeable is that higher masses contribute at lower ℓ values and vice versa. We show this later in more details in Figure 5.9. Although the variance is dominated by richer clusters, the mean Compton distortion is dominated by numerous smaller clusters. This is evident from Figure 5.8 where we plot C_ℓ^{**} vs ℓ for clusters in different mass ranges. Since the average y is least in the highest mass range, the resulting C_ℓ^{**} is the highest (see Equation (5.6)).

Finally, we come to a discussion of the effect of size and number densities of different masses

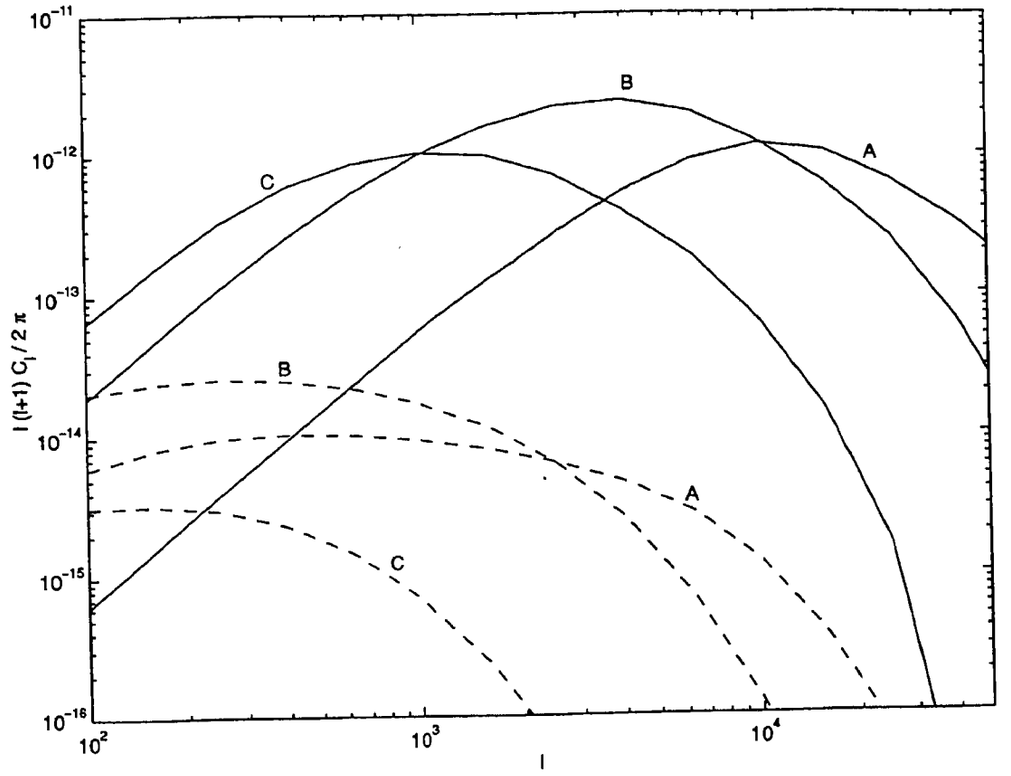

Figure 5.7: The SZE power spectra is plotted for different mass ranges: A) $10^{13-14}M_\odot$, B) $10^{14-15}M_\odot$ and C) $10^{15-16}M_\odot$. The solid lines are for Poisson and the dashed lines are for clustering power spectrum.

on the resultant shape of the power spectrum. For illustration, in Figure 5.9, we have considered the three cases: 1) model A : $10^{15} < M < 1.1 \times 10^{15}$ and $0.5 < z < 0.55$ 2) model B : $10^{14} < M < 1.1 \times 10^{14}$ and $1 < z < 1.05$, and 3) model C : $10^{14} < M < 1.1 \times 10^{14}$ and $0.5 < z < 0.55$. It is seen that for the same mass range, the model curve for B peaks at a higher ℓ value than that for model C. This is so since model B corresponds to a higher redshift and consequently a smaller effective angular size. Between models B and C, the model C has a higher amplitude due to the fact that for the mass range in consideration there are more structures at $z \sim 1$ than at $z \sim 0.5$, according to Press-Schecter formalism. For the same redshift range, the curve for model C peaks at a higher ℓ than model A, the reason being that model A has a higher mass and so larger angular size (from the '$M - r_{core}$' relation used in last chapter). It also has

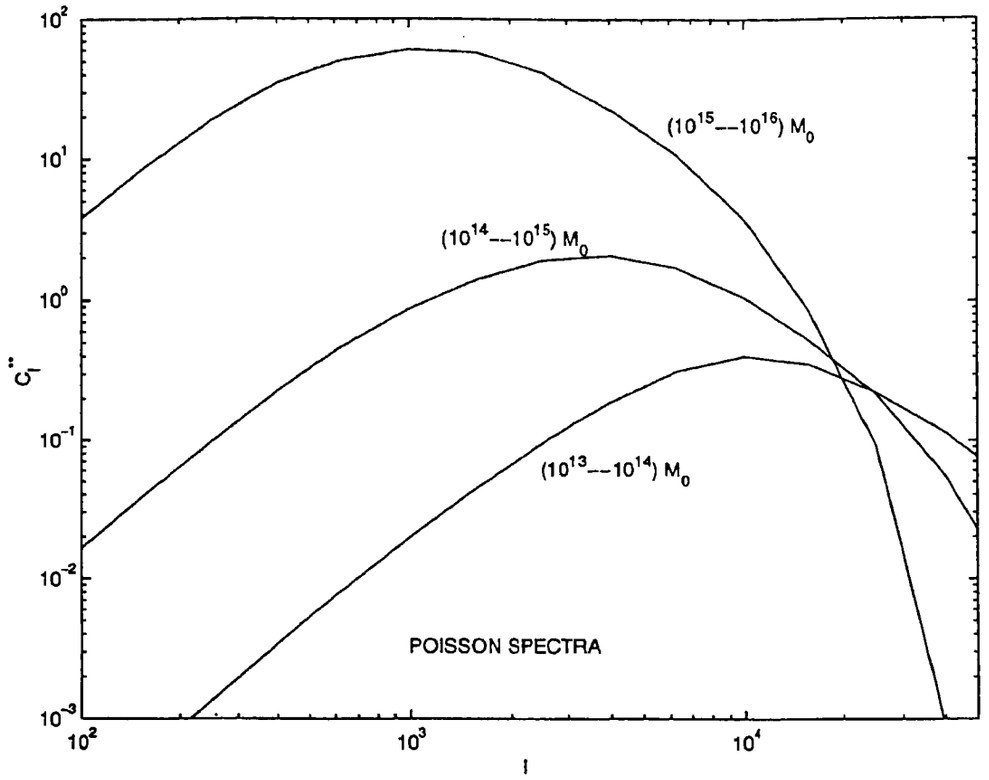

Figure 5.8: C_ℓ^{**} is plotted for different mass ranges

larger amplitude because along with larger size, it also has a larger gas pressure due to its higher temperature.

Having already used the TSZE power spectrum to constrain cosmological models, we now turn to use the power spectrum as a probe of specific gas physics of galaxy clusters.

5.4 Cluster gas mass fraction

5.4.1 A debate in cosmology

Clusters of galaxies, being perhaps the largest gravitationally bound structures in the universe, are expected to contain a significant amount of baryons of the universe. Moreover, due to their large angular sizes, it is easier to observationally estimate their total mass M_T, the gas mass M_g

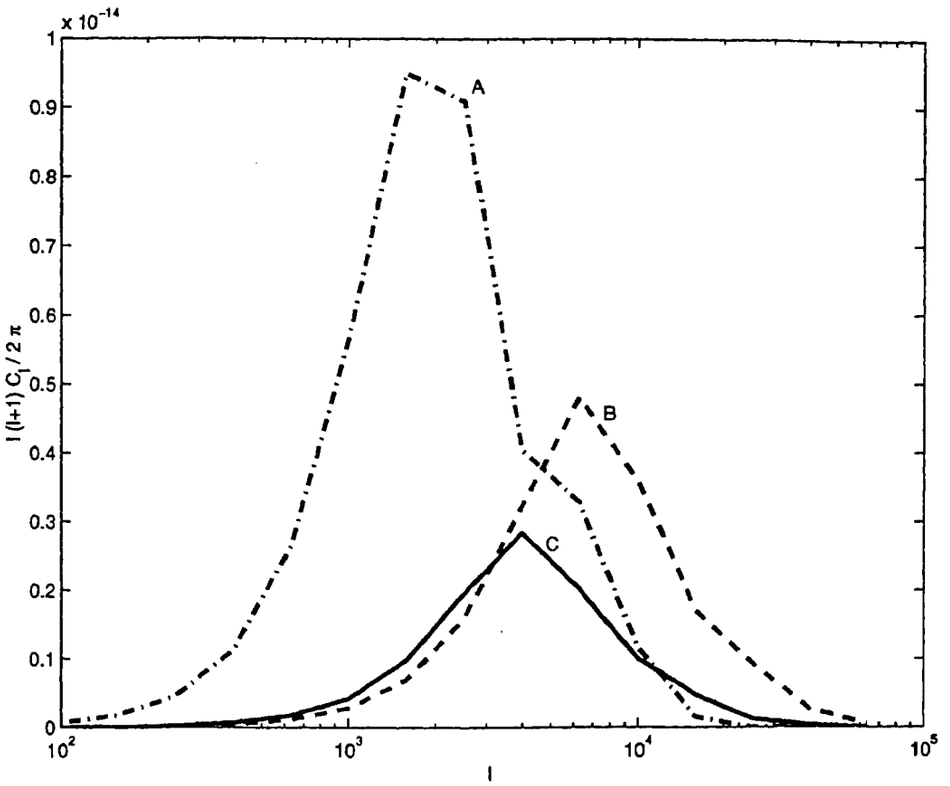

Figure 5.9: Poisson power spectra from objects in three different cases corresponding to different mass and redshift range. Details are in the text.

and hence the gas mass fraction ($f_g = \frac{M_g}{M_T}$). These estimates can be used as probes of large scale structure and underlying cosmological models. For example, the cluster f_g would give a lower limit to the universal baryon fraction Ω_b/Ω_m. Estimates of f_g have been obtained in a number of studies (*e.g.*White & Fabian 1995, Mohr et al. 1999, Sadat & Blanchard 2001) and the values obtained through these studies are in agreement within the observational scatter. A point to be noted here is that the estimated f_g depends on the distance to the cluster (*i.e.*, $f_g \propto d_A^{3/2}$). Hence, if f_g is assumed to be constant, then in principle, one can use the 'apparent' evolution of f_g over a large redshift range to constrain cosmological models (Sasaki 1996).

The question as to whether there is any evolution (as opposed to constancy) of gas mass fraction, however, is still under debate, with claims being made either way. For example, Schindler (1999) has investigated a sample of distant clusters with redshifts between 0.3 and 1 and conclude that

there is no evolution of the gas mass fraction. Similar conclusion has been drawn by Grego et al. (2000). On the contrary, Ettori and Fabian (1999) have looked at 36 high-luminosity clusters, and find evolution in their gas mass fraction (in both SCDM and ΛCDM universes); See also David et al. 1995, Tsuru et al. 1997, Allen & Fabian 1998, Mohr et al. 1999. Observations suggest that, though f_g of massive clusters ($T \gtrsim 5$ keV) appears to be constant, low mass clusters with shallower potential wells may have lost gas due to preheating and/or post-collapse energy input (David et al. 1990,1995, Ponman et al. 1996, Bialek et al. 2000). It is also well known that ICM is not entirely primordial and there is probably continuous infall of gas, thereby, increasing f_g with time. Thus, there is considerable debate regarding the evolution of gas mass fraction.

Keeping future SZ surveys in mind, in this section we look at the SZE power spectrum as a probe of the ICM. We show it to be a very sensitive probe of the evolution (or constancy) of f_g . Measurements of the primary anisotropy would give us 'precise' values of cosmological parameters (like $h, \Omega_m, \Omega_\Lambda, \Omega_b$). Hence, for our calculations, we assume that we know the values of cosmological parameters and do not worry about their effect on the SZE power spectrum. In that case, any feature of the SZE power spectrum can be attributed to specific cluster physics (like gas content). We note that, as shown below, this method of probing f_g is not biased from any selection effect that can occur while doing pointed SZE observations of X-ray selected clusters of galaxies, and hence is more desirable.

5.4.2 Modeling the cluster gas

We assume the ICM to follow a β-profile (see Chapter 4) with $\beta = 2/3$ for simplicity. The other physical parameters of the clusters are determined using the virial theorem and spherical collapse model. We closely follow Colafrancesco & Vittorio (1994) in our modeling. We have for the gas density, $n_e(r) = n_{e,0}\left(1 + \frac{r^2}{r_c^2}\right)^{-3\beta/2}$. We take the gas to be extended up to $R_v = pr_c$ with $p = 10$. The central gas density, $n_{e,0}$ is given by $n_{e,0} = f_g \frac{2\rho_0}{m_p(1+X)}$ where $X = 0.76$ is the average proton mass fraction and ρ_0 is the central gas mass density. To account for the fact that there is a final cutoff in the gas distribution we introduce a Gaussian filter at the cluster edge R_v given by $n_e(r) \rightarrow n_e(r)e^{-r^2/\xi R_v^2}$, where $\xi = 4/\pi$ is a fudge factor.

We parametrize the possible evolution of the gas mass fraction as

$$f_g = f_{g0}(1+z)^{-s}\left(\frac{M}{10^{15}h^{-1}M_\odot}\right)^k, \tag{5.7}$$

where the normalization is taken to be $f_{g0} = 0.15$, based on local rich clusters. We look at combinations of both mass and redshift dependence for a range of evolutionary models. In particular,

we look at a case of strong evolution given by $k = 0.5, s = 1$ (Colafrancesco & Vittorio 1994); $k = 0.1, s = 0.5$ (as suggested by Ettori and Fabian 1999); $k = 0.1, s = 0.1$ (weak evolution); $k = 0$ (no mass dependence) and $s = 0$ (no redshift dependence).

For the core radius r_c and the temperature, we use

$$r_c(\Omega_0, M, z) = \frac{1.69h^{-1}\mathrm{Mpc}}{p}\frac{1}{1+z}\times \left[\left(\frac{M}{10^{15}h^{-1}M_\odot}\right)\frac{178}{\Omega_0\Delta}\right]^{1/3} \tag{5.8}$$

$$k_BT = 7.76\beta^{-1}\left(\frac{\dot{M}}{10^{15}h^{-1}M_\odot}\right)^{2/3}(1+z)\mathrm{keV} \tag{5.9}$$

Here, $\Delta(z)$, β and p are as defined in the last chapter.

Putting everything together, we have the temperature distortion to be $\frac{\Delta T(\theta)}{T_{\mathrm{cmb}}} = g(x)y(\theta)$, with

$$y(\theta) = \left(\frac{\sigma_T n_{e0} r_c k_B T}{m_e c^2}\right)\times \frac{\pi e^{1/\xi p^2}}{\sqrt{1+(\theta/\theta_c)^2}}\mathrm{Erfc}\left(\sqrt{\frac{1+(\theta/\theta_c)^2}{\xi p^2}}\right). \tag{5.10}$$

The angular core radius $\theta_c = r_c/d_A$.

5.4.3 A signature of gas fraction evolution

We study the power spectrum of SZE from clusters of galaxies, under the assumption of a 'precise' and 'a priori' knowledge of the cosmological parameters. The results obtained below depend crucially on this assumption, which is reasonable since future observations of the primary CMB temperature anisotropies would, indeed, give us 'precise' values of the major cosmological parameters. The progress towards this 'precision-era' in cosmology is encouraging. Infact, current observational data have already fully or partially detected the first three acoustic peaks between $\ell \approx 200 - 800$ (Netterfield et al. 2001). We also assume that in the ℓ-range of relevance, thermal SZE from clusters of galaxies are the dominant contributors to the temperature anisotropy. The other secondary anisotropies are either smaller in strength or contribute at even higher ℓ's or have different spectral dependence (Aghanim et al. 2000; Majumdar et al. 2000).

We have plotted the Poisson SZE power spectrum in Figure 5.10. Clearly, the primary feature distinguishing a non-evolutionary constant f_g model from an evolutionary one is the position of the peak. The model with a constant f_g peaks at a higher l-value and also has greater power. The constant f_g model peaks at $l \sim 4000$. This result is in agreement with that of Komatsu & Kitayama (1999). If one assumes that there is no evolution of f_g with redshift (*i.e.*,, s=0), the peak is at

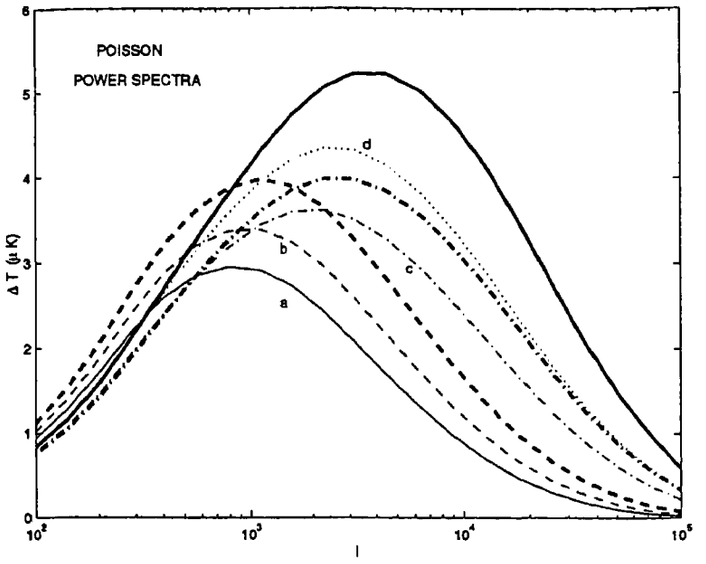

Figure 5.10: The Poisson power spectra due to SZE from galaxy clusters for different f_g models. The thick solid line corresponds to constant f_g model, the thick dashed line has no evolution with redshift and the thick dash-dotted line has no evolution with total mass. The thin lines are for the cases: a) k=0.5, s=1; b) k=0.5, s=0.5; c) k=0.1, s=0.5 and d) k=0.1, s=0.1.

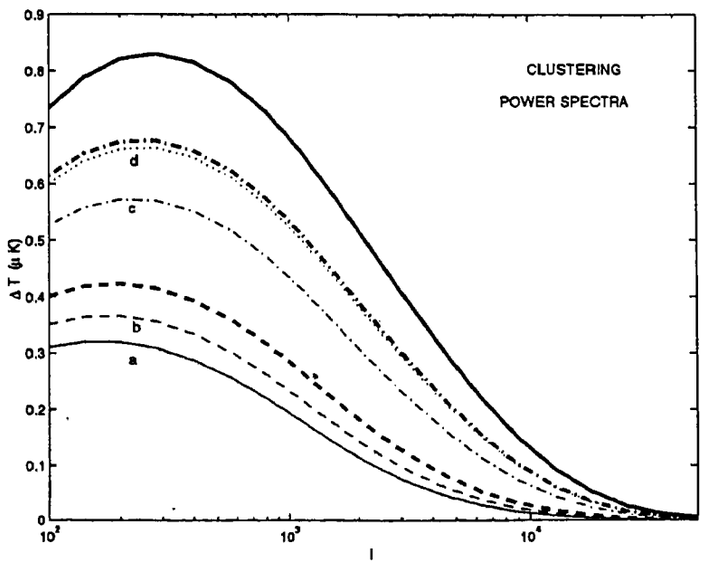

Figure 5.11: The Clustering power spectra. Notations same as in Figure 5.10.

$l \sim 1100$, whereas in the case of no dependence on mass (k=0), the peak is at $l \sim 2500$. Based on EMSS data (David et al. 1990), Colafrancesco & Vittorio (1994) (and also Molnar & Birkinshaw 2000) model f_g with k=0.5 & s=1. For this case, we see that the turnover is at a very low $l \sim 900$. Assuming a mild evolution (k=0.1, s=0.1), we get the peak at $l \sim 2100$. We also show results for (k=0.5, s=0.5) and (k=0.1, s=0.5). The last parametrization is based on the recent analysis of *ROSAT* data by Ettori & Fabian (1999). It is evident that the difference in the l-value of the peak for the constant f_g scenario from that for an evolutionary one can range between $\ell \sim 1500 - 3200$.. The position of the peak thus is a strong discriminatory signature of any evolution of f_g .

Following our discussion in the last section, it is easy to understand the shift in the peak of the SZE power spectrum. Let us consider the case s=0, *i.e.*, f_g depends only on total mass. From Equation (5.7), this means an enhanced reduction of f_g of smaller mass clusters relative to the larger masses and so a reduction of power at larger ℓ's, since smaller masses contribute at larger ℓ. Hence, the peak shifts to a lower l. For the case k=0, (*i.e.*, only redshift dependence), we now have structures at high z contributing less to the power (than without a redshift dependence). Since from Press-Schecter formalism, less massive structures are more abundant at high z, this negative dependence of f_g on redshift cuts off the contribution more of low mass structures than that of the more massive clusters. Hence, once again there is less power at high l and the peak shifts to lower l-value. The parametrization of Equation (5.7) affects the larger masses less, as evident from almost equal power seen at $l \lesssim 600$ for all models. The net effect is a reduction of power at smaller angular scales, and hence a shift in the position of the peak to a smaller multipole value.

We note that these results are independent of the arguments given (see Rines et al. 1999) to explain any possible evolution of f_g . There, f_g is *assumed* to be intrinsically constant but there is an 'apparent' change in f_g due to any change in the assumed cosmology. In such a case, if there is 'actually' even a slight evolution of f_g , then one can still account for it with a non-evolutionary model, by simply changing the cosmological parameters. In contrast, our method *does not assume a priori* any constancy or evolution of f_g and tries to look for it.

In Figure 5.11 we show the SZE clustering power spectrum. For all models, it falls off at a smaller l w.r.t the Poisson power spectrum. Since for clustering, the peak depends mainly on the average inter-cluster separation, which is fixed once the cosmology is fixed, there is no appreciable spread of the peaks in l-space. The only difference is in their relative power w.r.t each other which depends on the total gas mass available to distort the CMB. Addition of the clustering power spectrum to the Poisson case results in slight shift of the peaks to lower l's.

It maybe possible to measure the power spectrum of SZE with the ongoing and future high angular resolution CMB observations. In principle, observations with SUZIE, OVRO, BIMA and

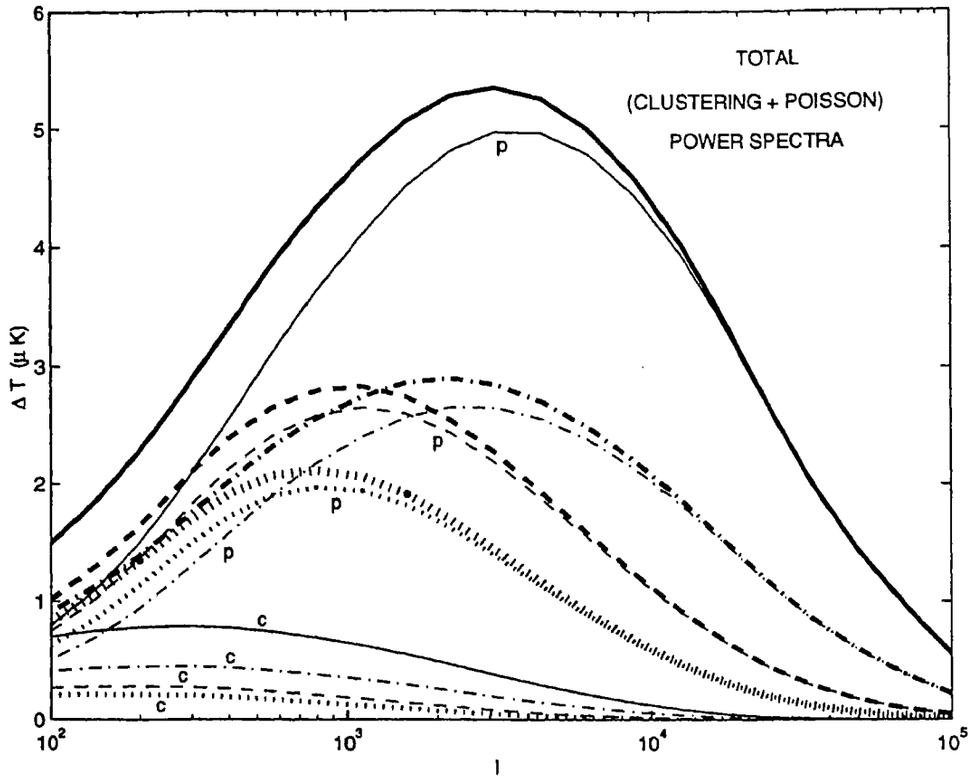

Figure 5.12: The total (Poisson + Clustering) power spectra (in thick lines) and the corresponding Poisson (labeled with 'p') and clustering spectra (labeled with 'c') are shown. The solid lines corresponds to constant f_g; the dashed line correspond to no evolution with redshift ; the dash-dotted lines correspond to no evolution with mass and the dotted line is for the case (k=0.5, s=1).

ATCA can probe the range in l from $\approx 1000 - 7000$ and a frequency range of $\approx 2 - 350$ GHz. The SZE power spectrum would also be measured with increased precision by the proposed ALMA and AMiBA (which is geared for blank sky surveys).

The observations will, however, measure the total power spectrum given by the sum of the Poisson and the clustering power spectrum. In Figure 5.12 we show the total power spectrum for 4 parameters sets, along with their Poisson as well as clustering power spectrum. Since for clustering, the peak depends mainly on the average inter-cluster separation, which is fixed once the cosmology is fixed, there is no appreciable spread of the clustering peaks in l-space. However, as is evident from the plot, the clustering power spectra are far smaller than the corresponding Poisson

spectra, and hence addition of the clustering spectrum to the Poisson spectrum does not shift the peaks significantly. Thus, for the total power spectra, the difference in the l-value of the peak of the constant f_g scenario from an evolutionary one, can range between $\ell \sim 1100 - 2500$. The peak position thus remains a strong discriminatory signature of any evolution in f_g.

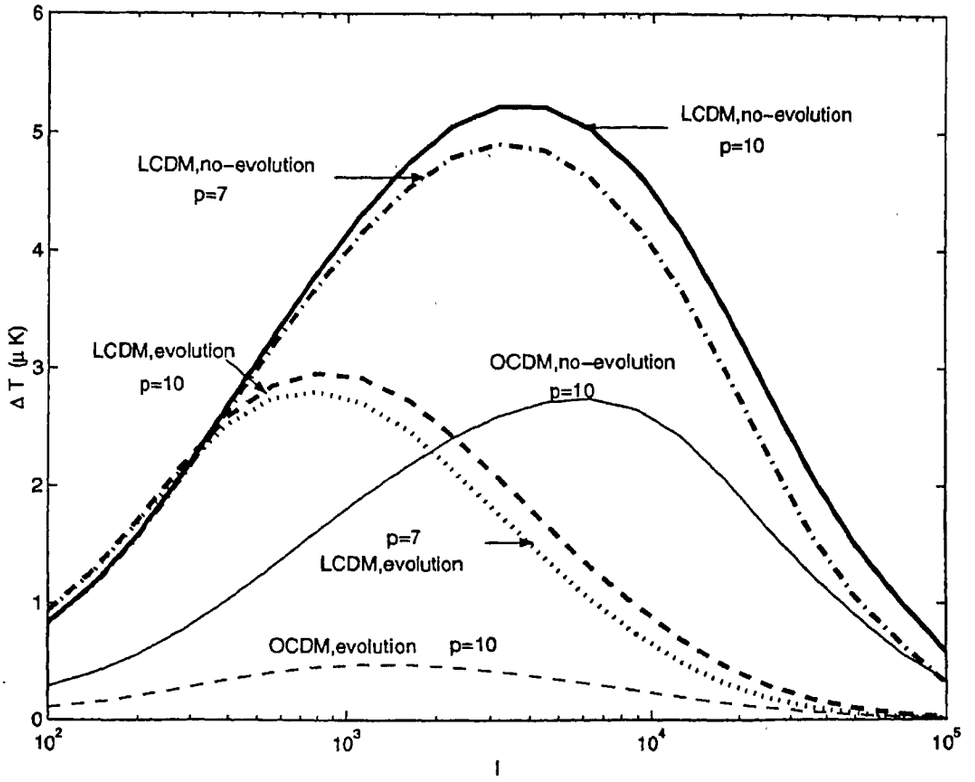

Figure 5.13: The Poisson SZE power spectra are plotted for different cosmologies and with different extension of the gas mass. The solid lines are for a ΛCDM, with $\Omega_m = 0.35, \Omega_\Lambda = 0.65, h = 0.65$, and the thin lines are for $OCDM$ with $\Omega_m = 0.35, h = 0.65$. The $OCDM$ lines have been multiplied by a factor of 10 in the plot. The solid and dashed lines are for gas mass extending up to $10r_c$, whereas the dash-dotted and the dotted lines are for extension up to $7r_c$.

Finally, let us comment on the validity and robustness of our results. In Figure 5.13, we show the results for an open universe ($\Omega_0 = 0.35, h = 0.65$). It is clearly seen that the peak positions for constant f_g and evolutionary models remain far apart. In fact, for same parameters of $k = 0.5, s = 1$, the difference between the peaks increases to ≈ 4500 from the value of ≈ 3000 in a flat universe. It

is seen that the turnover of the SZE power spectrum is insensitive to the mass cutoff, since the main contribution to the anisotropy comes from clusters with $10^{14}M_{\odot} < M < 10^{15}M_{\odot}$. In Figure 5.13, we also indicate the effect of having a more compact gas distribution with $p = 7$. We see that the shift in the peaks is negligible (though the height is reduced a little) and effect of any uncertainty on the extent of the cluster gas extends is not significant. The use of a single β to model the full gas distribution introduces little error, though a β-model fits the inner cluster regions better. This is because the major contribution to the anisotropy comes from around the core region, and increasing β slightly decreases the overall distortion, without changing the position of the peak, significantly. We also note that simulations predict a tight relation between the total mass and the gas temperature of a cluster (Evrard 1990, 1996) and so we not taken a evolving T in our analysis. The final conclusions should be interpreted in terms of any uncertainty that may creep in from our incomplete knowledge of cluster $M - T$ relationship.

5.5 Conclusions

We have computed the angular power spectrum of SZE from clusters of galaxies. we have tried to understand the shape and the amplitude of the power spectrum due to TSZE from galaxy clusters. Using the resultant power spectrum for different cosmological models and observational upper limits on small angular scale temperature anisotropy by from ATCA and BIMA observations, we have been able to constrain cosmological models. We have suggested a procedure to look for contribution to the power spectrum from high redshifts. We have also shown that the position of the peak of the power spectrum is a *strong discriminator* between different f_g models . One of the goals of arc minute scale observations of the CMB anisotropy is to measure the SZE power spectrum from blank sky surveys. Such observational results can be used to constrain f_g models. This also has the added advantage of being devoid of uncertainties that can creep in through 'selection biases' in estimating the f_g using pointed studies of X-ray selected galaxy cluster. Our method, thus, provides a powerful probe of evolution (or constancy) of gas mass fraction and can potentially resolve the decade long debate.

With this chapter, we come to the end of our probe of universe through SZE from galaxy clusters. In the next chapter, we go to the farthest parts of our universe and look at the distortion of the CMB from galactic winds at high redshifts.

Chapter 6

SZE at high redshifts: Distortions from galactic winds

6.1 Introduction

We have so far discussed the distortion of the CMB due to SZE from clusters of galaxies, in the context of targeted as well as non-targeted observations. SZ studies of X-Ray selected clusters typically look at distortions from clusters at low redshifts (say $z < 0.5$). With 'blank sky' surveys, one can further push back this redshift limit and look at contribution to the rms temperature fluctuations at arc minute resolution from a cosmological distribution of clusters. One can also extract the power spectrum of SZ distortion from these surveys. Since the density of clusters of galaxies decreases rapidly at higher redshifts, the above two methods together can probe redshifts only up to $z \approx 1$. To use SZ distortions from astrophysical objects as a probe of our universe at higher redshifts one must consider distortions due to lower mass objects. Dwarf galaxies, having masses in the range $10^7\,\mathrm{M}_\odot < M_{gal} < 10^{10}\mathrm{M}_\odot$ give us the opportunity to go to redshifts around 10 and more[1] This chapter is devoted to the study of SZ distortion from galactic winds arising out of these dwarf galaxies at high redshifts.

Recent studies of the epoch of reionization of the universe offer the following scenario for the first baryonic objects. Although the first objects form at redshifts $z \sim 40$ with masses of order 10^5 $\mathrm{M}_\odot$, UV radiation from stars formed in these objects obliterate the molecular hydrogen in other objects in their vicinity, thereby suppressing further formation of objects with masses $M \leq 10^8\,\mathrm{M}_\odot$

[1]Note that one can probe high z's with other objects as well, *e.g.*, quasar's

(Haiman, Rees & Loeb 1997, Ciardi et al. 1999). These objects with masses comparable to local dwarf galaxies appear later, at redshifts $z \lesssim 15$.

These dwarf galaxies are thought to have affected the intergalactic medium (IGM) in at least two ways. Along with the radiation from early black holes, they provided the UV radiation needed to re-ionize the IGM and keep it ionized thereafter. It is also possible that outflows from them provided the metals needed to explain the enrichment of the IGM (Miralda-Escudé & Rees 1997, Nath & Trentham 1997). Observations show that the metallicity of the IGM at $z \sim 3$ was $\sim 10^{-2.5}$ $Z_\odot$ (Songaila & Cowie 1996, Songaila 1997).

Recent studies on galactic outflows at high redshift contend that these winds could also have suppressed galaxy formation in the vicinity, for masses $\leq 10^9$ $M_\odot$, by mass stripping and gas heating (Scannapieco & Broadhurst 2000). They assume spherical shells of winds from dwarf spheroidals at high redshift and find that these outflows could have distorted the microwave background to an extent that is marginally below the current detection limits, with a mean Compton parameter $\sim 10^{-5}$. Thus, distortion of CMB from these outflows can be important and deserves detailed calculations and comparison with distortions from other phenomena.

The rest of this chapter is organized as follows. First, we discuss the motivations for looking at galactic winds. Next, we consider in detail the effect of the outflows from high redshift dwarf spheroidals on the cosmic microwave background. We then study the effect of kinematic SZE and the clustering of parent galaxies in addition to thermal SZE and Poisson distribution of sources. We discuss various properties of the outflows and calculate the angular power spectrum of the CMB distortions caused by the outflows originating at some initial redshift, z_{in}. Finally, we vary this initial redshift and study the dependence of the distortion on it. We find galactic winds to be an important source of secondary distortion of the microwave background at arc minute and sub arc minute scales.

Throughout this chapter, we assume a flat universe with a cosmological constant, with $\Omega_0 = 0.35$, $\Omega_\Lambda = 0.65$ and $h = 0.65$ as our fiducial model.

6.2 Enrichment of the IGM: A motivation for galactic winds

In the hot big bang model, elements of atomic number greater than 2 can only be substantially synthesized after the first stars are formed. These can then be distributed throughout the universe as the stars release the fusion products in stellar winds or supernovae ejecta. Stars can form most efficiently only in dense gas gravitationally bound in galaxies or protogalaxies. Observations,

however, show substantial metal enrichment of the IGM up to high redshifts. From observation of quasar absorption lines (Lyα 'forest' in the spectra of quasars at $z > 2$) one concludes the presence of metals over and above the smoothly fluctuating neutral hydrogen component of the IGM (e.g. Cen et al. 1994, Hernquist et al. 1996). High resolution spectroscopy has identified metal lines (mainly CIV and SiIV) associated with absorbers with column density $N(HI) > 10^{14.5}$ cm^{-2} (Cowie et al. 1995, Songaila & Cowie 1996, Ellison et al. 2000). These lines give useful information of the metallicity on the low density component of the IGM. The observations agree on an inferred metallicity of $Z \sim 10^{-2.5}\, Z_{\odot}$ for $2.5 \lesssim z \lesssim 3.5$ (Songaila & Cowie 1996, Rauch et al. 1997, Songaila 1997, Davé et al. 1998). However, very little is known about the variation and scatter of the metallicity as a function of density.

Since most cosmic metals are formed in stars, a fundamental question arises as to how these metals are finally distributed throughout the IGM. Three possibilities have been considered in the literature: 1) Enriched gas might become unbound during a merger or tidal interaction with another galaxy or by ram-pressure of the IGM on a galaxy (Gnedin & Ostriker 1997, Gnedin 1998, Cen & Ostriker 1999) and thereby pollute the IGM with metals. 2) radiation pressure on dust grains due to stellar light can remove the grains from the galaxy, which can then give metals after being destroyed by thermal sputtering (Ferrara et al. 1990, Aguirre et al. 2000) and 3) enrichment by galactic winds (Dekel & Silk 1986, Metzler & Evrard 1994,1997, Nath & Chiba 1995, Nath & Trentham 1997, Madau et al. 2000). It is this third method of enrichment of the IGM that we focus on in the rest of the chapter.

In all the studies mentioned above it has been seen that galactic winds can distribute metals into IGM far away from where they are formed. The cases where overlapping supernovae bubbles can drive a coherent wind across the galaxy before they cool have been investigated in dwarf galaxies (McLow & Ferrara 1999), elliptical galaxies(David et al. 1990,1991) and starburst spiral galaxies(Heckman et al. 2000). All these wind types described above have some common features : 1) The supernovae energy release is the main source of energy, with some critical supernova rate necessary for the galactic wind to form and blow out. 2) the wind speed initially exceed the escape speed of the parent galaxy, but later the wind is pressure confined at some radius 3) the wind energy is generally tied to the star formation rate and 4)Finally, if the shell swept is massive enough, it can confine the wind from expanding further. Or if the bubble has enough energy, then it can finally get fragmented due to Rayleigh-Taylor instabilities or because of density inhomogeneities in the IGM. These properties are, however, highly dependent on the properties of the IGM and on a better understanding of the energetics of the explosion and detailed physics of the fragmentation processes.

Galactic winds have been observed both locally (*e.g.*, Heckman 1997) and at high redshift (Franx et al. 1997, Pettini et al. 1998). Such winds have also been observed in starbusrt galaxies such as M82 (Lehnert et al. 1999). It is not, however, entirely clear what the efficiency of these outflows is in driving out the gas in the galaxy. Mac Low & Ferrara (1999) have recently shown that efficient blow away occurs only in halos with masses $M \leq 10^7$ $M_\odot$, and that a blowout occurs perpendicular to the disk for $10^8 \leq M \leq 10^9$ $M_\odot$. Their simulations assume a disk geometry. However, it is certain that galactic outflows do occur from other galaxies types as well.

To sum up, galactic winds offer one of the interesting possibilities to explain the enrichment of the metals in the IGM. To do so, they must originate at high redshifts. Due to energy input by the supernovae, the interior of the wind shells is hot and has higher pressure than the ambient medium. This gives us patches in the IGM which are capable of scattering the CMB photons (analogous to the ICM) and can act as an additional source of SZ distortion. This is the main motivation of the study outlined in this chapter.

6.3 Modeling the galactic winds

The evolution of a galactic wind in the IGM is similar to the evolution of a bubble following an explosion. There are a number of analytic solution representing spherically symmetric explosion (see McKee & Ostriker 1977, Weaver et al. 1977, McCray & Kafatos 1987, Ostriker & Mckee, 1988). These solutions mainly look at expanding bubbles in the inter stellar matter and hence neglect the expansion of the universe. For the case of an expanding bubble in the IGM one can no longer neglect the Hubble expansion. For the case of galactic wind, we follow the approach of Tegmark, Silk & Evrard (1993; hereafter TSE). They considered the evolution of the blastwaves with an initial energy input (which stops after $t_{burn} \sim 5 \times 10^7$ yr), which have thin shells sweeping up most of the ambient IGM gas. The shells are assumed to lose a small fraction $f_m = 0.1$ of their mass to the interiors, so that its total mass is given by $m(t) = \frac{4}{3}\pi R(t)^3 (1 - f_m) \rho_{igm}$, where we take the background density to be that of the IGM. Since $\rho_{igm}/\rho_{igm} = -3H$, one gets

$$\frac{\dot{m}}{m} = \left(r^3 \rho_{igm}\right)^{-1} \frac{d}{dt}\left(r^3 \rho_{igm}\right) = 3\left(\frac{\dot{R}}{R} - H\right), \tag{6.1}$$

if $\frac{\dot{R}}{R} > 0$. Otherwise, $\dot{m}/m = 0$. The shell acquires new mass when it expands faster than the Hubble flow, which finally catches up with the shell only at $t \to \infty$. Therefore, we have $\dot{R} > HR$ and $\dot{m} > 0$.

Following TSE, we now calculate the braking force on the shell. The shell must be acceler-

ated from the velocity $H\,R$ to $\dot{R}$ and hence experience the net braking force $\left(\dot{R} - H\,R\right)\dot{m}$. The interior pressure p drives the shell outwards with a force $p\,A = 4\pi r^2 p = 3mp/\rho_{igm}\,R$. Finally, there is the gravitationally braking force which, in our thin shell approximation, is given by $\frac{4}{3}\pi\,m\,G\,R\,(\rho_d + \rho_{igm})$, where ρ_d is the total density.

The thermal energy within the shell can be found from the equation of state for the plasma:

$$E_t = \frac{3}{2}pV = 2\pi\,p\,R^3\,, \tag{6.2}$$

and from energy conservation, we have

$$\frac{d\,E_t}{dt} = L - p\frac{dV}{dt}\,, \tag{6.3}$$

where L incorporates all sources of heating and cooling of the plasma. Adding all these, we obtain the Equation (6.5) (see below).

We assume, as in TSE, that the total mechanical luminosity of the out flow is $L_{sn} \sim 1.2(M_b/M_\odot)L$ where M_b is the baryonic mass of the parent galaxy and $L_\odot$ is the solar luminosity. Since the galactic winds last for $t_{burn} \sim 5 \times 10^7$ yr, the total energy in the galactic wind is $0.02 \times 0.007 \times M_b c^2$. The factor of 0.02 follows from the observations of Heckman, Armus & Miley (1990) who show that approximately 2% of the total luminosity of high redshift starburst galaxies goes into galactic winds. Another empirical observation is that for a solar neighbourhood initial stellar mass function, one has roughly one supernova for every $150\,M_\odot$ of baryons that form stars, with a typical kinematic energy per explosion of the order of 10^{51} ergs. If one assumes the galactic wind to have a constant mechanical luminosity L_{sn} for the duration of t_{burn}, then it can be shown that

$$L_{sn} = \frac{f_{sn}\,M_b\,c^2}{t_{burn}}\,\theta(t_{burn} - t) \sim 1.2(M_b/M_\odot)L_\odot\theta(t_{burn} - t), \tag{6.4}$$

where the efficiency $f_{sn} \approx 4 \times 10^{-6}$, assuming a constant energy release during a period of $t_{burn} \approx 5 \times 10^7$ years.

To determine the baryonic fraction, we can either use the baryonic fraction in clusters, or the baryonic fraction of matter in the diffuse IGM, with $\Omega_b = 0.05$. The latter for a low density universe, with $\Omega_0 = 0.35$ as in our model, corresponds to a baryonic fraction $f_b \sim 0.15$. Also, for clusters, White et al. (1993) has estimated that $f_b \geq 0.009 + 0.05h^{-3/2}$. Adopting the Hubble parameter $h = 0.65$, this gives $f_b \sim 0.1$. For these reasons, in this calculation we assume that $M_b = 0.1\,M$, where M is the total mass. However, we show the results for the assumption $M_b = 0.05\,M$, to show the effect of changes in f_b on the final constraints. Since the mechanical luminosity in this model is proportional to M_b, this will show the effect of changing the efficiency of winds on our results.

We now numerically solve for the radius and velocity of the shell, and the energy and particle density inside the shell. For the radius and velocity of the shells, we use the equation 1 of TSE, that is,

$$\ddot{R} = \frac{8\pi pG}{\Omega_{IGM}H^2R} - \frac{3}{R}(\dot{R} - HR)^2 - (\Omega_d + 0.5\Omega_{IGM})(0.5H^2R)\,. \tag{6.5}$$

Here, Ω_{IGM} is the ratio of the density of the intergalactic gas to the critical density, and Ω_d expresses the total density. We assume that $\Omega_{IGM} = \Omega_b = 0.05$ as constrained by big bang nucleosynthesis (for $h = 0.65$), since at redshift $z \sim 4$–5 most of the baryons are in the IGM (Rauch et al. 1998; Weinberg et al. 1997). The evolution of the total energy inside the shell is given by TSE as,

$$\frac{dE_t}{dt} = L_{sn} - 4\pi pR^2\dot{R} - L_{brem} - L_{comp}. \tag{6.6}$$

Here, the first term refers to the energy input from the galaxy, the second term describes the adiabatic loss, the third term describes the energy loss due to Bremsstrahlung and the last term is the energy loss rate due to inverse Compton scattering off the microwave background photons, which becomes important at high redshifts. L_{brem} is found to be always much smaller than L_{comp}, as was noted by TSE. We have neglected the energy dissipation of the shell due to its collisions with the IGM (which is shown in TSE to be small relative to other losses) to obtain a conservative estimate of the CMB distortion.

If the shells lose a fraction f_m to the interiors, then the particle density inside the shell of radius R evolves as (assuming a uniform density),

$$m\frac{dn}{dt} = f_m\frac{d\rho_{IGM}}{dt} + \frac{3}{R}\frac{dR}{dz}f_m\rho_{IGM}\,, \tag{6.7}$$

where ρ_{igm} is the mass density of the ambient IGM at the given redshift. It is worth noting at this point that the uncertainty in the efficiency of mass loss in galactic outflows, as discussed by Mac Low and Ferrara (1999), is not relevant here, as we assume that the entire mass in and inside the shell is provided by the ambient IGM (from Equation (6.7)); outflows only provide the mechanical energy needed for the wind to expand.

Once we know the density and temperature of the material inside the shell, we can write down the energy loss rate due to Compton cooling as

$$L_{comp} = \frac{4\pi^2}{15}(\sigma_T c n)\left(\frac{k_B T}{m_e c^2}\right)\left(\frac{k_B T_{cmb}}{\hbar c}\right)^4 \hbar c V, \tag{6.8}$$

where T is the temperature of the plasma interior of the shell and $V = \frac{4}{3}\pi R^3$. As has been shown in TSE, Compton cooling takes place on a timescale, $t_{comp} \sim 2 \times 10^{12} \times (1+z)^{-4}$ seconds, and hence is more important than X-Ray cooling at higher redshifts. TSE also takes into account energy loss due to ionization and dissipation. In our case we can neglect the ionization loss since the early supernovae driven winds are expected to expand into an IGM which has already been ionized by the same massive stars which gave rise to the supernovae later (Ferrara, Pettini & Shchekinov 2000). Moreover, as observed by TSE, the dissipational losses are not significant.

For initial conditions, we assume that the initial radius R_i of the shell is the radius of the dwarf spheroidal, which is obtained using the scaling of the optical size of elliptical galaxies with their total mass. We have $R_i = 1.2 \times 10^2 (M/10^{12} M_\odot)^{0.55}$ kpc (Saito 1979, Matteucci & Tornambre 1987). The scaling mentioned above is a useful relation, although its validity has not been updated with more recent data. Our wind solutions, however, do not depend strongly on the value of R_i, and therefore the exact validity of the scaling is not relevant here. The initial velocity is expected to be of the order of the thermal velocity of gas heated to 10^6 K.

With the above equations and initial conditions we calculate for a given initial redshift z_{in}, the wind parameters as functions of the mass of the parent galaxy and redshift, using a fourth order Runge-Kutta technique. We plot in Figure 6.1 the evolution of the radius (in physical coordinates). The electron temperature, the wind velocity and the electron densities are shown in Figures 6.2, 6.3 and 6.4 respectively. The winds are assumed to originate out of galaxies of masses $M = 10^7$ and 10^9 $M_\odot$ for $1 + z_{in} = 9, 11, 13$. We have checked that our results for radius and T_e match with that of Scannapieco & Broadhurst (2000) for similar parameters (their Figure 3).

Although, we have solved the wind evolution numerically, one can try to solve it analytically as well to sufficient accuracy (see TSE, for a detailed discussion). The behaviour of the expanding shell can then be seen to go through three qualitatively different phases representing interplay of a number of different physical effects :

- the initial phase, when gravity and Hubble flow are negligible and the radius is $R \propto t^{3/5}$
- the intermediate phase, when the supernovae explosion stops after 5×10^7 yrs, one gets the pressure driven snowplow phase and $R \propto t^{2/7}$ (for our case with no dissipational loss). This would have been the case in the absence of cooling and Hubble expansion. Cooling and pdV work reduce the pressure and slow down the expansion. One would then get the momentum conserving snowplow phase given by $R \propto t^{1/4}$ in the absence of Hubble expansion and gravity. Also with time, the IGM density drops. This boosts the expansion of the shell.
- At the asymptotically late phase, the shell gets frozen into the Hubble flow and $R \propto t^{2/3}$.

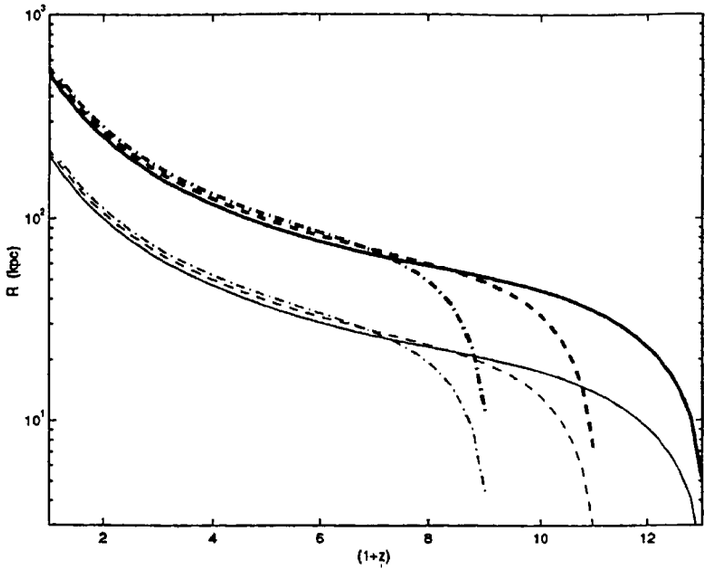

Figure 6.1: The evolution of the wind radius is shown for $(1 + z_{in}) = 9$ (dash-dot), 11 (dash) and 13 (solid line). The thick lines are winds originating from parent galaxy with mass $M = 10^9 M_\odot$ and the thin lines are for $M = 10^7 M_\odot$.

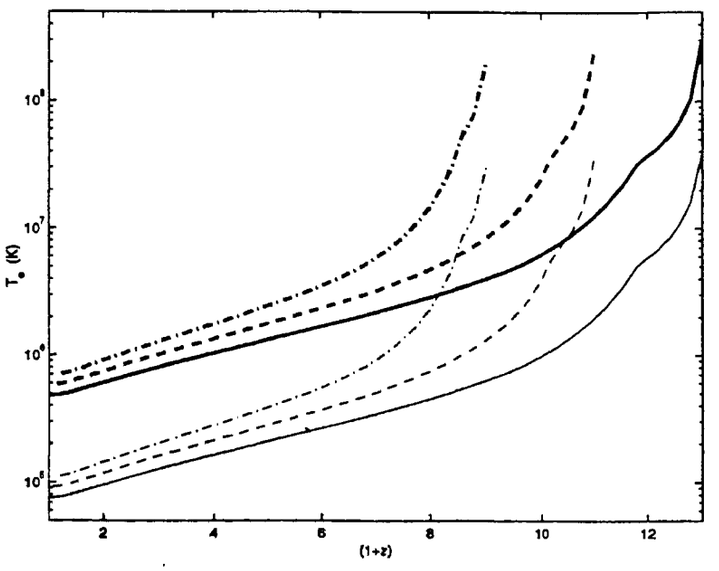

Figure 6.2: Evolution of the electron temperature of the gas inside the shells. Everything else are same as Figure 6.1 .

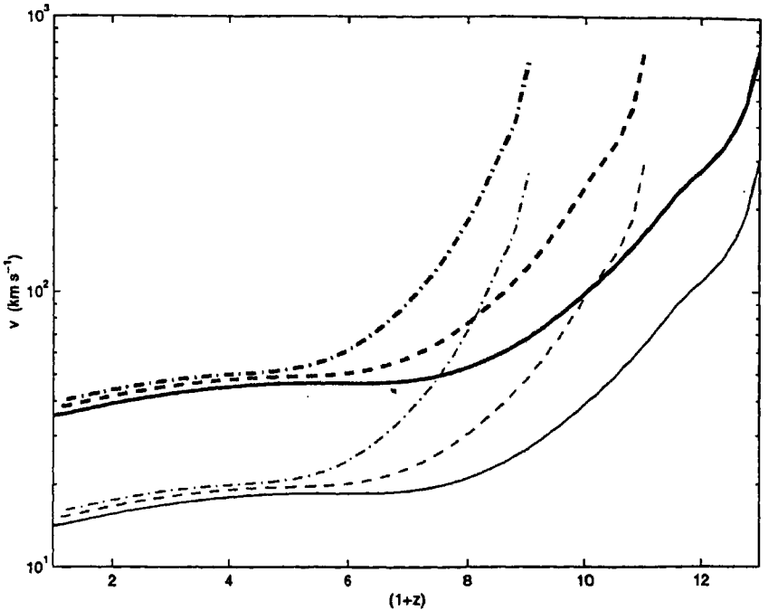

Figure 6.3: Evolution of the wind velocity. Everything else are same as Figure 6.1 .

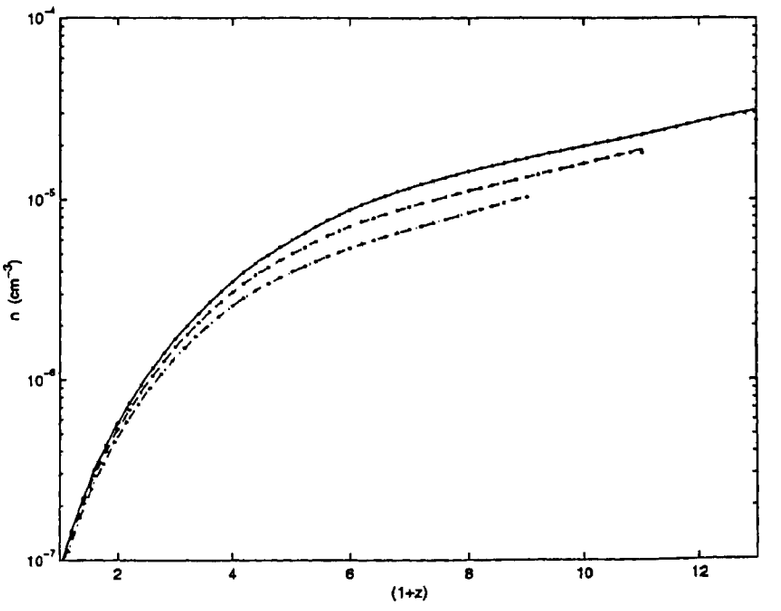

Figure 6.4: Evolution of the electron density of the gas within the shells. Everything else are same as Figure 6.1 .

Once we know how to model the evolution of the galactic wind arising out of the parent galaxy of mass M at some initial redshift z_i, we can go forward and look at an ensemble of galactic winds arising out of a cosmological distribution of galaxies.

6.4 Ensemble of galactic outflows

Although a series of outflows would probably occur in the universe, for simplification and tractability of the calculation, we consider the case of outflows originating at a single epoch, at z_{in}. We consider a large range of values for $3 \leq z_{in} < 15$. This assumption of a single initial epoch of the outflows can be justified to some extent because of the fact that after the first objects of mass of order $\sim 10^8$ $M_\odot$ start shining, the resulting UV background radiation and the winds both inhibit further formation of low mass objects: photons do this by heating up the IGM gas (Thoul & Weinberg 1996), and the outflows, by gas stripping (Ferrara, Pettini & Shchekinov 2000). Therefore, if there were widespread outflows associated with the epoch of first luminous objects with masses of order 10^8 $M_\odot$, it could not have lasted a long time.

We use the results of the previous section to set up an ensemble of galactic outflows from galaxies with masses $5 \times 10^7 \leq M \leq 10^{11}$ $M_\odot$, using the abundance of collapsed objects as predicted by a modified version of the Press-Schechter (PS) mass function given by Sheth and Tormen (1999) which matches N-body simulations well at galactic scales. We assume that the galaxy number density is linearly biased and traces the abundance of collapsed dark matter halos. The lower limit of mass of parent galaxies is motivated by the fact that the first baryonic objects to shine after the initial pause (due to destruction of molecular hydrogen) have virial temperatures of order 10^4 K with corresponding masses of order 5×10^7 $M_\odot$ (Haiman, Rees & Loeb 1997, Scannapieco & Broadhurst 2000). The motivation for upper limit of masses comes from the fact that a blowout seems to be inhibited for masses above $10^{12}(1+z)^{-3/2}\, M_\odot$, as reported by Ferrara, Pettini & Shchekinov (2000). We note, however, that although these limits apply strictly to disk galaxies, we assume them to valid for dwarf spheroidals as well.

The PS mass function essentially calculates the mass function of objects in terms of their collapse redshift z_c. The epoch of galactic winds occur later, and so, in principle, $z_{in} \leq z_c$. The difference between these two redshifts is, however, extremely small. There are two effects that can make z_{in} differ from z_c in principle: the extra time required for cooling and the time for the commencement of the galactic winds. Firstly, the change in the PS formalism due the effect of cooling which comes from replacing $(1+z_c)$ by $(1+z_c)(1+M/M_{cool})^{2/3}$, is negligible here, as $M_{cool} \sim 3.6 \times 10^{11}\, M_\odot$

(Peacock & Heavens 1990) which is larger than the objects considered here. In the above M_{cool} is the minimum mass at which cooling becomes efficient. Moreover, the timescale for the galactic wind to originate from dwarf galaxies is much smaller than a Hubble time at $z \sim 15$ (Nath & Trentham 1997). We, therefore, assume that $z_{in} = z_c$.

As in the previous chapters we use the transfer function of Bardeen et al. (1986) with the shape parameter given by Sugiyama (1995), and the Harrison - Zel'dovich primordial spectrum, to calculate the matter power spectrum $P_m(\mathrm{k})$. The resulting mass variance (σ_8) on scales of $8h^{-1}$ Mpc is normalized to 4-year COBE-DMR data using the fit given by Bunn & White (1997).

Once the objects are distributed in redshifts, we calculate their peculiar velocities with respect to the CMB frame of reference. We have, in the last chapter, already written down the redshift dependence of the peculiar velocity. We present the details below. The velocities are usually assumed to follow a Gaussian (Moscardini et al. 1996, Bahcall et al. 1994, Bahcall & Oh 1996), or Maxwellian distribution (Molnar & Birkinshaw 2000), which is completely defined by its rms value σ_v. For analytical simplicity we assume a mean peculiar velocity for all galaxies for a given redshift and cosmology, which is equal to the rms value σ_v of the distribution.

Following Molnar and Birkinshaw (2000), we assume a Maxwellian for the peculiar velocity distribution. Note, that this is expected if one has a Gaussian initial density field. Thus

$$P(v_r, z)\, dv_r \propto v_r^2 \exp\{-v_r^2/2\sigma_v(z)^2\} dv_r, \tag{6.9}$$

where $\sigma_v(z)$ is the Maxwellian width of the peculiar velocity distribution. The rms peculiar velocity calculated from linear theory, smoothed by a top-hat window function W_R of radius R is then

$$\langle v^2 \rangle_R(z) = H^2(z)\, a^2(z)\, f^2(\Omega_0, \Lambda)\, \sigma_{-1}(R) \quad , \tag{6.10}$$

where $a(z)$ is the scale factor and by definition we have

$$\sigma_j(R) = \frac{1}{2\pi^2} \int_0^\infty k^{2j+2} \tilde{P}(k) W(kR) dk \quad , \tag{6.11}$$

where $\tilde{P}(k)$ is the Fourier transform of the matter power spectrum (see Peebles 1980). For the case of velocity (Equation (6.10)) we have $j = -1$. The velocity factor $f(z) \equiv d\ln\delta/d\ln a$ can be written as

$$f(z) \approx \begin{cases} {\Omega_o}^{0.6}(z) & \Lambda = 0 \\ \Omega_o(z)\left[\frac{5}{2(1+z)D_g(\Omega_0,z)} - \frac{3}{2}\right] & \Lambda = 1 - \Omega_0 \end{cases} \quad , \tag{6.12}$$

where for the universe with cosmological constant $\Omega_o(z)$ and $D_g(z)$ are given by Equations (4.13) and (4.12).

Since we assume that massive objects form at the peaks of the density distribution, the cluster peculiar velocity rms differs from the one expressed above (see Peacock 1999). The bias can be expressed as (Bardeen et al. . 1986)

$$\langle v_r^2\rangle_R(z) = \langle v^2\rangle_R(z)\left[1 - \frac{\sigma_0^4(R)}{\sigma_1^2(R)\sigma_{-1}^2(R)}\right] \tag{6.13}$$

The Maxwellian width in Equation (6.10) is obtained from the rms peculiar velocity by averaging a Maxwellian

$$\langle v_r^2\rangle = \frac{\int_0^\infty v^4 \exp\{-v_r^2/2\sigma_v(z)^2\}dv}{\int_0^\infty v^2 \exp\{-v_r^2/2\sigma_v(z)^2\}dv} = 3\sigma_v^2. \tag{6.14}$$

Next, one expresses σ_v as (Normalization) $\times[H(z)a(z)f(z)]/[H(0)a(0)f(0)]$. The normalization at $z = 0$ is taken to be $v_{r0} = 400$ km s^{-1} for flat models with a cosmological constant (Gramann 1998). But we also show our results with a smaller $v_r(z = 0) = 300$ km s^{-1}. For SCDM and OCDM models one can write σ_v as

$$\sigma_v(\Omega_o, z) = (400\,\mathrm{km\,s^{-1}})\,\Omega_o{}^{0.6}(z)(\Omega_o(1+z) + 1 - \Omega_o)^{1/2}\ , \tag{6.15}$$

whereas for the ΛCDM model it is

$$\sigma_v(\Omega_o, \Omega_\Lambda, z) = 400\mathrm{kms}^{-1}\frac{1+z}{[\Omega_o(1+z)^2 + 1 - \Omega_o]^{1/2}}\frac{D_g(\Omega_o, 0)}{D_g(\Omega_o, z)}\left[\frac{5 - 3(1+z)D_g(\Omega_o, z)}{5 - 3D_g(\Omega_o, 0)}\right]\ . \tag{6.16}$$

In the above formula, $D_g(\Omega_o, z)$ is from Equation (4.12). Given a large number of realizations of a given cosmology, we expect the final result to be close to that obtained from using the mean velocity. Note, that the normalization of the peculiar velocity, though a good match to Gramann (1988) is greater than that quoted by Bahcall & Oh (1996).

6.5 SZ distortion from galactic winds

The hot gas in the interior of the shells is responsible for distorting the microwave background, introducing temperature anisotropies through Sunyaev-Zel'dovich effect. Thermal motion of the

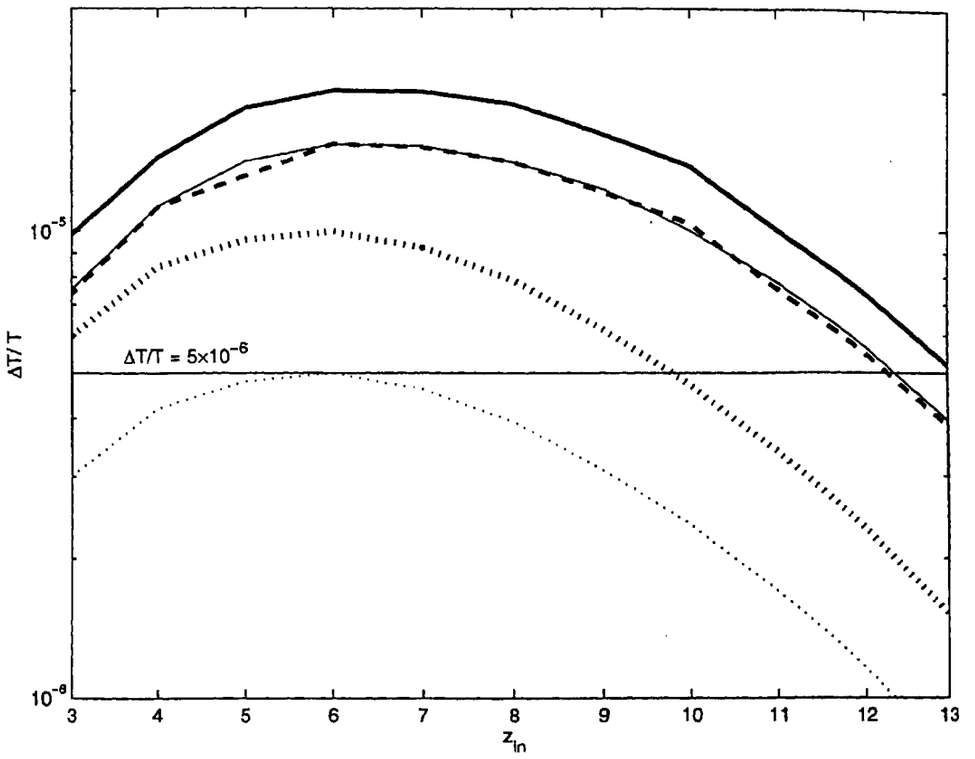

Figure 6.5: The temperature distortion $\frac{\Delta T}{T}$ (in the R-J limit) is plotted against z_{in} for both KSZE and TSZE effect due to winds. The thick solid curve is for KSZE with $v_r(z=0) = 400$ km s^{-1} and the thick dashed curve is for $v_r(z=0) = 300$ km s^{-1}. Both are with $M_b = 0.1M$. The thin solid curve is for KSZE with $v_r(z=0) = 400$ km s^{-1} and $M_b = 0.05M$. The dotted curves are for TSZE with the thick one for $M_b = 0.1M$ and the thin one for $M_b = 0.05M$. A horizontal line with $\frac{\Delta T}{T} = 5 \times 10^{-6}$ is shown for easy reference.

hot plasma heated by the evolving shell give rise to TSZE. This, as discussed in the next section, would turn out to be negligible compared to the kinematic SZE. The KSZE is due to the Doppler shift of the CMB photons due to the shells having a peculiar velocity. The spherical shells have the same peculiar velocities as the parent galaxies since they are accelerated by the same large scale density gradient. For a radial peculiar velocity v_r of the shell (w.r.t the Hubble flow) , the

amplitude of the kinematic SZE is given by

$$\frac{\delta T}{T} = \frac{v_r}{c} \times \int_{-R}^{R} \sigma_T n \, dl \,, \tag{6.17}$$

where n is the density inside the shell given by Equation (6.7) and v_r is ideally drawn from the Maxwellian distribution of peculiar velocities. For simplicity, we assume that the density and temperature inside the shells are uniform. At high redshift, this is a realistic approximation as the sound crossing time is less than the Hubble time. At lower redshifts, this approximation admittedly breaks down to some extent.

We note here once again, that in contrast to the CMB temperature change due to TSZE, the temperature change due to KSZE is independent of frequency (see Chapter 2). Thus one can utilize the different frequency dependence of temperature anisotropy of TSZE and KSZE to separate them out in any observation involving multiple frequencies. We shall use this frequency dependence to show the relative importance of distortion by winds compared to that due to galaxy clusters.

The ratio of the temperature change due to TSZE to that due to KSZE is given by $\frac{k_B T_e}{m_e c^2} / \frac{2v_r}{c}$. It is generally found that larger structures (like clusters of galaxies), which form later, will have a larger thermal SZ effect than kinematic SZ effect, whereas structures going back to high redshifts (like quasar ionized bubbles, black hole seeded proto-galaxies: see Aghanim et al. 1996,2000, Natarajan & Sigurdsson 1998) will have the opposite behaviour. CMB distortions due to galactic winds fall in the second category.

In Chapter 4, we have already introduced the power spectrum of SZ distortions from clusters of galaxies. We use the same technique for SZ distortions from galactic winds as well. We first consider the objects to be Poisson random distributed and consider the correlation between them later. The power spectrum, for distortion from winds, can then be written as

$$C_l^{Poisson} = \int_0^{z_{max}} dz \frac{dV(z)}{dZ} \int_{M_{min}}^{M_{max}} dM \frac{dn(M, z_{in})}{dM} |y_l(M, z)|^2 \quad , \tag{6.18}$$

where $V(z)$ is the comoving volume and dn/dM is the number density of objects. Once again we define the power spectrum, which is independent of frequency, as $C_l = C_l(x)/g^2(x)$, with $g(x)$ given by Equation (2.46) for TSZE. For KSZE $C_l = C_l(x)$. Note that $z_{max} \leq z_{in}$ in our case.

At high z we expect a significant contribution to the anisotropy from correlation among the structures. The clustering angular power spectrum for SZE from winds is

$$C_l^{Clustering} = \int_0^{z_{max}} dz \frac{dV(z)}{dZ} P_m \left[\int_{M_{min}}^{M_{max}} dM \frac{dn(M, z_{in})}{dM} b(M, z_{in}) y_l(M, z) \right]^2 \quad , \tag{6.19}$$

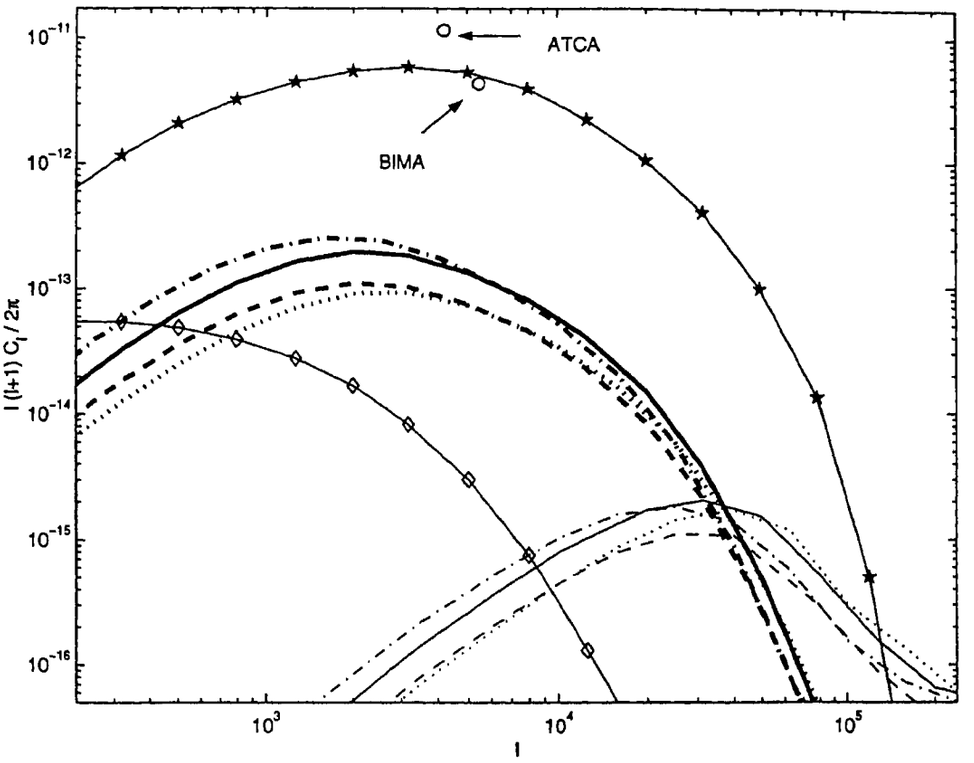

Figure 6.6: Angular Power spectrum due to kinematic SZ effect from winds are shown for different models. The thick lines show clustering power spectrum and the thin lines show Poisson power spectra. The models shown are : (1) $z_{in} = 9, v_r(z = 0) = 400$ km s^{-1} (solid line), (2) $z_{in} = 9, v_r(z = 0) = 300$ km s^{-1} (dashed line), 3) $z_{in} = 7, v_r(z = 0) = 400$ km s^{-1} (dot-dashed line) and $z_{in} = 11, v_r(z = 0) = 400$ km s^{-1} (dotted line). For comparison, Poisson (solid line with stars) and clustering (solid line with squares) spectra from from thermal SZ effect due to galaxy clusters are shown. We have used the same cosmological model as in Komatsu & Kitayama (1999) for comparison (with their figures 1 & 4). The ATCA and BIMA upper limits are also marked in the figure by the two open circles.

where $b(M, z)$ is the time dependent linear bias factor. The matter power spectrum, $P_m(k, z_{in})$, is related to the galaxy correlation function $P_g(k, M1, M2, z_{in})$ through the bias, *i.e.*,

$$P_g(k, M1, M2, z_{in}) = b(M1, z_{in})\, b(M2, z_{in})\, D_g^2(z_{in})\, P_m(k, z = 0) \tag{6.20}$$

where we take $b(M,z)$ to be given by $b(M,z) = (1+0.5/\nu^4)^{0.06-0.02n}(1+(\nu^2-1)/\delta_c)$ (Jing 1999). This expression for the bias factor matches accurately the results of N-body simulation for small halos. This fitting formula for bias does not underestimate the clustering of small halos with $\nu < 1$, and accurately fits simulation results of CDM models and scale-free models. The difference between the fitting formula and the simulation result is generally less than $\sim 15\%$. In the above equation $D_g(z)$ is the linear growth factor of density fluctuation, $\delta_c = 1.68$ and $\nu = \delta_c/\sigma(M)$, and we have utilized Limber approximation (Limber 1954) to set $k = l/r_z$, where r_z is the comoving angular diameter distance.

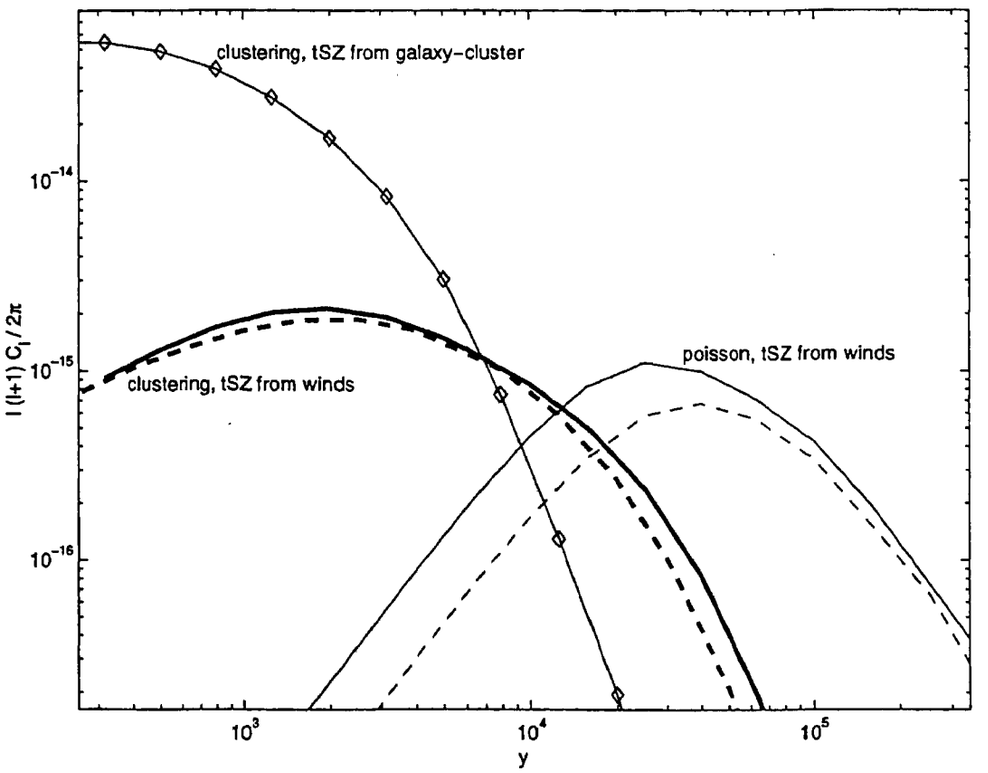

Figure 6.7: Angular Power spectrum due to thermal SZ effect due to winds are shown for different models. The thick lines show clustering power spectrum and the thin lines show Poisson power spectrum. The models shown are : (1)$z_{in} = 9$ (solid line), (2) and $z_{in} = 11$ (dashed line). For comparison, clustering (solid line with squares) spectrum from from thermal SZ effect due to galaxy clusters are shown.

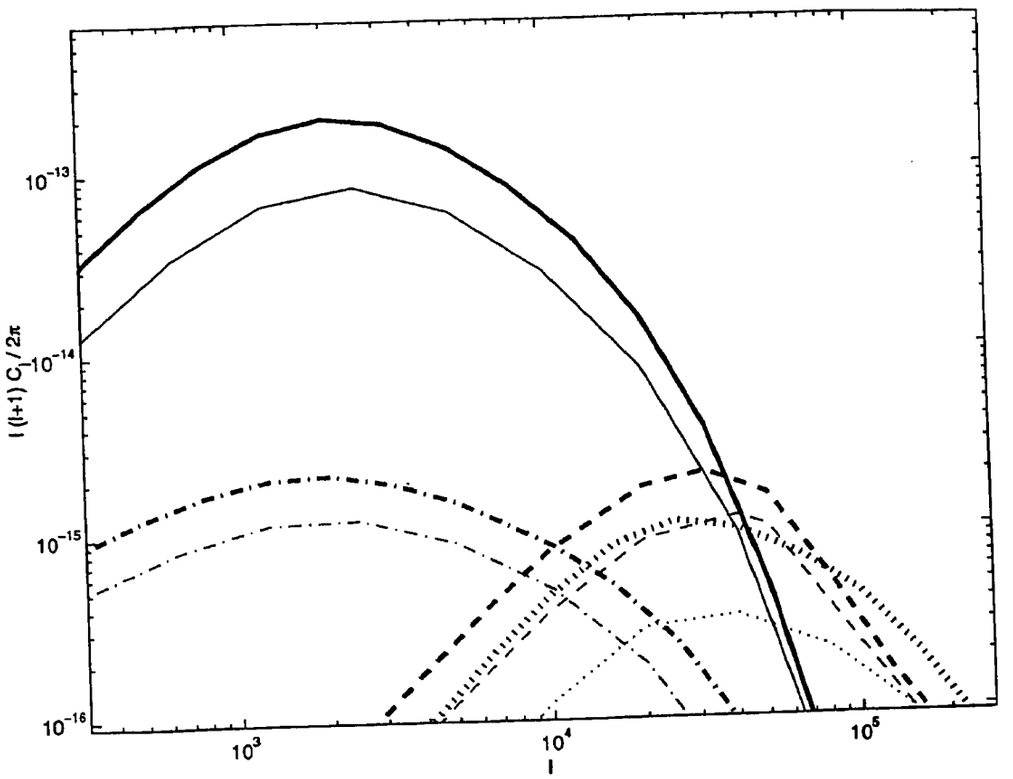

Figure 6.8: A comparison of the power spectrum for the two cases (i) $M_b = 0.1M$ (thick lines) and (ii)$M_b = 0.05M$ (thin lines) is shown, for $z_{in} = 9$ and $v_{r0} = 400$ km s^{-1}. The solid lines refer to clustering spectra due to KSZE; the dashes lines refer to the Poisson spectra for KSZE; the dot-dashed lines refer to the clustering spectra for TSZE ;and the dotted lines refer to the Poisson spectra for TSZE.

6.6 Results and discussions

We plot the mean Compton distortion due to TSZE and temperature distortion due to KSZE as functions of z_{in} in Figure 6.5. As can be seen from the figure, winds originating at redshifts $\sim$ 6-8 distort the CMB more than those which originate relatively earlier or those from more recent epochs. This can be naively understood as follows: the distortion of the CMB due to winds is proportional to the number of galactic winds originating at z_{in}; the distribution of the galaxies follows from the Press-Schecter formalism where the number density per comoving volume peaks

at redshift ~ 5 for the mass range relevant here, and falls off at higher redshifts. This combination produces the maximum distortion at an intermediate value of z_{in}.

We also show in Figure 6.5 our results for the case of $M_b = 0.05\,M$ (thin lines), which represents the case of winds with efficiencies decreased by a factor of two.

Next, we focus on the angular power spectrum of temperature anisotropy from galactic outflows. First, we plot in Figure 6.6 the anisotropy due to kinematic SZ effect from outflows with and without clustering. We plot the power spectra for outflows for three initial redshifts $z_{in} = 7, 9$ and 11. For $z_{in} = 9$, we present the results for $v_r(z = 0) = 400$ and 300 km s^{-1}. We also plot in Figure 6.6 the angular power spectra due to thermal SZ effect from clusters of galaxies, with and without clustering, for comparison.

It is evident from Figure 6.6, that the power spectrum due to clustering of the sources (thick lines) can be very important for CMB distortions due to winds at high redshifts. In comparison, for clusters of galaxies, the Poisson power spectrum is larger than the clustering power spectrum, as shown by Komatsu & Kitayama (1999). In that case, if flux limited clusters detected in X-ray surveys are subtracted, then clustering power spectrum can dominate at $l < 200$. In all the cases that we consider here, however, we find that clustering power spectrum is dominant below $l \sim 3 \times 10^4$. This is easy to understand in the following manner. Since, $C_l^{clustering}/C_l^{Poisson} \sim n(M,z)b^2(M,z)D_g^2(z)P_m(k)$, with $k \sim l/r(z)$, the bias increases at high z along with $r(z)$, thereby boosting up the clustering power spectrum. The evolution of bias with redshift has been studied by many authors both theoretically (Tegmark & Peebles 1998, Valageas, Silk & Schaeffer 2000) and through simulations (Blanton et al. 2000, Davé et al. 1999). All of these studies show that the bias increases rapidly with increasing redshift.

The thick lines in Figure 6.6 also show that the clustering spectra from winds are generally higher than the clustering spectra due to clusters of galaxies above $l \sim 10^3$ in almost all cases we consider. The clustering spectra from winds are, however, in general smaller than the Poissonian spectra due to clusters of galaxies.

The thin lines in Figure 6.6 show that the Poissonian spectra from winds (kinematic SZ) peak at $l \sim 4 - 6 \times 10^4$. Although it is swamped by the thermal SZ signature from galaxy clusters, we note that the frequency dependence of kinematic SZ effect is different from that of the thermal SZ effect. So, it would be possible in principle to separate them out. The above angular scale is an order of magnitude less than the the angular scale at which TSZE due to galaxy cluster peaks. This is beyond the ranges of observations with the upcoming Planck satellite, but is well within the range for ALMA. However, it may well be swamped by other secondary distortions of the CMB at

sub arc-min scales.

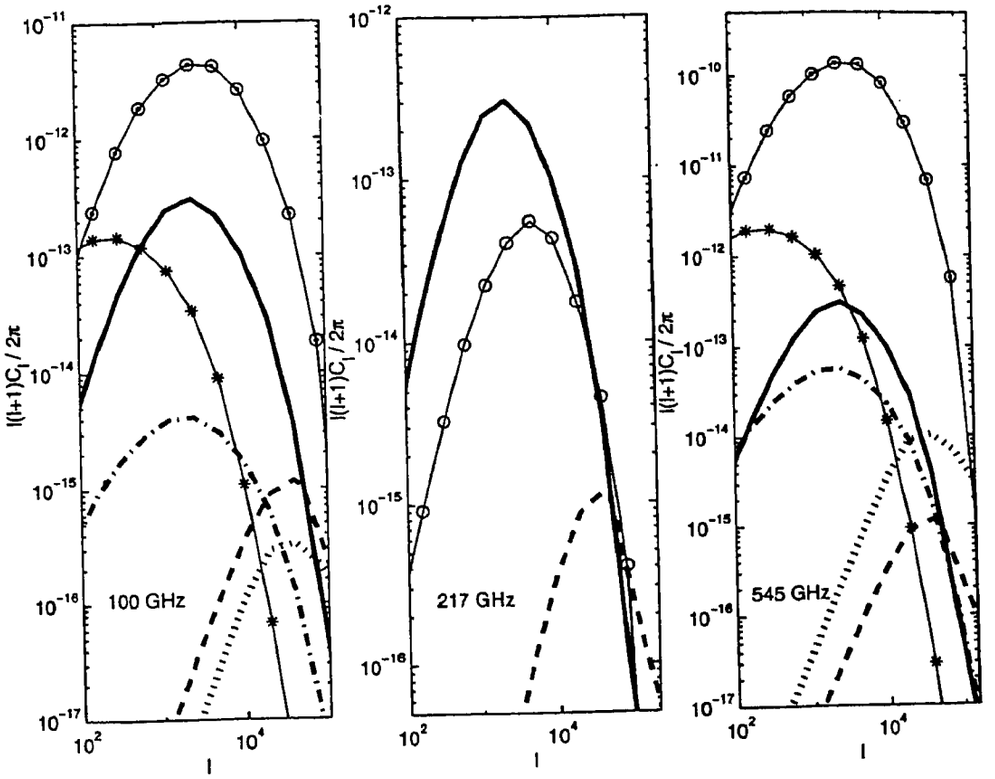

Figure 6.9: The figure shows the power spectrum at different frequencies. The thick lines in all the subplots are due to winds with $z_{in} = 9$; solid lines are for clustering spectra due KSZE with $v_{r,0} = 400$ km s^{-1} and the dashed lines are the Poisson spectra for the same; the dot-dashed lines are for clustering spectra due to TSZE from winds and the dotted lines are the Poisson spectra for the same. For comparison, in the left and the right figures, Poisson spectra for TSZE from clusters (lines with filled circles) and clustering spectra for the same (lines with stars) are shown. In the middle panel, the line with open circle shows the Poisson spectrum due to KSZE from galaxy clusters.

Recently, observational upper limits (shown in Figure 6.6 with open circle) have been put on the arc-minute scale distortion of the CMB temperature anisotropy observed by ATCA (Subrahmanyan et al. 1998) and BIMA (Holzapfel et al. 1999). In the R-J limit $\Delta T_l = T_{CMB}\sqrt{l(l+1)C_l}$. Angular power spectrum from any viable model must satisfy these upper limits in addition to the limit on

the mean y-distortion. In Chapter 4, we have used these limits to constrain cosmological models (Majumdar & Subrahmanyan 2000). None of our wind models, however, violate the ATCA and BIMA limits, and hence cannot be ruled out independent of the violation of COBE limit on y.

The result of the power spectrum due to clustering dominating the anisotropy brings about an interesting possibility to probe bias at high redshift. Komatsu & Kitayama (1999) have noted that a possible detection of the clustering spectrum due to galaxy clusters would give us information on bias at high redshift. In our case, we find that the clustering spectrum due to winds (KSZE) is much larger than the clustering spectrum from galaxy clusters (TSZE), and smaller than the Poissonian spectrum from galaxy clusters (TSZE), for a wide range of l. If the X-ray luminous clusters are removed, then it may be possible to detect the spectrum due to clustering of galaxies having galactic winds. Moreover, the different frequency dependence of kinematic and thermal SZE may allow us to separate these two effects. This may give valuable information about the evolution of bias at high redshifts, although we note that the parameters for the wind shells are not very certain, as we explain below.

We plot the power spectra due to thermal SZ effect from winds in Figure 6.7. As the figure suggests, the thermal SZ effect is much smaller than the kinematic SZ effect in both Poissonian and clustering cases. It is also much smaller than that from clusters of galaxies.

We compare the results with different efficiency of winds in Figure6.8, where we show the results for the cases $M_b = 0.1\,M$ (thick lines) and $M_b = 0.05\,M$ (thin lines). The curves show how a change of a factor of two in the assumption of wind efficiencies would change our results.

In Figure6.9, we have plotted the power spectra for both TSZE and KSZE distortions from winds for three representative frequencies. We show the results for 100, 217 and 545 GHz. These are 3 of the proposed 9 frequencies in which the Planck surveyor satellite mission would operate. The larger two frequencies would have a resolution of about $5'$, and so would be able to go to $l > 2000$. Note that at these l values the primary anisotropy drops and the power spectrum would be dominated by secondary anisotropies. Also, the clustering power spectra due to distortion by winds peak at these angular scales, as evident in Figure 6.6. At 100 GHz and 545 GHz, the effect from TSZE distortion due to clusters of galaxies is greater than that from winds. However, we can take advantage of the crossover in the frequency dependence of TSZE, as given in $g(x)$, where the contribution from TSZE goes to zero. The middle panel in Figure 6.9, shows the spectra at 217 GHz. At this frequency the TSZE from both cluster of galaxies and winds is zero, and we see that the clustering spectra due KSZE from winds exceeds the Poisson spectra from KSZE from galaxy clusters. This difference is further highlighted in Figure 6.10, where we plot the composite spectra (*i.e.*, sum of both Poisson and clustering spectra) for distortion due to galaxy clusters and wind at

217 GHz. It is clear that at this frequency, distortion due to wind peaks at $l \sim 2000 - 3000$ and is an order of magnitude greater than distortion due to galaxy clusters. One can thus hope to be able to detect SZ distortion due to galactic winds at high redshift with Planck. We also note that the anisotropies are likely to be detected and measured in future by the proposed long base line interferometers such as ALMA.

The above results, however, should be viewed in light of the uncertainties inherent in our calculation. Firstly, the parameters of the outflows are by no means certain. The mechanical luminosity of galaxies, for example, is somewhat uncertain. The efficiency of galactic outflows, and its dependence on the mass and redshift, are also not well known. At any rate, the curves in Figure 6.8 give an idea of the magnitude of changes that might occur if some of these assumptions are changed. Lastly, our assumption for a single epoch of galactic outflows might be naive. Also, we have assumed a mean peculiar velocity for all galaxies. Perhaps a simulation with a distribution in z_{in} and v_r would be able to address these issues in a better way.

We also note here that we have neglected the anisotropy caused by the inverse Compton cooling of the shells of outflows. Also, we have not taken into account the heating of the interior gas due to collision of the shell with the IGM. Our estimates of the anisotropy are, therefore, conservative.

Our results, however, seem to be robust with regards to the assumed upper mass limit for the out flowing galaxies, as long as the the upper limit is greater than $\sim 10^9$ $M_\odot$. We note that Scannapieco & Broadhurst (2000) have calculated the upper mass limit of out flowing galaxies in the ΛCDM universe at $z \sim 10$ to be of order 10^9 $M_\odot$. Our results do not change significantly if we assume this upper mass cutoff instead of the one described earlier.

As far as cosmologies other than the ΛCDM are concerned, we found that the resulting anisotropy is less in the case of a SCDM ($\Omega_o = 1, \Lambda = 0, h = 0.5$) universe for a given z_{in}. This is mainly because of the fact that structures form later in SCDM universe although the value of σ_8 is larger in this case, and since the contribution to the distortion in the case of wind is biased towards the high redshift. The anisotropy in the case of the OCDM universe ($\Omega_o = 0.35, \Lambda = 0, h = 0.65$) is slightly less than in the ΛCDM universe. There are two reasons for this: in the OCDM universe, firstly the COBE normalized σ_8 for OCDM is much less than in ΛCDM case, and secondly, peculiar velocities are also smaller at higher redshifts, for a given normalization at the present epoch.

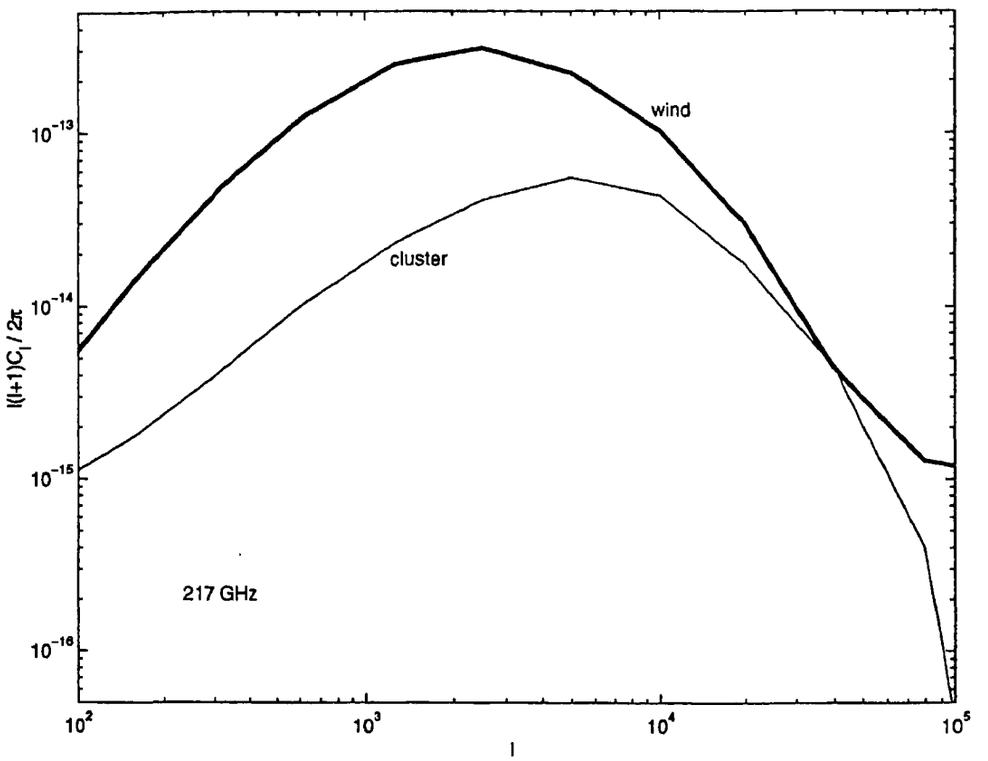

Figure 6.10: The composite power spectra (KSZE+TSZE, including contribution from both clustering and Poisson spectra) are shown for distortion from winds (thick line) and clusters (thin line), $z_{in} = 9$ and $v_{r0} = 400$ km s^{-1}. The spectra are calculated for the proposed Planck observation frequency of 217 GHz.

6.7 Conclusions

After studying in earlier chapters, the distortion of the CMB in the nearby universe due to inverse Compton scattering by the ICM, we have studied in this chapter, the SZ distortion from sources at far away universe. To do so, we have calculated the SZ distortion of the CMB due to galactic winds at high redshift, originating at a single epoch z_{in}, from galaxies of masses between 5×10^7 and 10^{11} $M_\odot$, in a ΛCDM universe. This has led us to probe our universe at redshifts of around $z \sim 10$ (*i.e.*, $\approx$ 10Gpc comoving distance away from us in our fiducial cosmological model, or equivalently when the universe was ≈ 0.035 its present age). We summaries our findings below:

(a) We confirm the previous estimates of the mean y-distortion due to thermal SZ effect. We,

however, found the kinematic SZ effect to be more important than the thermal SZ effect in terms of the effect on the angular power spectrum of distortions.

(b) We obtained the angular power spectrum of distortions with and without clustering of parent galaxies. The Poisson power spectrum due to kinematic SZ effect from winds is found to be comparable or larger than the SZ effect from clusters of galaxies for $l \gtrsim 10^5$.

(c) We found that clustering of low mass galaxies at high redshift could increase the angular power spectrum of distortions. The power spectrum due to clustering of parent galaxies of outflows (kinematic SZ) was found to be also larger than the clustering power spectrum from galaxy clusters (thermal SZ) and somewhat smaller than the Poisson power spectrum from galaxy clusters (thermal SZ). This is opposite to what one finds for galaxy clusters (as in Chapter 5). We have explicitly shown the frequency dependence of the various power spectra. It is possible that the clustering power spectrum from winds can be estimated after subtracting X-ray luminous clusters dominating the Poisson power spectrum from clusters, or by using the different frequency dependence for thermal and kinematic SZ effects, yielding information on bias of low mass galaxies at high redshift.

(d) We have shown how the total power spectra (kinematic and thermal SZ, including both Poisson and clustering effects) for winds will dominate over the corresponding spectra for clusters, at 217 GHz, a proposed frequency for the Planck satellite mission.

We conclude that the SZ distortion from galactic winds at high redshift, if present, could constitute an important source of secondary CMB anisotropy on arc minute and sub-arcminute scales. If discovered, it would help us constrain models of galactic winds and their evolution. In addition, it would give us a new probe of bias at high redshifts (higher or comparable to those probed by the upcoming quasar surveys). Finally, let us comment that starting from $z \lesssim 1$, we have probed redshifts as high as $z \sim 10$. We are now ready to probe the intermediate redshift. This we do in the next chapter where we consider the distortion of the CMB from radio galaxies.

Chapter 7

Probing the intermediate redshifts: SZE from radio galaxies

7.1 Introduction

In our quest to probe our universe from the nearby to the far distant regions, we have looked at cluster of galaxies and then at dwarf galaxies. There are a few other sources, however, containing energetic gas that can distort the CMB, and it is useful to estimate their contribution to the final distortion. Cocoons of radio galaxies, which consist of the energetic particles supplied by the jet (Scheuer 1974, Blandford & Rees 1974, Begelman & Cioffi 1989), is one such source. These radio galaxy cocoons allow us to probe our universe in the intermediate redshifts regions between that probed by dwarf galaxies and galaxy clusters. The present chapter is devoted to studying thermal SZ distortion of the CMB by radio galaxies, *i.e.*,, their cocoons and the shocked gas surrounding the cocoons. A schematic structure of a radio galaxy is shown in Figure 7.1, which is explained in detail in the next section.

We start by addressing a 'confusion' that seems to be present in the literature. Yamada et al. (1999) have investigated the SZ distortion from the population of radio galaxies in the universe and found that the mean y-parameter could be as large as 5×10^{-5}, which is above the limit obtained by COBE. This distortion was calculated using the pressure inside the cocoon and the volume of the cocoon. Since a relativistic non-thermal plasma coming from the hotspot occupies the cocoon, the distortion is due to the non-thermal population of particles. This distortion, as calculated by Yamada et al. (1999), has been referred to as the thermal distortion, although, as explained above,

it is due to the relativistic particles inside the cocoon. Enßlin & Kaiser (2000) have also studied the distortion from the cocoons of radio galaxies. They estimated the thermal distortion from the gas surrounding the cocoons, which is heated as the result of the work done by the cocoons on the surrounding medium, as well as the distortion due to the non-thermal electrons inside the cocoon. They, however, compared their estimate of the thermal distortion (of order 10^{-6}) due to the heated gas surrounding the cocoon with the non-thermal distortion calculated by Yamada et al. (1999). We would like to stress that while calculating the SZ distortion due to radio galaxies, one must pay close attention to the nature of the distortion *i.e.*, non-thermal (from the cocoon) and thermal (from the shocked gas), and estimate both the effects in a self consistent manner.

Enßlin & Kaiser (2000) have pointed out that the energy input rate used by Yamada et al. (1999) is much larger than implied by the observed radio luminosity function. They used a radio luminosity function which yielded a net energy input by radio galaxies that is less (by a factor ~ 50) than that used by Yamada et al. (1999). Assuming that a fraction of $\sim 25\%$ of the the jet luminosity is used in the pdV work on the surrounding gas, Enßlin & Kaiser (2000) estimated that the SZ distortion from the gas heated by the work done by cocoons is of order $\sim 10^{-6}$. They also investigated the distortion from the non-thermal plasma from 'radio ghosts' which are embedded in clusters and found the effect to be very small.

The purpose of the present chapter is three-fold: (1) to calculate the non-thermal SZ distortion using a better model for the evolution of the cocoon than used in Yamada et al. (1999), taking into account various different energy loss processes of a cocoon which were neglected by previous authors; (2) to calculate the thermal SZ distortion from the pdV work done, by summing over the work done by individual cocoons at different redshifts; (3) to investigate the dependence of the distortion on the cosmological model.

There is another reason to study the SZ distortion by radio galaxies. In a recent study, Yamada & Fujita (2001) have used the result of Yamada et al. (1999) to put a upper limit on the redshifts of preheating of clusters in the scenario that radio galaxies provide most of the non-gravitational heating of the cluster gas as required by recent observations (Ponman et al. 1999). Because of the implications of such limits to cosmology and cluster physics, it is worthwhile to do a thorough investigation of the basis of these limits, namely the SZ distortion of CMB due to radio galaxy cocoons

As in the previous chapter, we assume a flat universe with a cosmological constant, with $\Omega_0 = 0.35$, $\Omega_\Lambda = 0.65$ and $h = 0.65$ for our ΛCDM model. For our OCDM, we use $\Omega_0 = 0.35$ and $h = 0.65$. In the next section we start with a brief description of a model of radio galaxy evolution, before proceeding to build an ensemble of radio galaxies and then calculate the resulting distortion

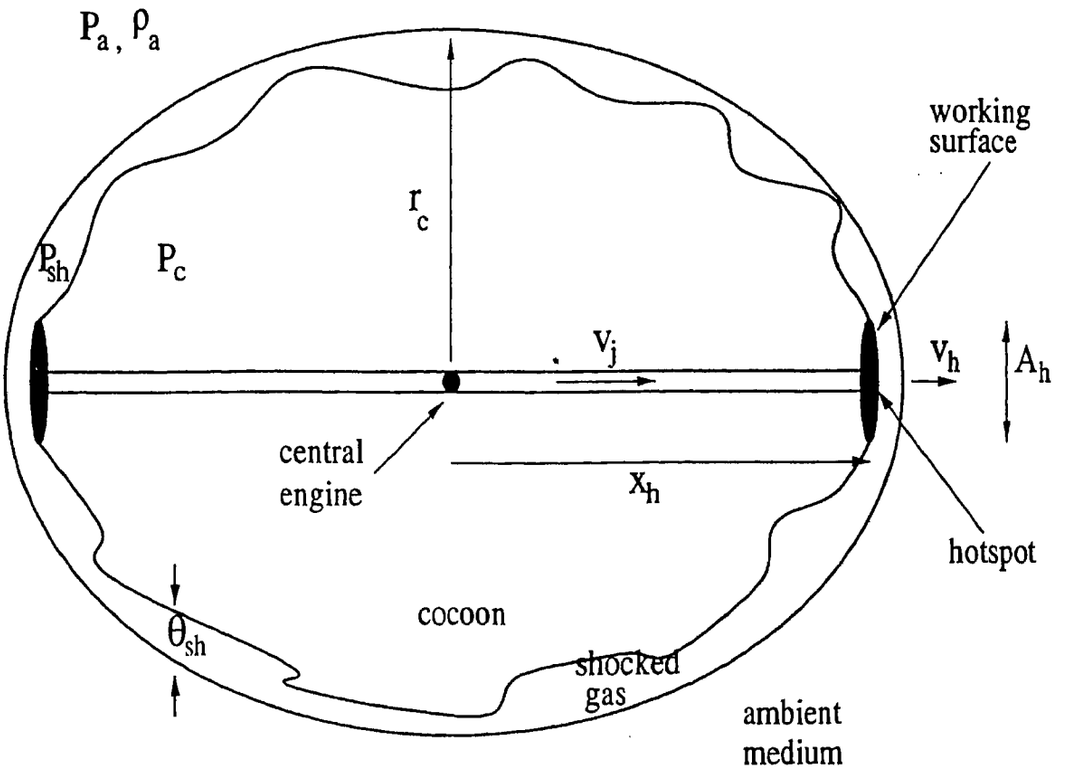

Figure 7.1: A schematic diagram of a radio galaxy

of the CMB from these objects.

7.2 Evolution of radio galaxy cocoons

We model the evolution of cocoons of radio galaxies following the approach of Begelman (1996). This simple model takes into account the fact that the cocoons are mostly over pressured compared to the surrounding medium and that the jet feeding the cocoon jitters in the 'dentist's drill' fashion as envisaged in Scheuer (1982) (see also Begelman & Cioffi (1989); Nath (1995)). Bicknell et al. (1997) modified this model by including the adiabatic expansion of the cocoon plasma (the pdV work done by it). We follow this model, and also include the effect of Hubble expansion, which may become important for large cocoons, say, or giant radio galaxies, of sizes of order of a few Mpc.

A cartoon of a radio galaxy is shown in Figure 7.1. Below we briefly explain the figure. The

jet emanating from the central engine, where the jet material has a speed v_j, produces a hotspot, which moves with a velocity v_h against the pressure of the ambient medium (P_a, with a mass density ρ_a). In the 'dentist's drill' scenario, the direction of the jet changes from time to time to produce a working surface of area A_h. The distance of the hotspot from the central engine is x_h and the transverse size of the cocoon is r_c. The shocked intergalactic gas (inside the shocked region of thickness $\sim \theta_{sh}$) with pressure P_{sh} is separated from the cocoon gas (with pressure P_c) by a contact discontinuity. The cocoon is filled with non-thermal particles, whereas the shocked region is filled with thermal plasma.

In this model, the distance of the hotspot from the central engine is determined by the balance of momentum flux of the jet and the ram pressure of the ambient medium. The transverse size is, however, determined by the pressure of the cocoon. The volume of the cocoon is given by $V_c = \epsilon_p 2\pi r_c^2 x_h$, where ϵ_p is a geometrical factor, which equals 1/3 for a semi-ellipsoidal cocoon, with major and minor axes x_h and r_c respectively. If E_c is the total energy inside the cocoon, then the corresponding pressure is given by $P_c = (1/3)(E_c/V_c)$, assuming a relativistic plasma inside the cocoon. If F_E is the jet luminosity, then one has,

$$\begin{aligned}
\frac{dx_h}{dt} &\sim \left(\frac{\beta_j F_E}{\rho_a c A_h}\right)^{1/2} + H(z)x_h\,, \quad t < t_{\rm life}\,, \\
&\sim \left(\frac{(P_c - P_a)}{\rho_a}\right)^{1/2} + H(z)x_h\,, \quad t > t_{\rm life} \\
\frac{dr_c}{dt} &\sim \left(\frac{(P_c - P_a)}{\rho_a}\right)^{1/2} + H(z)r_c\,, \\
\frac{dE_c}{dt} &\sim F_E - (P_c - P_a)\frac{dV_c}{dt} - L_r\,. \qquad (7.1)
\end{aligned}$$

Here $t_{\rm life}$ is the lifetime of the jet and L_r is the luminosity of the cocoon. The differences between the equations here and those of Bicknell et al. (1997) come from the inclusion of the Hubble expansion in the first two equations, and the loss of energy through radiation. It is, however, extremely difficult to model the radiation energy loss in a simple way. Kaiser et al. (1997) have tried to model the radiation loss as a function of time, in which radiations coming from electrons in different parts of the cocoon are summed over and tracked in time. It would be extremely time consuming for us to follow this procedure here, since we would like to sum over the distortions from an ensemble of cocoons.

We, therefore, use a simple approach to estimate L_r. We assume (as in Daly (1994) and Nath (1995)) that the radio luminosity can be approximately written as $L_r \sim \int_{E1}^{E2} N(E)dEP(E)$, where $N(E)dE \sim N_{tot}(\gamma/\gamma_l)^{-\alpha}d\gamma$ with $\alpha > 0$ is the number of relativistic electrons with energy between E and $E + dE$, and $P(E) \sim 1.6 \times 10^{-15}\gamma^2 B^2$, is the rate of synchrotron loss for a single electron in a magnetic field B and $E1$, $E2$ are the lower and upper energy cutoffs. Here, γ is the Lorentz

factor ($E = \gamma m^e c^2$), γ_l is the lower cutoff in the Lorentz factor and B is the magnetic field. If we assume that most of the cocoon energy is in the form of very lowest energy electrons, then $N_{tot} \sim E_c/(\gamma_l m_e c^2)$.

Enßlin & Kaiser (2000) have demonstrated that even after taking into account different energy loss mechanisms in the radio plasma in the cocoon, the electrons in the cocoon remain relativistic for a cosmological timescale. This means that $\gamma_l \gtrsim 1$. Also, Rawlings & Saunders (1991) found that $\gamma_l \sim 500$ for a 100 kpc size cocoon. Evidently, γ_l is a function of time. But here we simply use two extreme values of γ_l, namely $\gamma_l = 50$, 500, to demonstrate the importance of radiation energy loss in the context of SZ distortion. This prescription gives the radio luminosity at, say 178 MHz, of a cocoon with jet luminosity 10^{45} erg/s at an age of 10^7 yr, of order $\sim 3 \times 10^{28}$ W/Hz for an effective size of $\sim$ 100 kpc, and the luminosity falls to $\sim 10^{25}$ W/Hz when the effective size increases to $\sim$ 1 Mpc. This is comparable to the observed luminosities of radio galaxy cocoons (although usually one uses the distances of the hotspot as the size of the cocoon), as in Kaiser et al. (1997) (*e.g.*, their Figure 1). This lends credence to our simple estimate for the radiation loss from cocoons. We note here that this is still a conservative estimate of the radiation loss, since there is also loss of energy from inverse Compton scattering of the CMBR by the relativistic electrons.

For the ambient medium parameters, we assume (as in Yamada et al. (1999)) those of the intergalactic medium. We assume that the baryon density is given by $\Omega_b \sim 0.015h^{-2}$, given by the Big Bang nucleosynthesis. 1 We assume a temperature of $T_{IGM} \sim 3 \times 10^4$ K, typical for a photo ionized gas. Of course, the temperature does not play much of a role in the evolution of the cocoon as long as it remains over-pressured with respect to the surrounding medium (Nath (1995)). As was pointed out by Nath (1995), for the parameters relevant for the intergalactic medium, radio galaxy cocoons remain over-pressured for cosmological timescales. Also, to make calculations simpler we define an effective radius R_{eff}, such that R_{eff} is the radius of a sphere having the same volume as the volume of the cocoon.

The temperature of the ambient medium becomes important in high pressure regions, since here the pressure inside the cocoon attains similar values of the surrounding medium after a while.

We show in Figure 7.2 & 7.3 the evolution of the effective radius and pressure inside the cocoon with redshift, for the case when the jet is switched on at $(1 + z_{in}) = 14$ and 7. We assume that the jet remains active for $t_{\rm life} = 3 \times 10^7$ yr. In Figure 7.2 we show the evolution of the hot spot distances from the centre (dashed lines), the transverse sizes (dot-dashed lines) and the effective radii (solid lines) in the case in which we include energy loss due to pdV work, Hubble expansion and radiation. For the radiation loss we have assumed a $\gamma_l = 500$. Here, we have assumed an ambient density of Ω_b, a temperature of 3×10^4 K, and a jet luminosity of 10^{45} erg/s. We also

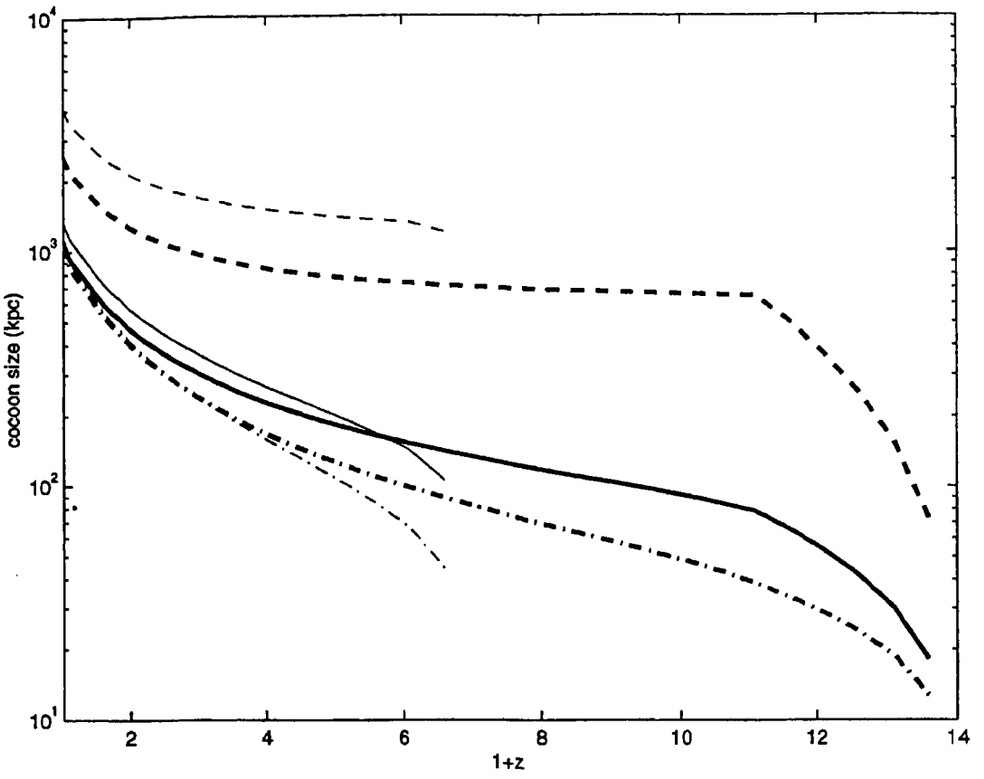

Figure 7.2: The cocoon size is plotted for a single cocoon, in a ΛCDM universe, originating at $(1+z) = 14$ (thick lines) and $(1+z) = 7$ (thin lines), where all the different energy losses are taken. The dashed lines show the hotspot distance from the centre, the dash-dotted line shows the transverse size and the solid line shows the effective radius (explained in the text). For comparison, the effective radius for the case of no energy loss is shown in dotted lines.

show the evolution in the case when no loss of energy is assumed (dotted line). As is clear from Figure 7.2, the loss of energy due to pdV work and radiation loss change the evolution of the cocoon pressure and size substantially.

In Figure 7.3, we show the evolution of the cocoon pressure. The pressure inside the cocoon as calculated here is consistent with the observed values. Subrahmanyan & Saripalli (1993) noted that the pressure inside the cocoons of giant radio galaxies with hotspot distances of $\sim$ 1 Mpc is of order 10^{-14} dynes cm^{-2}. We recover similar values of the pressure for such a cocoons.

We have also calculated the luminosity of the cocoon at different stages of its evolution and

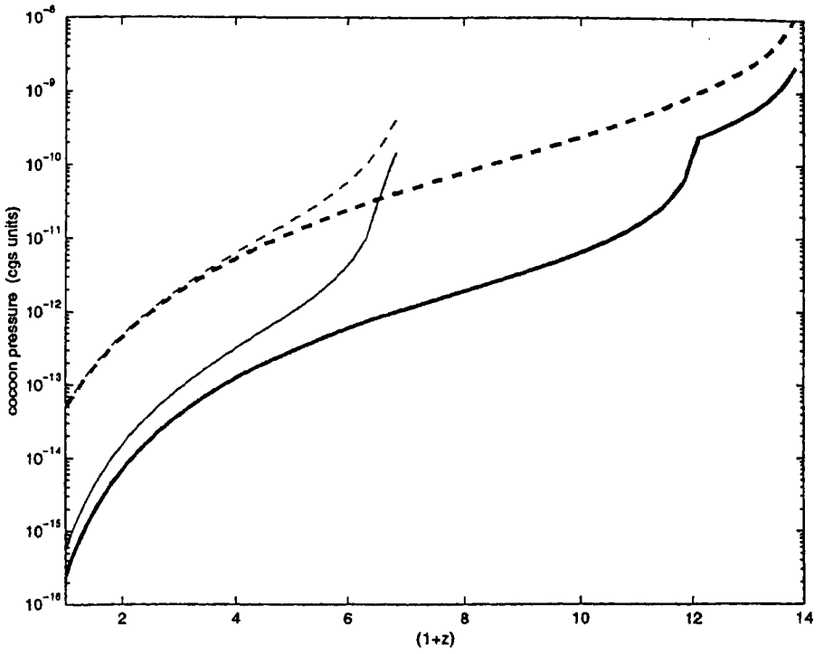

Figure 7.3: The cocoon pressure is plotted for a single cocoon, in a ΛCDM universe, originating at $(1+z) = 14$ (thick lines) and $(1+z) = 7$ (thin lines). The dashed lines are for no energy losses and the solid lines are for the case when all the losses are taken into account.

compared with the typical observed values. We find that for cocoons in the IGM, the luminosity at 178 MHZ is $\sim 3 \times 10^{28}$ W/Hz for an effective size of $\sim$ 100 kpc, and the luminosity falls to $\sim 10^{25}$ W/Hz when the effective size increases to $\sim$ 1 Mpc. This is comparable to the observed luminosities of radio galaxy cocoons as in Kaiser et al. (1997) (e.g., their Figure 1); note, though, that in most studies, the size of the cocoon is usually taken to be the distance of the hotspot from the centre. This lends credence to our simple estimate for the radiation loss from cocoons.

7.3 Ensemble of radio galaxy cocoons

We follow the approach of Yamada et al. (1999) to set up an ensemble of cocoons in the universe. The number density of radio galaxies is computed using the Press-Schechter mass function assuming that radio galaxies reside within halos of mass $M > 10^{12}$ $M_\odot$. Following them, we also assume that a constant fraction $f = 0.01$ of these galaxies has jet activity, and that the jet luminosity

F_E is given by the Eddington luminosity of the central black hole mass M_{BH}, where one uses a scaling $M_{BH} = 0.002 M_{sph}$, where M_{sph} is the mass of the spherical halo of the host galaxy. The jet luminosity is thought to be constant for a typical life time of $t_{\rm life} = 3 \times 10^7$ yr, and is assumed to be zero afterwards.

According to Yamada et al. (1999), the advantage of using the Press-Schechter formalism in counting the radio galaxies is that cocoons which are old and hardly radiate but which still contribute to the SZ distortion, are also included, whereas they are not counted in the observed radio luminosity function as was used by Enßlin & Kaiser (2000). It is difficult to estimate the real advantage of the Press-Schechter formalism in this context, however, since the extent of the population of low luminosity 'radio ghosts' still remains uncertain. We, shall nevertheless, follow the approach of Yamada et al. (1999), to estimate the total energy inputs from all the radio galaxies.

In using the Press Schecter mass function, we have as before used the transfer function given by Bardeen et al. (1986) and the shape parameter by Sugiyama (1995), along with scale invariant initial matter power spectrum. The final power spectra are COBE normalized

As was pointed out by Enßlin & Kaiser (2000), the net energy input rate due to all the radio galaxies calculated using the formalism of Yamada et al. (1999) is larger than that obtained by using the observed radio luminosity functions of radio galaxies. We note here that this is true even for individual radio galaxies. If one assumes a mass cutoff of $\sim 10^{12}$ $M_\odot$ on the radio galaxy mass, then the above prescription gives the minimum jet luminosity of order 2.5×10^{47} erg/s, whereas the typical observed jet luminosity ranges between 10^{44}–10^{46} erg/s (Rawlings & Saunders 1991). Thus, the Yamada et al. (1999) prescription over estimates the total energy input from radio galaxies. We, however, continue to use the parameters used by Yamada et al. (1999) to show the difference in the result we obtain using a better cocoon evolution model from the original Yamada et al. (1999) results. Here, we only note that lowering the jet luminosity of individual cocoons, or the net energy input rate by the radio galaxies, will further decrease the distortion.

7.4 Sunyaev-Zel'dovich distortion from non-thermal plasma

The hot gas in the interior of the cocoon can distort the microwave background, introducing temperature anisotropies. For a single radio cocoon which starts evolving from some initial redshift z_{in} ,the CMB distortion at a lower redshift z can be rewritten as

$$y_{sc}(z_{in}, z) \simeq \frac{\sigma_T}{m_e c^2} P_c(z_{in}, z)\, 2 R_{eff}(z_{in}, z) \tag{7.2}$$

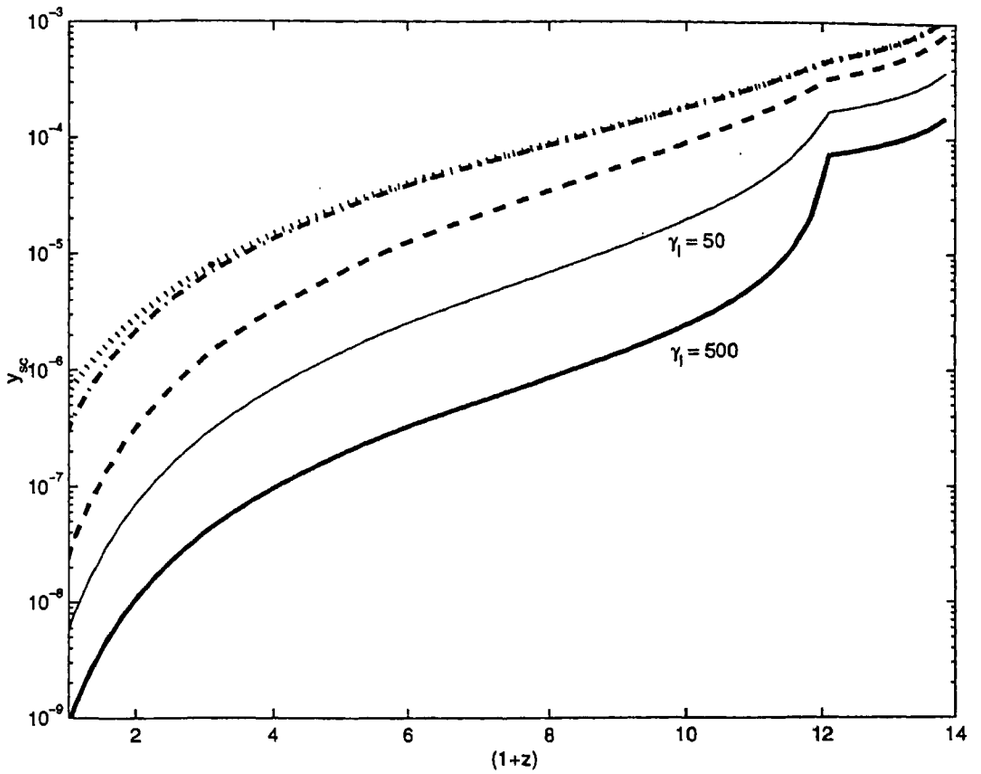

Figure 7.4: The effective y-distortion from a single cocoon originating at $(1 + z_{in}) = 14$ is shown. The effect of different energy losses are shown: dotted line (no loss), dash-dot (including Hubble loss), dashed (Hubble loss + loss due to work done) and solid (all losses including radiation). Thick solid has $\gamma_l = 500$ and thin solid has $\gamma_l = 50$.

where P_c is the non-thermal pressure inside the cocoon. For simplicity, we assume the pressure inside the cocoon to be uniform.

We have shown y_{sc} as a function of redshift in Figure 7.4, for a single cocoon originating at $(1 + z_{in}) = 14$, for the two cases when all the above mentioned loss processes are included (solid lines) and when no losses are assumed (dotted lines). We also show the cases when only Hubble loss is included (dash-dotted lines) and when all loses are taken except radiation loss (dashed line). For the cases, where all th energy losses are included, we show the results for both $\gamma_l = 50$ (thin solid line) and $\gamma_l = 500$ (thick solid line). The dotted line is consistent with the estimate of SZ-distortion by Yamada et al. (1999), as given by their equation (17) (after scaling the jet luminosity to 10^{45}

erg/s as we have used). We, therefore, find that energy loss processes substantially decrease the amount of SZ distortion.

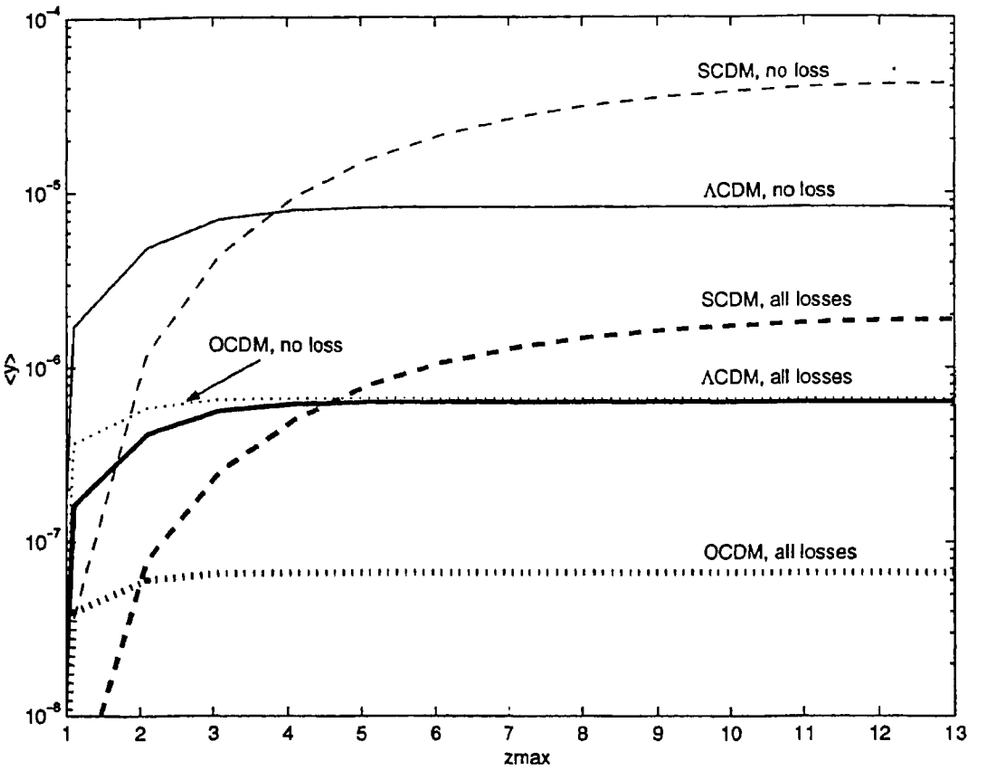

Figure 7.5: The mean y distortion from cocoons of radio galaxies are shown for different cosmological models. The dotted lines are for an OCDM universe, the dashed lines for SCDM and the solid lines for ΛCDM universe. The thin lines correspond to cases when no energy losses are taken and the thick lines are for for cases when all the different energy losses are taken. The 'SCDM, no loss' case has $< y >$ similar to that found in Yamada et al. (1999).

At this point, we note that though the cocoon distorts the CMB through the 'thermal SZE', since the electron population inside the cocoon is non-thermal in nature resulting in SZE which does not have the same spectral dependence of 'standard' thermal SZE which has the crossover frequency at $\sim$ 217 GHz. The effect of the non-thermal population of electrons is to shift the crossover frequency to a slightly higher value. Given the power law index of the electron energy distribution, then one can in principle calculate the spectral dependence of the SZ effect (see Birkinshaw 1999). This can

then be used to separate the SZ distortion due to the cocoon from other sources of thermal SZ effect (for example, from the ICM, if the cocoon resides in a cluster).

To calculate the mean y-distortion from the cocoons, we first have to know the rate of formation of the cocoons. This can be calculated from the PS distribution of the radio galaxy masses as

$$\frac{dn}{dM\,dz} \approx f \frac{d}{dz}\left(\frac{dn}{dM}\right) \tag{7.3}$$

where $f \sim 0.01$ (for a detailed discussion, see Yamada et al. (1999)).

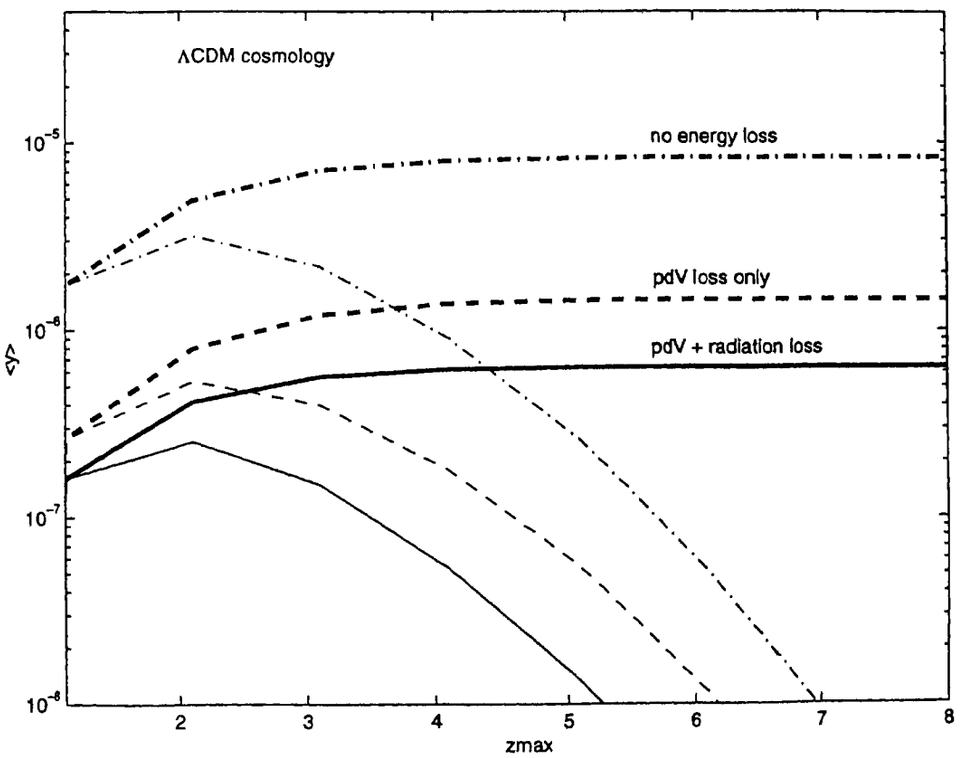

Figure 7.6: The mean y distortion from cocoons of radio galaxies in a ΛCDM universe is shown against the maximum redshift of the occurrence of radio galaxies. The thin lines show the differential contribution to y as a function of z, and the thick lines show the integrated y up to $z(max)$. The different losses taken in each case are mentioned in the figure.

The mean y can then be written as the integral of the product of the CMB distortion from single cocoons, the formation rate of cocoons, the volume element and the crossing probability.

Thus,

$$< y >= \int\int\int y_{sc}(z_{in},\, z)\, \frac{dn}{dM\, dz}(z_{in})\, \frac{dV}{dz}(z)\, \frac{\theta^2}{d\Omega}(z_{in},\, z))\; dz_{in}\, dz\, dM \tag{7.4}$$

Here, θ is the angular diameter of the cocoon and $\frac{\theta^2}{d\Omega}$ is the probability for the line of sight to cross the cocoon, where $d\Omega$ is the solid angle element. In the evaluation of the mean distortion by cocoons, Yamada et al. (1999) have approximated $\frac{dn}{dM\, dz}(z_{in})\, dz_{in}$ by $\frac{dn}{dM}$. We have not made this approximation; instead we explicitly take into account the formation rate of the cocoons as function of redshift z_{in}. Finally, the integration is done for $10^{12}\, M_{\odot} \leq M \leq 10^{14}\, M_{\odot}$ and $0 \leq z \leq 15$. However, there is practically no contribution to the y-distortion after $z \sim 4$.

We show in Figures 7.5 and 7.6 the integrated and differential distortion from the ensemble of cocoons, as a function of the maximum redshift up to which there can be radio galaxy cocoons in the universe. Here we also show the dependence of this distortion on the assumed cosmological model. It is clear that the distortion is largest in the COBE normalized sCDM, which was assumed by Yamada et al. (1999). It is clear that radio galaxies become rare beyond a redshift of ~ 4 and including the contributions of cocoons from higher redshifts do not add substantially to the integrated y-parameter (see Figure 7.6).

Figure 7.7 shows the angular power spectrum of distortion from the cocoons, distributed in a random manner (the Poisson spectrum; thick solid line), and including the clustering of the cocoons (the clustering spectrum, thick dashed line). We compare these power spectra to that from hot gas in clusters of galaxies. It is seen that the distortion from the non-thermal plasma of the cocoons (the Poisson spectrum) peaks at angular scales $l \sim 4000$; note, however, that the amplitude of the spectra are much smaller than those for clusters of galaxies. The power spectrum from the clustering of cocoons peaks at a lower l and is smaller than the Poisson power spectrum.

7.5 Thermal SZ distortion

As pointed out by Enßlin & Kaiser (2000), distortion from the gas heated by the work done by the cocoon can be substantial. This shocked gas in the periphery of the cocoon is separated from the non-thermal plasma inside the cocoon by a contact discontinuity. These authors argued that a fraction of about 1/4 of the total jet luminosity is used in the work done against the surrounding medium. Other authors, however, have come to different conclusions. Bicknell et al. (1997), e.g., found that for a cocoon embedded in a homogeneous medium, this fraction equals 3/8, and for a medium with a density profile of $\rho \propto r^{-2}$, the fraction is 1/2.

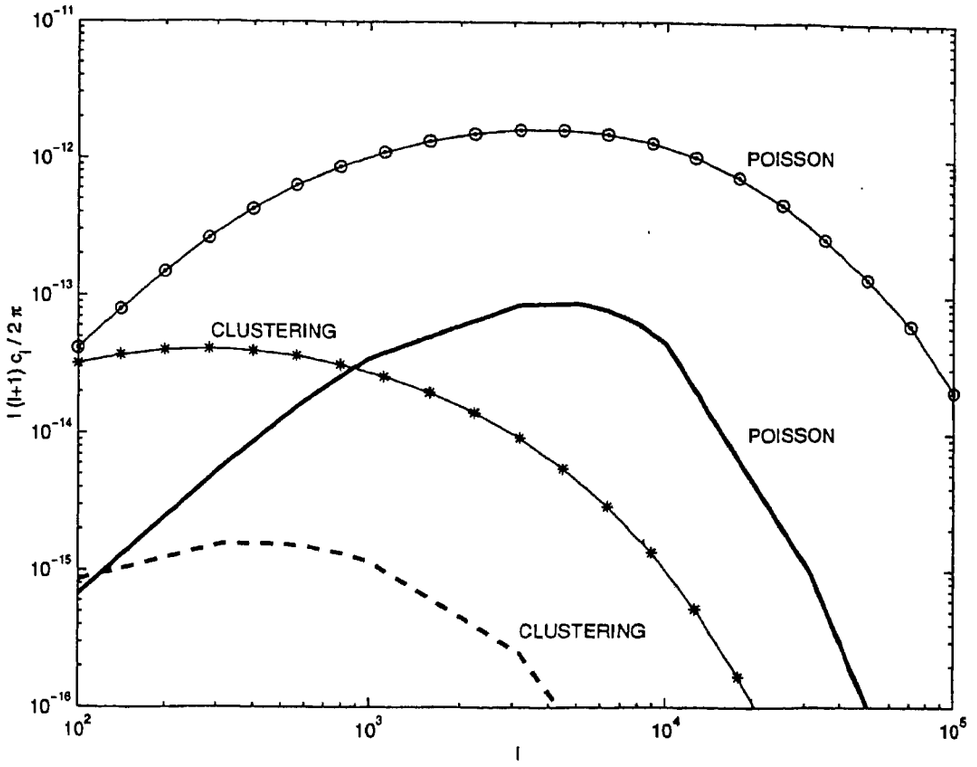

Figure 7.7: The power spectra of TSZE from radio cocoons are shown. The thick solid line shows the Poisson power spectrum and the thick dashed line shows the clustering power spectrum spectrum. For comparison, the corresponding cases for TSZE from galaxy clusters are also shown (thin solid lines with circles and stars, respectively). The underlying cosmology for all the cases is Ω_o =0.35, Ω_Λ =0.65 and h =0.65.

Instead of using any simple estimate, we have calculated the total energy spent by the cocoons in work done against the surrounding medium, using Equations (7.1). The advantage of this calculation is that it is self-consistent with the equations of evolution of the cocoon, which includes the pdV work done against the surrounding medium. In addition, it includes the work done by cocoons that are not included in the radio luminosity function used by Enßlin & Kaiser (2000).

If the total energy contained in the shock heated gas is supplied to the microwave background photons through inverse Compton scattering, then the extra energy density in the photons, red-

shifted to the present epoch, would be given by,

$$\Delta U_0 = \int_{z_{in}=0}^{z_{max}} dz_{in} \int_{z=0}^{z_{in}} dz \int dM \frac{dn}{dz_{in}\, dM} \frac{p\frac{dV}{dz}}{(1+z)^4}\,, \tag{7.5}$$

where we have used the Press-Schechter mass function as in the previous section. The factor of $(1+z)^{-4}$ accounts for the dilution of the energy density in photons due to the expansion of the universe upto the present epoch. This method was used by Enßlin & Kaiser (2000) in their estimate of the distortion from the thermal gas heated by the cocoons.

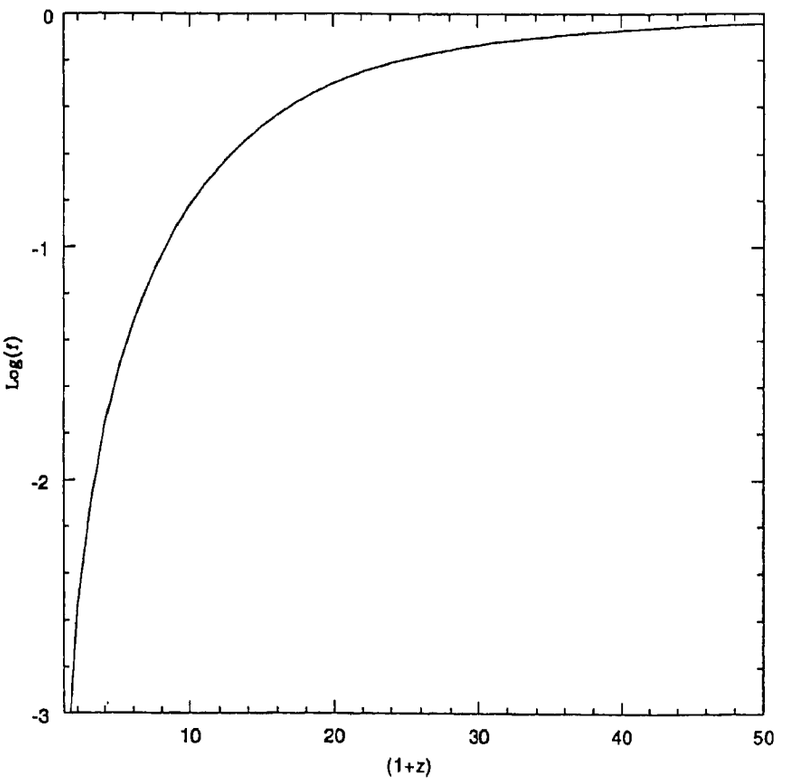

Figure 7.8: The evolution of logarithm of f_{iC} is shown for Λ-CDM cosmology.

We, however, note that energy loss due to inverse Compton scattering is but one of the many mechanisms of energy losses that are relevant for gas in the IGM. Especially, for gas at low redshifts, where most of the energy input from radio galaxies takes place, only a small fraction of its energy is lost to the microwave background photons. The efficiency of energy loss due to inverse Compton

scattering increases with redshift and it becomes the dominant mechanism of energy loss only at very high redshift. At low redshifts, however, one should be careful in calculating the amount of energy supplied to the microwave background photons.

We estimate the efficiency of energy loss due to inverse Compton scattering, f_{iC}, from a simple argument. The most important cooling mechanisms for hot gas in the IGM are adiabatic expansion, Bremsstrahlung and inverse Compton scattering. If their respective cooling timescales are denoted by t_{ad}, t_{ff} and t_{iC}, then one has,

$$f_{iC} \sim \frac{\frac{1}{t_{iC}}}{\frac{1}{t_{ad}} + \frac{1}{t_{ff}} + \frac{1}{t_{iC}}} . \tag{7.6}$$

Here, $t_{ad} = \frac{5}{1+z}(-dt/dz)$, $t_{ff} = \frac{(3/2)k_B}{1.44\times10^{-27}\sqrt{4}\times n_a(z)}$ (n_a is the ambient particle density at redshift z), and $t_{iC} = (45/\pi^2)(\hbar c/kT_\gamma)^4(m_e/\sigma_T\hbar) \sim 9 \times 10^{12}(1+z)^{-4}$ yr (e.g., Tegmark, Silk & Evrard 1993). We show the variation of this efficiency with redshift in Figure 7.8, for a gas at temperature 10^6 K. We have found that the efficiency is an extremely slow function of this temperature, since what determines the efficiency most in Equation (7.6) is the factor t_{ad} and not t_{ff}. We, therefore, treat f_{iC} as a function of redshift, and write $f_{iC}(z)$.

We can now rewrite our previous equation on the energy supplied to the microwave background radiation, including this efficiency factor, as

$$\Delta U_0 = \int_{z_{in}=0}^{z_{max}} dz_{in} \int_{z=0}^{z_{in}} dz \int dM \frac{dn}{dz_{in}\, dM} f_{iC}(z) \frac{p\frac{dV}{dz}}{(1+z)^4} , \tag{7.7}$$

The final y-distortion is then given by,

$$< y >= \frac{1}{4} \frac{\Delta U_0}{a T_{\rm cmb}{}^4} , \tag{7.8}$$

where a is the Stephan's constant and $T_{\rm cmb}$ is the present day temperature of the microwave background.

We have calculated the y-distortion in the ΛCDM universe (using Equations (7.7) and (7.8)) to be $\sim 5 \times 10^{-8}$.

This assumes the same scaling of the jet luminosity with the halo mass as in Yamada et al. (1999). As mentioned above, this scaling probably suffers from an over estimation of the jet luminosity of individual jets and the net energy input rate by radio galaxies. We estimate the net energy input rate (in a ΛCDM universe) to be $\sim 5 \times 10^{67}$ erg Gpc^{-3}, whereas Enßlin & Kaiser (2000) estimated the net energy input rate from the radio luminosity function used by them to be 10^{66} erg Gpc^{-3}. If the net energy input rate is indeed as small as this value, then we estimate that the thermal SZ distortion will be $\sim 10^{-9}$. This is almost three orders of magnitude smaller than the simple estimate of Enßlin & Kaiser (2000).

7.6 Distortion from cocoons in clusters

The results mentioned above assume that the medium surrounding the cocoon has the parameters of the intergalactic medium, with density given by Ω_b and temperature of 3×10^4 K. Most observed radio galaxies, however, reside in galaxy clusters, where the surrounding medium (the ICM) has much higher pressure. To compute the SZ distortion from cocoons in clusters one would have to use the probability of finding a radio galaxy in a cluster, which would be a function of masses (of radio galaxies and clusters) and time, and the cosmological model. One would also have to assume a model for the evolution of the ICM, and also take into account the spatial distribution of radio galaxies in clusters.

Here, we attempt to estimate from simple arguments the relative contribution to the y-distortion from radio galaxies in clusters and field radio galaxies. First, let us look at the y-distortion from individual cocoons inside the intra-cluster medium. We show in Figure 7.9, the evolution of a cocoon (with jet luminosity of 10^{45} erg/s and a lifetime of 3×10^7 yr), in a medium with density of $n \sim 10^{-3}$ cm^{-3} and $T \sim 10^8$ K, which we assume to be constant. The figure shows that although the size of the cocoon is much smaller compared to a cocoon in the intergalactic medium, the pressure inside the cocoon is much larger. This results in the y-distortion from a cocoon being much larger in the case of a cluster-cocoon compared to a field cocoon. The pressure, however, remains higher than the surrounding (ICM) pressure only for about 10^8 yr (irrespective of the redshift when the jet starts), after which it attains a pressure similar to that outside. It is difficult to determine the evolution of the cocoon, without computing the diffusion timescale among other things, to determine the timescale over which the cocoon would retain its identity. For simplicity, we assume that the cocoon does not contribute to any extra SZ distortion, in addition to the usual SZ distortion from the thermal gas in the ICM, after it attains the ICM pressure. This is in contrast to the case of cocoons in the IGM, where the cocoon remain over-pressured over an effective lifetime much longer than the jet lifetime and hence can continue to distort the CMB for a long time.

From Figure 7.9, we can see that the y-distortion of a cocoon in ICM is of order 10^{-4}, approximately an order of magnitude larger than in the case of a cocoon in the IGM. Cocoons in clusters are, therefore, good candidates for looking for SZ distortion from radio galaxy cocoons, although the small angular size of the cocoon can make the detection very difficult.

Secondly, one should compare the number densities of radio galaxies inside and outside clusters to estimate the relative contribution to the mean SZ distortion. We assume the masses of clusters to range between 10^{14}–10^{16} M$_\odot$. One can then calculate the total number of clusters up to a maximum redshift z_{max}. If we then assume that each cluster can have approximately 10 radio

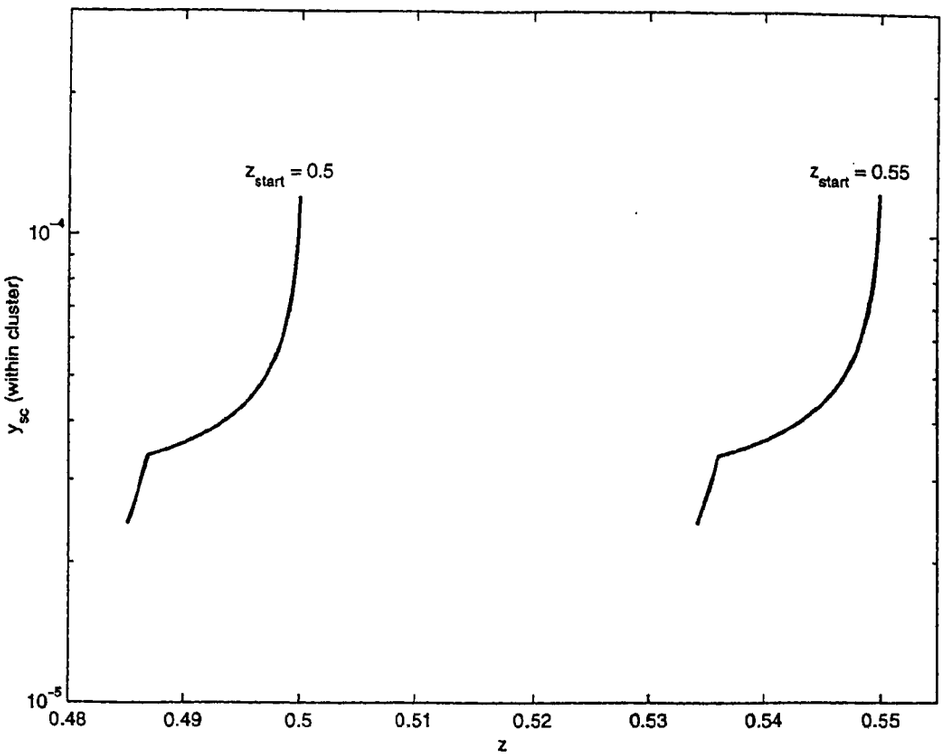

Figure 7.9: The evolution of the y-distortion of cocoons embedded in the ICM (with $n = 10^{-3}$ cm^{-3} and $T = 10^8$ K) is shown for two cases of cocoons originating at $1 + z = 1.5$ and 1.55. The lifetime of the jet is 3×10^7 yr in both cases, which shows up as a kink in the evolution. The cocoon then attains similar pressure as outside, which marks the end of the evolution in this plot. The period between the epoch of z_{start} and that of attainment of pressure equilibrium is of order $\sim 10^8$ years.

galaxies (as in, e.g., Berezinsky et al. 1997), then we can estimate the total number of radio galaxies in clusters. We can then estimate the mean y-distortion from cocoons in clusters. We have found this to be of order $\sim 5 \times 10^{-6}$, for a ΛCDM universe. This is an order of magnitude larger than the distortion from cocoons in the IGM, but still short of the COBE limit. In doing this estimate, we have used similar jet luminosities as for radio galaxies in the IGM. At this point, we would like to emphasize once again that the jet luminosities used are larger than the observed jet luminosities, and decreasing the assumed jet luminosity will further reduce the contribution

towards the CMB distortion by cocoons in clusters.

7.7 Preheating of the ICM by radio galaxies ?

Recently, Fujita (2000) and Yamada & Fujita (2000) have used the SZ distortion from radio galaxies in clusters to put an upper limit on the redshift of heating by radio galaxies. Observations show that the properties of the ICM are different from that expected from scaling arguments of self-similar gravitational collapse (e.g., Ponman et al. (1999) and references within). This has led to the idea of non-gravitational heating of the ICM from different sources, such as supernovae driven winds (Valageas & Silk 1999, Wu, Fabian & Nulsen 1999) and AGNs (Fujita 2000). The radio galaxies which are supposed to heat up the ICM would also distort the CMBR through SZ effect, and Yamada & Fujita (2000) use the results of Yamada et al. (1999) to put a constrain on the epoch of heating to be $z \lesssim 3$. This is in contradiction to the scenario in which the ICM is preheated, before the formation of the cluster. They, therefore, rule out the preheating scenario based on their limits.

From our estimate of the y-distortion of cocoons in clusters, with $y \sim 5 \times 10^{-6}$, it is however difficult to put any constraint on the energy input epoch as it does not violate the COBE limit. If clusters of galaxies each harbour more than ~ 30 radio galaxies (which seems unlikely, see *e.g.*, Berezinsky et al. 1997), only then the y-distortion from radio galaxies would violate the COBE limit. We, therefore, believe that the constraints put by Yamada & Fujita (2000) on the preheating redshift is premature.

7.8 Conclusions

We summaries, below, the work presented in this chapter:

- We have calculated the non-thermal SZ distortion from cocoons using a model of the evolution of the cocoon which takes into account loss of energy due to the work done against the ambient medium, radiation loss and the Hubble expansion. Using the scaling of the jet luminosity with the halo mass as in Yamada et al. (1999), we find that the final y-parameter is 6×10^{-7} in a ΛCDM universe. In a sCDM universe the distortion amounts to $y \sim 2 \times 10^{-6}$, compared to $y \sim 5 \times 10^{-5}$ as claimed by Yamada et al. (1999).

- We have calculated the power spectrum of anisotropy from the cocoons. The Poisson power spectrum peaks at $l \sim 4000$ with an amplitude much smaller than that of hot gas in the

clusters.

- If the net energy input rate is decreased by a factor of ~ 50, to be consistent with that implied by the observed radio luminosity function, then the distortion should be smaller by a similar factor. Also, if the jets are made of protons, and not electron-positrons, then the distortion will be smaller than our results here.

- We have also calculated, instead of using simple estimates, the thermal SZ distortion from gas heated due to the work done by cocoons. We have self-consistently included in our calculations the energy spent by cocoons on the ambient medium. We have then calculated the fraction of energy in the hot gas that is supplied to the microwave background photons through inverse Compton scattering, and calculated the final y-distortion. We find that the final y-parameter is 5×10^{-8} for a ΛCDM universe, using a population of radio galaxies as in Yamada et al. (1999). Decreasing the energy input rate by a factor ~ 50, will decrease the distortion to $y \sim 10^{-9}$, which is smaller than the earlier simple estimate by Enßlin & Kaiser (2000) by a factor $\sim 10^{-3}$.

- We have also estimated the distortion caused by cocoons embedded in the intra-cluster medium. For individual cocoons, we have found that the distortion could be as large as $y \sim 10^{-4}$, and have estimated that the population of cocoons in clusters could contribute to a mean y distortion of order $\sim 5 \times 10^{-6}$.

- Our refined calculation shows that the limits used by Yamada & Fujita (2001) to constrain the preheating redshift is premature.

With the above conclusion, we come to the end of the list of the main results to be reported in this thesis. We started with SZ distortions from clusters of galaxies at low redshifts and then studied distortions of the CMB by galactic winds at high redshifts. In this chapter we looked the intermediate redshift by estimating the distortion of the CMB by radio galaxies. Thus, we have probed different important sources of CMB distortions due to SZE from the present up to the time when the universe was approximately one percent of its present age.

Chapter 8

Epilogue

In the last seven chapters, we have used Sunyaev-Zel'dovich effect as a probe of the universe from the present epoch to redshift $z \lesssim 15$. To cover this wide range in redshifts, we have looked at SZE from different sources: the intra-cluster medium, the intergalactic medium energized by galactic winds, and cocoons of radio galaxies and shocked IGM around them. With these we have probed the underlying cosmology, the ICM, evolution of bias, specific physics of radio galaxies and so on. An overall conclusion to the work presented in the thesis is given below.

8.1 A summary of the results

The main new results obtained in this thesis are the following:

- We have looked at the reliability of estimation of H_o using SZE coupled with X-Ray observations and have pointed out a long list of uncertainties that can bias the estimation of H_o . We found cooling flows in clusters of galaxies to be a new and major source of error, which can lead to an over-estimation of H_o by greater than 10 % even when 80 % of the cooling flow region is neglected.
- Based on comparison of the rms temperature anisotropy obtained from simulated maps of SZ distortion with the ATCA limits on arc-minute scale temperature fluctuations, we have concluded that COBE-normalized CDM models of the universe with a high density parameter ($\Omega_o > 0.8$) can be ruled out. This constraint on the cosmology is independent of any present epoch measures of σ_8.
- We tried to understand the shape and the amplitude of the Sunyaev-Zel'dovich effect power

spectrum due to TSZE from galaxy clusters. Using the resultant power spectrum for different cosmological models and observational upper limits on small angular scale temperature anisotropy from ATCA and BIMA experiments, we have been able to constrain cosmological models. we have, then, shown the position of the peak of the power spectrum to bear a strong discriminatory signature of different gas mass fraction models

- We have calculated the SZ distortion of the CMB due to galactic winds at high redshifts and confirmed the previous estimates of the mean y-distortion due to thermal SZ effect. We, however, found the kinetic SZ effect to be more important than the thermal SZ effect. We found that clustering of low mass galaxies at high redshift could increase the angular power spectrum of distortions. We have shown how the total power spectra (kinetic and thermal SZ, including both Poisson and clustering effects) for winds will dominate over the corresponding spectra for clusters, at 217 GHz. Finally, we speculate that a possible detection of the power spectrum due SZE from winds can yield important information on bias at high redshifts.

- We have calculated the non-thermal SZ distortion from radio cocoons and estimated the final y-parameter to be $\sim 6 \times 10^{-7}$ in a ΛCDM universe. We found the the resultant Poisson power spectrum to peak at $l \sim 4000$ with an amplitude much smaller than that due hot gas in the clusters. We also estimated the thermal SZ distortion from gas heated by the work done by cocoons which was found to be $\sim 5 \times 10^{-8}$. For cocoons embedded in clusters, we found he distortion could be as large as $y \sim 10^{-4}$, and have estimated that the population of cocoons in clusters could give a mean y distortion of order $\sim 5 \times 10^{-6}$.

8.2 Future prospects

As we have noted earlier, in the near future, important improvements are like to occur in the spectral measurements of the SZE and in interferometric mapping of clusters using optimized interferometers. The first would be used to separate the KSZE from the TSZE for galaxy clusters and hence to set limits on the peculiar velocities of galaxy clusters which can in turn give us an idea of the underlying density field. The latter would be used for improved estimations of the Hubble constant and the gas mass fraction of galaxy clusters. Moreover, interferometer arrays would be used to measure the CMB distortions at small angular scales.

SZ surveys would be coming of age in the next few years, with the launch of satellite missions such as MAP and Planck and also dedicated ground based observational facilities like AmiBA. With good sensitivity, clusters could be selected without orientation-bias, and statistical interpretation

of SZE data for garnering information on specific cluster properties and cosmological parameters would become feasible. For example, it will possible to reduce the uncertainties in estimation of H_o coming due to non-sphericity of the clusters. Also, it will possible to constrain Ω_o by studying the integrated (and redshift dependent) number densities of clusters detected through SZE. Finally, cross-correlating CMB maps with X-ray and weak lensing maps would help to map the luminous matter distribution, along with its bias, in the universe. For targeted cluster studies, a cross-correlation of SZ and X-Ray observations would give us knowledge of the intra-cluster gas and its temperature distribution.

In this thesis, we have not dealt at all with polarization of the CMB due to scattering of the electrons causing the secondary anisotropies (Audit & Simmons, 1998; Sazonov & Sunyaev, 1999). Polarization is generated through Thomson scattering of quadrupole anisotropies. For clusters of galaxies, the polarization is proportional to the square of the transverse velocity of the clusters. Hence, it is weaker than KSZE. It has been shown (Audit & Simmons, 1998) that polarization has a strong frequency dependence and so for some clusters, at least, it should be detectable. This measurement, along with that of KSZE, would then give us the vectorial velocity of the cluster. Other than clusters, quasars outflows have also been argued to give rise to polarization signal (Natarajan & Sigurdsson, 1999). Along with temperature anisotropies, polarization studies would also provide an important probe of secondary CMB distortions.

Finally, before we end, we mention that in addition to the sources that we have studied in this thesis, there are several other possible astrophysical objects and/or systems which may, in principle, contribute to CMB anisotropies through SZE. A partial list includes SZ distortions from quasar outflows or from quasar ionized bubbles; from Lyman-α forests; from proto-galactic outflows etc. Other related sources of secondary CMB distortions would be from Reese-Sciama effect from transverse motions of clusters of galaxies; from the so called Vishniac effect and from gravitational lensing of secondary anisotropies. Study of the angular power spectra and and higher order statistics (like skewness etc) of the CMB anisotropy due to this 'zoo' of sources would give us new handles on the physics of astrophysical objects and would provide added constraints on cosmological models.

Thus, as far as the subject of secondary CMB anisotropies is concerned, the future looks exciting indeed.

Bibliography

[1] Abell, G.O., 1958, ApJS, 3, 211

[2] Aghanim, N., Désert, F.X., Puget, J.L., & Gispert, R., 1996, A&A, 311, 1

[3] Aghanim, N., De Luca, A., Bouchet, F. R., Gispert, R. & Puget, J. L., 1997, A& A, 325, 9

[4] Aghanim, N., Balland, C., & Silk, J., 2000, A&A, 357, 1

[5] Aguirre, A., Hernquist, L., Weinberg, D., Katz, N. & Gardner, J. 2000, (astro-ph/0006345)

[6] Allen, S. W., & Fabian, A., 1998, MNRAS, 297, L57

[7] Allen, S. W., Fabian, A. C., Johnstone, R. M., Arnaud, K. A., & Nulsen, P. E. J., 1999 : astro-ph/9910188

[8] Allen, S. W., 2000 : astro-ph/0002506

[9] Atrio-Barandela, F. & Mucket, J. P. 1999, APJ, 515, 465

[10] Audit, E., & Simmons, J. F. L., 1998, astro-ph/9812310

[11] Bahcall, N. A., Cen, r. & Gramann, M., 1994, ApJ, 430, L13

[12] Bahcall N. A. & Oh, S. P., 1996, ApJ, 462, L49

[13] Barbosa, D., Bartlett, J. G., Blanchard, A. & Oukbir, J., 1996, astro-ph/9607036

[14] Barbosa D., Bartlett J. G., Blanchard A., Oukbir J., 1997, in : Microwave Background Anisotropies, Proceedings of XIV Moriond Astrophysics Meetings, ed: Bouchet F., Gispert R., Guiderdoni B., Jean Tran Thanh Van

[15] Barbosa, D., Bartlett, J. G., Blanchard, A. & Oukbir, J., 1996, A & A, 314, 13

[16] Bardeen, J. M., Bond, J. R.,Kaisaer, N. & Szalay, A. S., 1986 ApJ, 304. 15

[17] Bartlett, J. G. & Silk, J., 1994, ApJ, 423, 12

[18] Bartlett J. G., 1997 in: From Quantum Fluctuations to Cosmological Structures, School held in Casablanca, ed Valls-Gabaud D., Hendry M. A., Molaro P., Chamcham K., A.S.P Conf Series, vol 126,

[19] Bartlett, J. G., Blanchard, A. & Barbosa, D., astro-ph/9808308

[20] Bartlett, J. G,. 2000 : astro-ph/0001267

[21] Begelman, M. C. 1996, in Cygnus A: Study of a Radio Galaxy, ed. C. L. Carilli & D. A. Harris (Cambridge : Cambridge Univ. Press), 209

[22] Begelman, M. C. & Cioffi, D. F. 1989, ApJ, 345, L21

[23] Berezinsky, V. S., Blasi, P., & Ptuskin, V. S., 1997, ApJ, 487, 529

[24] Bernstein, J., Dodelson, S., 1990. PRD, 41, 354

[25] Bialek, J. J., Evrard., A. E., & Mohr, J, 2000, preprint, (astro-ph/0010584)

[26] Bicknell, G. V., Dopita, M. A. & O'Dea, C. P. O. 1997, ApJ, 485, 112

[27] Birkinshaw, M. & Gull, S. F., 1978, Nature, 274, 111

[28] Birkinshaw, M., Gull, S.F., 1983, Nature, 302, 315

[29] Birkinshaw, M., Hughes, J. P., & Arnaud, K. A., 1991, ApJ, 379, 466

[30] Birkinshaw, M. & Hughes, J. P., 1994, ApJ, 420, 33

[31] Birkinshaw, M., 1999, Phys. Repts., 310, 97

[32] Blanchard A., Valls-Gabaud D., Mamon D. A., 1992, A&A, 264, 365

[33] Blanchard, A & Bartlett, J. G., 1998, A.& A, 332, 49L

[34] Blandford, R. D. & Rees, M. J. 1974, MNRAS, 169, 395

[35] Blanton, M., Cen, R., Ostriker, J. P., Strauss, M. A., & Tegmark, M ,2000, ApJ, 531, 1

[36] Bond J. R.,Crittenden R., Davis R. L., Efstathiou G., Steinhardt P. J., 1994, PRL, 72, 13

[37] Bond J. R., Myers, S. T., 1996, ApJS, 57, 211

[38] Bond J. R., Jaffe, A. H., 1998, astro-ph/9809403

[39] Bregman, J. E., Miller, E. D., & Irwin, J. A., 2001, astro-ph/1004317

[40] Brinkman, A. C., 2000, astro-ph/0011018

[41] Bryan G. L., Norman J. L., 1998, ApJ, 495, 80

[42] Bunn E. F., White D., 1997, ApJ, 480, 6

[43] Burles S., Nottel K. M., Turner M. S., astro-ph/9903300

[44] Carlberg, R. G. et al. 1997, astro-ph/9704060

[45] Carlstrom, J.E, Joy, M. & Grego, L., 1996, ApJ, 456, 75

[46] Caroll, S. M., Press, W. H. & Turner, E. L, 1992, ARA&A, 30, 499

[47] Cavaliere, A. & Fusco-Femiano, R., 1978, A & A, 70, 677

[48] Cen, R., Miralda-Escudé, J., Ostriker, J. P., & Rauch, M, 1994, ApJ, 427, L9

[49] Cen, R., & Ostriker, J. P., 1999, ApJ, 519, L109

[50] Challinor, A. & Lasenby, A., 1998, ApJ, 499, 1

[51] Challinor, A. & Lasenby, A., 1999, ApJ, 510, 930

[52] Challinor, A.D., Ford, M.T., & Lasenby, A.N., 2000, MNRAS, 312, 159

[53] Chandrasekhar, S., 1950. 'Radiative Transfer', New York:Dover

[54] Ciardi, B., Ferrara, A., Governato, F. & Jenkins, A. 2000, MNRAS, 314, 611

[55] Colafrancesco S., Mazzotta P., Rephaeli Y., Vittorio N., 1994, ApJ, 433, 454

[56] Colafrancesco, S., & Vittorio, N., 1994, ApJ, 422, 443

[57] Colafrancesco S., Mazzotta P., Rephaeli Y., Vittorio N., 1997, ApJ, 479, 1

[58] Cole, S. & Kaiser, N., 1988, MNRAS, 233, 637

[59] Cooray, A., 1998, A&A, 339, 623

[60] Cooray, A., 2000, PRD, 62, 103506

[61] Cooray, A., Hu, W., & Tegmark, M., 2000, preprint, (astro-ph/0002238)

[62] Cooray, A., 2001a, Ph.D. Thesis, University of Chicago

[63] Cooray, A., 2001b, preprint, astro-ph/0105063

[64] Cowie, L. L. & Binney, J., 1977, ApJ, 215, 723

[65] Cowie, L. L., Songaila, A., Kim, T., & Hu, E. M., 1995, AJ, 109, 1522

[66] Daly, R. A. 1994, ApJ, 426, 38

[67] da Silva, A., Barbosa, D., Liddle, A. R., Thomas, P. A., 1999, astro-ph/9907224

[68] da Silva, A., Barbosa, D., Liddle, A. R., Thomas, P. A., 2000, astro-ph/0011187

[69] Dave', R., Hellsten, U., Hernquist, L., Katz, N., & Weinberg, D. H., 1998, ApJ, 509, 661

[70] Davé, R., Hernquist, L., Katz, N., & Weinberg, D. H., 1999, Proceedings of Recontres Internationales de l'IGRAP, Clustering at High Redshift, Marseille (astro-ph/9910221)

[71] David, L. P., Arnaud, K. A., Forman, W., & Jones, C., 1990. ApJ, 356, 32

[72] David, L. P., Forman, W., & Jones, C, 1990, ApJ, 359, 29

[73] David, L. P., Forman, W., & Jones, C, 1991, ApJ, 380, 39

[74] David, L. P., Jones, C., & Forman, W., 1995, ApJ, 445, 578

[75] Dekel, A. & Silk, J. 1986, ApJ, 303, 39

[76] De Luca, A., Desert, F. X., & Puget, J. L., 1995, A&A, 300, 335

[77] Diego, J.M., Martinez-Gonzalez, E., Sanz, J. L., Benitez, N., & Silk, J., 2001, astro-ph/0103512

[78] Edwards D., Heath D., 1976, Ap Space Science, 41, 183

[79] Efstathiou, G., Bond, J. R., & White, S. D. M., 1982, MNRAS, 258, P1

[80] Eisenstein E. J., Hu W., 1999, ApJ, 511, 5

[81] Ellison S. L., Songaila, L. L., Schaye, J. & Pettini, M., 2000, AJ, 120, 1175

[82] Enßlin, T. A. & Kaiser, C. R. 2000, A& A, 360, 417

[83] Ettori, S., & Fabian, A. C., 1999, MNRAS, 30. 834

[84] Evrard A. E., 1990, in: Clusters of Galaxies, ed: Oegerle W. R., Fitchett M. J., Danly L, Cambridge University Press, New York

[85] Evrard, A. E., 1990, ApJ, 363, 349

[86] Evrard A. E., Metzler C. A., Navarro J. F., 1996, ApJ, 469, 494

[87] Fabian, A. C., Nulsen, P. E. J. & Canizares, C. R. 1984, Nature, 310, 733

[88] Fabian, A. C. 1994, ARAA, 32, 277

[89] Fabian, A., Mushotzky, R. F., Nulsen, P. E. J., & Peterson, J. R., 2000, astro-ph/0010509

[90] Ferrara, A., Aiello, S., Ferrini, J., & Barsella, B., 1990, A & A, 240, 259

[91] Ferrara, A., Pettini, M. & Shchekinov, Y. 2000, preprint, astro-ph/0004349

[92] Fixsen et al. 1996, ApJ, 473, 576

[93] Franx, M., Illingworth, G., Kelson, D., van Dokkum, P. & Tran, K.-V. 1997, ApJ, 486, L75

[94] Fujita, Y., 2000, astro-ph/0012252

[95] Girardi et al., 1996, ApJ, 457, 61

[96] Gnedin, N., & Ostriker, J. P., 1997, ApJ, 486, 581

[97] Gnedin, N., 1998, MNRAS, 294, 407

[98] Gramann, M., 1998, ApJ, 493, 28

[99] Grego, L., Carlstrom, J. E., Joy, M. K., Rees, E. D., Holder, J. P., Patel, S., Cooray, A., & Holzapfel, W. L., 2000, : astro-ph/0003085

[100] Groth E. J., Peeble P. J. E., 1975, A&A, 41, 143

[101] Gurvits, L.I., Mitrofanov, I.G., 1986, Nature, 324, 349

[102] Haiman, Z., Rees, M. & Loeb A. 1997, ApJ, 476, 458 (erratum 484, 985 (1997))

[103] Heath D. J., 1977, MNRAS, 179,351

[104] Heckman, T. 1997, RevMexAA, 6, 156

[105] Heckman, T. M., Armus, L., & Miley, G. K. 1990, ApJS, 74,833

[106] Heckman, T. M., Lehnert, M. D., strickland, D. K. & Armus, L., 2000, ApJS, 129, 493

[107] Henry J. P. et al. 1992, ApJ, 386, 408

[108] Herbig, T., Lawrence, C. R., Redhead, A. C. S., & Gulkis, S., 1995, ApJ, 449, L5

[109] Hernquist, L., Katz, N., Weinberg, D., & Miralda-Escudé, J., 1996, ApJ, 457, L51

[110] Holder, G. P., & Carlstrom, J. E., 1999, preprint, (astro-ph/9904220)

[111] Holder, G.P., Mohr, J.J., Carlstrom, J.E., Evrard, A.E. & Leitch, E.M., 2000, ApJ, 544, 629

[112] Holzapfel, W. L., et al. 1997, ApJ, 480, 449

[113] Holzapfel,W.L, Carlstrom, J.E., Grego, L., Holder, G, Joy, M., & Rees, E.D. 2000, preprint (astro-ph/9912010)

[114] Hu W., Scott D., Silk J., 1994, Phys. Rev. D. 49, 2

[115] Hu W., Sugiyama N., 1996, ApJ, 471, 54

[116] Hu, W., Fukugita, M., Zaldarriaga, M., & Tegmark, M., 2000, preprint, (astro-ph/006436)

[117] Hughes, J. P., Gorenstein, P., & Fabricant, D., 1988, ApJ, 329, 82

[118] Hughes, J. P., & Birkinshaw, M., 1998, ApJ, 501, 1

[119] Inagaki, Y., Suginohara, T. & Suto, Y., 1995, PASJ, 47, 411

[120] Itoh, N., Kohyama, Y. & Nozawa, S., 1998, ApJ, 502, 71

[121] Itoh, N., Nozawa, S. & Kohyama, Y., 2000, ApJ, 533, 588

[122] Jaffe, W. 1980, ApJ, 241, 925

[123] Jing, Y. P., 1999, ApJ, 515, L45

[124] Johnstone, R. M., Fabian, A. C., Edge, A. C. & Thomas, P. A., 1992, MNRAS, 255, 431

[125] Jones C., Forman W., 1984, ApJ, 276, 38

[126] Jones, M. et al. 1993, Nature, 365, 320

[127] Jones M., et al. 1997, ApJ, 479, L1

[128] Kaiser, C. R., Dennett-Thorpe, J. & Alexander, P., 1997, MNRAS, 292, 723

[129] Kaiser N., 1986, MNRAS, 222, 323

[130] Kamionkowski M., Spergel D. L., 1994, ApJ, 432,7

[131] Karzas, W., & Latter, R., 1961, ApJS, 6, 167

[132] Katz, J. I., 1987, 'High energy astrophysics' Addison-Wesley Publishing Company, IL

[133] Kellog, E., Baldwin, J. R. & Koch, D., 1975, ApJ, 199, 299

[134] Kobayashi, S., Sasaki, S., & Suto, Y., 1996, PASJ, 48, 107

[135] Koch, P., 1999, Diploma Thesis, ETH, Zürich

[136] Komatsu, E. & Kitayama, T. 1999, ApJ, 526, L1

[137] Komatsu, E., Kitayama, T., Suto, Y., Hattori, M., Kawabe, R., Matsuo, H., Schindler, S., & Yoshikawa, K., 1999, ApJ, 516, L1

[138] Kompaneets, A.S., 1956. Zh.E.F.T., 31, 876. Translation in Sov. Phys. JETP, 4, 730 (1957)

[139] Lacey C., Cole S., 1993, MNRAS, 262, 627

[140] Lahav, O., Loeb, A., & McKee, C. F., 1990. ApJ, 349, L9

[141] Lahav, O., Lilje, P. B.,Primack, J. R. & Rees, M, 1991, MNRAS, 251, 136

[142] Larson, R. B. 1974, MNRAS, 166, 585

[143] Lehnert, M. D., Heckman, T. M., & Weaver, K. A., 1999, ApJ, 523, 575

[144] Limber, D., 1954, ApJ, 380, 1

[145] Lineweaver C. H., Barbosa D., 1998 ApJ, 496, 624

[146] Loeb, A., McKee, C. F., & Lahav, O., 1991, ApJ, 374, 44

[147] Loeb, A., & Refregier, A., 1996, astro-ph/9610048

[148] Lubin, L. M., & Bahcall, N. A., 1993, ApJ, 415, L17

[149] Ma C. P., 1996, ApJ, 471, 13

[150] Mac Low, M. M. & Ferrara, A. 1999, ApJ, 513, 142

[151] Madau, P., Ferrara, A., & Rees, M., 2000, preprint, astro-ph/0010158

[152] Majumdar, S. & Subrahmanyan, R., 2000, MNRAS, 312, 724

[153] Majumdar, S., Nath, B. B., & Chiba, M., 2000, preprint, (astro-ph/0012016)

[154] Makino, N., & Suto, Y 1993, ApJ, 405, 1

[155] Makino, N., Sasaki, S. & Suto, Y., 1998, ApJ, 497, 555

[156] Markevitch, M., Forman, W. R., Sarazin, C. L. & Vikhlinin, A., 1998, ApJ, 504, 27

[157] Mathiesen, B., Evrard, A. E., & Mohr, J. J., 1999, ApJ, 520, L21

[158] Mathews, W. G., & Bregman, J. N., 1978, ApJ, 224, 308

[159] Matteucci, F. & Tornambe, A. 1987, A&A, 185, 51

[160] McCray, R. & Kafatos, M., 1987, ApJ, 317, 190

[161] McKee, C. & Ostriker, J. P., 1977, ApJ, 218, 148

[162] McKinnon, M.M., Owen, F.N., Eilek, J.A., 1990, AJ, 101, 2026

[163] Metzler, C. A., & Evrard, A. E., 1994, ApJ, 437, 564

[164] Metzler, C. A., & Evrard, A. E., 1997, preprint, astro-ph/9710324

[165] Miniati, F., Ryu, D., Kang, H., & Jones, T. W., preprint, astro-ph/0105465

[166] Miralda-Escudé, J. & Rees, M. J. 1997, ApJ, 478, 57L

[167] Mohr, J. J., Evrard, A. E., Fabricant, D. G., & Geller, M. J., 1995, ApJ, 447, 8

[168] Mohr, J. J.,Mathiesen, B., & Evrard, A. E., 1999, ApJ, 517, 627

[169] Molnar, S.M. & Birkinshaw, M., 1999, ApJ, 523, 78

[170] Molnar, S. M. & Birkinshaw, M., 2000, ApJ, 537, 542

[171] Moscardini, L., Branchini, E., Brunozzi, P. T., Borgani, S., Plionis, M. & Coles, P., 1996, MNRAS, 282, 384

[172] Myers, S.T., Baker, J.E., Redhead, A.C.S, Leitch, E.M., Herbig, T., 1997, ApJ, 485, 1

[173] Natarajan, P. & Sigurdsson, S. 1999, MNRAS, 302, 288

[174] Nath, B. 1995, MNRAS, 274, 208

[175] Nath, B. B. & Chiba, M., 1995, ApJ, 454, 604

[176] Nath, B. B. & Trentham, N. 1997, MNRAS, 291, 505

[177] Navarro, J. F., Frenk, C. S., & White, S. D. M., 1997, ApJ, 40, 493

[178] Netterfield, C. B. et al. 2001, astro-ph/0104460

[179] Nozawa, S., Itoh, N. & Kohyama, Y., 1998a, ApJ, 508, 17

[180] Nozawa, S., Itoh, N. & Kohyama, Y., 1998b, astro-ph/9802096

[181] Nozawa, S., Itoh, N., Kawana, Y. & Kohyama, Y., 2000, ApJ, 536, 31

[182] Nulsen, P. E. J., 1986, MNRAS, 221, 377

[183] Ostriker, J. P., & McKee, C., 1988, Rev. Mod. Phy., 60, 1

[184] Oukbir, J. & Blanchard, A., 1992, A & A, 262, 21L

[185] Oukbir, J. & Blanchard, A., 1997, A & A, 317, 1

[186] Padmanabhan, T., 1993, Structure Formation in the Universe, Cambridge University Press, Cambridge

[187] Padmanabhan T., Subramanian K., 1992, Bull. astr. Soc. India, 20, 1

[188] Padmanabhan, T., & Sethi, S., 2000, preprint, (astro-ph/0010309)

[189] Parijskij, Yu.N., 1973, Sov. Astr., 16, 1048

[190] Patel, S.K. et al. 2000, ApJ, 541, 37

[191] Peacock, J. S., & Heavens, A. F. 1990, MNRAS, 243, 133

[192] Peacock J. A., Dodds S. J., 1994, MNRAS, 267, 1020

[193] Peacock, J. A., 1999, Cosmological Physics., Cambridge University Press

[194] Peebles P. J. E., 1980, Large Scale Structure of the Universe., Princeton University Press, Princeton

[195] Peebles P. J. E., 1984, ApJ, 284, 439

[196] Peres, C. B., Fabian, A. C., Edge, A. C., Allen, A. W., Johnstone, R. M., & White, D. A.. 1998, MNRAS, 298, 416

[197] Perlmutter S., et al. 1998, Nature, 391, 51

[198] Persi F. M., Spergel D. N., Cen R., Ostriker J. P., 1995, ApJ, 442, 1

[199] Peterson et al. 2000, in A&A (XMM etc)

[200] Pettini, M., Kellogg, M., Steidel, C., Dickinson, K. E., Adelberger, K. L. & Giavalisco, M. 1998, ApJ, 508, 539

[201]

[202] Peebles, P. J. E., 1980, "Large Scale Structure of the Universe", Princeton, Princeton University Press

[203] Phillips, P.R., 1995, ApJ, 455, 419

[204] Pointecouteau, E., Giard, M., Benoit, A., Désert, F. X., Aghanim, N., Coron, N., Lamarre., J. A., & Delabrouille, J., 1999, ApJ, 519, L115

[205] Pointecouteau, E., Giard, M., Benoit, A., Désert, F. X., Bernard, J. P., Coron, N., & Lamarre, J. M., 2001, ApJ, 552, L42

[206] Ponman, T. J., Bourner, P. D. J., Ebeling, H., & Bohringer, H., 1996, MNRAS, 283, 690

[207] Press, W. H. & Schecter, P., 1974, ApJ, 187, 225

[208] Puy, D., Grenacher, D., Jetzer, P., & Signore, M., 2000, astro-ph/0009114

[209] Pyne, T., Birkinshaw, M., 1993, ApJ, 415, 459

[210] Rauch, M, Haehnelt, M. G., & Steinmitz, M., 1997, ApJ, 481, 601

[211] Rauch, M et al. 1998, ApJ, 489, 1

[212] Rawlings, S. & Saunders, R. 1991, Nat, 229, 312

[213] Rees, M. J. & Sciama, D., 1968, Nature, 217, 511

[214] Reese, E. D., et al. 1999 : astro-ph/9912071

[215] Reese, E.D. et al. 2000, ApJ, 533, 38

[216] Refregier, A., Komatasu, E., Spergel, D. N. & Pen, U.-L., 2000, PRD, 61, 123001

[217] Refregier, A., & Teyssier, R., 2000, astro-ph/0012086

[218] Rephaeli, Y., 1981, ApJ, 245, 351

[219] Rephaeli, Y., 1993, ApJ, 418, 1

[220] Rephaeli, Y., 1995a, APJ, 445, 33

[221] Rephaeli, Y., 1995b, ARA&A, 33, 541

[222] Rephaeli, Y., Lahav, O., 1991.ApJ, 372, 21

[223] Rephaeli, Y., Silk, J., 1995, ApJ, 442, 91

[224] Rephaeli, Y., Yankovitch, D, 1997, ApJ, 481, L55

[225] Richards E. A,, Fomalont E. B., Kellermann K. I., Partridge R. B., Windhorst R. A., 1997, AJ, 113, 1475

[226] Rines, K., Forman, W., Pen, U., Jones, C., & Burg, R., 1999, ApJ, 517, 70

[227] Rizza, E., Loken, C., Bliton, M., Roettiger, K., & Burns, J., 2000, ApJ, 119, 21

[228] Roettiger, K., Stone, J. M. & Mushotzky, R. F., 1997, ApJ, 482, 588

[229] Rybicki, G.B., Lightman, A.P., 1980. 'Radiative Processes in Astrophysics'. New York:Wiley

[230] Tsuboi, M., Miyazaki, A., Kasuga, T., Matsuo, H., Kuno, N., 1998, PASJ, 50, 169

[231] Sadat, R. & Blanchard, A., 2001, preprint (astro-ph/0102010)

[232] Sarazin, C. L. 1986, Rev. Mod. Phys., 58, 1

[233] Sarazin, C. L., 1988, X-ray emission from clusters of galaxies, Cambridge Astrophysics Series

[234] Sarazin, C. L. & White, R. E. 1987, ApJ, 320, 32

[235] Sarazin, C. L. & Graney, C. M. 1991, ApJ, 375, 532

[236] Sasaki, S., 1996, PASJ, 48, L119

[237] Saunders, R., 1995. Ap. Lett. Comm., 32, 339

[238] Saunders, R. et al. 1999: astro-ph/9904168

[239] Sazonov, S. Y., & Sunyaev, R. A., 1999, astro-ph/9903287

[240] Scannapieco, E. & Broadhurst, T. 2000 (astro-ph/0003104)

[241] Scaramella, R., Cen, R., & Ostriker, J. P., 1993, ApJ, 416, 399

[242] Scheuer, P. A. G. 1982, in IAU symp. 97, Extragalactic Radio Sources, ed. D. S. Heeschen & C. M. Wade (Dordrect : Reidel), 163

[243] Schindler, S., 1999, A&S, 349, 435

[244] Schlickeiser, R. 1991, A & A, 128, 23L

[245] Schmutzler, T. & Tscharnuter, W. M. 1993, A & A, 273, 318

[246] Seljak, U., Burwell, J., & Pen, U., 2000, astro-ph/0001120

[247] Sheth, R. K., & Tormen, G., 1999, MNRAS, 308, 119

[248] Shu, F. H., 1991. 'The physics of astrophysics, Volume 1: Radiation', University Science Books, Mill Valley, CA

[249] Silk, J. & White, S.D.M., 1978, ApJ, 226, L103

[250] Silverberg, R. F. et al, 1997, ApJ, 485, 22

[251] Smoot G. F.,et al. 1992, ApJ, 396, L1

[252] Soker, N. & Sarazin, C. L. 1988, ApJ, 327, 66

[253] Songaila, A., & Cowie, L L., 1996, AJ, 112, 335

[254] Songaila, A., 1997, ApJ, 490, L1

[255] Springel, V., White, M., & Hernquist, L., 2000, astro-ph/0008133

[256] Srianand, R., Petitjean, P., & Ledoux, C., 2000, astro-ph/0012222, to appear in Nature

[257] Sulkanen, M., 1999, ApJ, 522, 59

[258] Subrahmanyan R., Ekers R. D., Sinclair M., Silk J., 1993, MNRAS, 263, 416

[259] Subrahmanyan R., & Saripalli, S., 1993, MNRAS, 260, 908

[260] Subrahmanyan R., Kesteven M. J., Ekers R. D., Sinclair M., Silk J., 1998, MNRAS, 298, 1189

[261] Subrahmanyan R., Kesteven M. J., Ekers R. D., Sinclair M., Silk J., 1999, MNRAS, submitted

[262] Sugiyama, N., 1995, ApJS, 100, 281

[263] Sulkanen, M. E., Burns, J. O. & Norman, M. L. 1989, ApJ, 344, 604

[264] Sunyaev, R.A., 1980. Pis'ma Astron. Zh., 6, 387; translation in Sov. Astr. Lett., 6, 213

[265] Sunyaev, R.A.,& Zel'dovich, Ya.B., 1972. Comm. Astrophys. Sp. Phys., 4, 173

[266] Sunyaev, R.A., Zel'dovich, Ya.B., 1980a. ARA&A, 18, 537

[267] Sunyaev, R.A., Zel'dovich, Ya.B., 1980b, MNRAS, 190, 413

[268] Suto, Y., Sasaki, S. & Makino, Y., 1998, ApJ, 509, 544

[269] Suto et al., 1999, Advances in Space Research, in press

[270] Taylor, G.B., Wright, E.L., 1989, ApJ, 339, 619

[271] Tegmark, M., Silk, J., & Evrard, A. 1993, ApJ, 417, 54

[272] Tegmark, M. & Peebles, P. J. E. 1998, ApJ, 500, L79

[273] Thomas, P., Fabian, A. C. & Nulsen, P.E.J. 1987, MNRAS, 228, 973.

[274] Thoul, A. & Weinberg, D. 1996, ApJ, 465, 608

[275] Tozzi P., Governato F., in : The Young Universe: Galaxy formation at Intermediate and High Redshifts, ed: Fontana A., Giallongo E., ASP Conference Series, vol 146, 1998, 461

[276] Tsuboi et al. 1998, PASJ, 50, 169

[277] Tsuru T.G., et al. 1997, preprint, (astro-ph/9711353)

[278] Valageas, P., Silk, J. & Schaeffer, R , 2000, astro-ph/0001207

[279] Viana, P. T. P., & Liddle, A., 1996, MNRAS, 281, 323

[280] Vittorio N., Colafranseco S., Mazzotta P., Rephaeli Y., 1997 in : Microwave Background Anisotropies, Proceedings of XIV Moriond Astrophysics Meetings, ed: Bouchet F., Gispert R., Guiderdoni B., Jean Tran Thanh Van

[281] Vishniac, E. T., 1987, ApJ, 322, 597

[282] Voit, G. M., & Donahue, M., 1998, ApJ, 500, L111

[283] Waxman, E. & Miralda-Escude', J., 1995, ApJ, 451, 451

[284] Weaver, R., McCray, R., Castor, J., Shapiro, P., & Moore, R., 1977, ApJ, 218, 377

[285] Weinberg, D. H., Miralda-Escudé, J., Hernquist, L. & Katz, N. 1997, ApJ, 490, 564

[286] Weinberg S., 1972, Gravitation and Cosmology., John Wiley & Sons Inc., New York

[287] White, D. A., & Fabian, A. C., 1995, MNRAS, 273, 72

[288] White, M., Carlstrom, J.E., Dragovan, M. & Holzapfel, W.L., 1999, ApJ, 514, 12

[289] White, R. E., & Sarazin, C. L., 1987, ApJ, 318, 629

[290] White S. D. M., Navarro J. F., Evrard A. E., Frenk C. S., 1993, Nature, 366, 429

[291] Wise, M. W. & Sarazin C. L., 1993, ApJ, 415, 58

[292] Wright, E.L., 1979, ApJ, 232, 348

[293] Wu, K. K. S., Fabian, A. C., & Nulsen, P. E. J., 1999, astro-ph/9907112

[294] Yamada, M., Sugiyama, N. & Silk, J. 1999, ApJ, 522, 66

[295] Yamada, M., & Fujita, Y., 2001, astro-ph/0105102

[296] Yoshikawa, K., Itoh, M. & Suto, Y., 1998, PASJ, 50, 203

[297] Yoshikawa, K., & Suto, Y., 1999, ApJ ,513, 549

[298] Zel'dovich, Ya. B., & Sunyaev, R. A. 1969, Ap&SS 4, 301;

[299] Zhang, P., & Pen, U., 2000, astro-ph/0007462

" The Moving Finger writes; and, having writ
Moves on: nor all the Piety nor Wit
Shall lure it back to cancel half a line,
Nor all thy Tears wash out a Word of it.

Ah, but my Computations, People say,
Reduced the Year to better Reckoning? - Nay,
'Twas only striking from the Calendar
Unborn Tomorrow, and dead Yesterday "

Rubáiyát of Omar Khayyám

TAMAM SHUD